UNIVERSIDAD COMPLUTENSE DE MADRID

FACULTAD DE CIENCIAS FÍSICAS

TESIS DOCTORAL

Cambio climático: sensibilidad a la termodinámica y la hidrología del subsuelo

Climate change sensitivity to the thermodynamics and the hydrology of the subsurface

MEMORIA PARA OPTAR AL GRADO DE DOCTOR

PRESENTADA POR

Félix García Pereira

DIRECTOR

Jesús Fidel González Rouco

UNIVERSIDAD COMPLUTENSE DE MADRID

FACULTAD DE CIENCIAS FÍSICAS

Programa de Doctorado en Física

TESIS DOCTORAL

Cambio climático: sensibilidad a la termodinámica y la hidrología del subsuelo

Climate change sensitivity to the thermodynamics and the hydrology of the subsurface

MEMORIA PARA OPTAR AL GRADO DE
DOCTOR EN FÍSICA

Presentada por
Félix García Pereira

Director
Jesús Fidel González Rouco

Madrid, 2025

Funding and technical support

Félix García Pereira was funded by the *Formación de Personal Investigador* (FPI) contract no. PRE2019-090694, which was financially supported by the GreatModelS (RTI2018-102305-B-C21) and SMILEME (PID2021-126696OB-C21) projects from the *Ministerio de Ciencia e Innovación* (MICINN). The FPI contract (PRE2019-090694) also financed a short stay of 3 months at the Max Planck Institute for Meteorology (MPI-M, Hamburg, Germany). He also received some funding for traveling by the *Consejo Superior de Investigaciones Científicas* (CSIC) under the call i-LINK 2021, project no. LINKB20082. The last part of his thesis was funded by the PTI Clima, a joint collaboration initiative between the *Agencia Estatal de Meteorología* (AEMET) and CSIC, under contract no. E-28-2024-1735868.

The climate simulations with the MPI-ESM1.2-LR and its land module, JSBACH, used in this thesis were conducted with computing resources granted by the Scientific Steering Committee (WLA) of the Deutsches Klimarechenzentrum (DKRZ), under project ID bm1026. We also acknowledge the availability of data coming from the Coupled Model Intercomparison Project (CMIP) simulations and provided by the World Climate Research Programme's Working Group on Coupled Modeling. The subsurface temperature data in Sierra de Guadarrama presented in this thesis were collected by the Guadarrama Monitoring Network (GuMNet) and AEMET.

Agradecimientos / Acknowledgements

Estos cinco años han pasado verdaderamente rápido. Todavía vivíamos inmersos en la pandemia que puso el mundo del revés cuando Fidel me ofreció embarcarme en esta aventura a la que llaman doctorado. Si os soy sincero, jamás había pensado en la posibilidad de hacer un doctorado. Temido por muchos y sufrido por unos pocos, diría que doctorarse te coloca los pies en la tierra, y la cabeza en su sitio. Hoy en día, en un mundo regido por la métricas propias de un sistema económico capitalista neoliberal, parecería que el doctorado consistiese en publicar dos (quizás tres) artículos en revistas científicas de cierto impacto. Sin embargo, echando la vista atrás, diría que el doctorado es mucho más que eso. Es un viaje intelectual, pero también personal. Son esas decenas de charlas y seminarios apasionantes que abren mentes, y derriban prejuicios. Son esas tardes y noches de flexo, café y frustración cuando las cosas no salen, y de alegría y celebración cuando se resuelven los problemas. Son esos plots, mil veces repetidos, y esos códigos y programas que acaban perdidos en la última de las carpetas y acabas utilizando años después. Es ese borrador que va tomando forma en el cajón, y zarandeado por mil bolígrafos rojos (o plumas azules, según el gusto personal del revisor) acaba publicado. Es ese primer congreso con tu gente de la "facul", y sus incontables cervezas. Son esas conversaciones de café con la gente del grupo, de las que salen innumerables ideas científicas, y no tan científicas. Y es, por encima de todo, ese apoyo constante de aquellos que desde dentro y fuera de la ciencia te quieren, respetan y acompañan en esta fase del camino, quizá la más importante de la vida de un científico.

A todos ellos, ¡gracias, gracias, y gracias! Gracias Fidel, por ser un director estupendo, un científico riguroso, un confidente, y un amigo. Hemos compartido muchas cosas, hasta habitación de hotel. Hemos discutido mucho, científica y no científicamente (a veces hasta enseñarnos los dientes), pero nuestro amor y respeto intelectual siempre ha prevalecido. Me llevo una formación inmensa y una experiencia vital que sin ti simplemente no habría tenido lugar. Gracias Cristina por ser mi eterna escudera. Recuerdo aquel día que nos conocimos en el despacho de Fidel cuando yo todavía no era técnico de GuMNet. Creo que una de las razones por las que decidí aceptar el trabajo fue por la buena impresión que me causó la que sería mi futura compañera de trabajo. Desde el primer día me recibiste con cariño y alegría, y procuraste compartir conmigo todo lo que sabías. Por tu respeto, amor, y generosidad, y sobre todo por los laaaargos tutoriales de Shell, gracias. A este binomio se han unido más recientemente Nagore y Luana (mi niiiiiña). Gracias a las dos por aparecer en el camino. Habéis compartido conmigo un cambio de instituto (en el caso de Luana añadido a una mudanza intraibérica) y la construcción de una pequeña familia en un nuevo lugar. Creo que esta última fase del doctorado no sería sin vosotras. Luana, me quedo con tu cariño y con tu eterna generosidad. Siempre estás atenta a que todos estemos bien, muchas veces sacrificando tu propio bienestar. ¡Lo que unió Iberia que no lo separe Portugal! Nagore, las tía chula del grupo, gracias por acompañarme estos dos últimos años. Tener una nueva compañera tiene sus retos y dificultades, pero creo que hemos aprendido a entendernos y trabajar bien en equipo, pese a nuestras diferencias. Juntos podemos más. Gracias Elena y Jorge por compartir conmigo tantos momentos buenos estos últimos años. Aunque estéis retirados en vuestra aldea gala particular (algunos lo llaman CIEMAT), siempre estáis presentes. Elena, gracias por ser una persona tan cariñosa, empática, y cercana. Es difícil conocer a gente que le brinde tanto amor a los demás como lo haces tú. Jorge, gracias por ser un tío tan entrañable, abierto y generoso. Estoy seguro de que repetiremos paellas, cenas de traje (lo que pillé por casa) y viajes a Hamburgo. Espero que en el futuro se una a estos viajes Sara, la más reciente incorporación al grupo. Todavía no nos conocemos mucho, pero estoy seguro de que compartiremos buenos momentos. No quiero cerrar este párrafo sin dedicarle un recordatorio a l@s chic@s del IGEO: Alejandra, Bernat, Blanca, Ignacio, Isa, Manu, Marta, Nora, Samu, Tanea y Teresa. Gracias por hacerme el cambio a un nuevo sitio de trabajo tan fácil, sois estupend@s.

Me voy ahora a por mi gente de PalMA-ICE. Gracias Dani por acompañarme en este camino. No diría que nos descubrimos en el máster, pero qué buena casualidad que la ciencia nos juntara en el doctorado. Tener un amigo tan friki como yo con el que poder discutir sobre la ecuación de conducción del calor,

y a la vez poder estar diciendo paridas una hora seguida es un lujo al alcance de muy pocos. Creo que los dos hemos crecido juntos como científicos, y eso es una suerte. Es una suerte, y también un estímulo intelectual, tener a una persona con tanto talento a tu lado. Allá donde estés, en Bélgica, o petándolo en el MIT con tus ecuaciones e ideas felices, siempre te echaré de menos. Hablando de paridas, no podía faltar en la salsa mi querido Sergi. Gracias por ser el tío con las opiniones más férreas del laboratorio. Haber compartido cientos de cafés y eternas discusiones contigo me ha enseñado mucho, ¡¡sobre todo paciencia!! Eres un paleoclimatólogo brillante, y una persona curiosa y fascinante, no pierdas tu esencia. Otro que me ha dado buenas alegrías ha sido mi querido políglota de dos metros, Jan Swierczek Jereczek. Gracias por ser una persona tan especial. Tu mente es tan bonita y compleja como tus outfits (y tus apellidos). Creo que hablo por todos cuando digo que siempre tienes un punto de vista interesante, una sugerencia constructiva, o una palabra de apoyo en el momento necesario. Espero que sigamos compartiendo la pasión que tenemos por la cocina: que sepas que mis lentejas las voy a seguir haciendo con chorizo. Lucía, la representante de Adidas infiltrada en el grupo, gracias por hacernos reír a todos en los días malos. Aunque llegaste más tarde al grupo, creo que has contribuido a crear una atmósfera chula que hace que nos sintamos todos más en familia. No olvidaré tus historias con final imprevisto que te mantienen en vilo hasta el final, eres una mina de anécdotas memorables. Antonio, gracias por tu paciencia y generosidad. Siempre que he necesitado ayuda con burocracias o procedimientos varios has estado ahí para ayudarme. Hemos compartido además muchas conversaciones interesantes en Viena, y en Madrid. Sigue siendo fiel a ti mismo y a las cosas que te gustan, que nadie te diga cómo tienes que vivir. Marisa y Jorge, gracias por ser mis segundos padrinos científicos. Marisa, gracias por compartir con todos nosotros tu sabiduría, rigor y saber hacer investigadores. Gracias también por cuidarnos a todos con cariño, y procurar que la ciencia del día a día sea más llevadera en un entorno burocrático y académico cada vez más hostil. No pierdas tu pasión por la actualidad, y por la significación y reivindicación políticas cuando los demás se quedan callados. Jorge, gracias por compartir conmigo tu insaciable curiosidad científica. No dejes de ser una fuente inagotable de preguntas interesantes. Conocer a personas como tú es muy inspirador para quienes vienen detrás.

No me olvido de mi gente de TROPA. Elena, gracias por tu eterna sonrisa. A veces decidida, a veces poseída por la pachorra, tienes esa magia de las personas buenas. Siempre estás ahí para sacarnos a todos una risas con tus anécdotas y ocurrencias. Nos lo hemos pasado muy bien juntos, y me llevo muy buenos recuerdos. Estoy seguro de que seguiremos sumando viajes (espero que no Hackatones) a nuestra lista de vivencias compartidas. Lucía TROPA, gracias por ser

tan cariñosa y tan cercana. En un mundo individualista y a veces socialmente hostil, creo que es realmente difícil encontrar personas tan empáticas como tú. Gracias por ser tan buena confidente. Sigue siendo tan chiripitifláutica como eres, mantén ese hambre insaciable por la lectura y el arte, y no pierdas esa generosidad tan buena que tienes. Álvaro, nuestro imbatible montañero, gracias por compartir esta aventura conmigo desde el principio. Eres un currante nato, y un compañero dispuesto a ayudar a quien haga falta para que salga del paso. No pierdas tu pasión por la escalada, ni por la cerveza al sol en paraninfo los jueves por la tardes (a partir de las 6). Pablo y Víctor, gracias por apoyarme en esta última etapa. Sois dos científicos brillantes, y dos jugadores de pádel sobresalientes. El mundo se lleva dos talentos inconmensurables, y con un gran corazón. Antonio TROPA, Pablo Ortega (Ortiz) Corral (alias POC), Juan, Víctor, Javi, Ilaria... Son muchas las personas que habéis sido parte activa de mi viaje estos años. A todos vosotros, y a los que me deje por el camino, gracias por brindarme vuestro tiempo.

Por último, me gustaría dedicarle unas palabras cariñosas a los míos, a los de casa. Javi, gracias por acompañarme en este camino, y en todos los demás. Me brindas cariño, paz, y felicidad todos los días. Gracias por ser tan generoso, por aguantarme en los días malos (y en los no tan malos), y por reinventar la rutina para que la vida sea más amena. No sé qué haría sin ti. Lucía, gracias por crecer conmigo año a año. Nos hemos convertido en dos adultos de los que aquellos adolescentes estarían bien orgullosos. Gracias por sufrir esta etapa conmigo, y por invitarme a vino y darme los mejores consejos cuando los necesito. En el crecimiento año a año no pueden faltar mis más viejos amigos, Alicia y Marcos. Alicia, gracias por ser mi hermana no-de-sangre, y por acompañarme en todas las etapas de la vida desde que tengo uso de razón. Eres una inspiración tan grande que es difícil imaginar que habría sido de mí sin ti; si hoy soy casi doctor es en gran parte gracias a ti. Marcos, gracias por ser mi confidente y amigo desde la tierna pre-adolescencia. Hemos vivido tantas cosas juntos que me es muy difícil imaginarme un futuro sin ti. Es poético que mientras yo deposito esta tesis, tu te conviertes en FEA (sin ser nada de eso tú). Seguro que seguimos consiguiendo cosas juntos. Mis niñas de Villalba, Alba, Ana, Estela y Vero, gracias por estar siempre a mi lado. Desde distintos momentos de nuestra adolescencia, hemos aparecido en nuestras vidas y nos hemos querido y cuidado hasta hoy. Mola ver que pese a que ya lo hemos hecho todo junt@s, nos seguimos reinventando: lo que Villalba unió que no lo separe la Alpargata Rota y su pareja. A este selecto club también pertenecen Marina, Paula, Raquel y Armando, cuya compañía y amistad quiero agradecer. Armando, gracias por ser mi terapeuta gratuito y mi gurú vital. Mi gran evolución personal y sentimental estos últimos años no se en-

tiende sin ti. Nos quedan muchos paseos por Casa de Campo, muchos y abrazos, y muchas cañas en la Paula. Espero que a esas cañas también se nos una de vez en cuando Gonzalo, el otro miembro del team Márquez. Gracias por acogerme también cuando llegué al barrio y por hacerme reír con tus anécdotas locas y ocurrencias variadas. Por último, no me quiero olvidar de mi búnker, Dani, Irene y Raúl. Gracias por compartir conmigo tantas fiestas del pueblo, viajes, y experiencias memorables. Juntos nos hemos reído, hemos llorado (alguna que otra vez), y nos hemos confesado. Seguro que nos quedan muchos momentos por vivir. A tod@s vosotr@s, y a la gente que me deje por el camino (mi memoria no pasa por su mejor momento) ¡¡Os quiero mucho mucho mucho!!

Por último, quería dedicarles esta tesis a mis padres, por haberme dado las bases para llegar hasta aquí, cada uno a su manera. Gracias mamá por tu amor incondicional, tu presencia constante y tu apoyo en los momentos felices, pero también en los difíciles. Has sido mi mayor sostén a lo largo de este camino. Gracias papá por tu apoyo generoso en momentos clave de mi vida y por tu parte en todo lo que he llegado a ser. A demás familia, en Valladolid, Vigo, o Terrassa, gracias infinitas. Os quiero mucho a tod@s.

To conclude, I would also like to have a few words in English for the non-Spanish speakers. Thank you Johann for the fantastic months in Hamburg. I enjoyed much our cultural excursions and interesting talks together with Gesine. Thank you also for inviting me to give a talk in the Joint Seminar Cycle of the MPI-M as part of my stay there. It was an amazing opportunity to doing an overview and outreaching the activity I did in my PhD. In that regard, I am also very grateful to Stefan Hagemann for his warm welcome at HEREON. Thank you for sharing your expertise and for welcoming me so generously into your home. I would also like to thank the scientific support of my collaborators at the MPI-M, Philipp de Vrese, Stephan Lorenz, and Tobias Stacke. I would also like to have a especial mention for the friends I made in Hamburg and contributed to feel it home: Quan, Nina, Amruta, Marius, Julian, Moritz, Danai, Xiuhua, Fetimeh, and Dian. Thank you for all the moments we shared, the dinners and conversations, and for supporting me with dealing with the cold and darkness. My stay at the MPI-M would not have been the same without you.

Contents

Climate change sensitivity to the thermodynamics and the hydrology of the subsurface

Nowadays, the Earth is experiencing a fast climate change due to the emission of greenhouse gases and aerosols resulting from human activity. The net effect of these emissions is a positive energy imbalance of about 1 W/m^2, which has resulted in a global warming of more than 1 ^oC since the mid-19th century. This warming affects the various components of the climate system (ocean, atmosphere, cryosphere, land surface, and biosphere) in different ways, leading to changes in their respective states and interactions. Due to its lower thermal inertia and static nature, the land surface has warmed more than the ocean, by approximately 1.6 ^oC relative to the 1850–1900 mean. This intense warming impacts on various key soil processes that are relevant in the interaction between the atmosphere and the land surface and thus influence continental climate. Some of these processes are related to soil moisture availability and are part of the hydrological cycle, such as surface runoff, infiltration, evaporation, or drainage. Other processes have different kinds of nature: thermodynamic, like the soil temperature variability and thermal propagation with depth; hydro-thermodynamic, like permafrost thaw or desertification; biological, as soil respiration; or mechanical, like erosion. This thesis focuses on the hydro-thermodynamic role of the soil, its relevance to other terrestrial and atmospheric processes and its potential feedback to global warming.

Aim of the study

The main objectives of this thesis are to expand the current understanding of the processes that shape the hydro-thermodynamics of the soil and subsurface

layers, and to analyze the sensitivity of climate change to modifications in these processes. More specifically, the thesis aims at characterizing the transport and storage of underground heat as a direct consequence of surface warming, with a particular focus on its interaction with soil hydrology. This interaction is especially sensitive and relevant to the global climate in high-latitude regions, where permafrost thaw has the potential to release large amounts of carbon-rich trace gases, such as methane, thereby intensifying global warming. To achieve the objectives of this thesis, both observational data and climate simulations have been employed. Observational soil monitoring data are often scarce and primarily limited to shallow depths, with deep observations being rare. By contrast, climate models offer a continuous but simplified representation of soil thermodynamics, which poses challenges in analyzing the impacts of climate change on soil thermodynamics and hydrology. The integration of these two approaches allows for a more comprehensive and robust assessment of the objectives of this thesis.

Main results and conclusions

The first objective of this work is to analyze the observational thermodynamic regime of the subsurface using a subsurface temperature database extending down to 20 meters depth from a set of six weather stations in the *Sierra de Guadarrama*. Heat conduction at these sites is characterized by evaluating the attenuation and phase shift of the annual surface temperature wave with depth, rendering estimates of the thermal diffusivity. The results illustrate the overall conductive nature of the subsurface, with a quasi-linear increase in thermal diffusivity with depth, more intense in the transition between soil and bedrock. This increase indicates that changes in the parent material composition produce variations in thermal diffusivity. In order to analyze these variations at shorter time scales than the annual wave, a new spectral methodology is introduced. The spectral methodology assesses the underground attenuation of the entire spectrum of harmonics that conform the surface temperature signal. The analysis of temperature series down to one meter depth revealed that seasonal soil moisture changes can induce thermal diffusivity changes, thus opening the possibility of estimating soil moisture from temperature.

The analysis of subsurface hydro-thermodynamics at longer time scales requires of climate model experiments. The representation of subsurface thermodynamics in Land Surface Models (LSMs) that are part of the latest generation of Earth System Models (ESMs) is based on the conductive hypothesis. However, LSMs resolve heat propagation imposing a zero-flux bottom boundary condi-

tion at a finite depth (bottom boundary condition placement, BBCP), rather than treating the subsurface as semi-infinite, as in the real-world. This depth is usually insufficient, which results in an underestimation of the land heat uptake and an overestimation of positive temperature trends with depth associated with global warming. Previous works demonstrated that changes in the depth of the BBCP do not impact surface temperature variability using standalone LSM simulations. In this work, the validity of this statement is tested using two fully-coupled simulations of the last two millennia (0–2100 CE) with the Max Planck Institute Earth System Model (MPI-ESM), one with a BBCP at 10 m and another at 1,400 m. The results show that changing the BBCP depth has no impact on surface temperature variability in coupled simulations. This allows for the use of surface temperatures as the upper boundary condition to obtain corrected estimates of the land heat uptake from different data sources (observational databases, reanalyses, ESMs) using a simple one-dimensional heat conduction model. The estimates obtained show a clear dependence of the land heat uptake on the BBCP depth. It is also demonstrated that this dependence stems from a reduction in the ground heat flux, which in turn leads to an overestimation of the sensible and latent turbulent heat fluxes at a global scale and in humid areas, respectively. Therefore, limiting the BBCP depth has implications for the long-term surface energy balance under global warming.

Finally, this thesis seeks to understand the interaction between soil thermodynamics and hydrology. This interaction is especially relevant for soils subjected to phase changes in soil moisture, such as permafrost. For that purpose, a set of experiments with different representations of the mean hydrological state, depth, and discretization in the historical period and future warming scenarios (MPIESM-PePE) is conducted using a modified version of the MPI-ESM with a more realistic soil hydrology in permafrost regions. The results show a clear impact of soil hydrology and BBCP depth in producing changes in future projections of permafrost extent loss and active layer subsidence with climate change. Overall, the results of this thesis underscore the need to improve the representation of the subsurface hydro-thermodynamics in climate models.

Cambio climático: sensibilidad a la termodinámica y la hidrología del subsuelo

En la actualidad, la Tierra experimenta un proceso acelerado de cambio climático provocado por la emisión de gases de efecto invernadero y aerosoles derivados de la actividad humana. El efecto neto de estas emisiones es un desequilibrio energético positivo de aproximadamente 1 W/m^2, lo que ha dado lugar a un calentamiento global superior a 1 ^oC desde mediados del siglo XIX. Este aumento de temperatura afecta de forma distinta a las distintas componentes del sistema climático (océanos, atmósfera, criosfera, superficie terrestre y biosfera), alterando su estado y sus interacciones. Como resultado de su menor inercia térmica y naturaleza estática, la superficie terrestre se ha calentado más que los océanos, alcanzando un aumento aproximado de 1,6 ^oC respecto al promedio de 1850–1900. Este calentamiento afecta a numerosos procesos fundamentales del suelo que influyen en la interacción entre la atmósfera y la superficie terrestre, y por tanto, en el clima continental. Algunos de estos procesos están relacionados con la humedad de suelo y son parte del ciclo hidrológico, como la escorrentía, infiltración, evaporación y drenaje, mientras que otros tienen carácter termodinámico (como la propagación de temperatura en profundidad), hidro-termodinámico (como el deshielo del permafrost o la desertificación), biológico (como la respiración del suelo) o mecánico (como la erosión). La presente tesis se centra en el papel hidro-termodinámico del suelo, su relevancia para otros procesos terrestres y atmosféricos y su posible retroalimentación del calentamiento global.

Objetivos principales del estudio

Los principales objetivos de esta tesis son ampliar el conocimiento sobre los procesos que regulan la hidro-termodinámica del subsuelo, y analizar cómo cambios en estos procesos pueden afectar al clima. Se busca caracterizar cómo se transporta y almacena el calor en el subsuelo como consecuencia directa del calentamiento superficial, poniendo énfasis en su interacción con la hidrología del suelo. Este vínculo es especialmente sensible y relevante en las regiones de altas latitudes, donde el deshielo del permafrost podría liberar grandes cantidades de gases de efecto invernadero como el metano, intensificando el calentamiento global. Para abordar estos objetivos, se han utilizado tanto datos observacionales como simulaciones climáticas. Los datos observacionales son escasos y suelen estar limitados a medidas poco profundas, mientras que los modelos climáticos resuelven una termodinámica del suelo muy simplificada, lo que dificulta el análisis de los efectos del cambio climático en la hidro-termodinámica del suelo. La combinación de ambas fuentes permite una evaluación más sólida y completa de los objetivos de esta tesis.

Resultados principales y conclusiones

El primero objetivo de esta tesis es analizar el comportamiento térmico del subsuelo utilizando datos de temperatura de hasta 20 metros de profundidad de seis estaciones meteorológicas de la Sierra de Guadarrama. Se determina la atenuación y el desfase de la onda anual con la profundidad, lo que permite estimar la difusividad térmica del subsuelo. Se observa que el régimen termodinámico dominante es la conducción, con una difusión térmica que aumenta casi linealmente con la profundidad, especialmente en la transición entre el suelo y la roca madre. Esta variación refleja cambios en la composición del material. Para estudiar estos cambios a escalas temporales más cortas que el ciclo anual, se introduce una nueva metodología espectral capaz de analizar cómo se atenúan las distintas frecuencias de temperatura en el subsuelo. Este análisis, aplicado a series de temperatura de hasta un metro de profundidad, muestra que los cambios estacionales en la humedad del suelo también pueden modificar su difusividad térmica, lo que abre la posibilidad de estimar la humedad del suelo a partir de datos de su temperatura.

El análisis de la hidro-termodinámica del subsuelo a escalas de tiempo más largas requiere de simulaciones climáticas. Los Modelos de Superficie Terrestre (LSMs), integrados en los Modelos del Sistema Tierra (ESMs), simulan la con-

ducción de calor imponiendo una condición de contorno de flujo cero a cierta profundidad ("profundidad de frontera inferior" o BBCP). Sin embargo, esta condición de contorno se establece a una profundidad insuficiente, resultando en una subestimación de la captación de calor por la tierra, y una sobreestimación del calentamiento en profundidad debido al cambio climático. Aunque estudios anteriores muestran que modificar esta profundidad no afecta a la temperatura superficial haciendo uso de simulaciones de suelo desacopladas, esta tesis lo verifica mediante dos simulaciones acopladas del periodo 0—2100 d.C. con el modelo climático del Instituto Max Planck (MPI-ESM), una con BBCP a 10 m y otra a 1.400 m. Los resultados confirman que la profundidad del BBCP no altera la variabilidad de la temperatura superficial, lo que permite usar las temperaturas de superficie como condición de contorno para estimar de manera más precisa la captación de calor del suelo de distintas fuentes de datos (observaciones, reanálisis, ESMs) haciendo uso de un modelo unidimensional de conducción de calor. Los resultados revelan que dicha captación depende significativamente de la profundidad del BBCP. Además, una profundidad insuficiente de la BBCP reduce el flujo de calor hacia el subsuelo, generando una sobreestimación de los flujos turbulentos de calor latente y sensible en áreas húmedas y a escala global, respectivamente. Por tanto, limitar la profundidad de la BBCP afecta al balance energético a largo plazo en el contexto del calentamiento global.

Por último, la tesis busca caracterizar cómo la termodinámica del suelo se relaciona con la hidrología. Esta interacción es especialmente relevante en suelos donde se producen cambios de fase de la humedad, como el permafrost. Para ello, se realiza un conjunto de simulaciones del priodo histórico y escenarios de calentamiento futuro (MPIESM-PePE) que incluye diferentes combinaciones de estado hídrico medio, profundidad del BBCP y resolución vertical utilizando una versión modificada del modelo MPI-ESM con una hidrología del suelo más realista en zonas de permafrost. Los resultados muestran que tanto la representación de la hidrología como la profundidad del BBCP impactan significativamente sobre la pérdida de permafrost y la subsidencia de la capa activa en proyecciones de cambio climático futuro. En general, los resultados de esta tesis subrayan la necesidad de mejorar la representación de la hidro-termodinámica del subsuelo en los modelos climáticos.

List of acronyms

AEMET	Agencia Estatal de Meteorología/Spanish Meteorological Agency
ALT	Active Layer Thickness
AOGCM	Atmosphere-Ocean Coupled General Circulation Models
BBCP	Bottom Boundary Condition Placement
BRH	Borehole
BTP	Borehole Temperature Profile
CA	Classic Analytical approach
CE	Common Era
CMIP5	Coupled Model Intercomparison Project Phase 5
CMIP6	Coupled Model Intercomparison Project Phase 6
C_v	Volumetric heat Capacity
DJF	December–January–February
EBM	Energy Balance Model
ECMWF	European Centre for Medium-Range Weather Forecasts
ED	Extremely-Dry
EMIC	Earth system Model of Intermediate Complexity
ERA5-L	ERA5-Land Reanalysis
ESM	Earth System Model
EW	Extremely-Wet
FAO	Food and Agriculture Organization
FTP	Forward Temperature anomaly Profile
GCM	General Circulation Model
GHF	Ground Heat Flux
GHGs	Greenhouse Gases
GST	Ground Surface Temperature
GuMNEt	Guadarrama Monitoring Network

HTC	Hydro-Thermodynamical Coupling
HTCp	Hydro-Thermodynamical Coupling in Permafrost regions
IPCC	Intergovernmental Panel on Climate Change
IPCC	IPCC Assessment Report
JJA	June–July–August
JSBACH	Johann Sebastian BACH land surface model
LHF	Latent Heat Flux
LIA	Little Ice Age
LnA	Natural Logarithm of the Amplitude
LSM	Land Surface Model
LULC	Land Use Land Cover
MAAT	Mean Annual Air Temperature
MAGST	Mean Annual Ground Surface Temperature
MAST 5 m	Mean Annual Subsurface Temperature at 5 m depth
MCA	Medieval Climate Anomaly
M_e	Radiant exitance
MPI-M	Max Planck Institute for Meteorology
MPI-ESM	Max Planck Institute Earth System Model
MPIESM-PePE	MPI-ESM Permafrost Physics Ensemble
NH	Northern Hemisphere
PE	Permafrost Extent
PFT	Plant Functional Type
PMIP4	Paleoclimate Modelling Intercomparison Project Phase 4
P2k+	Extended Past two millenia (0–2100)
P2k+d	P2k+ deep
P2k+s	P2k+ shallow
QC	Quality Control
RCP	Representative Concentration Pathway
RMSE	Root Mean Squared Error
R_N	Surface Net Radiation
SAT	Surface Air Temperature
SD	Semi-Dry
SEB	Surface Energy Balance
SH	Southern Hemisphere
SHF	Sensible Heat Flux
SpM	Spectral Method
SSP	Shared Socioeconomic Pathway

ST	Subsurface Temperature
STP	Subsurface Temperature anomaly Profile
SW	Semi-Wet
TRCH	Trench
TTOP	Temperature at the TOP of permafrost PE diagnosis
ZAA	Zero-Annual Amplitude PE diagnosis
30ENS	30 historical and SSP5-8.5 MPI-ESM simulation
ENSemble	
κ	Thermal conductivity
λ	Thermal diffusivity

Chapter 1
Introduction

This chapter lays the foundations for understanding the motivations of this thesis and the relevance of the results and potential implications derived from them. First, a brief description of the relevance of land surface and subsurface thermodynamics and hydrology in the current state and future evolution of the climate system is presented in Section 1.1. To understand the role of the land surface within climate, it is important to understand the mechanisms ruling the Earth's and surface energy balance. Section 1.2 revisits the basic concepts of climate science and their connection to the land surface. The interest in subsurface heat transfer stems from research in the context of paleoclimate reconstruction of the last millenium. Specifically, Section 1.3 provides the reader with a short history of borehole climatology and how this branch of climate science helped to put the frame for a better understanding of land surface and subsurface thermodynamics.

However, climate reconstruction is obviously not the only motivation for studying the underground heat transfer. As the human action is producing a positive terrestrial energy imbalance, assessing the thermal response of the different climate components is key for characterizing the extent and implications for other physical and biological processes dependent on temperature. Therefore, the thermal regime of the surface and subsurface and its monitoring from observational data are addressed in Section 1.4.

The analysis of the subsurface thermal regime at longer timescales requires the use of climate models. However, state-of-the-art climate models include a simplified representation of how heat propagation with depth operates. The representation of the subsurface heat propagation by climate models and its limitations are described by Section 1.5. One of the main consequences of this oversimplification of the subsurface thermal regime in climate models is a constraint in land heat uptake, which is described and discussed in Section 1.6. Moreover, the simplifica-

tion of land surface processes in climate models is not limited to thermodynamics, but also to hydrology. The interaction between thermodynamics and hydrology is especially relevant for the Arctic soils, which contain large fractions of permafrost. Section 1.7 discusses the existing modeling gap in permafrost dynamics and the challenges associated with realistically representing its hydrological state and evolution under the ongoing Arctic warming conditions. Finally, Section 1.8 presents the structure and the major research questions that motivate this work. Overall, this chapter constructs a framework that addresses the importance of the hydro-thermodynamics of the ground surface and subsurface for the climate system and how it responds to anthropogenic climate change conditions.

1.1 The land surface in a changing climate

Scientific evidence suggests that life first evolved in the Earth's primitive oceans around 3.5 billion years ago (Schopf, 1993), 1 billion years after our planet's formation (Halliday and Canup, 2023). Plants started to spread over the continents around 400 million years ago (Le Hir et al., 2011), but human life did not begin in Africa until 2–2.5 million years ago (Antón, 2012), comparatively not so long ago. Since then, the human evolution up to our days has been inevitably tied to the land surface. The land surface, i.e., the emerged part of the continents, is the basis of the terrestrial microbial, plant and animal life, which ultimately includes humans. Its vast extension, of around 149 million km^2 (a 29.2 % of the Earth's surface), and diversity in mineral, freshwater, and organic resources served as the key foundation and livelihood for the establishment and development of the human civilization.

However, our intensive and extensive exploitation of the overland resources since the Industrial Revolution (Vitousek et al., 1997) has triggered an unprecedented environmental crisis in human history (Chen et al., 2021); this crisis is multi-fold. The massive consumption of organic resources, i.e., plant and animal stocks, has led to a considerable loss in biodiversity (Butchart et al., 2010; Pereira et al., 2012), and ultimately to the extinction of thousands of species (Ceballos and Ehrlich, 2023). The overexploitation of rivers, lakes, aquifers, and other freshwater sources has provoked the depletion of multiple emerged water bodies (e.g., the Aral Sea, Gaybullaev et al., 2012), surface erosion (Svoray, 2022), and an increase in human migrations linked to the scarcity and unfair distribution of water resources (Stoler et al., 2022). Land use land cover (LULC) changes since the beginning of the Industrial Revolution resulting from the construction of urban settlements, factories, and farms, or the sowing and growing of

crops have drastically reduced the forested surface area (Hu et al., 2021; Winkler et al., 2021), a key climate regulator (Bonan, 2008) and the main environment for many ecosystems that are now in danger (Forzieri et al., 2022). Furthermore, our farming and industrial activities have released immeasurable quantities of pollutants that contaminate the air, soil, and subsurface running waters and aquifers, reaching lakes, rivers and eventually the seas and oceans (Kondratyev et al., 2004; Gioia et al., 2011). The combination of the previous factors is producing a global change that is drastically reshaping the planet we inhabit. Nevertheless, perhaps the most dramatic and potentially disruptive consequence of the human action is climate change (Park, 2015; Chen et al., 2021).

The agriculture, farming, construction, transportation, and industry, among other human activities, are intensive in fossil energy resources (Lamb et al., 2022). The combustion of fossil fuels has released massive amounts of carbon rich gases into the atmosphere. These gases (Section 1.2) have the capability of boosting the planet's natural greenhouse effect, i.e., the absorption and subsequent release of long-wave radiation emitted by the surface, and are hence known as greenhouse gases (GHGs). Last estimates by Friedlingstein et al. (2022) quantify GHG emissions to be of 455 ± 25 GtC in 1850–2020, increasing carbon dioxide, methane, and nitrous oxide pre-industrial concentrations from 284.3 ppm, 808.2 ppb, and 273.0 ppb (Meinshausen et al., 2017), to 412.5 ppm, 1879.2 ppb, and 333.0 ppb by 2020 (Blunden and Boyer, 2021), respectively. GHGs have atmospheric lifetimes that span from a few years (methane) to hundreds of years (carbon dioxide), contributing to both short-term and long-term global warming (Canadell et al., 2021). As a result of the anthropogenically enhanced greenhouse effect, global mean near-surface air temperature has increased by 1.09 [0.95 to 1.10] °C since the end of the 19th century (Chen et al., 2021; Gulev et al., 2021). This warming has been significantly larger over land than over the ocean, with temperature values in 2011–2020 being 1.59 [1.34 to 1.83] °C and 0.88 [0.68 to 1.01] °C higher than 1850–1900, respectively (Chen et al., 2021).

Like the other components of the climate system, the land surface is vulnerable to current climate change. Warming of the land surface and near-surface soil has an impact on its biogeochemical activity (Soong et al., 2021), enhancing the metabolic activity of microorganisms, mineral weathering, and decomposition of soil organic matter (Schlesinger and Emily, 2013). It also affects soil hydrology (Krakauer et al., 2013) and increases soil respiration (Zhang et al., 2016; Pries et al., 2017), contributing to an acceleration of the terrestrial carbon cycle (Bond-Lamberty and Thomson, 2010; Pries et al., 2017). Soil warming has also relevant impacts on high latitude regions, where permafrost thaw due to warming can produce changes in soil hydrology (Andresen et al., 2020; Burke et al., 2020), compromising the structural stability of the terrain. This can eventually

lead to the subsurface collapse (Abbott and Jones, 2015; Pegoraro et al., 2021), posing risks to infrastructure (Rotta Loria, 2023) and reshaping landscapes. Additionally, permafrost triggers the release of pollutants (e.g., Schaefer et al., 2020) and reactivates the microbial decomposition of large fossil carbon deposits stored within the permafrost (Turetsky et al., 2019). This microbial activity releases carbon into the atmosphere in the form of methane and carbon dioxide, further enhancing global warming (e.g., Burke et al., 2013; de Vrese et al., 2023).

1.2 The climate system and the energy balance: the role of the land surface

Understanding the land surface responses to climate change requires stepping back to the broader framework in which they occur: the Earth's climate system. The Earth's climate is the result of the energy balance between the incoming and reflected shortwave solar radiation and the net long-wave radiation emitted by the planet itself (Peixóto and Oort, 1984). The Earth is primarily warmed by the incoming solar short-wave radiation. A fraction of the downward radiation (around a 30 %, Goode et al., 2001; Loeb et al., 2009) is reflected back to the space during its path through the atmosphere and at the surface, which is known as the albedo effect. The rest is absorbed by the different climate components, i.e., the atmosphere, the cryosphere, the ocean, and the land surface. The Earth behaves as a grey body, hence emitting long-wave radiation proportionally to the fourth power of its surface temperature, according to the Stefan-Boltzmann law (Boltzmann, 1884). In order to keep the energy balance, the Earth must radiate back the energy away at the same rate. In a planet without atmosphere, the incoming solar, and the outgoing short- and long-wave radiation components would determine the energy equilibrium at the surface. However, the Earth is enveloped by a gaseous atmosphere rich in trace gases like carbon dioxide, methane, and water vapor, which absorb a considerable fraction of the outgoing long-wave radiation emitted by the surface and re-emit it back to the surface. This produces the natural greenhouse effect, which modulates climate variability, preventing large diurnal and seasonal surface temperature variations (Hansen et al., 1995; Stjern et al., 2020) and increasing the atmospheric and ground surface temperatures to a range compatible with life (Serreze, 2010).

The Earth's energy state is shaped by a series of mechanisms that have the ability to regulate the incoming and outgoing energy of the system, known as climate forcings. These include those of natural origin, such as volcanic aerosols and solar radiation changes, or the anthropogenic emissions of GHGs, ozone and

aerosols. The climate system responds to these forcings at various temporal and spatial scales, producing global or regional changes in temperature, precipitation, and weather patterns. For instance, major volcanic eruptions cool the planet over annual to inter-annual timescales due to aerosol injection in the stratosphere (Robock, 2000; Stenchikov et al., 2009; Jungclaus et al., 2010; Myhre et al., 2013), while GHG increases affect the energy balance over decades to centuries and longer timescales (Frölicher et al., 2014; Frölicher and Paynter, 2015). These effects interact with internal variability, i.e., natural stochastic fluctuations in the climate system, which also shape regional weather and extreme events (Rahmstorf and Coumou, 2011; Seneviratne et al., 2021).

At the ground surface, the energy balance is determined by the net incoming radiation and the turbulent heat fluxes: the Sensible Heat Flux (SHF), controlled by the surface temperature, and the Latent Heat Flux (LHF), which is driven by water phase changes. The remainder of this balance is the Ground Heat Flux (GHF), which drives the subsurface heat propagation. The downward or upward GHF entails the uptake or release of energy stored underground, respectively (Huang, 2006; Sadeghi et al., 2021; García-García et al., 2023). The surface turbulent fluxes regulate the evapotranspiration (Wang and Dickinson, 2012), which in turn affects the formation of clouds, altering the ratio of incoming and outgoing long-wave radiation and changing the albedo (Stephens, 2005; Gettelman and Sherwood, 2016). Additionally, changes in the LULC and the snow cover also modify the albedo, causing relative warming or cooling that affects the near-surface weather and climate (Melo-Aguilar et al., 2018). Since land surface acts as the lower boundary condition for the atmosphere, changes in the surface fluxes have the potential to influence the general atmospheric circulation and weather patterns (Pielke, 2001; Laird and Kristovich, 2002), changing the occurrence and distribution of precipitation, wind, and temperature extremes at different temporal and spatial scales (Rahmstorf and Coumou, 2011; Seneviratne et al., 2021). This, in turn, affects soil temperature and moisture conditions (Miralles et al., 2019; García-García et al., 2023), subsequently shaping the surface fluxes and land heat uptake (Cuesta-Valero et al., 2016, 2023; Steinert et al., 2024).

Although the physical processes governing the land surface and subsurface hydrology and thermodynamics are well-understood, they remain poorly represented in the latest generation of climate models. Biases in the representation of the subsurface heat transfer can have remarkable effects on near-surface land thermodynamic and hydrological processes and their interactions, e.g., the overestimation of soil temperatures with warming (González-Rouco et al., 2021; Steinert et al., 2021b). This overestimation is especially concerning in high-latitude regions, since it leads to enhanced permafrost degradation (Hermoso de Mendoza et al., 2020; Steinert et al., 2021b; de Vrese et al., 2023; Nitzbon et al., 2023;

Steinert et al., 2023). In turn, the hydro-thermodynamic state of the soil plays a great role in key aspects such as the Earth's carbon cycle (Bond-Lamberty and Thomson, 2010; Abbott and Jones, 2015; Pries et al., 2017; Turetsky et al., 2019), the soil water availability (Andresen et al., 2020; de Vrese et al., 2023), and the characteristics of the ground surface and canopy (Niu and Yang, 2004; Hoek van Dijke et al., 2020; Mu et al., 2021), all of which affect regional and global climates (Jung et al., 2010; Green et al., 2017). The soil temperature is also relevant for agriculture, since it influences root and plant growths (Kaspar and Bland, 1992) as well as crop productivity (Hu et al., 2024). Additional to the impacts underground, a poorly resolved subsurface hydrology can modify the surface heat fluxes, subsequently impacting on surface temperatures (Ban-Weiss et al., 2011), which can modify soil respiration (Zhang et al., 2016; Pries et al., 2017) and moisture levels (Krakauer et al., 2013), and lead to soil temperature extremes (Miralles et al., 2019; García-García et al., 2023). The extent of these effects depends on factors such as regional climate interaction with land cover (Pitman et al., 2009; Pongratz et al., 2010; Green et al., 2017; O et al., 2022), and soil properties (Steinert et al., 2021b). In conclusion, a proper understanding of land surface and subsurface thermodynamics and hydrology is essential for accurately representing land-atmosphere interactions across different spatial and temporal scales (Forster et al., 2021), and for assessing the potential feedback processes of the land surface and subsurface on climate change.

1.3 A bit of history: borehole temperature reconstruction and the understanding of subsurface heat propagation

The understanding of the mechanisms underlying the energy transfer below the ground surface into the terrestrial crust came by the hand of the borehole climatology (González-Rouco et al., 2009). At the beginning of the 20th century, Lane (1923) and later Birch (1948) noted that the ground surface temperature (GST) signal penetrated into the subsurface when attempting to derive geothermal heat flow estimates from borehole data. These studies considered this surface-driven signal as noise hindering the calculation of long-term geothermal heat flow values, and therefore, an undesirable perturbation that had to be filtered out. It was not until the second half of the 20th century when the GST penetration into the terrestrial crust was found to have a potential application in past climate reconstruction of the Common Era (CE), a topic gaining attention at that time as climate researchers attempted to frame the current anthropogenically-driven climate change in the context of the preindustrial climate variability (Smerdon

and Pollack, 2016). A pioneer study by Cermak (1971) demonstrated that the past GST time evolution could be recovered from subsurface vertical temperature profiles logged in boreholes (i.e., borehole temperature profiles, BTPs) using the heat conduction law (Carslaw and Jaeger, 1959):

$$\frac{\partial T}{\partial t}(z,t) = \kappa \frac{\partial^2 T}{\partial z^2}(z,t), \tag{1.1}$$

which describes the dependence of temperature, T, on depth, z, and time, t. This dependence is controlled by the thermal diffusivity of the medium, κ. Equation 1.1 is a partial differential equation with no direct analytical solution, so Cermak (1971) made some assumptions to simplify its resolution: (1) the terrestrial crust is a half-infinite space, (2) the thermal diffusivity is constant with depth, (3) there are not additional heat sources or sinks, and (4) horizontal heat conductive transfer as well as (5) advection and (6) latent heat exchanges are negligible. Additionally, it was considered that GST differences consist of a series of K time step temperature changes. Hence, each time step produces a temperature change in the subsurface, ΔT_k, that is added to changes from previous time steps (Mareschal and Beltrami, 1992). Under these conditions, the resolution of the heat conduction law (Eq. 1.1) for BTPs is reduced to resolving a linear matrix equation of the form $\mathbf{T(z}_i\mathbf{)}=\mathbf{A}_{ij}\mathbf{T}_s\mathbf{(t}_j\mathbf{)}$, where $\mathbf{T(z}_i\mathbf{)}$ represents the BTP values and $\mathbf{T}_s\mathbf{(t}_j\mathbf{)}$ the past GST evolution (i.e., ΔT_k), and $\mathbf{A}_{ij}$ is a coefficient matrix given by the expression:

$$A_{ij} = \left[erfc\left(\frac{z_j}{2\sqrt{\kappa t_i}}\right) - erfc\left(\frac{z_j}{2\sqrt{\kappa t_{i-1}}}\right) \right] \tag{1.2}$$

where the $erfc$ is the complementary error function. The past GST evolution ($\mathbf{T}_s$) can be obtained by inverting the coefficient matrix ($\mathbf{A}$), i.e., $\mathbf{T}_s=\mathbf{A}^{-1}\mathbf{T}$. In practice, the borehole inversion is most of the times an overdetermined system of equations (i.e., more equations than unknowns), so its resolution is based on eigenvalue decomposition methods such as the Singular Value Decomposition (Mareschal and Beltrami, 1992; Jaume-Santero et al., 2016; Cuesta-Valero et al., 2021b), or Bayesian Inversion methodologies (Hopcroft et al., 2007; Groenke et al., 2024). The limitations of the different BTP inversion techniques and their associated uncertainties are out of the scope of this thesis, but are treated by Mareschal and Beltrami (1992), González-Rouco et al. (2009), Hopcroft et al. (2009), and Melo-Aguilar et al. (2020).

Borehole temperature reconstructions are part of a broad catalogue of proxy-based (i.e., indirect or surrogate sources of climate observation) temperature reconstructions of the CE, which include information derived from tree rings,

speleothems, lake and ocean basin sediments, coral reefs, or written documentary climate records, among others (Jones et al., 2009; Masson-Delmotte et al., 2013; Smerdon and Pollack, 2016). Furthermore, BTPs have been applied to estimating the land heat storage since the pre-industrial era resulting from global warming (Mareschal and Beltrami, 1992; Huang et al., 2000; Beltrami et al., 2002; Cuesta-Valero et al., 2021b, 2023, see Section 1.6). These estimates are the only observational source of global land heat uptake prior to the 2000s (Cuesta-Valero et al., 2025), and the uncertainties associated with the temporal and spatial sampling of borehole logs and other methodological issues have been assessed using climate models as a surrogate reality (González-Rouco et al., 2006; Melo-Aguilar et al., 2020). Climate simulations (e.g., MacDougall et al., 2008; Cuesta-Valero et al., 2016) have also been used to provide independent estimates of land heat uptake. However, limitations in their representation of subsurface thermodynamics (Section 1.5) led them to underestimate the observational values (Section 1.6). To understand this discrepancy between model simulations and observations, a deeper look into the physical mechanisms driving land surface and subsurface temperature variability and heat propagation is now necessary.

1.4 The subsurface heat propagation: operating mechanisms and associated uncertainties

The land surface and the atmosphere are intimately connected (Section 1.2). They interact by exchanging mass, momentum, and heat through the turbulent fluxes, which operate at diverse spatial and timescales (Mauder et al., 2020). However, this interaction does not always entail the full coupling of their respective thermal states. There is a series of physical and biological factors that disrupt the thermal connection between the near-surface air and the ground surface, acting as barriers that produce either colder or warmer GSTs vs surface air temperatures (SATs) at daily to seasonal scales. The main cause of SAT–GST decoupling is snow cover (Sokratov and Barry, 2002; Bartlett et al., 2005; Zhang, 2005; Melo-Aguilar et al., 2018). The snow has a very low thermal conductivity ($0.25\ \mathrm{WK^{-1}m^{-1}}$, Sturm et al., 1997), so it operates as a very effective insulator of the ground surface, preventing GSTs from dropping as a response to severely cold SATs in wintertime across large areas of mid- and high-latitudes of the Northern Hemisphere (NH, Zhang et al., 2018). Another factor producing ground-air thermal decoupling is the evaporative cooling of the ground surface (Ban-Weiss et al., 2011; García-García et al., 2023). This mechanism is prominent in the tropics and in mid-latitude wet areas in summer, such as the coastal regions and the west

basins of the Atlantic and Pacific oceans. Evaporative cooling hinders the diurnal GST increase as a response to the incoming short wave radiation via the emission of LHF. Therefore, by contrast to the snow insulation, the evaporative cooling effect produces colder GSTs than SATs. Even though both mechanisms play a remarkable role in SAT–GST coupling in large regions at seasonal scales, their long-term effect has been indicated by climate model experiments to be very limited and constant with time (Melo-Aguilar et al., 2018). Global variations of the SAT–GST coupling might occur ought to seasonal variations in snow cover, near-surface soil moisture, or LULC changes associated with global warming (Mann and Schmidt, 2003; García-García et al., 2016; Melo-Aguilar et al., 2018; Yuan et al., 2021).

Several observational (Sokratov and Barry, 2002; Bartlett et al., 2005; Melo-Aguilar et al., 2022; Zhang et al., 2018) and modeling studies (Cook et al., 2008; Melo-Aguilar et al., 2018; Krinner et al., 2018; García-García et al., 2019) have reported the existence and onset of the snow insulation effect. However, only a few studies have assessed the seasonal behaviour of the snow cap and the snow insulation effect in mountainous areas, and more specifically in the Mediterranean region. This thesis analyzes the snow seasonality and its impact on SAT–GST coupling at four monitoring stations located in the Sierra de Guadarrama, a mountainous range located in the central part of the Iberian Peninsula (Chapter 3, García-Pereira et al., 2024a).

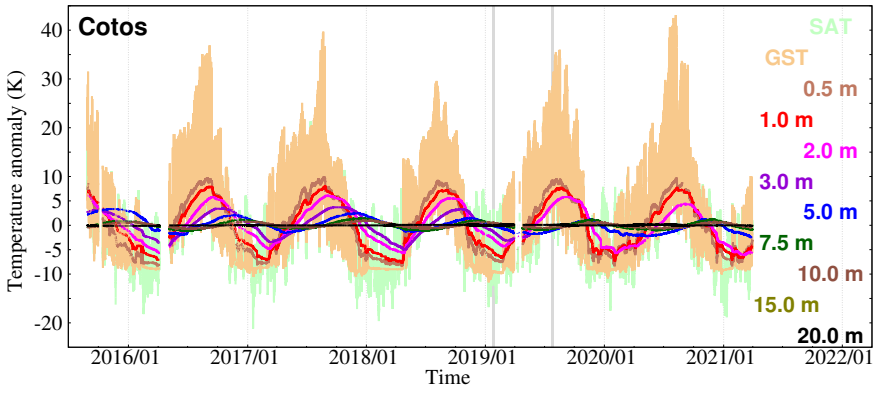

Figure 1.1: SAT, GST, and subsurface temperature anomalies at hourly resolution (K) with respect to the annual mean at Cotos.

The underground propagation of GST variations determine the thermal state and variability of the subsurface, acting as a boundary condition. The conti-

nental land subsurface constitutes the solid component of the climate system. It conforms the shallowest part of the terrestrial crust, and consists of two differentiated vertical sections: the soil and the bedrock. The soil is a thin layer, usually no deeper than 10 m (Shangguan et al., 2017), composed by sediments and eroded fragments of rocks and minerals blended with organic matter and water, which depending on the temperature can be in form of soil moisture or ice. The soil is porous, heterogeneous, and comprehends a series of layers with different compositions known as soil horizons (de Vries, 1963). The material in soil horizons is progressively more compacted and consolidated with depth. The bedrock is the hard and mostly impermeable rock located beneath the soil. It is more homogeneous and dense than the soil. Since both soil and bedrock are overall solid, heat conduction is their primary mode of heat transfer. Heat conduction (Section 1.3) is controlled by the heat conduction law (Eq. 1.1). If it is assumed that the subsurface is an homogeneous solid medium with no horizontal temperature gradients, no internal heat production, and the GST is regarded as a sum of sinusoidal harmonics of different amplitude and frequency, the underground temperatures can be expressed following Carslaw and Jaeger (1959):

$$T(z,t) = T_0 + \sum_{i=1}^{N} A_i e^{-z\sqrt{\pi f_i/\kappa}}\, cos(2\pi f_i t - z\sqrt{\pi f_i/\kappa}), \tag{1.3}$$

where z represents the subsurface depth; t the time; f_i, and A_i the frequency, and amplitude at the ground surface of the ith harmonic, respectively; $T(z,t)$ the subsurface temperature at depth z and time t; κ the thermal diffusivity of the subsurface; and T_0 the mean GST. Equation 1.3 evidences the exponential amplitude attenuation (i.e., signal decay) and linear phase shift that GST harmonics experience when they penetrate into depth. Both mechanisms are a direct function of the frequency of the oscillation, and depend on the thermal diffusivity of the subsurface. This parameter is a physical property determined by the mineral and organic composition of the materials conforming the subsurface, and varies with depth due to vertical differences in this composition (García-Pereira et al., 2024a), porosity, or variations in soil moisture content (Melo-Aguilar et al., 2022; García-Pereira et al., 2024a). As a consequence of the heat conduction law (Eq. 1.2 and 1.3), the higher frequency GST harmonics propagate faster, but are also more rapidly filtered out and only detectable near the surface. By contrast, the penetration of low frequency changes takes longer but progresses deeper into the subsurface. For instance, the daily cycle hardly reaches a depth of 50 cm, while the annual cycle propagates down to 15 m (Putnam and Chapman, 1996). In conclusion, the subsurface acts as a low-pass filter, where the intensity of the filtering decreases for higher thermal diffusivity values.

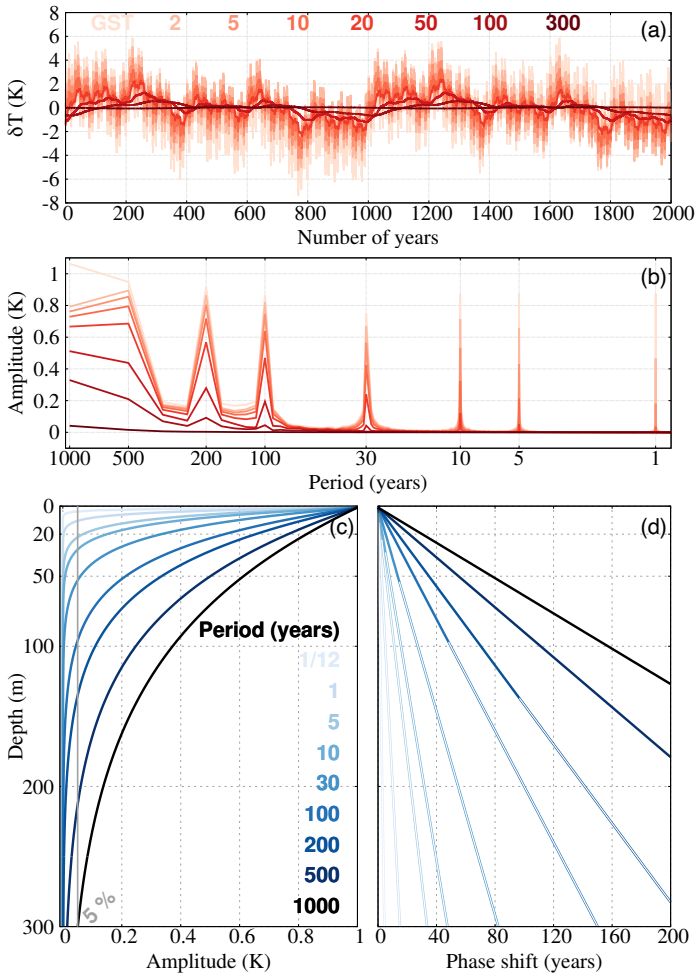

Figure 1.2: Conductive propagation of a synthetic GST signal underground. (a) Ground surface and subsurface temperature variability (in K) at different depths (see legend) of a 2000-year-long synthetic temperature series composed by a sum of sinusoidal harmonics of amplitude 1 K and periods of 1/12, 1, 5, 10, 30, 100, 200, 500, and 1000 years. The GST sinusoidal waves are in phase. The thermal diffusivity of the subsurface is $\kappa = 10^6$ m^{2}s^{-1} (b) Amplitude periodogram of the temperature series in (a). Note that the x-axis is logarithmic. (c) Analytical amplitude attenuation (shown as amplitudes in K) and (d) phase shift (years) with depth of the single sinusoidal thermal waves with different period lengths (see legend) composing the GST in (a). Phase shift values in (d) whose amplitude is less than 5 % GST's amplitude (grey vertical line in c) are plotted with white fill. Adapted from Pollack and Huang (2000).

The nature of amplitude attenuation and phase shift of temperature harmonics with depth as a result of heat conduction is portrayed in Fig. 1.1 (García-Pereira et al., 2024a), which shows the hourly temperature evolution at different subsurface depths at Cotos. This monitoring station, located at the Sierra de Guadarrama (Spain), belongs to the Guadarrama Monitoring Network (GuMNet*; Vegas-Cañas et al., 2020). It can be noted that, as the signal propagates with depth, the high-frequency variations seen in the SAT and GST time series (e.g., daily fluctuations; shading in Fig. 1.1) are progressively damped and become almost completely absent at a depth of 0.5 m. By contrast, the annual cycle is still detectable within the upper 10 m, but fully attenuated at 20 m depth. Furthermore, the phase shift with depth can be observed by tracking the displacement in time of the annual maxima and minima of temperature at every level. Such mechanisms are also evident in Fig. 1.2, which represents the underground propagation of a synthetic GST signal of 2000 years length composed by a sum of harmonics with an amplitude of 1 K and periods of 1 month and 1, 5, 10, 30, 100, 200, 500, and 1000 years. This propagation is controlled by the thermal diffusivity, which was fixed at a constant value of 10^{-6} m^2s^{-1}, in the range of the observed values for the mineral components commonly conforming the bedrock. As the GST signal penetrates into depth, the highest frequency oscillations are rapidly attenuated, so that at 20 m only decadal and lower frequency temperature variations are still visible (Fig. 1.2a). The spectral composition of the GST signal and its attenuation is clearly shown by the amplitude periodograms (Brigham and Morrow, 1967) at different depths in Fig. 1.2b. Even though some extent of spectral leakage disrupts the interpretation of Fig. 1.2b for the lowest frequency spikes, it can be noted that the harmonics with periods of 1000 to 100 years still show a detectable signal at 100 m depth. This is also depicted by Fig. 1.2c, which illustrates the underground attenuation of the different harmonics in Fig. 1.2a,b. Figure 1.2c evidences the exponential nature of this attenuation, and how it increases with the frequency of the harmonic. Thus, less than a 5 % of the temperature amplitude at the ground surface for the harmonics of 1 month, 1, 5, 10, 30, 100, 200, 500, and 1000 years is still present below 4, 11, 23, 32, 53, 96, 136, 214, and 302 m depths, respectively. Figure 1.2d shows the phase shift of the harmonics in Fig. 1.2a–c, illustrating their linear relation of it with depth described by the solution in Eq. 1.3. Although the higher frequency harmonics shift comparatively more (in rad), their period is also smaller, so the result of computing the phase shift in time units (years in this case) is a greater phase shift of the long-term signals. For instance, the 1000-year GST harmonic is shifted around 157 years at 100 m, whereas the 100-year cycle only 49 years. This means

* www.ucm.es/gumnet/

that it takes around 49 years for the 100-year GST harmonic and 157 years for the 1000-year GST harmonic to propagate to a subsurface depth of 100 meters.

In the idealized example in Fig. 1.2, heat propagation fully occurs by downward conduction of the GST signal in an homogeneous mean (i.e., with a fixed thermal diffusivity). However, subsurface temperatures recorded both in near-surface and deep subsurface BTP logs have shown that other heat transfer mechanisms can also influence the temperature distribution below the surface. This is the case of vertical and horizontal subsurface fluid movements (hydraulic advection, Diao et al., 2004; Ferguson, 2015) variations in the conditions of the terrain (surface erosion or burial, e.g., thermokarst; Pegoraro et al., 2021) or air and water convection through the soil (and to a lesser extent bedrock) pores (Gao et al., 2008; Tong et al., 2017). These mechanisms can overrule heat conduction when determining the temperature variations with depth, especially in areas with vertical and horizontal groundwater movements due to a high permeability of the bedrock (Olofsson, 1994). Moreover, changes in the soil moisture content have the capability to modify the near-surface properties (Ochsner et al., 2001; Melo-Aguilar et al., 2022), where the soil is less consolidated and porous. Higher values of the soil moisture content lead to higher thermal diffusivity and conductivity values (Sorour et al., 1990; Arkhangelskaya and Lukyashchenko, 2018; Dai et al., 2019), enhancing temperature propagation in the first meter of soil (Melo-Aguilar et al., 2022). Although all these mechanisms can disrupt the conductive thermal regime, there is evidence that conductive heat transport of the surface temperature variations dominates the distribution of temperature within the subsurface (González-Rouco et al., 2009). This evidence mainly stems from near-surface (usually down to 1 m) soil temperature observational data monitored at meteorological stations with soil instrumental in the U.S. (Smerdon et al., 2004; Bartlett et al., 2006; Bell et al., 2013), Canada (Qian et al., 2011), the Russian Arctic (Sherstyukov and Sherstyukov, 2015), Europe (Cermak et al., 2014; Demetrescu et al., 2007; Melo-Aguilar et al., 2022; Petersen, 2022; Dorau et al., 2022), Australia (Knight et al., 2018), and China (Zhang et al., 2016). In most of the cases, soil temperature data have been used to assess the downward propagation of the recent SAT trends (e.g., Zhang et al., 2016; Petersen, 2022), or to yield estimates of the apparent thermal diffusivity of the column targeting the amplitude attenuation and phase shift of the annual cycle with depth (e.g., Smerdon et al., 2003, 2004; Melo-Aguilar et al., 2022). However, the number of sites with this kind of data is still really scarce and, in most of the cases, the temporal extension of the series is limited, insufficient to evaluate the long-term response of the subsurface to the surface warming. Moreover, only a few sites count also on a continuously monitoring installation of subsurface temperatures below 10 m (e.g., the Sporilov Observatory in Prague, Cermak et al., 2014; Fargo, Smerdon

et al., 2003), so the understanding of the propagation of subsurface temperatures in the soil-bedrock transition is insufficiently documented. In this thesis, subsurface temperature data coming from six sites in the Sierra de Guadarrama (García-Pereira et al., 2024a) is employed to expand previous knowledge regarding the temperature propagation into the subsurface. All of the sites count on continuously monitored near-surface temperature time series at different depths in 1-meter-deep trenches, and four of them also include deep subsurface temperature measurements down to 20 m. Chapter 3 contains a thorough analysis of the conductive regime using this data, characterizing the vertical and temporal variations of the apparent thermal diffusivity and their potential connection to changes in the parent material and soil moisture content.

1.5 The representation of the subsurface heat propagation in climate models

Given the scarcity of observational subsurface temperature records, complementary sources of information are essential to assess the thermodynamic and hydrological mechanisms governing soil and bedrock dynamics, and its response to temperature changes at the ground surface. This is especially concerning in the current context of global warming, since soil temperature increase as a response to ground surface warming has multiple alarming consequences already described in Section 1.1. The latest generation of climate models, the Earth System Models (ESMs, Eyring et al., 2016), avert the temporal and spatial limitations of the observations by resolving a detailed representation of the climate system at an evenly distributed spatial grid and time frame. The ESMs represent the highest level of realism and complexity at the hierarchy of computational models utilized to represent the climate system (Flato, 2011; Randall et al., 2018, , see Fig 1.3a). This hierarchy also includes, sorted from a simpler to a more complex resolution of the climate system, the Energy Balance Models (EBMs, e.g., Crowley, 2000), the Earth system Models of Intermediate Complexity (EMICs, Claussen et al., 2002; Weber, 2010), the General Circulation Models (GCMs, e.g., Kasahara and Washington, 1967; Giorgetta et al., 2018), and the Atmosphere-Ocean Coupled General Circulation Models (AOGCMs or CGCMs, e.g., Manabe et al., 1991; Voss and Mikolajewicz, 2001).

At a first stage of the climate modeling evolution (González-Rouco et al., 2024), EBMs (Budyko, 1969; Sellers, 1969) were developed to assess the response of the climate system, usually in terms of the surface temperature, to changes in the radiative balance. The EBMs do not resolve the two- or three-dimensional

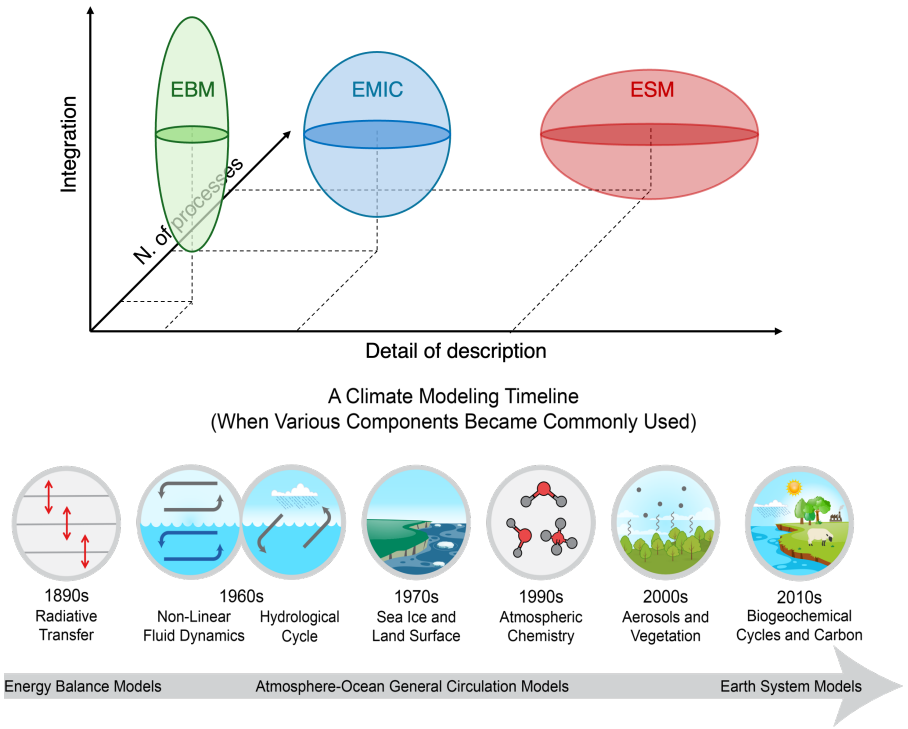

Figure 1.3: Evolution of climate modeling. (Top) Degree of detail in physical description (X-axis), number of processes (Y-axis), and level of integration (Z-axis) of various numerical models used in climate studies: Energy Balance Models (EBMs, green ellipsoid), Earth system Models of Intermediate Complexity (EMICs, blue sphere), and Earth System Models (ESMs, red ellipsoid). Adapted from Claussen et al. (2002). (Bottom) Physical, chemical, and biogeochemical components incorporated into climate models over the last 120 years. Note that the number and nature of climate-relevant processes implemented in models have accelerated over the last 30 years (obtained from Hayhoe et al., 2017).

spatial response of the system, but provide a single-point or latitudinal picture of it. The EBMs were superseded by a set of more complex models capable to resolve the conservation of mass, momentum, and energy ruling the different climate components and their interactions, in a three-dimensional grid, usually known as global climate models (Randall et al., 2007). The less sophisticated in terms of the amount of physics included and spatial resolution are the EMICs (Claussen et al., 2002), which account for the key processes needed to resolve the climate response to changes in the external forcing (i.e., the hydrological cy-

cle, orography, atmospheric and oceanic circulations, and dynamic response of ice sheets). A more thorough description of the physics ruling the atmospheric circulation was brought by the GCMs, lately superseded by the AOGCMs (e.g., González-Rouco et al., 2003), which resolve the atmospheric circulation coupled with the ocean dynamics. In the last decades, the representation of the climate system has been substantially improved to progressively include all the climate components and simulate the complex interaction between them, finally leading to the ESMs (Fig. 1.3a). The state-of-the-art generation of ESMs, participating in the Coupled Model Intercomparison Project Phase 5 (CMIP5, Taylor et al., 2012), and 6 (CMIP6, Eyring et al., 2016), resolve the internal dynamics and interaction between the atmosphere, ocean, land, and cryosphere, accounting for many aspects of the system not regarded so far, such as the atmospheric chemistry and aerosols, land surface interactions including soil and vegetation, land and sea ice, and an interactive carbon cycle and/or biogeochemistry (Fig. 1.3b). The resolution of the current ESMs is usually broad, of around 200 (100) km over the land (ocean) surface in their low-resolution versions (Eyring et al., 2016), and 50 (25) in their high-resolution (Haarsma et al., 2016). This entails that some physical processes are simplified, parametrized, or even ignored (von Storch, 2010; Palmer and Stevens, 2019). Even though ESMs are only a representation of the real climate system (Oreskes et al., 1994), they are the most suitable tool to study the influence of natural and anthropogenic variations on the Earth's climate system (Hegerl and Zwiers, 2011; Duan et al., 2019) and their corresponding impacts on global ecosystems (Bonan and Doney, 2018) and socio-economic activities (e.g., Burke et al., 2015; Hsiang et al., 2017).

Within Earth System Models (ESMs), the Land Surface Models (LSMs) are responsible for simulating the internal dynamics of the land surface and subsurface, as well as their coupling to the other climate components, i.e., the atmosphere and biosphere (Blyth et al., 2021). LSMs were originally conceived to serve as a bottom boundary of the atmosphere in meteorological prediction, by supplying the atmospheric models with conditions for the energy, water, and momentum fluxes at the ground surface (Manabe, 1969). Since those early developments, LSMs have significantly grown in both scope and complexity (Pitman, 2003; Fisher and Koven, 2020). Nowadays, LSMs resolve a wide range of processes occurring at the land surface that contribute to the land-atmosphere interaction, such as the surface energy balance, the snow dynamics, or the organic layer evolution (e.g., Ekici et al., 2014). They also account for the land-vegetation mutual dependencies, which include the plant physiology, the vegetation responses to disturbances produced by LULC changes or wildfires, or the near-surface carbon, and nitrogen cycles (e.g., Fisher et al., 2019). Moreover, LSMs comprehensively simulate the subsurface by resolving the main mechanisms of the soil thermodynamics, hydrol-

ogy, and biogeochemistry, such as the underground heat conduction and water transport (e.g., Guimberteau et al., 2018; Lawrence et al., 2019; Reick et al., 2021), or the movement and decomposition of the underground organic matter deposits (e.g., Burke et al., 2017).

Several of the previously mentioned processes play a critical role in determining the thermodynamic and hydrological states of the subsurface, like the insulating effects of the organic layer (Lawrence and Slater, 2008; Lawrence et al., 2008; Chadburn et al., 2015) and snow cover (Ekici et al., 2014), the phase changes of soil moisture to ice when temperatures fall below freezing (Ekici et al., 2014; Sapriza-Azuri et al., 2018; Steinert et al., 2021b), the dynamic calculation of soil thermal properties (Wang et al., 2016; Sapriza-Azuri et al., 2018; Steinert et al., 2021b), or the propagation of heat down to the bottom layer of the model. At this depth, the conservation of energy is ensured prescribing a zero-flux bottom boundary condition for the heat, so no energy losses or gains can occur. This is the so-called zero-flux bottom boundary condition placement (often referred to as BBCP, or simply LSM depth; Alexeev et al., 2007; González-Rouco et al., 2009; Hermoso de Mendoza et al., 2020; Steinert et al., 2021a).

Indeed, a key limitation of LSMs when resolving the downward thermal propagation of the GST variability arises from the prescription of too shallow BBCP depths. Due to the high computational cost of ESMs, subsurface processes are simplified by discretizing the soil profile into a finite number of vertical layers. Hence, the solution of the heat conduction equation for a vertical half-infinite space given by Eq. 1.2 (Carslaw and Jaeger, 1959) does not apply in LSMs. In contrast, vertical heat conduction is solved imposing a zero-flux bottom boundary condition at a certain depth, which halts the deeper penetration of heat and subsequently thwarts the resolution of a temperature profile beyond this depth. Historically, the downward propagation of GST variations by heat conduction into the deep soil and bedrock was neglected (Pitman, 2003; Fisher and Koven, 2020), as the temperature signal due to land-atmosphere interactions relevant on meteorological timescales (hours to days) penetrate only a few tens of centimeters (Tong et al., 2017). Overall, the majority of ESMs participating in the CMIP5 (Taylor et al., 2012) and CMIP6 (Eyring et al., 2016) use a BBCP located at 3 to 10 m in their LSMs, with a few exceptions using the Community Land Model (CLM, BBCP at approx. 40 m, Lawrence et al., 2019). These depths are insufficient to correctly resolve the underground propagation of the surface temperature changes and long-term warming trend, with consequences for the near-surface temperature variability (e.g., Hermoso de Mendoza et al., 2020; González-Rouco et al., 2021; Steinert et al., 2021a), the land heat uptake resulting from the terrestrial energy partitioning of the positive energy imbalance (e.g, Cuesta-Valero et al., 2016; García-Pereira et al., 2024b; Steinert et al., 2024), or the correct

representation of the permafrost active layer and extent (e.g., Ekici et al., 2014; Chadburn et al., 2015; Burke et al., 2020; Steinert et al., 2021b, 2023).

1.6 Land heat uptake in the terrestrial energy budget

The effects of the different climate forcings compensate one another if there exists a state of energy balance, resulting in a long-term stable climate (Section 1.2). However, if the intensity of one or more forcing factors changes, an energy imbalance occurs, subsequently triggering a change in the Earth's climate conditions, or climate change. Prior to the nineteenth century, the governing forcing factors were of natural origin. For instance, climate fluctuations at centennial timescales during the CE were mainly driven by changes in the solar and volcanic forcings (Fernández-Donado et al., 2013; 2k Consortium, 2013; Sigl et al., 2015). At a wider time frame, changes in the energy balance are dominated by periodic fluctuations in the orbital parameters (eccentricity, axial tilt, and precession) first defined by Milutin Milankovitch (Milankovitch cycles, Milankovitch, 1941; Ganopolski, 2024). An illustrative example is the Quaternary period (the past 2.6 million years), during which the climate system underwent a succession of glacial and interglacial stages driven by changes in the orbital forcing (Hays et al., 1976; Paillard, 2015). However, since the 19th century, natural forcing variations have been overshadowed by the intensification of anthropogenic forcing due to unprecedented carbon emissions (Zeebe et al., 2016). The enhanced greenhouse effect due to the anthropogenic emission of GHGs has produced a positive energy imbalance at the top of the atmosphere. This additional input of energy is partitioned among the different climate components. This partitioning is often denoted as the terrestrial energy budget (Forster et al., 2021; von Schuckmann et al., 2020, 2023). In the last five decades, the land stored around 6 % (4.3–6.6 %, 21 ± 2 ZJ) of the terrestrial energy surplus, as derived from observational estimates (von Schuckmann et al., 2020; Cuesta-Valero et al., 2021a, 2023), being the second largest contributor after the ocean (ca. 90 %, 324 ± 8 ZJ, Levitus et al., 2012; Abraham et al., 2013; von Schuckmann et al., 2020). The massive ocean energy absorption is mainly caused by its large heat capacity (Brewer and Peltzer, 2019), and its efficient meridional and vertical transport of heat due to the surface currents and the thermohaline circulation (Hansen et al., 2005; Forster et al., 2021; von Schuckmann et al., 2020, 2023).

Regardless of whether the amount of heat absorbed by land is comparatively small, climate models should realistically represent it within the terrestrial energy budget. State-of-the-art ESMs participating in the CMIP5 quantify the land

contribution to be roughly 2 % (Cuesta-Valero et al., 2021a), underestimating observational results that suggest values around 6 % (Forster et al., 2021; von Schuckmann et al., 2023). This underestimation of land heat uptake in ESMs can alter the surface energy balance (Mottaghy and Rath, 2006; García-García et al., 2023), with impacts on soil hydrology (Krakauer et al., 2013), particularly in permafrost regions (Andresen et al., 2020). The amount of energy absorbed by land and how it is distributed is also relevant for other soil processes, such as respiration or productivity (Pries et al., 2017), and for its biogeochemical activity (Soong et al., 2021). Furthermore, a correct representation of the terrestrial energy budget helps in understanding the interactions between the different climate components and shaping the climate change influences on near-surface climate (Forster et al., 2021).

Observational land heat uptake estimates have been derived from BTP log collections (Mareschal and Beltrami, 1992; Huang et al., 2000; Beltrami et al., 2002; Cuesta-Valero et al., 2021b, 2023). BTPs record transient temperature perturbations relative to the steady geothermal gradient. Assuming that the subsurface acts as a half-infinite fully conductive medium (Carslaw and Jaeger, 1959, see Section 1.3), BTPs provide information about the land heat uptake up to their logging date (Cuesta-Valero et al., 2021b). BTP logs are scarce and show uneven distributions of sampling dates and locations, as well as variable vertical resolution and depths. These factors have some impact on resulting estimates of land heat uptake (Beltrami et al., 2015; Melo-Aguilar et al., 2018, 2020). Nevertheless, estimates derived from BTPs are, so far, the only observational source of information to quantify the land contribution to terrestrial energy budget for the entire industrial era (Forster et al., 2021; von Schuckmann et al., 2023; Cuesta-Valero et al., 2025).

State-of-the-art ESMs have been incapable of properly reproducing observational land heat uptake estimates. Their limited capability to store energy stems from imposing a BBCP in their LSMs (Section 1.5), usually at 10 m or even closer to the surface (Cuesta-Valero et al., 2016; García-Pereira et al., 2024b; Steinert et al., 2024). These depths are insufficient to account for the heat available to be stored in the subsurface during the industrial period, rendering them inadequate for estimating long-term heat storage (MacDougall et al., 2008; González-Rouco et al., 2009; Cuesta-Valero et al., 2016; González-Rouco et al., 2021). Moreover, the physical boundary for heat penetration imposed by the zero-flux BBCP biases the subsurface temperature variability near the BBCP, limiting the amplitude attenuation of the temperature harmonics (Smerdon and Stieglitz, 2006) and, therefore, overestimating the temperature variability (Alexeev et al., 2007; Steinert et al., 2021a). To ensure the full decoupling between the BBCP and the ground surface for climate simulations of the industrial era, the BBCP must be located

at least at 170 m (Steinert et al., 2021a). For longer-term simulations spanning multi-centennial or millennial timescales, like the ones developed within the Paleoclimate Modelling Intercomparison Project (PMIP, Kageyama et al., 2018), ESMs should include deeper BBCP depths to accommodate longer lasting and deeper subsurface energy transfer (Smerdon and Stieglitz, 2006; Alexeev et al., 2007; Steinert et al., 2021a).

Some simulation-based efforts have been devoted to deriving unbiased estimates of land heat uptake using deepened LSMs. Standalone one-dimensional half-infinite space heat conduction forward models (González-Rouco et al., 2006, 2009) were used to yield artificial global mean surface temperature histories and land heat uptake estimates, forced by either observational-based SAT (Huang, 2006) or simulated GST data (Stevens et al., 2007; MacDougall et al., 2008). More recently, modifications of the BBCP depth (Hermoso de Mendoza et al., 2020; González-Rouco et al., 2021) and soil hydrology (Steinert et al., 2021b) have been introduced into LSMs in standalone mode, and their impact on heat uptake and subsurface temperature variability extensively discussed. However, the impact of these LSM changes has not yet been explored within a fully-coupled ESM. In Chapter 4, the impacts on temperature variability and land heat uptake of including a deeper LSM in long-term fully-coupled (i.e., the LSM coupled with the rest of climate components) ESM simulations are analyzed (García-Pereira et al., 2024b). Moreover, the physical mechanisms operating at the ground surface leading to different values of the land heat uptake are explored (García-Pereira et al., 2025b) and connected to the BBCP depth using an ensemble of standalone LSM simulations with different depths (González-Rouco et al., 2021) in Chapter 5.

1.7 Interactions between subsurface thermodynamics and hydrology: relevance for high-latitude permafrost soils

Soil temperature increase and land heat uptake occur globally as a response to the energy imbalance at the surface (Sections 1.2 and 1.6). However, this warming is spatially heterogeneous. Since the late 19th century, global mean near-surface air temperature has risen by 1.1 °C (Gulev et al., 2021), with the Arctic warming more than twice this amount (2.3 °C, Gulev et al., 2021) due to Arctic amplification (Rantanen et al., 2022). The intensified soil warming in these NH high-latitude regions is particularly concerning since they encompass large areas of perennially frozen soils, or permafrost (Turetsky et al., 2019). The intense and continuous surface warming is propagated to the soil and causes permafrost thaw, which produces its progressive degradation and eventual loss. Since permafrost

soils store vast deposits of organic matter, its thaw make them susceptible to microbial decomposition. This activity releases massive amounts of GHGs into the atmosphere (Turetsky et al., 2019), mostly methane (under anaerobic conditions, Knoblauch et al., 2017), and carbon dioxide (aerobic conditions, Chen et al., 2021). With an estimated 1,100 petagrams of carbon (PgC) stored in near-surface permafrost soils (Hugelius et al., 2014), this carbon release intensifies the greenhouse effect, creating a positive feedback that accelerates global warming (the permafrost carbon-climate feedback, Burke et al., 2013; Schuur et al., 2022). However, permafrost thaw does not only have implications at a global scale, but it also has remarkable regional impacts. Permafrost degradation produces soil compression and subsidence of the affected areas and the emersion of water bodies (Vonk et al., 2015), which pose structural risks for infrastructures in the Arctic (Hjort et al., 2018). Moreover, triggers contamination problems derived from mercury release to the atmosphere and soil waters (Schaefer et al., 2020). A good understanding of soil dynamics of permafrost areas is therefore crucial to foreseeing the global consequences of their degradation and evaluating the risks for the Arctic population and ecosystems (Parmesan et al., 2022).

The state of permafrost has been monitored on relatively scarce and inhomogeneously distributed sites across the Arctic. These sparse measures have been aggregated so as to create observational products that allow for the study of the state of permafrost at a global scale. Some of these observational initiatives have targeted specific variables, as is the case of the Circumpolar Active Layer Monitoring Network (CALM, Brown et al., 2000), which assesses the long-term response of the active layer thickness (ALT), i.e., the maximum permafrost thawed depth in summer. In addition, other networks, e.g., the Global Terrestrial Network for Permafrost (GTN-P, Biskaborn et al., 2015), monitor a wider range of variables, including permafrost temperatures at different levels. Despite their great value, these observational products offer a limited representation of permafrost areas due to the poor temporal and spatial sampling (Biskaborn et al., 2019), and the uncertainty associated with the thermal and hydrological properties of the terrain (Heuvelink, 2018). Hence, despite the relevance of permafrost for the climate system, a continuous and spatially even detection of permafrost presence is still limited at the global scale (Brown et al., 2002; Obu et al., 2019).

As with the estimation of land heat uptake (Section 1.6), state-of-the-art ESMs avert the spatial and temporal heterogeneity of permafrost observations. ESMs allow for assessing the thermodynamic and hydrological response of permafrost-affected areas to the combination of natural and anthropogenic forcing. Near-surface temperatures and soil moisture resolved by LSMs within ESMs are subsequently used to derive estimates of PE and ALT evolutions (Burke et al., 2020; Steinert et al., 2023). ESM simulations from the CMIP5 and CMIP6 agree on a

severe decrease of PE and deepening of ALT in the industrial era (Koven et al., 2013; Burke et al., 2020; Steinert et al., 2023). However, there is considerable multi-model variability in the results, with differences in PE decrease and mean ALT deepening estimates that reach ca. 10 million km^2 (Steinert et al., 2023) and 2 m (Burke et al., 2020) by the end of the 21st century, respectively. These discrepancies are mainly due to the different climate sensitivity of the ESMs and the different modeling of soil hydrology and thermodynamics by their LSMs, which are particularly relevant for Arctic regions (Slater and Lawrence, 2013). The representation of different processes related to surface and soil hydrology in the Arctic, such as snow insulation (Cook et al., 2008; Krinner et al., 2018; Mudryk et al., 2020; Menard et al., 2021; Zhu et al., 2021), the inclusion/omission of organic matter and moss insulation effects (Walvoord and Kurylyk, 2016), surface runoff (Abdelhamed et al., 2023), or vertical drainage impedance in the presence of ice (Andresen et al., 2020), can lead to relative wetter or drier permafrost states (de Vrese et al., 2023). The hydrological state of permafrost subsequently affects the soil moisture availability and water cycle evolutions under future warming Shared Socioeconomic Pathway scenarios (SSPs, 2015–2100, Andresen et al., 2020). Moreover, a more realistic representation of these processes within LSMs can lead to estimates of ALT and PE that are closer to the latest observational estimates (Chadburn et al., 2015), or help identify and understand biases and uncertainties ESMs have when representing permafrost dynamics. On the other hand, the prescription of insufficiently deep BBCPs leads to overestimating soil temperature trends (see Section 1.4, González-Rouco et al., 2021; Steinert et al., 2021b), which are especially intense in NH high latitudes. These temperature biases yield an overestimation of ALT deepening and PE loss with warming, being more remarkable for the deep permafrost (Hermoso de Mendoza et al., 2020; García-Pereira et al., 2025a). This limitation in LSMs, namely the prescription of overly shallow BBCP depths, is especially sensitive for assessing the vulnerability of large areas in Alaska and Siberia underlain by yedoma, deep organic-rich permafrost formed in the Pleistocene that contains up to an additional amount of about 400 PgC (Schuur et al., 2022).

Previous studies have explored the impacts of a better representation of certain thermodynamic and hydrological features of the LSM on PE and ALT in standalone LSM simulations (Ekici et al., 2014; Chadburn et al., 2015; Hermoso de Mendoza et al., 2020; Yokohata et al., 2020; Steinert et al., 2021b). Chapter 6 examines for the first time the potential role of Arctic soil wetness, soil depth, and layer discretization in driving changes in simulated permafrost temperature variability, PE loss, and ALT deepening in the industrial period using fully-coupled ESM simulations (García-Pereira et al., 2025a).

1.8 Motivation of this thesis

The thermodynamic and hydrological states of the ground surface and subsurface contribute to determining the climate over land. Mass, heat, and momentum transfer via turbulent heat fluxes define the land-air interactions and mutual dependencies at different temporal and spatial scales. In a stable climate, there are no changes in the external forcing and these fluxes are equilibrated in the long-term, so there is a surface energy balance. However, this balance has been perturbed since the last half of the 19th century due to the anthropogenically enhanced greenhouse effect, which induces a positive energy imbalance that is partitioned between the different climate components. Land heat uptake, which is a consequence of the positive energy imbalance at the ground surface, is producing a soil temperature increase. Soil warming is concerning for climate stability, since it triggers permafrost and the subsequent activation of the organic matter microbial decomposition in NH high latitudes. It also enhances soil respiration. In both processes land acts as a net source of carbon and, therefore, positive feedback on global warming. Therefore, understanding the underground heat transfer of surface temperature trends (Section 1.8.1), quantifying the contribution of the land heat uptake in the terrestrial energy partitioning (Section 1.8.2) and the uncertainties associated with estimating it from ESMs (Section 1.8.2, 1.8.3), as well as assessing the degradation of the Arctic permafrost due to global warming (Section 1.8.4) are important scientific questions that allow for exploring the climate change sensitivity to subsurface physical processes.

1.8.1 Characterizing the underground thermal regime from subsurface temperature observations

Observational subsurface temperature records are essential to understand the real-world mechanisms ruling the underground heat transfer, and the associated uncertainties. Previous literature has reported that underground heat transfer occurs mainly by conduction (Section 1.4). However, changes in the material, soil moisture content, or soil moisture thawing/freezing processes have the potential to disrupt the conductive regime, altering the downward propagation of GST changes. The relative importance of these processes has not been widely studied, since observational subsurface temperature data are globally scarce and time limited (Section 1.4). This is especially concerning in high latitude and mountain areas, where the presence of a seasonal snow cap and the near-surface soil freezing might disrupt the conductive thermal regime. Moreover, monitoring stations

having continuous time series usually measure shallow subsurface temperatures, many of them in the first meter of the soil. Deep subsurface data, reaching the bedrock, are exceptional. This hinders the study of heat transfer variations due to changes in the material. Additional data sources are essential to assess the thermodynamic and hydrological mechanisms governing soil and bedrock dynamics, and its response to temperature changes at the ground surface.

Thermodynamic and hydrological drivers of the soil and bedrock thermal regimes in central Spain (García-Pereira et al., 2024a) complements the existing evidence by analyzing the thermodynamic structure of the soil at various locations in the Sierra de Guadarrama, a high-altitude mountain range in Central Spain. To do so, data coming from four stations that belong to the monitoring network GuMNet (Cotos, CTS; Hoyas, HYS; Raso del Pino I, RSI; Herrería, HRR) and two from AEMET (Spanish Meteorological Office; Puerto de Navacerrada, NVC; Segovia, SGV) are used. GuMNet stations have relatively short series (2015–2021) of trench soil temperature and moisture data to a depth of 1 meter and borehole temperature data to a depth of 20 meters, whereas AEMET stations provide comparatively longer series (1989–2018) but only of trench temperatures. The underground propagation of temperature is characterized by assuming that heat transport occurs purely through conduction, disregarding transport by advection or radiation. Apparent thermal diffusivity values, the soil parameter controlling the velocity and intensity of the conductive propagation, are obtained based on the attenuation of amplitude and phase shift of the annual cycle with depth. Apparent thermal diffusivity is studied for the full subsurface column available (20 m for GuMNet and 1 m for AEMET sites), and layer-by-layer, which permits to detect vertical variations of this parameter with depth. Additionally, the amplitude attenuation of the annual cycle methodology is extended to analyze the entire temperature spectral domain, which allows for an evaluation of temporal changes in soil thermal diffusivity near the ground surface, and its potential connection with soil moisture changes. This line of research is extensively addressed in Chapter 3.

1.8.2 Estimating land heat uptake in the industrial period from different data sources

As already discussed, the anthropogenic greenhouse effect is producing a positive energy imbalance. How this extra energy input is partitioned between the different climate components is a long-standing question in climate research, and has

been studied using both observational and modeling data sources (Section 1.6). The latest observational estimates point at the ocean as the most prominent sink of the radiative imbalance, which absorbed around 90 % of the energy surplus in the last five decades. The second greatest contributor to the terrestrial energy partitioning is the land. The latest observational estimates based on borehole data quantify the land contribution to be 6 % in the last five decades, more than the contribution of the atmosphere and cryosphere together (4 %). Nevertheless, other studies based on state-of-the-art ESMs scale this figure down to 2 %. This underestimation stems from LSMs having a too shallow representation of the subsurface, which severely constrains the land heat uptake simulated by ESMs.

First comprehensive assessment of industrial-era land heat uptake from multiple sources (García-Pereira et al., 2024b) addresses this discrepancy studying the impacts of deepening the BBCP on ground surface and subsurface long-term temperature variability and land heat uptake in fully-coupled experiments. Two forced simulations of the past 2000 years (P2k) with the Max Planck Institute ESM (MPI-ESM) using deep and shallow LSM versions are compared. Chapter 4 shows that the deep P2k simulation captures about 4 times more heat than the standard shallow in the historical period, and well above the estimates provided by other ESMs. However, deepening the MPI-ESM BBCP does not affect the simulated temperature at the ground surface. As a consequence, it is shown that the land heat uptake values of ESMs with shallow LSM components can be corrected considering their simulated surface temperatures and propagating them with a standalone heat conduction forward model. This methodology is extended to all available GST sources, including observational data, reanalyses, and the latest CMIP6 simulations. All these complementary land heat uptake estimates contribute to gain confidence in the relevance of the BBCP depth to correctly represent the thermal response of the terrestrial subsurface within ESMs. Moreover, the corrected estimates can be used as a metric to determine the climate sensitivity of different data sources.

1.8.3 Assessing why shallow BBCP depths limit land heat uptake and its potential explanation at the ground surface

State-of-the art ESMs have been proved incapable of correctly representing subsurface temperature variability and trends and land heat uptake associated to ground surface warming. ESMs imposing too shallow BBCPs limit land heat up-

take and its contribution to the terrestrial energy partitioning, while producing an overestimation of temperature variability with depth (Sections 1.5 and 1.8.2). Although this temperature bias with depth is well established in the literature, neither temperature variability or trend differences have been found so far at the ground surface for both standalone LSM simulations or fully-coupled experiments. The omission of the geothermal flux in LSM thermal schemes could be a plausible explanation for this discrepancy. However, its value is stable at geological timescales, so it does not modify the energy balance at the ground surface at multi-decadal or centennial timescales.

Insufficient soil depth constrains ground heat flux in Land Surface Models (García-Pereira et al., 2025b) demonstrates that variations in the BBCP depth lead to changes in the GHF, which in turn drive the differences in land heat uptake portrayed by state-of-the-art ESMs. This conclusion is derived from a set of standalone simulations using the LSM of the MPI-ESM, JSBACH, with varying BBCP depths. Furthermore, this work investigates whether the disruption of the heat conductive regime caused by imposing the BBCP plausibly explains the constrained GHF. To test this, GHF estimates are derived using the one-dimensional heat conduction forward model introduced in Chapter 4, forced with GSTs from JSBACH simulations with different BBCP depths. Additionally, the influence of varying GHF values on the surface energy balance across different hydro-climates is explored. The most relevant results and insights given by this work are presented in Chapter 5 of this thesis.

1.8.4 Evaluating permafrost sensitivity to climate change under different configurations of the subsurface thermo-hydrodynamics

Global warming is particularly intense and sensitive in Arctic regions, which encompass large areas of perennially frozen soils (Sections 1.1 and 1.6). Permafrost degradation with warming enhances the release of substantial amounts of carbon into the atmosphere, which in turn boosts global warming. However, the increasing temperature is not the only factor affecting permafrost degradation. Water availability changes affecting the Arctic, induced by changes in the global weather patterns, considerably affect the soil moisture and ice presence and subsequently the thermal structure in permafrost regions. The interaction between soil hydrology and thermodynamics is still poorly represented by most of the state-of-the-art

LSMs within ESMs in terms of the BBCP depth, vertical resolution, and coupling between hydrology and thermodynamics.

Permafrost sensitivity to changes in soil hydro-thermodynamics in historical and scenario simulations with a modified version of the MPI-ESM (García-Pereira et al., 2025a) explores the response of the MPI-ESM in historical and future scenario simulations to changes in the hydrological and thermodynamic features of JSBACH in permafrost-affected regions. Several processes determining the coupling between soil hydrology and thermodynamics that are still not included in the standard CMIP6 version of the MPI-ESM are implemented in permafrost areas. This comprises the allowance for soil moisture phase changes (i.e., soil freezing and thawing below or above the melting point, respectively), the dynamic calculation of soil thermal parameters, or the inclusion of a multi-layer snow scheme. An ensemble of experiments with the MPI-ESM, the MPI-ESM Permafrost Physics Ensemble (MPIESM-PePE), was performed. The MPIESM-PePE includes simulations combining three different vertical discretizations, along with three configurations that generate comparatively drier (DRY) or wetter (WET) conditions with respect to the reference version of the MPI-ESM (REF) in permafrost regions. Results show that deepening JSBACH reduces the intensity of soil warming in permafrost regions, reducing the deep permafrost degradation and constraining the active layer thickening by the end of the 21st century in high radiative forcing scenarios. Nevertheless, the largest impacts on permafrost extent and active layer thickness are produced by the sensitivity to hydrological settings, which yield diverging soil moisture and warming conditions during the 21st century. An analysis and discussion of the main results of this work is presented in Chapter 6 of this thesis.

Chapter 2
Subsurface data sources: observations and model simulations

The subsurface heat propagation and its interaction with soil hydrology and biogeochemistry have been widely studied making use of in-situ observations (Sections 1.4 and 1.5). However, observational data are limited in their vertical and spatial coverage, and in most of the cases also temporally constrained. ESM simulations, although physically limited (Section 1.6), provide a continuous spatio-temporal representation of the soil thermal and hydrological structure, being a very useful complementary source of information for land surface and subsurface climate studies. This chapter describes the data sets employed in this thesis, both instrumental records and model experiments. Section 2.1 presents an ensemble of instrumental subsurface temperature records obtained at six sites in the area of the Sierra de Guadarrama, in central Spain. The compilation process, a general description of the available data, and the quality control procedure applied to the data are explained. Section 2.2 describes the main features of the ESM used in this thesis, the MPI-ESM, and its LSM, JSBACH. The MPI-ESM has been extensively used herein to assess various issues related to the response of land surface and subsurface to surface climate: temperature variability (Chapters 4 and 5); land heat uptake (Chapter 4); ground heat flux and surface energy balance (Chapter 5); as well as permafrost active layer thickness and extent (Chapter 6). Section 2.2 includes a description of the standard MPI-ESM and JSBACH physics, the modifications done to JSBACH to obtain a deeper representation of the BBCP, and the thermo-hydrodynamic features and setups introduced to the model in Arctic areas. Finally, Section 2.3 briefly presents complementary data sources that contributed to the analyses done in this thesis.

Table 2.1: Name, code, coordinates (longitude, latitude), altitude, and time span of available subsurface temperature data at both the GuMNet and AEMET observational sites.

Name	Code	Lon. (°)	Lat. (°)	Alt. (m a.s.l.)	Time span
GuMNet					
Herrería	HRR	-4.136	40.582	920	2016.06.11 to 2021.03.31
Raso del Pino I	RPI	-3.969	40.874	1803	2017.07.19 to 2020.01.11
Cotos	CTS	-3.961	40.825	1873	2015.09.16 to 2021.03.31
Hoyas	HYS	-3.955	40.834	2019	2015.10.03 to 2021.03.31
AEMET					
Segovia	SGV	-4.118	40.945	1005	1989.01.01 to 2012.07.31
P. de Navacerrada	NVC	-4.011	40.793	1894	1998.06.01 to 2018.12.31

2.1 Observational subsurface data in Sierra de Guadarrama

The observational subsurface data analyzed in Chapter 3 consist of temperature time series from six locations distributed over the Sierra de Guadarrama. Table 2.1 includes a more detailed description of the name, code, geographical position, and date range of available data of each location. The Sierra de Guadarrama is part of the Sistema Central, a mountain system that splits the Spanish Central Plateau into a southeastern side, with altitudes of around 600 m a.s.l. (above sea level), and a northwestern side, of higher elevation (ca. 750 m a.s.l.). Elevations in the sierra span from 900 at the foothills to ca. 2200—2400 m a.s.l. at the summits. Two sites, NVC and SGV, belong to AEMET, and the rest are part of GuMNet. The latter was created in 2014 with the aim of gaining further insights into climate variability in mountain environments in central Spain (Vegas-Cañas et al., 2020). GuMNet consists of 10 atmosphere and subsurface monitoring stations, which cover a vertical gradient ranging from 900 to 2200 m a.s.l., spreading over the mountainous terrain of the Sierra de Guadarrama. In this work, four stations were selected that provide information on atmospheric variables and subsurface temperatures (Fig. 2.1a). In all the cases, vegetation cover at the sites consists of short grass that changes minimally during the year. No site has trees or shrubs within the fenced perimeter of the monitoring station.

The subsurface thermal regime is monitored by two different arrangements. Near-surface soil temperatures are measured at various levels in trenches (TRCHs; Fig. 2.1b) at all the sites. TRCHs are excavations forming a slope in which the frontal wall was used to analyze the vertical structure of soil horizons (Brady and Weil, 2017) and to insert soil temperature reflectometer sensors down to a depth of about 1 m. TRCHs were refilled with the previously extracted material. Deeper temperatures in the soil and bedrock are monitored within cased bore-

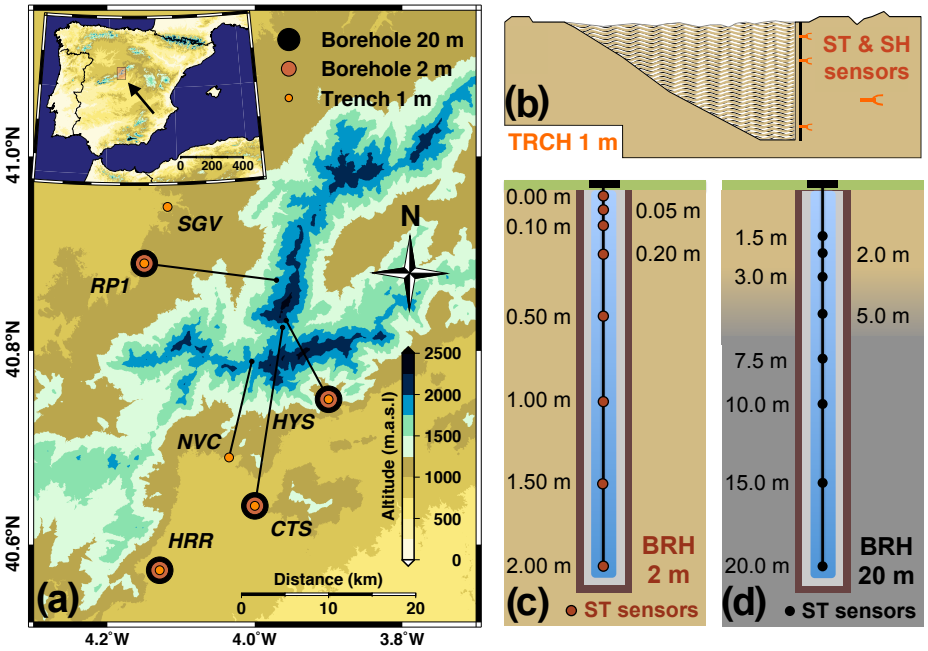

Figure 2.1: (a) Subsurface data availability over the area of the Sierra de Guadarrama used in this work. The map in the inset (left upper corner) points out the location of the Sierra de Guadarrama in the Iberian Peninsula. The extension covered by the map in (a) is represented by the orange-shaded area in the inset. (Right) Conceptual sketches of subsurface equipment for 1 m TRCHs (b), 2 m (c), and 20 m BRHs (d). The same distribution of subsurface temperature (referred to as ST in the figure) sensor depths is carried out at every site (c, d). Sensors in TRCHs are unevenly placed within the first meter of the ground at different sites. Pale yellow (grey) background color refers to soil (bedrock) in all panels. The transition depth between soil and bedrock (blurred area in d) is only intended for illustration and takes place at different depths for each site. Colors and shapes of the symbols are also illustrative. In addition to subsurface temperature data, all the stations provide SAT measurements as well as soil moisture content (referred to as SH in the figure) in the TRCHs.

holes (BRHs). They consist of a small diameter (ca. 76 mm) cylindrical drill in depth where a casing was inserted and afterward filled up with a silicone gel. Temperatures therein are measured with calibrated platinum resistance thermometers embedded inside the casing (Fig. 2.1c,d). For the sake of having a finer vertical resolution in the soil near the surface and some level of redundancy, two BRHs were installed at these sites: a deep one going down to 20 m (BRH 20 m in Fig. 2.1 and Table 2.2) and a shallow one of 2 m (BRH 2 m in Fig. 2.1). Table 2.2

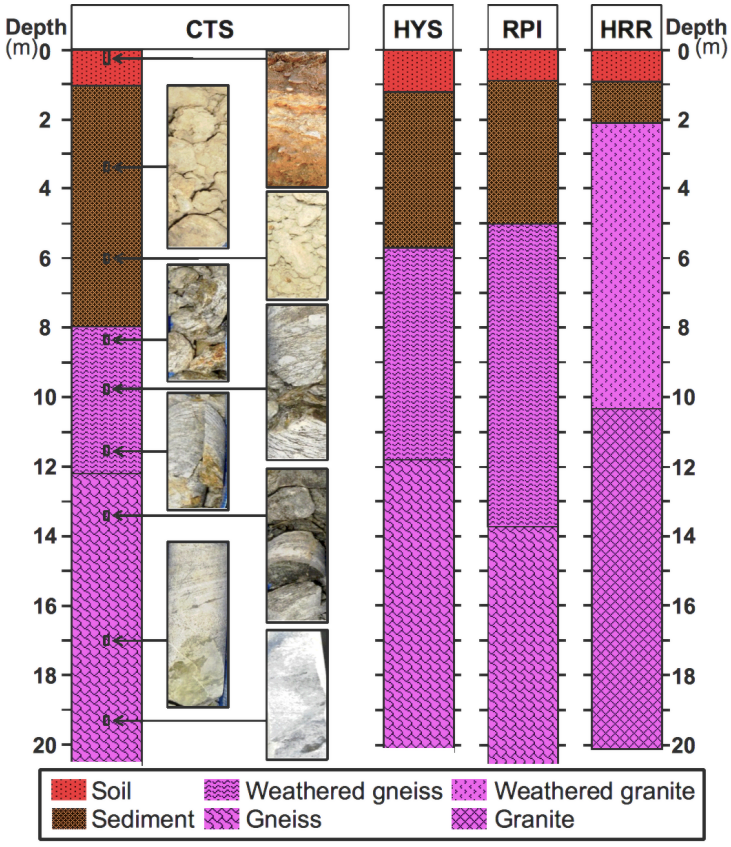

Figure 2.2: Subsurface mineral composition of the BRH cores extracted when drilling at CTS, HYS, RPI, and HRR. The top soil layer (red) covers approximately the first soil meter at every site, whilst sediments (brown) depth varies from one site to the other. Bedrock (magenta) underneath is of gneiss or granite, normally weathered at the top. In the case of CTS, some photos of the material at different depths are also included for illustration.

provides a detailed list of the depths at which subsurface temperature sensors were installed. Levels with malfunctioning sensors are marked with a dash.

During the BRH drilling process at the GuMNet sites, the extracted cores were preserved. They were subsequently sampled and characterized. The result is shown in Fig. 2.2, where the limits between the soil, sediment, and rock layers were determined. The superficial soil layer is made up of different soil horizons

Table 2.2: Depths corresponding to the available individual temperature series in the TRCHs and BRHs at each of the sites used in this work (see Table 2.1 for codes). Dash indicates missing data due to sensor malfunction.

Soil temperature sensor depths (m)														
TRCH 1 m						**BRH 2 m**				**BRH 20 m**			
CTS	**HYS**	**RPI**	**HRR**	**NVC**	**SGV**	**CTS**	**HYS**	**RPI**	**HRR**	**CTS**	**HYS**	**RPI**	**HRR**
0.10	0.20	0.20	0.20	0.05	0.05	GST	GST	GST	GST	1.50	1.50	1.50	1.50
0.65	0.50	0.45	0.50	0.10	0.10	0.05	-	0.05	-	2.00	2.00	2.00	2.00
1.00	0.75	0.80	1.00	0.20	0.20	0.10	-	0.10	0.10	3.00	-	3.00	3.00
				0.50	0.50	0.20	0.20	-	0.20	5.00	5.00	5.00	5.00
				1.00	1.00	0.50	0.50	0.50	0.50	7.50	-	7.50	7.50
						1.00	1.00	1.00	1.00	10.00	10.00	10.00	10.00
						1.50	1.50	1.50	1.50	-	15.00	15.00	15.00
						2.00	2.00	2.00	2.00	20.00	20.00	20.00	-

(Brady and Weil, 2017) containing an O and/or A horizon (i.e., topsoil) followed by E and/or B (i.e., subsoil) and several C (i.e., parent material) horizons that reach a depth of approximately 1 m. The underlying sediment layer contains eroded material of loose debris rocks that have accumulated at the corresponding locations. The CTS, HYS, and RPI profiles are located over gneiss rock and HRR on granite rock. In all the profiles, the upper layers have weathered bedrock, and with depth this bedrock is unweathered and compact. This information was used in Chapter 3 to compare changes in apparent thermal diffusivity to changes in mineral composition and textures with depth.

Subsurface temperature measurements are taken at a 10-minute time resolution at every GuMNet station. As a first step prior to the analysis carried out in this work, subsurface data were subjected to quality-control and resampling procedures. AEMET stations, NVC and SGV, were independently processed and resampled to daily resolution as described in Melo-Aguilar et al. (2022). The quality control of GuMNet sites focused first on removing data outliers. Since subsurface temperature sensors are connected in series in both BRHs and TRCHs (see Fig. 2.1b–d), erroneous extreme values are most often recorded at all levels simultaneously. Thus, to avoid discarding values that might be correct meteorological extremes, this correction was applied for both BRHs and TRCHs using the deepest time series to detect the erroneous values. The lowermost level was used because it shows the lowest temperature variability due to conductive damping of the surface signal. This reduces the range of high-frequency variability in the series except for the erroneous data, which makes non-reliable outliers easier to detect (Fig. 2.3). First, outliers flagged as physically implausible were removed, i.e., values falling below 230 K or exceeding 350 K. The detection of outliers

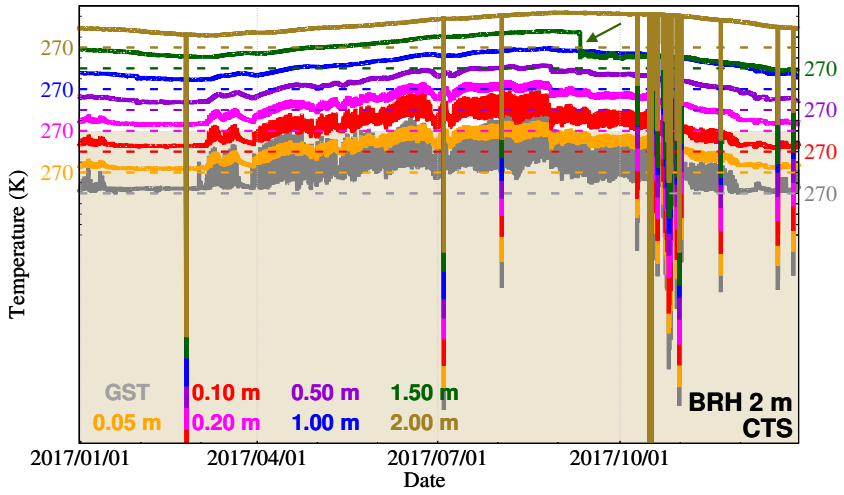

Figure 2.3: Example of errors in BRH 2 m at CTS in the year 2017. The 10-minute GST observations (grey) and those of temperatures for seven levels below the surface are shown. Time series are shifted an offset equivalent to 10 K and ticks are included every 5 K for clearer visualization. The value of 270 K is shown for all levels as a reference. The olive color band at the bottom represents the level of 230 K for the 2 m depth temperature time series, used to determine nonphysical values. The segment of the level of 1.5 m pointed by the arrow indicates a shift in the mean temperature value. Time values after the shift are subsequently eliminated.

below 230 K can be considered redundant since the next step would have detected all the values lying beneath this threshold. Second, the remaining spikes were flagged and discarded. Spikes were detected by calculating the sequential differences of each value minus its preceding one and screening the values in the interval, where Q1, Q3, and IQR are the first and third quartiles and the interquartile range of the distribution of temperature differences (Tukey, 1977). Time steps whose difference values were missing or outside of the screening interval were removed. Figure 2.3 shows an example of such spike screening for the BRH 2 m at CTS. The outliers depict coinciding failures at all the levels. The procedure is very conservative as the bottom levels have very low temperature variability and all spikes are identified and removed at each level. Note the decrease in high-frequency variability with subsurface depth, which is consistent with a heat conduction process (Section 1.4). Once outliers were removed, time series were subjected to a one-by-one inspection, and periods with clear drifts or strong changes in variability were manually removed (check Table 2.3 for a list

of removed periods at CTS and HYS). Figure 2.3 also shows an example of one such period for the 1.5 m depth temperatures at CTS (green arrow).

Table 2.3: Record of periods discarded at CTS and HYS for the analysis subsequently performed in this work. Records are sorted by log depths (descending) and span from the dates indicated up to the present.

Code	Sensor	Depth (m)	Timespan (from)
CTS	BRH 2 m	1.5	2017.09.11
	BRH 20 m	3.0	2019.05.21
	BRH 20 m	2.0	2019.04.09
	BRH 20 m	1.5	2018.08.19
HYS	BRH 2 m	2.0	2018.08.31
	BRH 2 m	1.5	2018.09.14
	BRH 2 m	1.0	2017.09.21
	BRH 20 m	2.0	2019.11.03

After applying the aforementioned quality-control procedures, the GuMNet series were resampled at hourly resolution, which filtered out noisy intra-hourly variability unnecessary for the subsequent analysis of the data. This was attained by calculating pseudo-hourly time series, which was carried out with a nearest-neighbor resampling technique (Brandsma and Können, 2006) by selecting the 10-minute data closest to the hour. Finally, the resulting series were averaged to obtain daily mean subsurface temperatures that were subsequently used to analyze the propagation of the annual cycle.

In addition to subsurface temperature data, all the stations include SAT measurements as well as soil moisture content within the trench-monitoring levels. SAT is recorded at 2 m above the ground surface at all the sites using a temperature probe encapsulated within a shield. Snow cover data are also available at CTS, HYS, and RPI (see the codes in Table 2.1). Snow depth is measured with an ultrasonic snow depth sensor that captures the distance to the surface. Depth values are obtained from the subtraction of the surface level measured from the reference ground surface level value. These additional data were used to explore potential drivers of the SAT–GST seasonal decoupling and temporal changes in soil apparent thermal diffusivity at some sites.

2.2 Simulated subsurface data: the MPI-ESM and its land component JSBACH

The state-of-the-art ESM used for the analyses in Chapters 4, 5, and 6 of this thesis is the Max Planck Institute for Meteorology (MPI-M) Earth System Model, version 1.2, in low resolution (MPI-ESM1.2-LR or simply MPI-ESM, Mauritsen et al., 2019). The MPI-ESM is the reference ESM of the MPI-M and one of the members contributing to the CMIP6 (Eyring et al., 2016), and therefore to the results presented in the Intergovernmental Panel on Climate Change Assessment Report 6 (IPCC AR6, Masson-Delmotte et al., 2021). The MPI-ESM consists of the atmosphere model ECHAM6.3 (ECHAM, Stevens et al., 2013), and the ocean model MPIOM1.6 (MPIOM, Jungclaus et al., 2013). The MPIOM includes the resolution of the ocean biogeochemistry by the HAMOCC module (Ilyina et al., 2013). The LSM used by the MPI-ESM is the JSBACH3.2 (JSBACH, Reick et al., 2021), which includes the simulation of subsurface thermodynamics as well as the land-based part of the hydrological cycle. JSBACH is directly connected to ECHAM through the surface exchange of mass, momentum, and heat. ECHAM and MPIOM are communicated by the OASIS3-MCT coupler (Craig et al., 2017). Therefore, in fully-coupled experiments, the four components resolved by the MPI-ESM work in pairs (MPIOM & HAMOCC and ECHAM & JSBACH) coupled by OASIS3-MCT. This coupling occurs once a day of simulation, while the individual time step length is 45, 7.5, and 30 minutes of simulation for MPIOM, ECHAM, and JSBACH, respectively. Even though the reference simulations with the MPI-ESM participating in the CMIP6 are conducted in fully-coupled mode (Maher et al., 2019), its four components can also be run offline or standing alone, which allows for more specific analysis on the physical processes that generate ocean, atmosphere, or land surface and subsurface climate variability (Mansfield et al., 2023). In both fully-coupled or standalone modes, the MPI-ESM can be run at multiple spatial resolutions. In the low-resolution "LR" setup used in this thesis, the ECHAM resolution is T63/L95 and MPIOM is GR1.5/L40, which corresponds to a 1.875^o (1.5^o) grid cell width over land (the ocean).

The land component of the MPI-ESM, JSBACH, resolves a simplified representation of the thermodynamic, hydrological, and biogeochemical processes that determine the land surface, soil, and bedrock conservation of mass, momentum, and heat. Conservation of mass involves the capture, release and transport of soil carbon, nitrogen, and moisture. In fully-coupled MPI-ESM simulations, the hydrological interaction between JSBACH and ECHAM occurs as a result of a water balance between precipitation, runoff, evapotranspiration, and soil moisture storage at the ground surface. The carbon and nitrogen cycles can be prescribed fixed or interactive with ECHAM, via land-air exchanges due to carbon and nitrogen

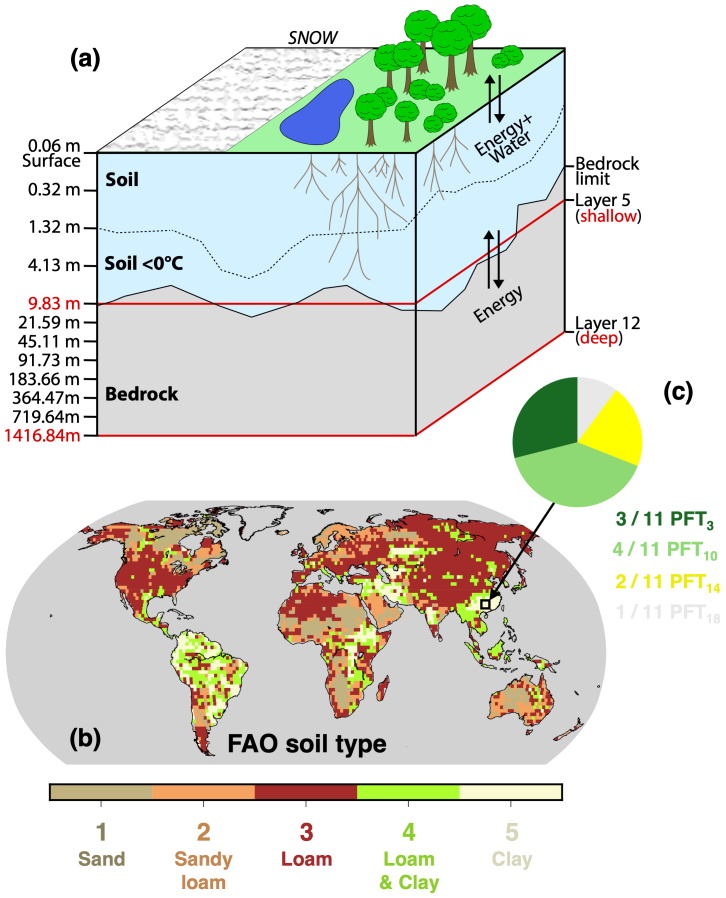

Figure 2.4: Main land surface and soil features of the JSBACH standard version. (a) Three-dimensional sketch of a JSBACH grid box. The mid-layer depth values for the default 5-layer (5L) vertical discretization, with a BBCP placed at 9.83 m ("shallow"), are given on the left part of the y-axis. These values are also shown for the 12-layer "deep" discretization, with the BBCP at 1416.84 m. Adapted from González-Rouco et al. (2021) (b) Soil types used by JSBACH according to the FAO classification by Dunne and Willmott (1996): sand, sandy-loam, loam, mixture of loam and clay, and clay. Different soil thermal and hydraulic properties are prescribed based on these soil types. (c) Idealized illustration of the land cover type tiling of a grid box in Southern China. In this example, 3 out of 11 tiles would be covered by PFT_3 (tropical deciduous trees), 4 by PFT_{10} (raingreen shrubs), 2 by PFT_{14} (pasture), and 1 by PFT_{18} (swamp). See Reick et al. (2021) for an exhaustive description on the different soil types and PFTs implemented in JSBACH.

pools. The thermodynamic interaction between JSBACH and ECHAM is ruled by the surface energy balance, by which changes in the surface net radiation are balanced out by the turbulent (sensible and latent) and ground heat fluxes, and changes in the surface temperature (see Chapter 5). In standalone simulations, the surface energy and water balances are determined by atmospheric boundary conditions (temperature, precipitation, wind speed, etc.) coming from ECHAM or MPI-ESM simulations, or other data sources. Any feedback from the land surface to the atmosphere is overruled by the atmospheric conditions prescribed in the next time step.

The relative contribution of the different mass and heat fluxes at a grid box scale depends on the land surface conditions and soil properties in both standalone JSBACH and fully-coupled MPI-ESM simulations. For the computation of the land surface conditions, JSBACH divides every grid box into smaller units or 'tiles', which account for the subgrid scale heterogeneity. Each tile in each grid box is associated with only one land cover type, which can be either a plant functional type (PFT; e.g., tropical evergreen forest, coniferous deciduous trees), bare soil (deserts) or glacier.

Table 2.4: Volumetric heat capacity (C_v) and thermal diffusivity (κ) for the different soil types used in JSBACH. These types correspond to the five soil classes defined by the FAO (see Fig 2.4b). In the absence of snow, these values are used to resolve the subsurface thermodynamics. Thermal conductivity (λ) is computed as $\lambda=\kappa C_v$. Snow presence modified soil thermal parameters (see Section 2.2.1). The weighted global mean (without considering snow) is also provided (last column in bold).

Soil type (Unit)	Sand	Sandy Loam	Loam	Loam & Clay	Clay	Snow	**Global (w/o snow)**
C_v (10^6 $Jm^{-3}K^{-1}$)	1.93	2.10	2.25	2.36	2.48	0.64	**2.22**
κ (10^{-7} m^2s^{-1})	8.70	8.00	7.40	7.10	6.70	4.90	**7.90**

The surface conditions are modified when there is snow, which modifies the surface albedo. Furthermore, surface and soil thermal conditions are further influenced by the insulating properties of the snow cover. The reference version of JSBACH solves a single-layer or 'bucket' snow scheme (Fig. 2.4a) with a fix value of the thermal conductivity (0.31 $Wm^{-1}K^{-1}$) and volumetric heat capacity (6.35 10^5 $Jm^{-3}K^{-1}$, see Table 2.4). As the snow accumulates and thickens, JSBACH modifies the thermal properties of the upper soil layers depending on the snow depth (Reick et al., 2021). In practice, this means that the snow layer functions as if it were embedded into the soil column, shifting the active thermal interface deeper into the ground. This resolution of the snow by JSBACH effectively insulates the near-surface ground from SAT variations (snow insulation effect, Cook

et al., 2008; Krinner et al., 2018), with the top of the snow layer acting as the top of the soil model (Schulz et al., 2001), and the bottom acting as a boundary condition for the underground transfer of heat and water. Under snow-free conditions, soil properties, such as soil thermal conductivity, volumetric heat capacity, and porosity, can be either prescribed by initial files, or computed dynamically. In the standard configuration of JSBACH used in this thesis, the soil properties take constant values according to the five soil types defined by the Food and Agriculture Organization (FAO, Dunne and Willmott, 1996, Fig. 2.4b, see also Table 2.4 for consulting the exact values). The number of tiles is fixed to 11 (Fig. 2.4c).

Table 2.5: Number, mid-layer depth, bottom layer depth, and thickness of each layer in the JSBACH vertical discretizations used in Chapters 4 (fully-coupled P2k+s and d experiments), and 5 (standalone JSBACH experiments) of this thesis (see also Fig. 2.4).

Layer number	Mid-layer depth (m)	Bottom layer depth (m)	Thickness (m)
1	0.03	0.06	0.06
2	0.19	0.32	0.26
3	0.78	1.32	1.00
4	2.68	4.13	2.81
5	6.98	9.83	5.70
6	15.71	21.59	11.76
7	33.35	45.11	23.52
8	68.42	91.73	46.62
9	137.70	183.66	91.93
10	274.07	364.47	180.81
11	542.06	719.64	355.17
12	1068.24	1416.84	697.20

The initial files do not only prescribe the JSBACH soil properties (when non-dynamic), but also the subsurface vertical structure. In the standard configuration of JSBACH, the subsurface heat transport is resolved down to a zero-flux BBCP at 9.83 m (Fig. 2.4a), which is also the maximum depth that the soil can reach. Water transport is resolved down to the soil-bedrock limit, which varies from 0.10 to 12.45 m depending on the local features and is prescribed by the JSBACH initial files. For grid boxes with greater soil than BBCP depth values, the full vertical profile is constituted by soil and the hydrology is solved just down to the BBCP depth (Fig. 2.4a). The subsurface is discretized in five layers that are increasingly thick with depth and extend down to the BBCP at 9.83 m. This vertical discretization will be denoted as "shallow" in this thesis (Fig.

Table 2.6: Overview of the simulations used in this thesis. Name of the ensemble, number of members, vertical discretization, hydrological configuration and reference for the standalone simulations with JSBACH, and fully-coupled simulations with the MPI-ESM, used in Chapter 5, as well as in Chapters 4 and 6, respectively.

Ch.	Ensemble	N. of members	LSM vertical discretization	Hydrology configuration	Reference
4	MPI-ESM P2k+	2	5L (s), 12L (d) (Table 2.5)	REF	García-Pereira et al. (2024b)
5	JSBACH	8	5L to 12L (Table 2.5)	REF	González-Rouco et al. (2021) García-Pereira et al. (2025b)
6	MPIESM-PePE	9	5L, 11L, 18L (Table 2.7)	REF WET, DRY	García-Pereira et al. (2025a)

2.4a). A more detailed description on the mid-layer and bottom layer depths and thickness of every layer is provided by Fig. 2.4a and Table 2.5. JSBACH only considers vertical heat conduction for the resolution of the subsurface thermodynamics, thus neglecting the contribution of advection and horizontal diffusion of heat (Carslaw and Jaeger, 1959), and the warming effect of the geothermal flow (Lucazeau, 2019). Water transport occurs by vertical diffusion and percolation, with no horizontal flow nor hydrological communication between contiguous grid boxes. Moreover, JSBACH does not consider soil water phase changes at freezing, which entails it is not capable to reproduce permafrost dynamics. This limitation was addressed by Ekici et al. (2014) and Steinert et al. (2021b) in JSBACH standalone simulations, and extended to MPI-ESM fully-coupled simulations in this thesis (see Section 2.2.2 and Chapter 6).

A brief overview of the simulations used in each chapter, along with the corresponding modifications made to JSBACH thermal vertical discretization and hydrology, is provided in Table 2.6. This compendium serves as a reference for understanding the differences in the thermodynamic setups and hydrological configurations across the experiments described in Sections 2.2.1 and 2.2.2.

2.2.1 Simulated subsurface data: deepening the MPI-ESM in climate simulations of the Common Era

As it was already discussed in Section 1.5, the prescription of shallow BBCPs when resolving the underground heat conduction in LSMs is a limiting factor in state-of-the-art ESM simulations. This is the case for the MPI-ESM (González-Rouco et al., 2021; Steinert et al., 2021b; García-Pereira et al., 2024b; Steinert

et al., 2024), whose LSM, JSBACH, imposes a BBCP at 9.83 m depth, resulting in a biased representation of the subsurface temperature profile and an underestimation of the land heat uptake at decadal and longer term scales (Steinert et al., 2021a). To put this BBCP depth in context, JSBACH is not even deep enough to correctly resolve the downward propagation of the annual cycle, which penetrates down to 15 to 20 m depending on the thermal diffusivity (see Section 1.4). Thus, the standard configuration of the MPI-ESM is not suitable to properly simulate the subsurface response to the industrial warming.

In order to explore the impacts on climate variability of imposing a deeper BBCP in standalone LSM simulations, González-Rouco et al. (2021) developed a vertically extended discretization of JSBACH. They conducted an ensemble of eight historical (1850–2005) and Representative Concentration Pathway (RCP) 8.5 W/m^2 scenario (RCP8.5, 2006–2100) simulations with increasingly deeper positions of the BBCP, progressively extending the JSBACH vertical scheme from 5 to 12 layers (see Table 2.5). To achieve a moderate increase of the thickness values with depth while having a higher vertical resolution near the surface, González-Rouco et al. (2021) used an exponential law (Oleson et al., 2013) of the form $z_i = a(e^{b(i-b)} + c)$, with i being the layer number, $a = 0.334$, $b = 0.674$, and c = -1.450. Since this law produces small deviations from the standard shallow JSBACH depth values of the upper 5 layers, values of layer 1–5 in the new vertical discretizations are left unchanged, and the law is only applied to derive the depths of layer 6–12. An exhaustive analysis on surface and subsurface temperature variability and change and land heat uptake in the different discretizations is presented by González-Rouco et al. (2021). This thesis uses this ensemble of standalone JSBACH simulations to explore the ground surface physical mechanisms explaining the dependence of the land heat uptake with the BBCP depth. The methodology and results of this study are presented in Chapter 5.

To evaluate whether the subsurface temperature variability changes reported by González-Rouco et al. (2021) impact on SAT, land heat uptake, and terrestrial energy budget, Steinert et al. (2024) conducted a fully-coupled MPI-ESM simulation covering the industrial period (1850—2100) under different SSP scenarios. The simulation used a 12-layer vertical scheme with a BBCP at 1416.84 m. This discretization ("deep" hereafter) ensures that the bottom subsurface layer is detached from the ground surface, i.e., is irresponsive to GST changes, at multi-centennial and millennial scales. This thesis extends the evaluation by Steinert et al. (2024) to long-term scales by presenting the first full forcing ESM simulation covering the past two millennia (Past2k, 0–1850), the historical period (1850–2014), and the 21st future warming in the lowest and highest radiative emission scenarios (SSP1-2.6 and SSP5-8.5, respectively, 2015–2100) including a deep LSM vertical discretization in fully-coupled mode. The interval encompass-

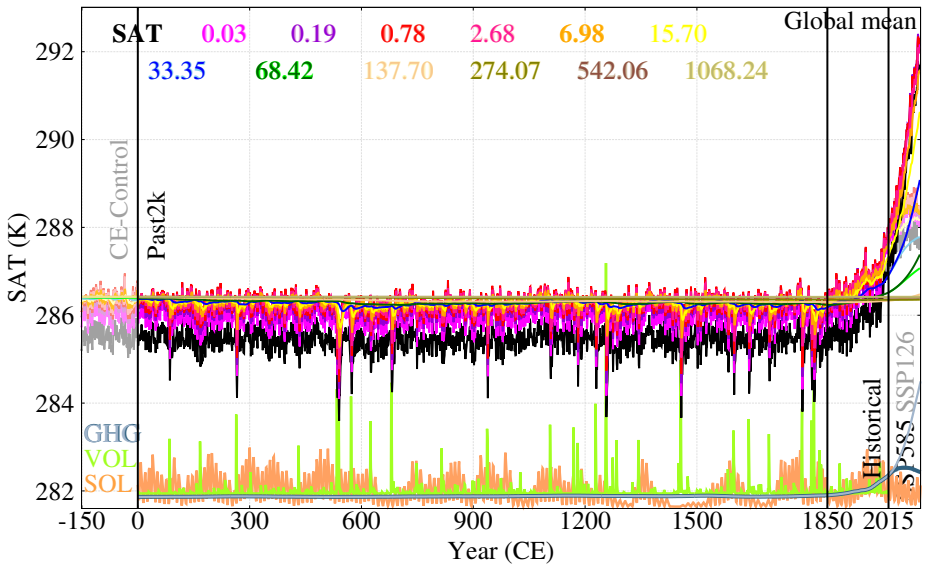

Figure 2.5: Yearly global mean SAT and subsurface (see levels in the color legend) temperature variability in the P2k+d simulation. Temperatures in year 180 of the P2k+ CE-Control run are used as initial conditions for the P2k+d simulation in year 1 CE. The Past2k, historical, and SSP scenario are separated by vertical bars. The evolution of temperature data in the CE-Control and SSP1-2.6 scenarios are given in clear colors. Apart from the global mean temperatures, the yearly evolution of the GHG concentration, volcanic aerosol optical depth and solar spectral irradiance are also depicted as standardized anomalies (no units) to have a rough estimation of the forcing.

ing 0–2100 CE is denoted hereafter as P2k+. The ground surface and subsurface temperature variability and land heat uptake of the P2k+ deep (P2k+d) simulation presented herein is compared in Chapter 4 to a previous P2k+ experiment with the standard shallow version (P2k+s) of the MPI-ESM. The P2k+s simulation is the MPI-M contribution to PMIP4 (van Dijk et al., 2022). Both experiments follow the PMIP4 tier-3 forcing protocol defined by Jungclaus et al. (2017), which is an extension of tier-1 past1000 forcing to the past so as to cover the whole CE. In summary, yearly changes of the volcanic forcing (Toohey and Sigl, 2017), solar spectral irradiance (Vieira et al., 2011), orbital parameters (Berger, 1978), and greenhouse gases (Meinshausen et al., 2017) were considered. LULC was prescribed constant until 850, and changes according to reconstructed land-use and anthropogenic land-cover data thereafter (Hurtt et al., 2020). To

depart from a climate equilibrium state by the beginning of the CE, the P2k+d simulation was restarted from a 1000-year-long control simulation with an equilibrated deep subsurface and constant conditions of year 0 CE (CE-Control). The CE-Control run was subsequently restarted from a spin-down MPI-ESM simulation to year 0 CE conditions, initialized from pre-industrial control (piControl) conditions.

The P2k+d yearly global mean SAT and temperature at the 12 subsurface layers is represented in Fig. 2.5. The standard anomalies of the volcanic, solar, and GHG forcings are also portrayed. There is a clear short-term drop in SAT and near-surface soil temperatures as a response to the major volcanic eruptions of the CE, which is due to the reduced incoming solar radiation produced by a large injection of aerosols into the stratosphere (see Section 1.2). Furthermore, the accumulative effect of volcanic together with changes in solar activity produce long-term temperature variability, with relatively warm periods (e.g., the maximum of the Medieval Climate Anomaly, MCA, around the 12th century) succeeded by clearly colder stages (e.g., the end of the Little Ice Age, LIA, in the 18th and early 19th century). The preindustrial forced variability is overshadowed by the strong industrial warming since the 20th century associated with a large increase in the GHGs concentration. This concentration peaks around 2050 in the low radiative emission, SSP1-2.6, so does temperature. In case of the SSP5-8.5, both the GHG concentration and temperature trends skyrocket, with SAT and near-surface global mean temperatures being up to 6 K warmer than in the pre-industrial period. As mentioned above, having a P2k+d simulation permits a wider analysis of the impacts of changing the BBCP on short- and long-term temperature variability, both as a response to the low preindustrial and to the intense GHG forcing of the Anthropocene. Also, a long millennial P2k+d experiment provides realistic, i.e., consistent with external forcing, preindustrial initial conditions for subsurface temperatures down to the bottom layer in 1850, which is essential to avoid biases when assessing the industrial land heat uptake and terrestrial energy imbalance. All these analyses and the comparison to the P2k+s simulations are extensively addressed in Chapter 4. In addition to the P2k+ experiments, Chapter 4 also considers an ensemble of 30 historical and SSP5-8.5 simulations (hereafter denoted as 30ENS) run with the MPI-ESM. The experiments use the same model version as P2k+s and serve the purpose of tackling the uncertainties in SAT, GST, and subsurface temperature variability and land heat uptake due to internal variability.

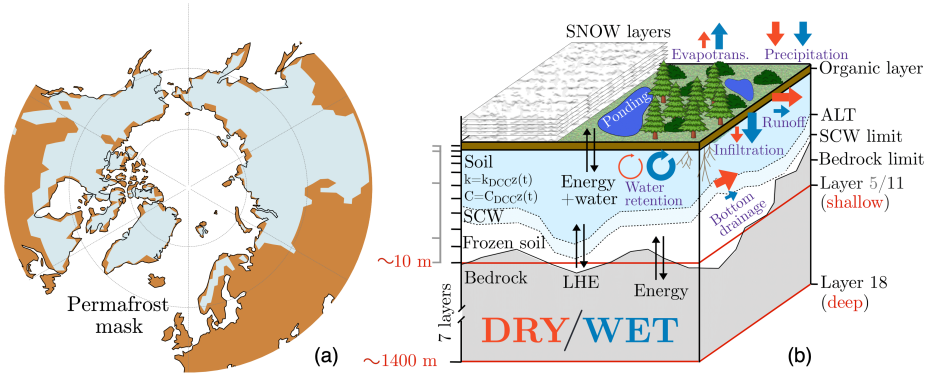

Figure 2.6: HTCp changes applied to JSBACH standard version. (a) NH (45–90ºN) land permafrost affected areas (shaded light blue) in the late historical period (Hugelius et al., 2013, 2014), which are taken as the mask where the HTCp physics are implemented. Outside the area portrayed by the permafrost mask in (a), the REF (Fig. 2.4a) configuration of JSBACH is used. (b) Conceptual sketch showing the features and the intensity (arrow size) of different thermodynamic and hydrological processes for HTCp DRY (red) and WET (blue) configurations.

2.2.2 Simulated subsurface data: improved resolution of the thermo-hydrodynamics in permafrost areas

The standard version of JSBACH (Fig. 2.4a) does not include any coupling processes between soil thermodynamics and hydrology, which prevents soil ice from forming under freezing conditions. This limitation was addressed by Ekici et al. (2014) and Steinert et al. (2021b) by incorporating the occurrence of water phase changes with temperature, and the dynamic calculation of soil thermal properties in previous versions of JSBACH. However, these changes were run only in standalone LSM simulations. A modified version of JSBACH allowing for hydro-thermodynamic soil coupling in permafrost regions (HTCp hereafter, Fig. 2.6b) was introduced by de Vrese and Brovkin (2021) and de Vrese et al. (2023) and is used in this work in fully-coupled ESM simulations. The HTCp physics are only active across the areas covered by the mask shown in Fig. 2.6a (Hugelius et al., 2013, 2014), which represents the observed early 21st century PE. Furthermore, the JSBACH standard vertical scheme of five layers (5L) with a soil depth of 9.83 m was deepened and refined near the surface. An enhanced vertical resolution accounts for a better representation of thermo-hydrodynamical processes near the surface (Chadburn et al., 2015). Further, a more realistic deeper soil depth per-

Table 2.7: Number, mid-layer depth, bottom layer depth, and thickness of each layer in the three JSBACH vertical discretizations used in Chapter 6 of this thesis. Note that 5L corresponds to the vertical structure in the standard JSBACH version, and 11L and 18L correspond to the vertical resolution enhancement and extension introduced in this work (see also Fig. 2.6b).

Layer number	Mid-layer depth (m)	Bottom layer depth (m)	Thickness (m)
		5L	
1	0.03	0.06	0.06
2	0.19	0.32	0.26
3	0.78	1.32	1.00
4	2.68	4.13	2.81
5	6.98	9.83	5.70
		11L / 18L	
1	0.03	0.06	0.06
2	0.18	0.30	0.24
3	0.42	0.54	0.24
4	0.66	0.78	0.24
5	0.92	1.06	0.28
6	1.21	1.36	0.30
7	1.59	1.82	0.46
8	2.14	2.46	0.64
9	3.03	3.60	1.14
10	4.67	5.74	2.14
11	7.86	9.98	4.24
12	14.33	18.68	8.70
13	27.66	36.64	17.96
14	55.42	74.20	37.56
15	113.49	152.78	78.58
16	235.28	317.78	165.00
17	490.91	664.04	346.26
18	1027.76	1391.48	727.44

mits an unbiased representation of subsurface temperature variability and land heat uptake (González-Rouco et al., 2021; Steinert et al., 2021a). Thus, two new vertical layering schemes are introduced: an 11-layer (11L) scheme with a BBCP depth of 9.98 m, and a deepened 18-layer (18L) scheme with a BBCP depth of 1391.48 m (Fig. 2.4a). The 11L scheme substitutes the original 5L discretization by enhancing the vertical resolution while keeping the same BBCP depth. The 18L scheme shares the top 11 layers with the 11L scheme and adds seven additional layers to reach a depth of 1391.48 m. Imposing such a deep zero-flux BBCP

guarantees that the bottom layer temperature is detached from surface temperature variations at multi-centennial and millennial simulations (García-Pereira et al., 2024b). A detailed description of the layer depth and thickness values of 5L, 11L, and 18L schemes can be found in Table 2.7 and Fig. 2.4a. The design of the layering follows an exponential function of the form $z_i = aexp[b(i-b)+c]+d$ (Oleson et al., 2013; González-Rouco et al., 2021), similar to the discretization already described in Section 2.2.1. In this case, the coefficients a, b, c, and d were set to 0.00198, 0.743, 83.77, and 0.0585, respectively. These values aimed at representing a BBCP depth for the 5L and 11L configurations that was virtually equal while keeping a thickness of 0.03 m for the first soil layer. The same coefficients were used to estimate the thickness of layers 12–18 for the 18L configuration (Table 2.7).

A more realistic feature in HTCp in comparison with JSBACH is that both the soil water phase and thermal properties vary with temperature and moisture content, respectively. This allows for the existence of ice in Arctic soils, which is not represented by JSBACH. Other new hydrological features included comprise interactions between soil hydrology and vegetation, which considers the representation of the organic layer insulation, the allowance for supercooled water, a finer representation of percolation and drainage by accounting for the effect of soil ice impedance, and an improved multi-layer snow scheme. Additionally, a wetland scheme was introduced, so surface ponding affection on soil properties is accounted for. A thorough description of these changes can be found in de Vrese et al. (2023).

Moreover, the HTCp allows for controlling some of the hydrological processes involved in the surface and near-surface soil water cycle within the permafrost areas (Fig. 2.6a). Two combinations of parameters (hereafter referred to as configurations) based on de Vrese et al. (2023) were used to generate two subsets of experiments with relatively drier or wetter states of the Arctic, which will be labeled as DRY and WET, respectively. The DRY configuration (red labels and arrows in Fig. 2.6b) exhibits weak local moisture recycling due to low infiltration rates and drainage resistance. Consequently, the near-surface permafrost degradation results in progressively drier soils under this configuration. By contrast, the WET configuration (blue, Fig. 2.6b) assumes favorable infiltration coupled with high drainage resistance, leading to moist soils. An intense local moisture recycling is also fostered by imposing a low resistance to evapotranspiration. Outside of the permafrost mask (Fig. 2.6a), the soil physics correspond to those used in the standard configuration of JSBACH (Fig. 2.4a). This configuration will be referred to as REF hereafter, to distinguish it from the WET and DRY variants. In addition to two sets of DRY and WET simulations with different vertical discretizations, a third set of experiments was conducted using the REF

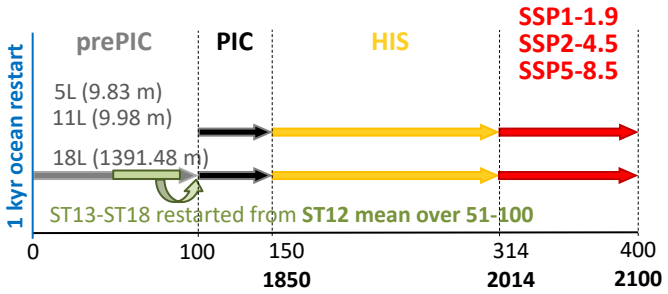

Figure 2.7: Experimental setup of the MPIESM-PePE. Scheme of preindustrial control (PIC, black), historical (HIS, yellow), and 21st century climate change Shared Socioeconomic Pathway forcing scenario (SSP1-1.9, SSP2-4.5, and SSP5-8.5, red arrows) simulations for each of the REF, WET, and DRY configurations of the MPIESM-PePE. This sequence was also run with different vertical discretizations of 5, 11, and 18 layers (5L, 11L, and 18L, respectively); see Table 2.7 and Fig. 2.6b. PIC is conducted with conditions of 1850 for 50 years. The historical run (HIS) is started at year 50 of PIC for the three vertical discretizations. To speed up subsurface temperature equilibrium in the vertical column for the 18L simulations, a prior preindustrial control (prePIC) phase of 100 years is run. The subsurface temperature mean for the last 50 years at the 12th layer for the prePIC is used to restart temperatures at layers 13th to 18th in the 18L configuration (see Table 2.7 and text for the details).

physics globally. This served as a benchmark to evaluate the effects of applying the WET and DRY configurations across the permafrost domain.

Combining the three configurations of the hydro-thermodynamics (the HTCp WET and DRY, and the JSBACH REF) and the three vertical discretizations of the subsurface (5L, 11L, and 18L) yields a total number of nine experiments, which constitute the MPI-ESM Permafrost Physics Ensemble (MPIESM-PePE hereafter). All the MPIESM-PePE simulations extend from 1850 to 2100. The study focuses on assessing the combined impact of the different configurations and vertical discretizations on permafrost-related variables under industrial forcing conditions. The experiment setup follows the scheme in Fig. 2.7. In all the simulations the ocean component was initialized from a long-term ocean simulation restart that had been stabilized to preindustrial conditions. Each 5L and 11L MPIESM-PePE experiment was run first in a piControl (PIC) phase of 50 years, which simulates a climate state compatible with the external forcing in 1850 and provides initial conditions for the historical runs (HIS; 1850 to 2014). These runs are subsequently continued into the 21st climate change stage under different radiative forcing scenarios (SSP1-1.9, SSP2-4.5, and SSP5-8.5, O'Neill et al., 2016), following the standard forcings of CMIP6 (Eyring et al., 2016). However, subsurface temperatures at the deepest layers of the 18L simulations do not

have enough time to transit to a new equilibrium state within a 50-year-long PIC (González-Rouco et al., 2021). Therefore, a pre-piControl (prePIC) phase of 100 years is run before PIC for the 18L experiments to equilibrate the subsurface vertical structure. To speed up temperature convergence, the mean subsurface temperature of the last 50 years of prePIC of layer 12 (ST12) is imposed as the initial condition for the deepest layers (ST13 to ST18) in the 18L PIC simulations. The rest of the STs are just continued from the last timestep in prePIC.

A thorough evaluation on the impacts of changing both the subsurface vertical discretization and configuration in MPIESM-PePE for ground and near-surface temperature variability, ALT, and PE is provided in Chapter 6.

2.3 Additional sources of subsurface climate information

2.3.1 CMIP6 simulations and subproducts

GST and subsurface temperature data of historical period and SSP5-8.5 scenario simulations from the available CMIP6 ESMs (Eyring et al., 2016, see Table 2.8) were used in Chapter 5 to derive estimates of the land heat uptake. This added up to 36 simulations stemming from 22 different ESMs and some model variants, 38 if accounting for P2k+ simulations (Section 2.2.1) since 1850. The temperature at the first soil layer was used as GST. Only the first ensemble member was selected for every specific ESM. In the case of the 30ENS (Section 2.2.1), only the first member was considered for the analyses hereafter and is referred to as MPI-ESM1.2-LR in Table 2.8. Some features of the LSM of every CMIP6 ESM, such as the number of soil layers, BBCP depth, and horizontal resolution can be found in Table 2.8. It is noteworthy that most CMIP6 ESMs include BBCP depths lower than 14 m, which is not sufficient to properly represent the propagation of the temperature annual cycle into the soil column (Section 1.4). Only 14 out of 38 members impose a BBCP depth below 40 m, still shallower than the 170 m BBCP depth recommended to correctly simulate the propagation of the centennial climate change signal (González-Rouco et al., 2021; Steinert et al., 2021a). Thus, land heat uptake estimates for CMIP6 simulations are derived both by integrating the LSM subsurface temperatures and by using a half-infinite standalone heat conduction forward model. The comparison of both methods serves to sort out the role of the BBCP on limiting the land heat uptake. This is explained in detail in Chapter 4.

Table 2.8: CMIP6 experiments used in this thesis (Col. 1) and their corresponding horizontal resolution (Col. 2) and LSM component (Col. 3). The number of layers (Col. 4) in the LSM and the BBCP depth (Col. 5), as well as temperature trends in the three different periods assessed in Fig. 4.3 (1950–2000, 1960–2020, and 1971–2018; Cols. 6–8) for every CMIP6 model and the multi-model mean are also provided. Information for the deep LSM configuration of the MPI-ESM (see Section 2.2.1) is also included (line 18, bold).

	ESM	**Resolution** **N. gridpoints**	**LSM**	**N. of layers**	**BBCP depth** [m]	**1950–2000** [Kdec^{-1}]	**1960–2020** [Kdec^{-1}]	**1971–2018** [Kdec^{-1}]	**Reference**
1	ACCESS-CM2	1.88^{o}x1.25^{o} (6240)	CABLE2.4	6	4.0	0.08	0.28	0.32	Bi et al. (2020)
	ACCESS-ESM1-5	1.88^{o}x1.25^{o} (6240)	CABLE2.4	6	4.0	0.14	0.33	0.40	Ziehn et al. (2020)
2	BCC-CSM2-MR	1.13^{o} (11583)	BCC-AVIM2	10	3.4	0.06	0.20	0.24	Wu et al. (2019)
3	CAMS-CSM1-0	1.13^{o} (11583)	CLM1.0	10	3.4	0.00	0.12	0.14	Chen et al. (2019)
4	CanESM5	2.81^{o} (1849)	CLASS3.6/CTEM1.2	3	4.0	0.20	0.38	0.40	Swart et al. (2019)
5	CAS-ESM2-0	1.41^{o} (7322)	CLM4.0	15	42.1	0.03	0.20	0.25	Zhang et al. (2020)
6	CESM2	1.25^{o}x0.94^{o} (12376)	CLM5.0	25	49.6	0.11	0.27	0.29	Danabasoglu et al. (2020)
	CESM2-WACCM	1.25^{o}x0.94^{o} (12376)	CLM5.0	25	49.6	0.08	0.30	0.36	Gettelman et al. (2019)
7	CMCC-CM2-SR5	1.25^{o}x0.94^{o} (12376)	CLM4.5	15	42.1	0.09	0.23	0.28	Cherchi et al. (2019)
	CMCC-ESM2	1.25^{o}x0.94^{o} (12376)	CLM4.5	15	42.1	0.13	0.21	0.22	Lovato et al. (2022)
8	CNRM-CM6-1	1.41^{o} (7437)	Surfex 8.0c	14	12.0	0.19	0.25	0.26	Voldoire et al. (2019)
	CNRM-CM6-1-HR	0.5^{o} (58356)	Surfex 8.0c	14	12.0	0.12	0.24	0.26	Voldoire et al. (2019)
	CNRM-ESM2-1	1.41^{o} (7437)	Surfex 8.0c	14	12.0	0.15	0.24	0.30	Séférian et al. (2019)
9	E3SM-1-1	1^{o} (14545)	ELM1.0	15	42.1	0.03	0.30	0.37	Golaz et al. (2019)
	E3SM-1-1-ECA	1^{o} (14545)	ELM1.0	15	42.1	0.06	0.28	0.35	Golaz et al. (2019)
10	EC-Earth3	0.7^{o} (29572)	HTESSEL	4	1.9	0.16	0.39	0.46	Döscher et al. (2021)
	EC-Earth3-Veg-LR	1.13^{o} (11583)	HTESSEL	4	1.9	0.12	0.26	0.29	Döscher et al. (2021)
11	FGOALS-f3-L	1.25^{o}x0.94^{o} (12376)	CLM4.0	15	42.1	0.15	0.25	0.28	HE et al. (2020)
	FGOALS-g3	2^{o} (3503)	CLM4.0	15	42.1	0.14	0.24	0.23	Li et al. (2020)
12	GFDL-CM4.0	1.25^{o}x1^{o} (11642)	GFDL-LM4.0.1	20	10.0	0.07	0.29	0.35	Held et al. (2019)
	GFDL-ESM4-0	1.25^{o}x1^{o} (11642)	GFDL-LM4.0.1	20	10.0	0.02	0.21	0.26	Dunne et al. (2020)
13	GISS-E2-1-G	2.5^{o}x2^{o} (2908)	GISS LSM	6	3.5	0.01	0.23	0.24	Kelley et al. (2020)
	GISS-E2-1-H	2.5^{o}x2^{o} (2908)	GISS LSM	6	3.5	0.08	0.20	0.23	Kelley et al. (2020)
	GISS-E2-2-G	2.5^{o}x2^{o} (2908)	GISS LSM	6	3.5	-0.05	0.11	0.12	Rind et al. (2020)
14	HadGEM3-GC31-LL	1.88^{o}x1.25^{o} (6215)	JULES-GL7.0	4	3.0	0.04	0.32	0.40	Williams et al. (2018)
	HadGEM3-GC31-MM	0.83^{o}x0.55^{o} (31481)	JULES-GL7.0	4	3.0	0.05	0.28	0.32	Williams et al. (2018)
15	IPSL-CM6A-LR	2.5x1.26^{o} (4617)	ORCHIDEE 2.0	18	90.0	0.13	0.26	0.32	Boucher et al. (2020)
16	KACE-1-0-G	1.88^{o}x1.25^{o} (6215)	JULES-GL7.0	4	3.0	0.10	0.28	0.33	Lee et al. (2019)
17	MIROC6	1.41^{o} (1849)	MATSIRO6.0	6	14.0	0.06	0.20	0.23	Tatebe et al. (2019)
	MIROC-ES2L	2.81^{o} (1849)	MATSIRO6.0	6	14.0	0.07	0.23	0.26	Hajima et al. (2020)
18	MPI-ESM1.2-LR	1.88^{o} (4172)	JSBACH$_s$	5	9.8	0.13	0.24	0.30	Mauritsen et al. (2019)
	MPI-ESM1.2-LR	**1.88^{o} (4172)**	**JSBACH$_d$**	**12**	**1416.0**	**0.07**	**0.24**	**0.27**	**González-Rouco et al. (2021)**
19	MRI-ESM2-0	1.13^{o} (11583)	HAL 1.0	14	10.0	0.05	0.23	0.27	Yukimoto et al. (2019)
20	NorESM2-LM	2.5x1.9^{o} (3057)	CLM5.0	25	49.6	0.05	0.27	0.33	Seland et al. (2020)
	NorESM2-MM	1.25^{o}x0.94^{o} (12376)	CLM5.0	25	49.6	0.06	0.26	0.33	Seland et al. (2020)
21	TaiESM1	1.25^{o}x0.94^{o} (12376)	CLM4.0	15	42.1	0.03	0.27	0.34	Wang et al. (2021)
22	UKESM1-0-LL	1.88^{o}x1.25^{o} (6215)	JULES-GL7.0	4	3.0	0.06	0.32	0.41	Sellar et al. (2019)
	MEAN TREND					**0.09**	**0.26**	**0.30**	

Table 2.9: Characteristics of the observational-type global surface temperature data sets used in this work and their trends for various periods. The first seven rows account for reanalysis data, while the last five are for instrumental data. GST data were used, except in the cases marked with (1), for which SAT data were used. The soil temperature at the first layer was taken as GST in every case. Glacier areas (Antarctica and Greenland) were excluded from the calculations. Temperature trends in the three different periods assessed in Fig. 4.3 (1950–2000, 1960–2020, and 1971–2018) for every data set and the means for reanalyses and observational subsets are also provided. (2) indicates cases in which the interval of trend evaluation is shorter due to limited data availability.

Name	**Time span**	**Resolution (N. gridpoints)**	**Institution**	**1950–2000 [Kdec^{-1}]**	**1960–2020 [Kdec^{-1}]**	**1971–2018 [Kdec^{-1}]**	**Reference**
20CRv3	1836–2015	1^o (16779)	NOAA/ESRL/PSD	0.11	0.20[2]	0.25[2]	Slivinski et al. (2019)
CERA20c	1901–2010	1.125^o (13184)	ECMWF	0.06	0.17[2]	0.27[2]	Laloyaux et al. (2018)
ERA20c	1900–2010	1.125^o (13184)	ECMWF	0.09	0.22[2]	0.35[2]	Poli et al. (2016)
ERA5-Land	1950–2021	0.1^o (1668600)	ECMWF	0.09	0.20	0.25	Muñoz Sabater et al. (2021)
NCEP1	1948–2021	2.5^o (2707)	NCEP/NCAR	0.03	0.15	0.19	Kalnay et al. (1996)
JRA55	1958–2021	1.25^o (10679)	JMA	0.10[2]	0.20	0.26	Ebita et al. (2011)
LMRv2.1[1]	1–2000	2^o (4174)	NOAA	0.13	0.20[2]	0.27[2]	Tardif et al. (2019)
MEAN TREND				**0.09**	**0.19**	**0.24**	
BEST[1]	1750–2022	1^o (16779)	Berkeley Earth	0.16	0.25	0.29	Rohde and Hausfather (2020)
CRUTEM5[1]	1857–2021	5^o (667)	MOHC	0.13	0.24	0.28	Osborn et al. (2021)
GISTEMPv4[1]	1880–2021	2^o (4174)	NASA-GISS	0.16	0.27	0.31	Lenssen et al. (2019)
NOAAGlobalTemp[1]	1880–2021	5^o (667)	NOAA	0.14	0.24	0.27	Zhang et al. (2019)
UDEL[1]	1900–2017	0.5^o (66744)	Univ. of Delaware	0.13	0.23	0.28	Willmott and Matsuura (2018)
MEAN TREND				**0.14**	**0.25**	**0.29**	

[1] SAT used instead of GST. [2] Temperature trend value is given for a shorter period due to limited data availability.

Apart from GST and subsurface temperature data, PE estimates by Steinert et al. (2023) derived from CMIP6 data in the industrial period are used in Chapter 6. The time evolution of the PE under two permafrost definitions, TTOP and ZAA (see Section 6.1), for 34 CMIP6 historical and SSP5-8.5 experiments are compared with the nine simulations of the MPIESM-PePE. This comparison allows for evaluating how extreme WET and DRY configurations are in representing PE, thus disentangling the potential role of Arctic soil hydrology in reshaping permafrost degradation.

2.3.2 Reanalysis and observational datasets

Global mean temperatures at the ground surface over land coming from 7 global reanalyses and 5 gridded observational databases have also been used (Table 2.9) in Chapter 4 to derive land heat uptake estimates. GST data were used from 6 of the sources (see Table 2.9), whilst SAT was taken as a surrogate of the GST evolution when GST was not available (6 data sources, see Table 2.9). This substitution leans on the assumption that SAT and GST are strongly coupled in long-term scales (Melo-Aguilar et al., 2018). All sources cover the whole 20th century, except for ERA5-Land, NCEP1, and JRA55. Further, all of them except LMRv2.1 cover the first decade of the 21st century. These datasets will allow for obtaining land heat uptake estimates complementary to BTP-based values (Beltrami, 2002; Cuesta-Valero et al., 2021b, 2023; von Schuckmann et al., 2023).

Gridded observations were used also in Chapter 6 to evaluate the results from the MPIESM-PePE. PE observational data come from the Permafrost Climate Research Data Package version 3 of the European Space Agency Climate Change Initiative database (ESApCCIv3). ESApCCIv3 provides NH (north of 30^{o}) gridded global maps of permafrost mean annual SAT, GST, and subsurface temperature, ALT, and PE at yearly resolution for the period 1997–2018. The database is generated by using a thermal permafrost model (CryoGrid, Westermann et al., 2023), with a BBCP depth of 100 m, driven and constrained by satellite data. Both Moderate Resolution Imaging Spectroradiometer (MODIS, Justice et al., 2002) land surface temperature data coming from the Terra satellite and ERA5 reanalysis data are assimilated for this purpose. Furthermore, to enhance accuracy, ensemble methods are employed, providing not only permafrost probabilities but also measures of uncertainty. A more technical description of the assimilation and modeling procedures to create the ESApCCIv3 database can be found in Obu et al. (2021).

Chapter 3
Thermodynamic and hydrological drivers of the subsurface: an observational study in Central Spain*

In situ continuous observations of subsurface temperature and moisture variability at multiple vertical levels are fundamental for characterizing the physical mechanisms governing underground heat and water transport and their interactions. This chapter presents an assessment of the main thermodynamic and hydrological mechanisms driving observational subsurface temperature variability, based on an ensemble of four short and deep and two long and shallow records from the Sierra de Guadarrama (Section 2.1).

The first part of the assessment (Section 3.2.1) explores the coupling between SAT and GST across different timescales. The second part focuses on the subsurface propagation of GST variations driven by heat conduction. The intensity and speed of this propagation are controlled by the apparent thermal diffusivity, which is assessed by evaluating the amplitude attenuation and phase shift of the annual cycle (Section 3.2.2). Variations in thermal diffusivity due to the parent material and depth are then analyzed through vertical profile measurements. Finally, the annual-cycle methodology is extended to analyze the attenuation of the entire frequency spectrum, which allows for yielding short-term thermal diffusivity changes and their potential relationship with soil moisture variations (Section 3.2.3).

* The main contents of the chapter are included in the published research article:
García-Pereira, F., J. F. González-Rouco, T. Schmid, C. Melo-Aguilar, C. Vegas-Cañas, N. J. Steinert, P. J. Roldán-Gómez, F. J. Cuesta-Valero, A. García- García, H. Beltrami, and P. de Vrese, 2024: Thermodynamic and hydrological drivers of the soil and bedrock thermal regimes in central Spain. *SOIL*, 10, 1–21, DOI: 10.5194/soil-10-1-2024.

3.1 Methods

The SAT–GST seasonal coupling was explored by quantifying the offset and correlation of seasonal (December-January-February, DJF; June-July-August, JJA) and annual temperatures at 2 m above the ground surface with GSTs taken from the top level temperatures in the BRH 2 m set up. The estimates were obtained from the complete time span of available data at each site (Tables 3.1 and 3.2).

Furthermore, the subsurface temperature distribution was analysed by assuming that GST perturbations are propagated downwards by heat conduction. Considering that every level is at a thermal equilibrium state, horizontal heat transport may be neglected. Thus, the problem is reduced to resolve the one-dimensional time-dependent heat conduction equation (Eq. 1.1). If GST is assumed to follow a sinusoidal (e.g., annual) cycle, subsurface temperatures at any depth z can be derived as follows (Hurley and Wiltshire, 1993; Smerdon and Stieglitz, 2006):

$$T(z,t) = T_0 + A_0 e^{-z\sqrt{\pi f_a/\kappa}}\, cos(2\pi f_a t - z\sqrt{\pi f_a/\kappa}), \tag{3.1}$$

where T_0 and A_0 are the mean temperature and wave amplitude of the annual cycle at the ground surface, respectively, f_a is the frequency of the annual cycle, and κ is the thermal diffusivity, which is a direct function of thermal conductivity (λ), and inverse of density (ρ) and heat capacity (c), i.e., $\kappa = \lambda/\rho c$. Equation 3.1 shows that the annual cycle amplitude is attenuated and phase shifted with depth. The amplitude attenuation is exponential and the phase shift is linear with depth and dependent on the thermal diffusivity, i.e., increasing this parameter produces both a greater amplitude attenuation and phase shift (see Section 1.4).

Amplitude and phase values of the annual cycle at every level were obtained by least-squares fitting subsurface temperature series at a daily resolution to an annual-period sinusoidal wave. Then, a linear regression analysis on the annual cycle amplitude (phase shift) values with depth was applied to yield estimates of the apparent thermal diffusivity of the subsurface, since the resulting slope is equal to $\sqrt{\pi f_a/\kappa}$ in Equation 3.1. Amplitude and phase shift values coming from every installation (TRCH 1 m, BRH 2 m, and BRH 20 m) were independently adjusted and normalized to prevent any disruption due to blending data from different sources when assessing heat propagation from ground surface to 20 m depth. Normalization was achieved by dividing the amplitude values of the annual cycle at every level by the amplitude value at the ground surface, and by subtracting the phase shift value at the ground surface from the phase shift values of the annual cycle at every level. The values at the ground surface were obtained through a linear regression adjustment. Once normalized, all amplitude

and phase shift values were brought together and linearly adjusted to obtain a single estimate of thermal diffusivity for the whole subsurface profile at every station. A similar methodological approach based on the analysis of the annual cycle has been widely used in the literature (e.g., Smerdon et al., 2004; Pollack et al., 2005; González-Rouco et al., 2009) and it will be referred to as the Classic Analytical approach, CA hereafter. This CA framework was also used to estimate changes in apparent thermal diffusivity with depth, either by considering changes between pairs of subsurface levels or identifying depths where significant changes in apparent thermal diffusivity occur. This was achieved using a two-phase regression analysis (Solow, 1987, 1995; Melo-Aguilar et al., 2018), which determines whether there is a change point for which linear fits to the segments before and after the change point significantly improve the results compared to a linear fit to the complete curve.

Beyond the regular nature of the annual cycle, GST variability encloses perturbations at different frequencies. If GST is considered as a sum of temperature harmonics, each harmonic is also propagated with depth following Carslaw and Jaeger (1959):

$$T(z,t) = T_0 + \sum_{i=1}^{N} A_0 e^{-z\sqrt{\pi f_i/\kappa}}\, cos(2\pi f_i - z\sqrt{\pi f_i/\kappa}), \tag{3.2}$$

where f_i is the frequency of each wave component in a spectral decomposition, as yielded by a Fourier periodogram (Brigham and Morrow, 1967). Equation 3.2 shows amplitude attenuation and phase shift are frequency-dependent. More precisely, amplitude attenuation grows exponentially with frequency, i.e., high-frequency harmonics decay increasingly faster with depth, whilst low-frequency perturbations can penetrate deeper into the subsurface. For instance, the daily cycle hardly reaches a depth of 50 cm, while the annual cycle propagates down to 15 m (e.g., Putnam and Chapman, 1996, or Fig. 1.1). The temperature spectral attenuation with depth can be expressed as:

$$\zeta = \sqrt{P_z(\omega)/P_{GST}(\omega)} = e^{-z\sqrt{\pi f/\kappa}} \tag{3.3}$$

where $P_{GST}(\omega)$ and $P_z(\omega)$ are the spectral power densities of GST and that at a given level z, respectively:

$$P_z(\omega) = \frac{1}{N_s}\left|\sum_{t=1}^{N} T(z,t)e^{-i\omega t}\right|^2,\ with\ \omega = 2\pi f \tag{3.4}$$

where N_s is the temporal resolution of the temperature time signal at z, $T(z,t)$, f is the frequency and ω is the angular frequency of the different wave compo-

nents of $T(z,t)$. In order to minimize the undesirable effect of Gibbs' noise at high frequencies, the spectral power density was calculated making use of Welch's modified periodogram (Stoica and Moses, 1997). Because the periodogram calculation requires evenly spaced data, data gaps were previously filled by linear interpolation. As the spectral attenuation must follow an exponential relationship with frequency, the spectral amplitude attenuation curves attained from the analysis of Equation 3.3 were subsequently linearized (i.e., taking the natural logarithm) and linearly fitted by least-squares to the values obtained at all available depths:

$$(ln\zeta)^2 = \frac{\pi z^2}{\kappa} f \tag{3.5}$$

Estimates for the apparent thermal diffusivity of the soil layer in between the ground surface and level z can be retrieved by dividing πz^2 by the regression line slope, $\pi z^2/\kappa$, in Equation 3.5. To prevent poor signal-to-noise ratios at high frequencies from biasing the analysis, amplitude attenuation values at frequencies higher than the corresponding e-fold decay cut-off frequency (i.e., spectral harmonics attenuated more than e times) were filtered out at every level. To determine this frequency at every site and level, near-surface soil thermal diffusivity values coming from the CA are used. However, it is possible to use a physically plausible prior thermal diffusivity value (ca. 10^{-6} m^2s^{-1}) to calculate this frequency, leading to very similar results and thus making the e-fold frequency calculation independent from the CA.

The alternative approach to the CA described above will be referred to as the Spectral Method (SpM) from now on. Whereas the CA needs at least a few years of data to provide reliable fits of the annual cycle to subsequently retrieve the apparent thermal diffusivity, the SpM can be applied to data at shorter time intervals. That makes it suitable to analyze short time series, which is the case of some of the time series presented in this work. Consequently, the SpM was used in this work to retrieve apparent thermal diffusivity values in the first meter of the soil at every station. These values were then compared to the estimates coming from the CA to assess the robustness of the results from both methods. Furthermore, the SpM allows some insight into short-term changes in soil apparent thermal diffusivity and its potential relation with changes in snow cover and soil moisture content.

3.2 Results

3.2.1 Temperature variability at the ground surface

In order to illustrate the amplitude attenuation and shift with depth, Fig. 3.1 compiles all the subsurface temperature series at hourly resolution coming from BRH 20 m, BRH 2 m, and TRCH 1 m at HRR; SAT is also represented to illustrate the coupling at the surface. A first inspection reveals that the only regular temperature variation at all levels, both in timing and magnitude, is the annual cycle. The daily cycle, while regular in occurrence, changes a lot in magnitude due to weather conditions and seasonality. The annual cycle is the most prominent at the ground surface (ca. 9 K amplitude) despite the fact that both SAT and GST also show remarkable daily temperature variations (ca. 4 K amplitude). It is noteworthy how the annual cycle decreases in amplitude with depth to be imperceptible at 15 m, where annual temperature variations are of the same order as the accuracy of the sensor, i.e., 0.1 K. Furthermore, the increasing lag in the occurrence of temperature maxima in summer and minima in winter are indicative of the phase shift due to conductive propagation of the temperature variations. Both phenomena can be inferred either by observing the subsurface temperature series or the sinusoidal curves adjusted to an annual cycle (blue dashed lines). Moreover, SAT and GST daily variabilities are similar during the year except in winter, when GST variability is smaller in comparison with SAT. For the other soil levels, warm or cold anomalies that last a few weeks are propagated only in the first meter of the soil.

The long-term mean temperatures with depth for CTS, HYS, RPI, and HRR are shown in Fig. 3.2. The annual vertical mean temperature of the profile, which is observed below the depth at which the annual cycle has been attenuated (ca. 15 m), is remarkably higher at HRR (286.8 K) than at CTS (281.3 K), HYS (279.2 K), and RPI (280.9 K). The JJA and DJF temperature profiles further depict the seasonal temperature variations towards warmer values in summer and colder values in winter, as well as the amplitude attenuation of these seasonal variations with depth. JJA and DJF temperature profiles converge at a depth of around 5 m at all sites to then cross over, which is a sign of the phase shift of the annual cycle. The transition from the BRH 2 m to the BRH 20 m profiles show noticeable discontinuities that are of the order of 2.7 K and 2.2 K at HYS and about 1.5 K and 1 K at HRR for the 1.5 and 2 m temperature levels, respectively. These discontinuities are most likely due to heterogeneous soil and sediment formations. The uppermost soil and sediment layers vary according to the sites and in all cases reach a depth greater than 2 m (Fig. 2.2). In the case of HYS, for instance, the greatest annual temperature difference between the 2 m and 20 m BRHs is

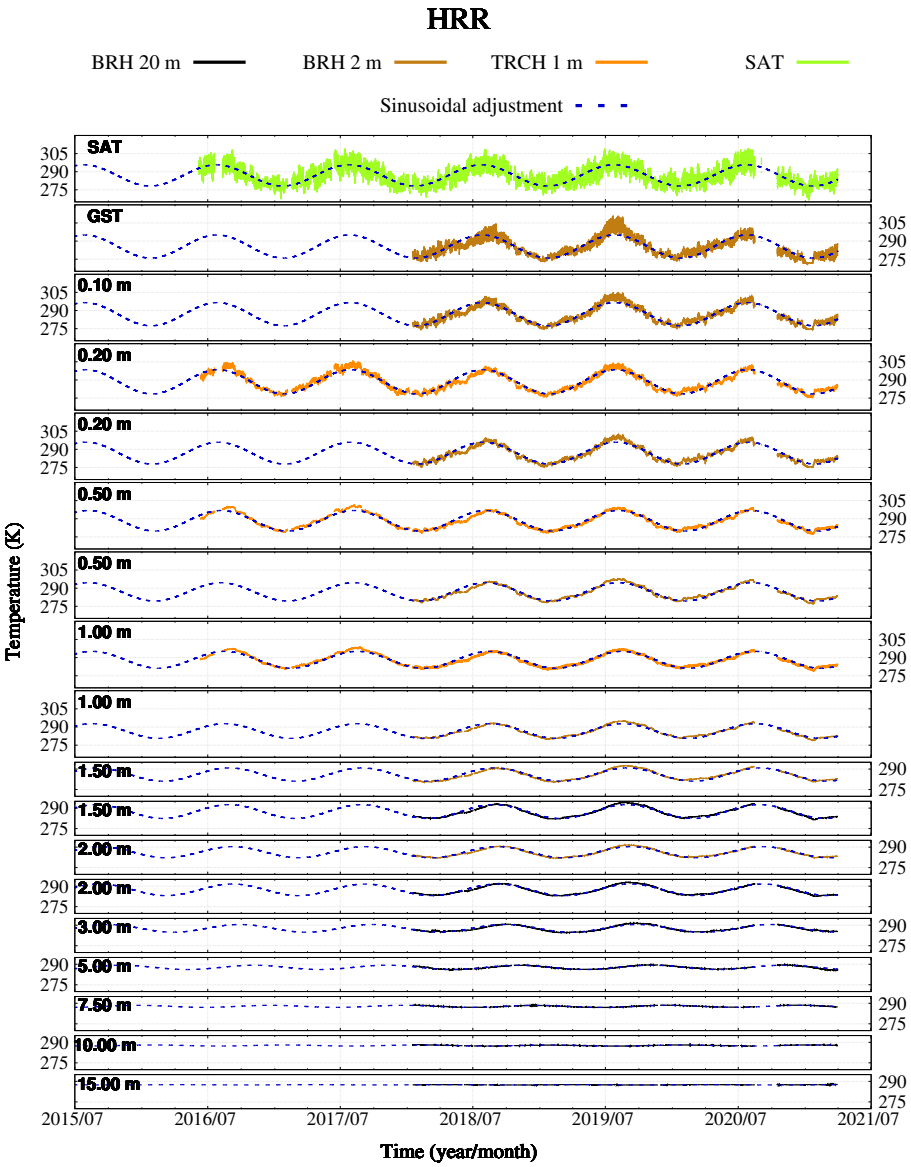

Figure 3.1: SAT, GST, and subsurface temperatures (K) at HRR. Subsurface temperatures stem from the BRH 20 m (black lines), BRH 2 m (brown lines), and TRCH 1 m (orange lines). Blue dashed lines show the resulting fit to an annual cycle at each depth.

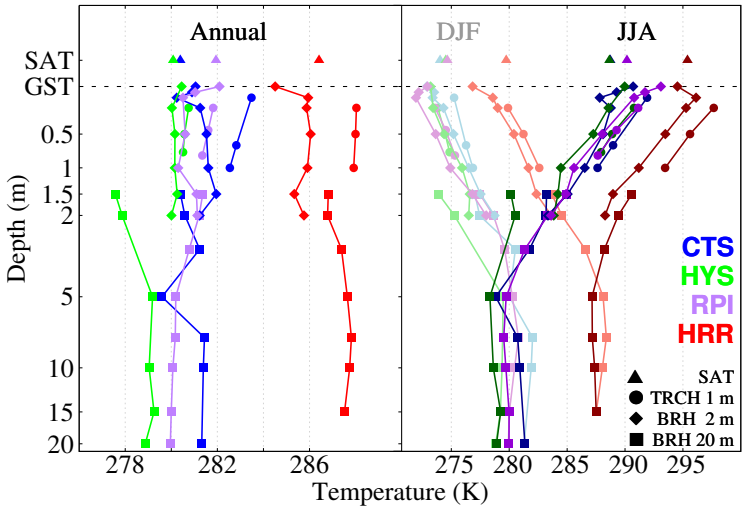

Figure 3.2: SAT (triangles) and subsurface temperature profiles (continuous line with diamonds for BRH 2 m, squares for BRH 20 m, and circles for TRCH 1 m) at CTS (blue), HYS (green), RPI (purple), and HRR (red) for their respective whole time spans (see Table 2.1). Annual mean temperatures are shown on the left-hand side of the figure, whilst JJA (DJF) is shown on the right in dark (light) colors.

observed at 1.5 m depth. The site is on a middle slope with a slope gradient of 10 to 15 % and the soil horizons have a sandy loam to a sandy clay loam texture. What is most notable is the varying content of rock fragments (15 to >80 %) within the different soil horizons. This is further observed throughout the sediment layer where rock fragment distribution varies with depth and is very weathered. Therefore, temperature variations over short distances within the uppermost soil and sediment layers are expected due to their different properties. This will also influence the water infiltration and circulation. With regard to SAT–GST coupling, Fig. 3.2 shows the annual cycle is less pronounced for SAT than GST due to radiative warming and cooling of the ground surface, resulting in a negative SAT–GST offset in summer and positive in winter. The distribution of SAT and GST mean values of the sites agree with their different altitudes, which yields a vertical gradient of -5.81 K km^{-1} in SAT given by Vegas-Cañas et al. (2020) for the area of the Sierra de Guadarrama. SATs in Fig. 3.2 comply well with this value, rendering a gradient of -6.55 K km^{-1}, larger in magnitude due to this subset of sites being distributed over the higher altitudes of the region. Subsurface temperatures with depth follow the distribution of SAT at HYS and

HRR, with HRR exhibiting higher values for the whole profile. However, this pattern is not observed at RPI and CTS, as RPI shows lower temperatures below 5 m despite SAT and GST being warmer, which might be due to processes within the soil that have not been further investigated in this paper.

Temperature anomalies with respect to the long-term mean at each depth for CTS and HRR are shown in Fig. 3.3. This allows for a more clear visualization of the amplitude attenuation and phase shift with depth. Two cycles are clearly identified again at both sites: the daily cycle, which is visible at GST and hardly noticeable at 0.5 m (Fig. 3.3a,b), and the annual cycle, with an amplitude reduction and phase shift that are traceable down to 15 m. Nevertheless, there are two differences that are worth mentioning. On the one hand, GST and subsurface temperatures underneath at CTS show some constant signal time periods in winter that are not found in SAT, as shown in Fig. 3.3c, where SAT and GST are represented for a shared period in January 2019 at CTS and HRR. As soon as a snow layer emerges at CTS on January 19, 2019, GST oscillations are suppressed despite SAT still varies. This is due to the combination of the soil insulating effect of snow cover (Bartlett et al., 2005; Zhang, 2005) and the zero-curtain effect, which halts temperatures at the ground surface to drop much below zero due to latent heat release (Outcalt et al., 1990). This behaviour is not shared by HRR, since at this lower altitude a regular seasonal snow layer is less frequent. Hence, HRR is snow-free during the same dates, so SAT and GST variations are strongly coupled. On the other hand, note that SAT variability differs from one site to the other, being the amplitude of the daily cycle greater and the annual cycle smaller at CTS than at HRR, as illustrated by greater differences of SAT variations in July 2019 with respect to those in January 2019. This is consistent with SAT annual variability decreasing and intra-annual increasing with altitude in the same area, as shown by Vegas-Cañas et al. (2020).

Table 3.1: SAT–GST differences in mean (K) and Pearson's correlation coefficient using daily data. The annual wave was previously filtered out both from SAT and GST data for this analysis. Non-significant ($p > 0.05$) differences and correlations are shown in bold.

Code	SAT - GST (K)			Correlation coefficient		
	Annual	JJA	DJF	Annual	JJA	DJF
CTS	-1.80	**0.21**	-3.45	0.61	0.57	0.54
HYS	-0.47	0.52	-0.59	0.68	0.83	0.43
RPI	-0.92	**-0.34**	-2.37	0.58	0.75	**0.16**
HRR	-1.58	-2.36	**-0.11**	0.59	0.44	0.74
NVC	-1.99	-3.52	-1.38	0.71	0.56	0.67
SGV	-0.46	-1.65	**0.20**	0.81	0.76	0.77

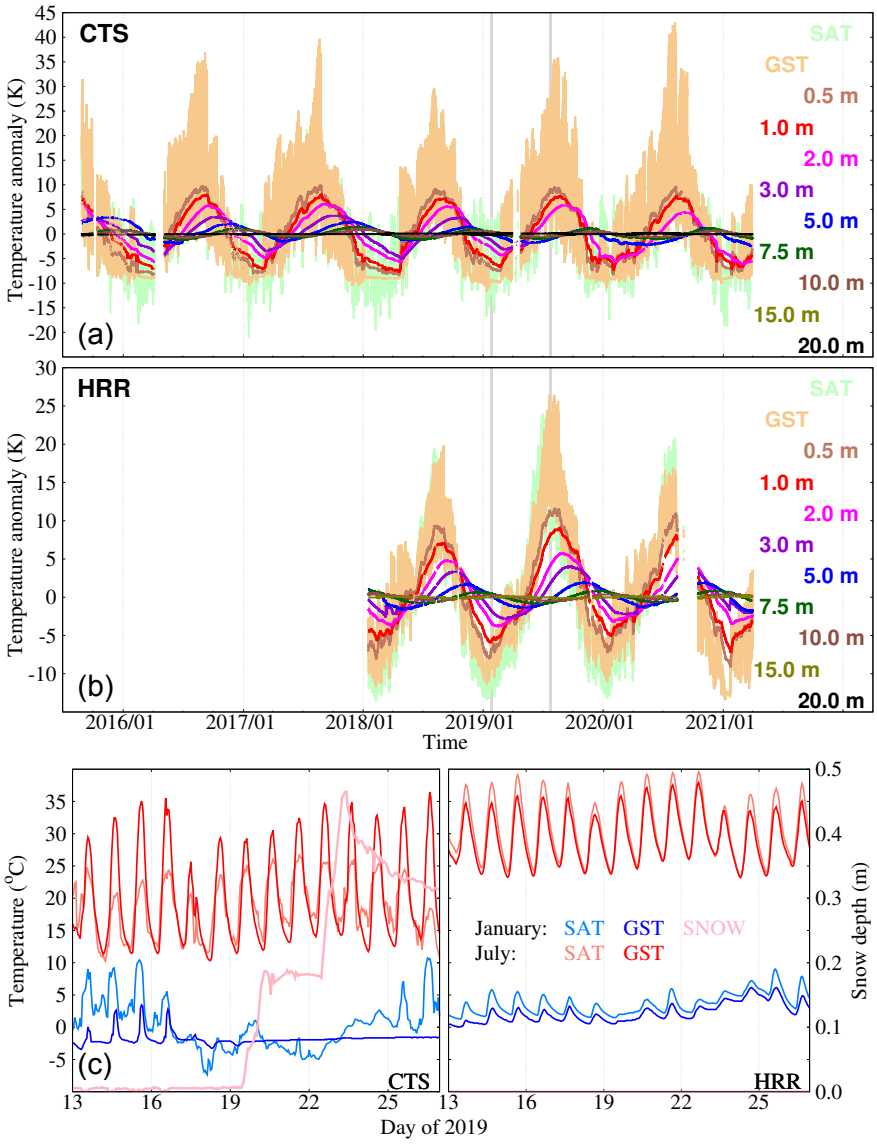

Figure 3.3: SAT, GST, and subsurface temperature anomalies (K) with respect to the annual mean at CTS (a) and HRR (b). (c) SAT (light) and GST (°C; dark colors) changes during 10 days in January (blue) and July (red) 2019 and the evolution of the snow cover (m; light pink) at CTS and HRR.

Air-ground temperature seasonal decoupling is further explored in Table 3.1, where SAT–GST differences and Pearson's correlation coefficient were computed after filtering out the annual cycle. SAT–GST differences show that on average GST is warmer than SAT, with annual differences being negative. Correlations using daily data are all significant ($p<0.05$, Student's t-test) and above 0.58 for all sites. Differences tend to be larger during DJF, likely due to the insulating effect of snow cover, which hampers soil cooling and disrupts SAT–GST coupling. During JJA, significantly warmer GSTs are found at HRR, NVC, and SGV, likely due to surface radiative warming. Additionally, correlation analysis yields the smallest values in DJF at the highest altitude sites, i.e., RPI, HYS, and CTS, which is linked to the presence of a more steady seasonal snow layer than at the lowest sites. Low correlation is found in JJA at HRR, which might be due to weaker latent heat fluxes connected to Iberian soils' summer drought (Vicente-Serrano et al., 2013). Nevertheless, the diverse local responses at the various sites could be due to land cover differences, water or latent heat exchanges, or other factors (Cermak and Bodri, 2016; Cermak et al., 2017) that have not been further examined herein.

Table 3.2: Apparent thermal diffusivity values (10^{-6} m^2s^{-1}) obtained from the amplitude attenuation, $\ln(A/A_0)$, and phase shift, ϕ, for TRCH 1 m only (first column), the first meter of depth using a blend of TRCH 1 m and BRH 2 m data (second column), and BRH 20 m (third column) at CTS, HYS, RPI, HRR, SGV, and NVC.

	TRCH 1 m		1 m		BRH 20 m	
	$ln(A/A_0)$	ϕ	$ln(A/A_0)$	ϕ	$ln(A/A_0)$	ϕ
CTS	0.88 ± 0.16	0.85 ± 0.06	0.87 ± 0.57	0.70 ± 0.26	1.41 ± 0.21	1.44 ± 0.38
HYS	0.73 ± 0.28	1.26 ± 0.33	0.45 ± 0.15	0.58 ± 0.33	1.38 ± 0.29	1.07 ± 0.13
RPI	0.46 ± 0.18	0.84 ± 0.29	0.42 ± 0.09	0.67 ± 0.20	1.41 ± 0.27	1.49 ± 0.40
HRR	0.50 ± 0.17	0.69 ± 0.21	0.45 ± 0.12	0.68 ± 0.10	1.20 ± 0.16	1.15 ± 0.19
NVC	0.82 ± 0.51	1.75 ± 1.24				
SGV	0.55 ± 0.24	0.77 ± 0.07				

3.2.2 Subsurface thermal regime: the CA

The subsurface thermal structure in the area of the Sierra de Guadarrama is assessed hereafter. The conductive propagation of GST changes is first addressed by applying the CA (Section 3.1). Results for CA over the whole profile for every site are included in Fig. 3.4. As can be seen, CTS, HYS, RPI, and HRR

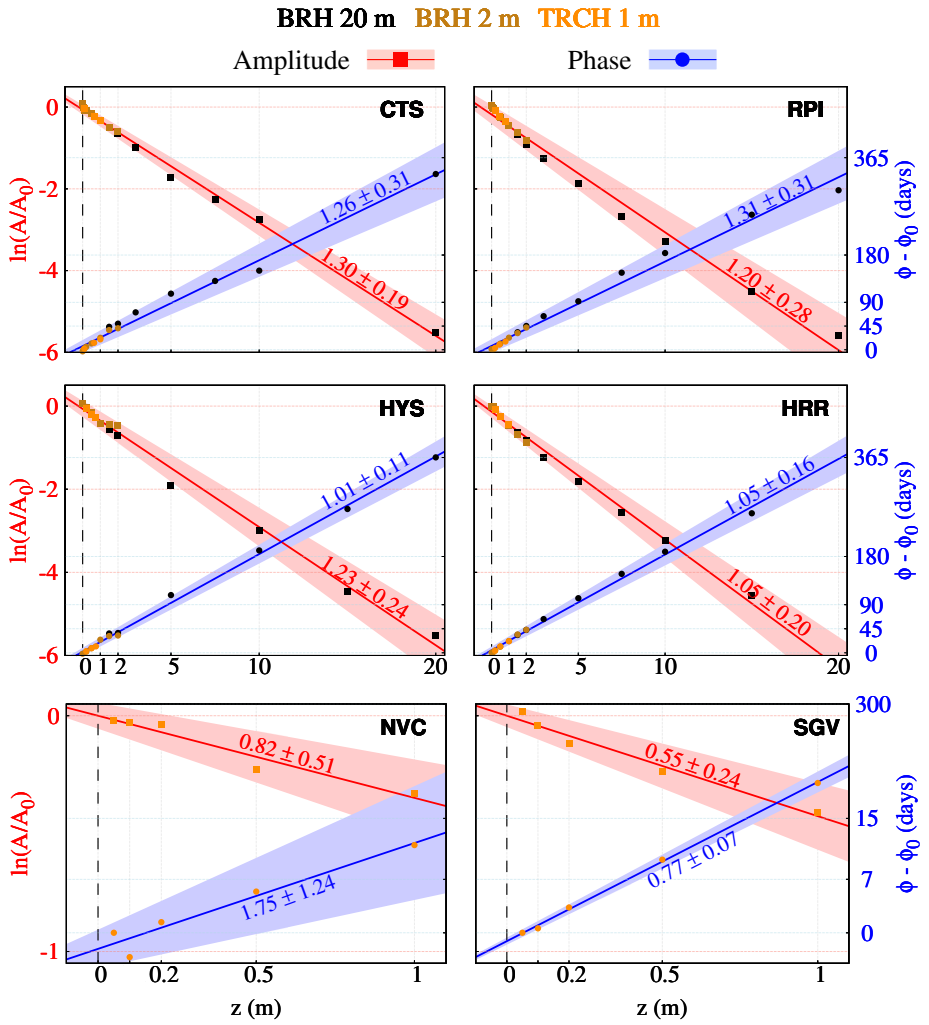

Figure 3.4: Phase shift in days (blue) and the logarithm of amplitude ratios (red) vs. depth at CTS, HYS, RPI, HRR, NVC, and SGV (see Table 2.1). Points in orange, brown and black stem from a least-squares adjustment for sinusoidal fitting of the annual cycle of TRCH 1 m, BRH 2 m, and BRH 20 m data, respectively. Diffusivity values (10^{-6} m^2s^{-1}) are retrieved by linearly fitting all the points available at every site (see text for details). Regression lines, confidence intervals using a significance level of $p = 0.05$ and diffusivity values for the logarithm of the amplitude ratios (phase shift) are included in red (blue).

integrate data coming from both BRH 2 m, BRH 20 m, and TRCH 1 m down to 20 m, while NVC and SGV provide TRCH 1 m data. Hence, apparent thermal diffusivity values only account for the first meter underground at these two sites. For the rest of the sites, all the information at each location down to 20 m is used to derive apparent thermal diffusivity estimates. Table 3.2 segregates results for the case in which only TRCH 1 m would be considered, as well as for the cases that include information available down to 1 m (TRCH 1 m + BRH 2 m) and down to 20 m using only BRH 20 m. This information complements the estimates provided in Fig. 3.4.

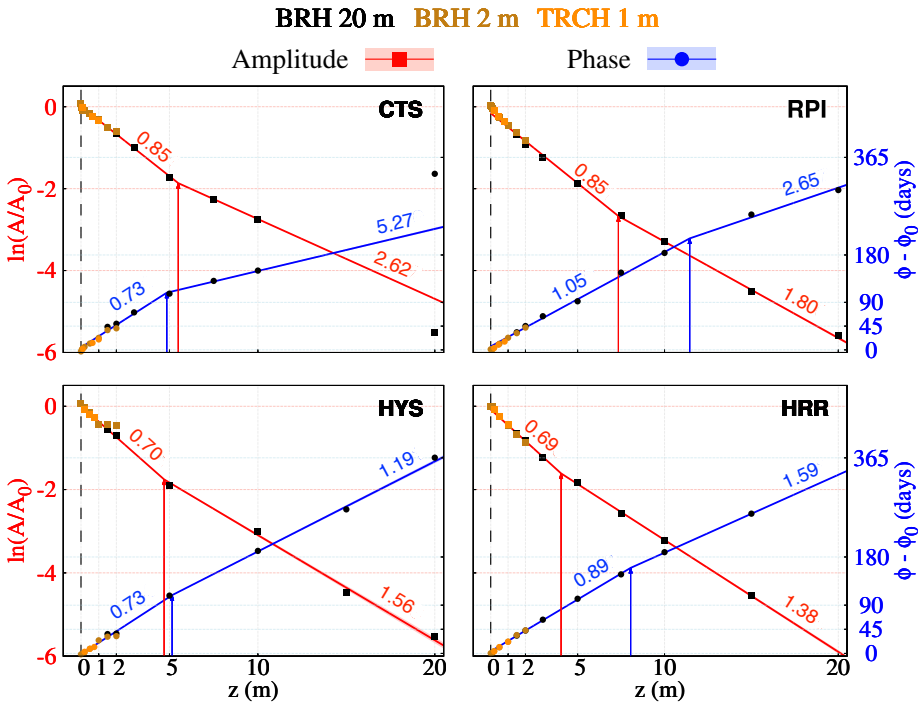

Figure 3.5: Two-phase regression of the points shown in Fig. 3.4. Lines represent the linear trends that are the best fit to the data before and after the estimated point of change for the logarithm of the amplitude ratio (phase shift), depicted in red (blue). Apparent thermal diffusivity values (10^{-6} m^2s^{-1}) before and after the change point are given as well in every case. The 20 m level at CTS was omitted from the analysis.

Thermal diffusivity estimates, i.e., apparent thermal diffusivities, yielded from the slope of the regression lines for both phase shift and amplitude attenuation are very similar for all deep sites, generally in the range of 1–1.3 10^{-6} m^2s^{-1}. These values are close to the mineral diffusivity values for quartz (ca. 1.4 10^{-6} m^2s^{-1}) and feldspar (ca. 1.1 10^{-6} m^2s^{-1}), two of the main components of gneiss and granite (de Vries, 1963), which are the dominating materials found at the sites of this study (Fig. 2.2). The observations at SGV render values that fall below this range, with apparent diffusivity values between 0.5 and 0.8 10^{-6} m^2s^{-1}. While subsurface temperatures at CTS, HYS, RPI, and HRR extensively cover the soil and bedrock depths, NVC and SGV only include data within the first meter of the soil, which can yield very different thermal diffusivity estimates with respect to the other sites. Near the surface the different composition, compactness, and soil moisture content can account for the different apparent diffusivity values. In fact, if apparent diffusivity is estimated at all sites using only TRCH 1 m observations, values in the range of 0.46 (RPI) to 0.88 10^{-6} m^2s^{-1} (CTS) are attained (Table 3.2). Furthermore, if both TRCH 1 m and BRH 2 m temperatures within the first meter are considered, values hardly change and range from 0.42 (RPI) to 0.87 10^{-6} m^2s^{-1} (CTS). It is often the case that apparent diffusivity values rendered by amplitude attenuation and phase shift within the first meter of the soil can differ considerably, as shown for NVC in Fig. 3.4. This is an indication that changes in apparent thermal diffusivity occur towards the surface, as seen at NVC and SGV in Fig. 3.4. Additionally, changes in the conductive regime may occur within these depths due to soil moisture variability (Melo-Aguilar et al., 2022), freezing and thawing processes (Gao et al., 2008), and near-surface evaporation and latent heat exchanges (Tong et al., 2017) affecting the soil (see Section 1.4).

The regression spread when considering deep sites in Fig. 3.4 can be remarkable, scaling up to 25 % at RPI. Even if the logarithm of the amplitude damping and phase shift for the whole soil column can be considered linear in a first approach, values do not seem to distribute randomly around the regression line. For instance, between 2 and 7 m all sites tend to show larger amplitude attenuations and phase shifts, hence indicating changes in the regression line slope, i.e., diffusivity, with depth. A further analysis using a two-phase regression model (Fig. 3.5, Solow, 1987, 1995), confirms there is a tilt in the slope, indicating a significant change in the apparent thermal diffusivity values with depth. Even though the coefficient of determination is very high and significant for every site both for the single CA in Fig. 3.4 and for the two-phase CA in Fig. 3.5 regression lines, always above 0.9, there is a significant reduction of the square sum of residuals in the second case. For instance, this quantity plunges from 5.67 to 1.02 at HYS and from 8.22 to 0.62 at RPI for amplitude attenuation and from 3.21

to 0.91 day^2 and 11.46 to 1.20 day^2 for phase shift, respectively. This indicates that the two-phase regression represents the data more accurately than a single linear regression model. Since amplitude attenuation and phase shift values at every depth were normalized before applying the CA (see Section 3.1), the change point position is certainly not produced by gathering information from TRCH 1 m and the BRHs. A change in apparent thermal diffusivity might be indicative of the soil-bedrock transition, where porous non-consolidated material is progressively substituted by consolidated and more comprised material, which yields higher diffusivity values with depth (de Vries, 1963; Pollack et al., 2005). Apparent diffusivity values scale up from 0.7–1 to 1.4–2.6 10^{-6} m^{2}s^{-1} at most of the sites, which is consistent with the aforementioned transition. In Fig. 3.5, CTS and HYS show similar change point values for the amplitude attenuation and the phase shift analysis around 5 m. However, there is more uncertainty at RPI and HRR, where the amplitude attenuation yields shallower change points (7 and 4 m) than the phase shift analysis (11 and 8 m, respectively).

The previous changes in apparent diffusivity inferred by the CA can be partially traced back to the soil-bedrock transitions observed in Fig. 2.2 (see Section 2.1), where the profiles of subsurface composition have a superficial soil layer which is succeeded by accumulated sediments and crystalline materials of granite and gneiss. Results coming from the CA and the stratigraphy of the samples agree at HYS, placing the soil-bedrock transition at a depth of 5 m. However, the CA underestimates the observed soil-bedrock transition depth at CTS, where the bedrock starts in the sampled cores at 8 m (Fig. 3.5). The fact that the amplitude attenuation and phase shift CA results do not coincide at RPI and HRR might be also an indication that other factors influence the occurrence of change points (e.g., soil moisture). Moreover, both values overestimate the soil-bedrock transition depth given by the samples, at 5 and 2 m for RPI and HRR, respectively. In conclusion, considering the combined results from the stratigraphy and the CA for the four sites, it becomes clear that there is some uncertainty in the relationship between subsurface material and apparent thermal diffusivity changes, and other influences play a role in producing changes in thermal properties with depth.

The aforementioned sample analysis illustrates that changes in subsurface material do not occur abruptly but rather progressively into depth, contributing to changes in apparent thermal diffusivity with depth as well. For that reason, subsurface diffusivity profiles were derived by applying the CA level by level for CTS, HYS, RPI, and HRR (Fig. 3.6). This shows that diffusivity increases with depth at every site, which agrees with a previous analysis conducted at Fargo (Smerdon et al., 2003). Whilst RPI and HRR manifest a more linear behaviour, apparent thermal diffusivity values at CTS and HYS differ considerably from one layer to

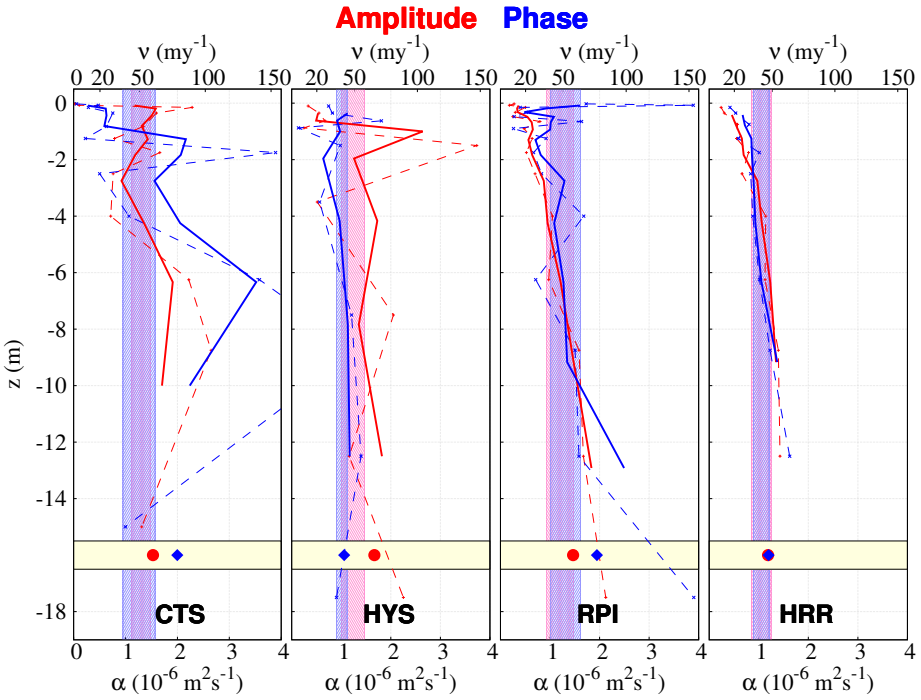

Figure 3.6: Thermal diffusivity (κ, 10^{-6} m^2s^{-1}) and wave velocity (ν, m yr^{-1}) profiles with depth (m). The red curves were obtained from normalized amplitude attenuation values $ln(A/A_0)$ and the blue ones from phase shift values with depth. Dashed (solid) lines represent the raw (3-running layer thickness-weighted average) estimate. Points at the bottom of the profile (shaded yellow) represent the thickness-weighted average of the whole subsurface profile. Shaded areas in red (blue) represent the thermal diffusivity values obtained by linearly fitting amplitude attenuation (phase shift) in Fig. 3.4.

the other, with the profiles being particularly variable near the surface. In general, mean diffusivity values and spread attained in Fig. 3.4 are well represented by the profiles, being higher at the deepest layers. Since diffusivity estimates in Fig. 3.6 are weighted by the layer thickness, small values in the thinner soil layers near the surface are down-weighted and the total vertical estimates tend to be greater than those provided in Fig. 3.4. Overall, Fig. 3.6 agrees well with results derived from Figs. 2.2, 3.4 and 3.5, and Table 3.2, better illustrating the deviations from the linear behaviour for the natural logarithm of amplitude attenuation and the

phase shift with depth identified in Fig. 3.4. These deviations are explained by an increase in apparent thermal diffusivity with depth.

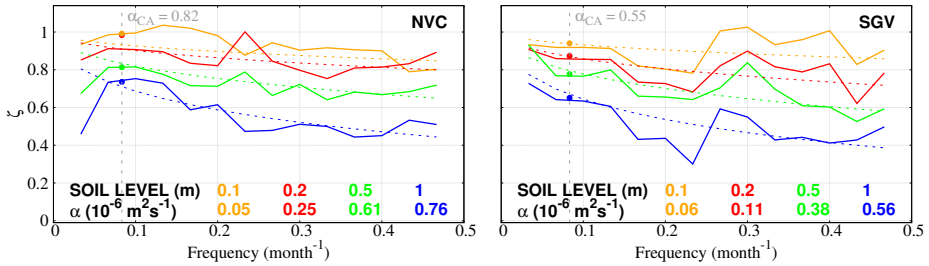

Figure 3.7: SpM amplitude attenuation analysis at NVC (left panel) and SGV (right panel). Monthly time series at both sites were selected for a common interval spanning from 1999 to 2008. Missing data were linearly interpolated. Spectral attenuation curves are calculated as a ratio of amplitudes of the Welch's periodogram at (Stoica and Moses, 1997) 0.1 (orange), 0.2 (red), 0.5 (green), and 1 (blue) m temperature levels with respect to GST. Solid (dashed) lines represent observed (theoretical) curves at every level. Diffusivity values below come from least-squares fitting the observed to theoretical curves. Diffusivity values in grey (top left of each panel) show the result of the CA for the amplitude attenuation of the annual cycle (1/12 month^{-1}) shown in Fig. 3.4. Colored points at the annual frequency (vertical grey dashed line) show the corresponding result of the CA for the amplitude attenuation at every level with respect to GST, which can be compared with the corresponding SpM observed (solid) and theoretical (dashed) values.

3.2.3 Subsurface thermal regime: the SpM

The heterogeneity in soil composition and moisture spatial and temporal variability can produce changes in thermal diffusivity near the surface. To study this effect, the SpM is introduced in the analysis, taking into account the damping of all temperature perturbation amplitudes in the frequency spectrum, although overseeing alterations of the conductive regime due to convection, advection or latent heat exchange processes (Gao et al., 2008; Tong et al., 2017). Nevertheless, it can provide some hints on the diffusivity changes with depth and time. An example of its performance is given in Fig. 3.7, where it was applied to monthly temperature data at SGV and NVC in 1999–2008. Apparent thermal diffusivity was retrieved at 0.05, 0.1, 0.25, and 0.5 m layers assessing the spectral amplitude attenuation of GST in its propagation to the 0.1, 0.2, 0.5, and 1 m levels,

respectively. Results for both sites show soil thermal diffusivity increases with depth, being higher for NVC than for SGV. The value of apparent thermal diffusivity for the whole soil column derived from the SpM at SGV (see points in Fig. 3.7) agrees with the CA estimate at the annual frequency from Fig. 3.4 (1/12 month^{-1}; 0.55 for CA vs. 0.56 10^{-6} m^2s^{-1} for SpM), while it is slightly smaller at NVC (0.82 vs. 0.76 10^{-6} m^2s^{-1}). The consistency of CA and SpM in reproducing the amplitude attenuation of the annual cycle indicates the robustness of SpM in reproducing CA results. Furthermore, SpM allows for extending the amplitude attenuation analysis to the whole harmonic spectrum. This entails that shorter periods, i.e., higher frequencies than the annual cycle, can be considered. In fact, the application of the SpM is not limited to data at monthly resolution but is applicable to higher temporal resolutions.

Fig. 3.8 expands the use of the SpM as an example to estimate thermal diffusivity values for weekly (a), 3-daily (b), daily (c), and 3-hourly (d) resolutions at HRR. It is observed how the SpM consistently reproduces the amplitude attenuation of the annual cycle stemming from CA at every resolution. Moreover, Fig. 3.8 shows the effect of frequency in amplitude decay: whilst in Fig. 3.8a, the observed amplitude attenuation curves show an exponential decay in every case, with values over $1/e$ except for 1 m, all levels in Fig. 3.8d are affected by poor signal-to-noise ratios at the high frequencies. Therefore, filtering out unreliable amplitude attenuation values at high frequencies with a suitable criterion (e-fold decay in our case) becomes crucial to prevent unbiased thermal diffusivity estimates. If the whole frequency band was considered in the SpM, unbiased estimates would still be attained at shallow soil layers and low frequencies, but poor performance should be expected at the deep and high ones, respectively.

As has already been mentioned, soil properties are especially heterogeneous near the surface, due to interactive changes in soil material, texture (Cermak et al., 2017), moisture, and hydrology (Pollack et al., 2005; Gao et al., 2008; Tong et al., 2017). The last factor mostly affects subsurface thermal conductivity and volumetric heat capacity by filling up the empty pore spaces embedded in the soil (Arkhangelskaya and Lukyashchenko, 2018), which in turn modifies apparent thermal diffusivity. Figure 3.8e explores the relation between soil moisture content and apparent thermal diffusivity near the surface at HRR.

The SpM at 3-hourly resolution (Fig. 3.8e) in a 10-day running window is applied to derive an intra-monthly evolution of apparent thermal diffusivity at the shallowest layers (0.1 m and 0.2 m), which is subsequently compared to changes in soil moisture and precipitation. It is observed that soil moisture presents a seasonal cycle, with extremely low content values in summer and relatively high but variable values in winter and spring. Transitions between these two states are remarkably abrupt, with soil moisture content increasing substantially by the

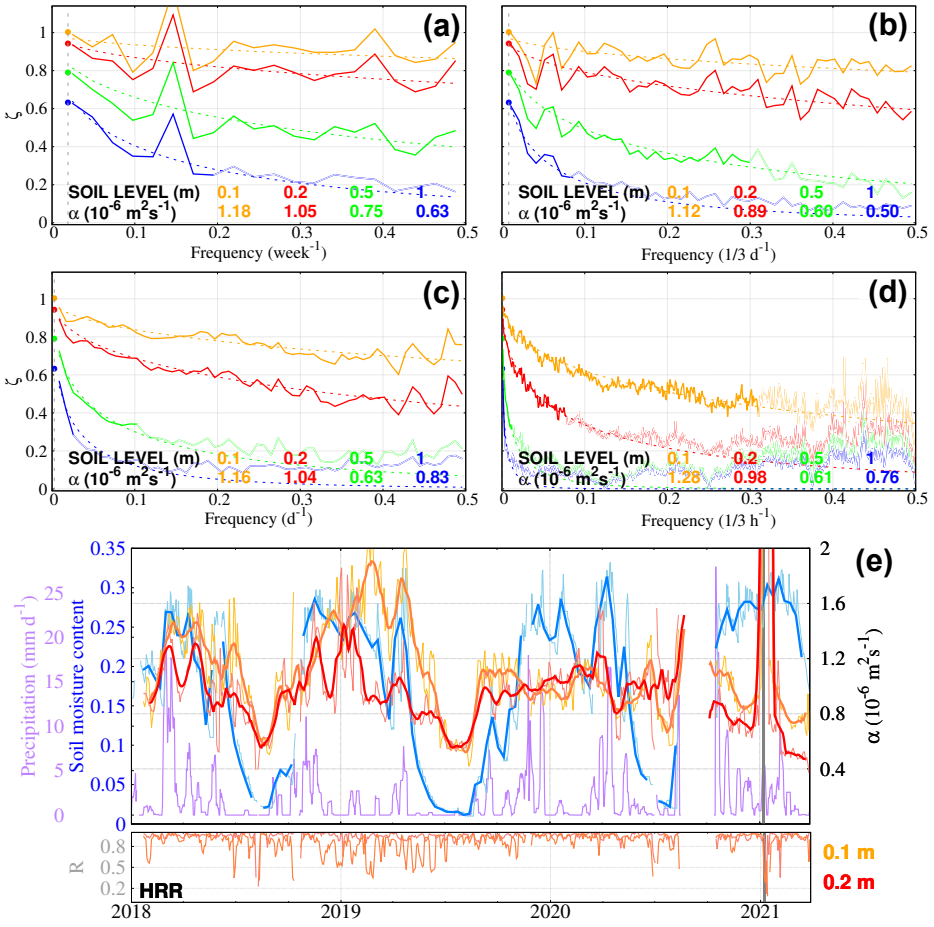

Figure 3.8: As in Fig. 3.7, SpM analysis of subsurface temperature attenuation at HRR for weekly (a), 3-daily (b), daily (c), and 3-hourly (d) data. The hollow parts of the observed attenuation curves were excluded in the estimation of apparent thermal diffusivity, according to the e-fold decay criterion explained in Section 3.1. (e) Precipitation, soil moisture content, and estimated near-surface thermal diffusivity from applying the SpM at the 0.1 m (light orange) and 0.2 m (light red) levels with respect to the GST with a 10-day running window at 3-hourly resolution; 11-day low pass running averages are provided in dark colors. Soil moisture content at 4 cm is shown at daily (10-daily) resolution in light blue (blue). Precipitation at 10-daily resolution is shown in purple. Least-square regression correlation (R) for SpM at every time step is given below in each case. The gray shaded thick line represents the only time interval (4 days) with snow insulation in Fig. 3.3c for HRR.

beginning of autumn and responding to enhanced precipitation, and the opposite occurring by the end of spring. In contrast to other sites in the Sierra de Guadarrama, HRR is rarely snow-covered in winter, which usually occurs after high-impact snow events (e.g., Filomena, which hit the Iberian Peninsula in January 2021, shading in Figs. 3.3c and 3.8e, Fernández-Castillo et al., 2025). Apparent thermal diffusivity also shows a seasonal behaviour, which corresponds to soil moisture low-frequency variability. In summer, poor soil moisture content reduces apparent thermal diffusivity values. However, even though diffusivity in winter increases with soil moisture content, the relation between these two variables at the high frequencies is not conclusive. For instance, the evolution of diffusivity in winter-spring 2018 at both soil levels correctly mimics soil moisture content variations (Fig. 3.8e), yet fails to capture its strong variations in winter 2020. This agrees on a clear increase of apparent thermal diffusivity from dry to wet soils, but a rather stable diffusivity in wet soils close to its field capacity observed by Arkhangelskaya and Lukyashchenko (2018). An analogous result for thermal conductivity by Dai et al. (2019) complies with this result as well. Moreover, SpM fails to provide reliable estimates of apparent thermal diffusivity when the ground is insulated by the snow, due to signal loss in the whole frequency band. This is clearly shown in Fig. 3.8e in January 2021, when the R coefficient, that is the square root of the goodness-of-fit of the amplitude attenuation to an exponential function, becomes extremely low.

Inter-annual correlation is hard to establish from our assessment due to the shortness of the time series in Fig. 3.8. However, previous studies (e.g., Melo-Aguilar et al., 2022) suggest soil moisture and apparent thermal diffusivity changes are to some degree proportionally related. Nevertheless, the lack of strong evidence of a linear relationship between apparent thermal diffusivity and soil moisture could also suggest that heat conduction is not the only mechanism of heat transfer near the surface. Heat convective transport via soil moisture and latent energy fluxes, water advection, and horizontal heat transport due to uneven temperature changes at the ground surface can also contribute to modifying the vertical heat conduction regime near the surface. The use of a running window SpM over longer time series or developing an alternate SpM based on a conductive-convective amplitude attenuation (Gao et al., 2008; Tong et al., 2017) solution to the heat conduction equation might better define this relation in wet soils.

3.3 Discussion and conclusions

The subsurface thermal structure at six sites in the Sierra de Guadarrama is consistent with the hypothesis of conduction being the main heat propagation mechanism of SAT changes into depth. On the one hand, SAT changes are transferred to the near-surface at the ground. Although SAT and GST are coupled at long-time scales, snow insulation, and zero-curtain effects produce a decoupling in winter in the uppermost stations (CTS, HYS, and RPI), which are affected by the presence of a seasonal snow cap (Figs. 3.2 and 3.3). This result agrees with previous studies carried out at cold and snowy sites, such as Fargo (North Dakota, US, Smerdon et al., 2003), Emigrant Pass (Utah, US, Bartlett et al., 2006), Bistrița (Romania, Demetrescu et al., 2007), and Hveravellir (Iceland, Petersen, 2022).

On the other hand, GST changes are propagated to depth by heat conduction to an extent controlled by the apparent thermal diffusivity of the subsurface. A CA method based on the amplitude attenuation and phase shift of the annual cycle yielded values that are between 1 and 1.3 10^{-6} m^2s^{-1} for the whole vertical profile (20 m) at most of the sites (Fig. 3.4), which are in the range of typical diffusivity values for granite or gneiss, main materials found in the Sierra de Guadarrama's subsurface (Fig. 2.2). These values are higher than those observed at other sites (e.g., Fargo, Prague, Cape Henlopen, Smerdon et al., 2004), which include shallower measures. If apparent thermal diffusivity is assessed near the surface, the values are smaller and closer to the previous literature (0.4 to 0.8 10^{-6} m^2s^{-1}; Table 3.2). A subsequent two-phase adjustment (Fig. 3.5) and a profile derivation based on CA (Fig. 3.6) portrays an increase of thermal diffusivity with depth at all sites, being more remarkable near the soil-bedrock transition. Evaluating thermal diffusivity changes with depth using a CA can therefore be a useful approach to determine soil depth at observational sites when no BRH rock samples are available. The deep monitoring profiles at the Sierra de Guadarrama are unique and provide a wider insight into the subsurface thermal structure, which may have implications for calibrating soil and bedrock properties in models (Tong et al., 2016; Dai et al., 2019) and monitoring land heat uptake in the terrestrial energy budget (Cuesta-Valero et al., 2022; von Schuckmann et al., 2023; Cuesta-Valero et al., 2025).

Near-surface (i.e., 1 m) soil apparent thermal diffusivity vertical and temporal heterogeneity is further explored by introducing a new SpM, which extends the analysis of temperature amplitude attenuation to the whole frequency spectrum. The SpM reports consistent apparent thermal diffusivity values in the first soil meter at SGV, NVC, and HRR with those previously derived with the CA for each of the respective sites regardless of the time resolution of the input data. Then, it

was used in an intra-monthly (10-daily) sliding window to explore apparent thermal diffusivity changes in time at the ground surface at HRR (Fig. 3.8e). Results suggest this parameter presents a seasonal cycle that is positively correlated with soil moisture, mostly under soil drought conditions. However, the fact that these changes are poorly correlated under high soil moisture contents might indicate that heat conduction is not the main heat transfer mechanism in wet soils. Heat transport via water advection and phase changes might not be negligible near the surface, so thermal structure in the shallow soil could be better characterized using a modification of SpM that complies with a conduction-convection heat transfer equation (Gao et al., 2008; Tong et al., 2017). Even so, the results show the potential of the SpM for inferring soil moisture content changes from soil temperatures, becoming a powerful tool for evaluating soil drought and water resource availability from observational and simulation-based subsurface temperature data.

Chapter 4
Land heat uptake in the industrial period: a comprehensive assessment from multiple data sources*

Chapter 3 demonstrated the conductive nature of the ground subsurface using observational temperature data series. GST variations are propagated downwards, experiencing an exponential amplitude attenuation and linear phase shift that is more intense for the highest frequencies. Atmospheric temperature trends associated with global warming also penetrate underground, being progressively less intense with depth. This underground temperature increase is caused by a positive heat uptake by the terrestrial subsurface. Quantifying this energy input in absolute terms is relevant to have a correct picture of the relative contribution of the different climate components to the terrestrial energy imbalance partitioning (see Section 1.6).

This chapter addresses the limitations that state-of-the-art ESMs have on the representation of land heat uptake due to the prescription of a zero-flux BBCP. In this context, SAT, GST, and subsurface temperature responses to forcing are assessed in two fully-coupled simulations of the CE with shallow and deep representations of the LSM (Sect. 4.2.1). Their long-term land heat uptake is also evaluated (Sect. 4.1.2, 4.2.1). The comparison evidences that deepening the BBCP increases much the land heat uptake, but does not remarkably affect the simulated surface temperature. Therefore, unbiased estimates of the land heat uptake due to industrial warming can be obtained by conducting standalone half-infinite forward model experiments forced by the surface temperatures from different sources as top boundary conditions (Sect. 4.1.1). This methodology is used to derive estimates of land heat uptake using all available observational datasets, reanalysis products, and state-of-the-art ESM experiments (Sect. 4.2.2).

---

* The main contents of the chapter are included in the published research article:
García-Pereira, F., J. F. González-Rouco, C. Melo-Aguilar, N. J. Steinert, E. García-Bustamante, P. de Vrese, J. Jungclaus, S. Lorenz, S. Hagemann, F. J. Cuesta-Valero, A. García-García, and H. Beltrami, 2024: First comprehensive assessment of industrial-era land heat uptake from multiple sources. *Earth System Dynamics*, 15, 547–564, DOI: 10.5194/esd-15-547-2024.

4.1 Methods

4.1.1 Subsurface temperatures generation

A half-infinite one-dimensional heat conduction forward model (Mareschal and Beltrami, 1992; Cuesta-Valero et al., 2023) is used to propagate yearly surface temperature data from the sources in Tables 2.8 and 2.9, and the P2k+ simulations (both d and s, Table 2.6) and produce forward temperature anomaly profiles (FTP hereafter):

$$FTP(t_N, z) = \sum_{i=1}^{N} T(t_i) \left[erfc\left(\frac{z}{2\sqrt{\kappa t_i}}\right) - erfc\left(\frac{z}{2\sqrt{\kappa t_{i-1}}}\right)\right] \quad (4.1)$$

where $T(t_i)$ is the annual global mean surface temperature anomaly at time step t_i, κ is thermal diffusivity, and z is depth. To compute FTPs at a certain time step, surface temperature data are trimmed to the interval spanning from the initial year (t_1; e.g., 1850, 1950, 1960, and 1971) to t_i. Temperature anomalies are calculated by computing annual anomalies with respect to the temperature value of the first year of the trimmed interval, t_1. This allows for departing from equilibrium initial conditions. These FTPs are equivalent to the BTPs used to yield observational land heat uptake estimates, which are derived by subtracting the geothermal gradient (mean state) from the absolute log temperature values (Mareschal and Beltrami, 1992; Huang et al., 2000). An ensemble of 3 different FTPs per time step was obtained using different thermal diffusivity values resulting from a Monte Carlo random sampling method of local properties (Davison and Hinkley, 1997), which accounts for the uncertainty in temporal and spatial soil heterogeneity (Cuesta-Valero et al., 2022). The Monte Carlo method consisted of averaging 100 different global maps of thermal diffusivity with values randomly sampled from a realistic range of 0.5 to 1.5 10^{-6} m^2s^{-1}. The sample size was the original number of gridpoints over land for every data source in Tables 2.8 and 2.9. Then, percentiles 2.5, 50, and 97.5 of the 100 values were taken as the three thermal diffusivity values for computing the global FTPs. This is the approach for every data source except for the P2k+ simulations, for which 0.79 10^{-6} m^2s^{-1} is taken as the thermal diffusivity to produce the FTP, which is the weighted global mean of the FAO values used by JSBACH to resolve the temperature vertical scheme (see Table 2.4). All the FTPs were resolved down to a common depth of 1417 m so that results could be comparable to the estimates derived from the P2k+d simulation, limited by a zero-flux bottom boundary condition at 1417 m. This comparison is possible since this BBCP depth ensures the thermal decoupling between the ground surface and the bottom layer, which is equivalent to the

subsurface acting as a half-infinite conductive medium (González-Rouco et al., 2021; Steinert et al., 2021a). As the uncertainties associated with local thermal properties and subsurface depth are tackled when calculating the FTPs, global differences between mean FTPs and land heat uptake estimates from different sources cannot be due to these factors.

In addition, both subsurface temperature data coming from P2k+ (Table 2.6) and CMIP6 simulations (Table 2.8) are used. Temperatures at different subsurface levels for every time step are aggregated to yield subsurface temperature profiles. Subsurface temperature anomaly profiles (STPs hereafter) are subsequently computed by subtracting the initial temperature profile from this $T(t_i, z)$, as follows:

$$STP(t_i, z) = T(t_i, z) - T(t_1, z) \tag{4.2}$$

where $T(t_i, z)$ is the subsurface temperature at depth z and time step t_i, and, i.e., the subsurface temperature profile at time step t_i, and $T(t_1, z)$ is the initial subsurface temperature profile.

4.1.2 Land heat uptake estimation

The annual time evolution of the land heat uptake, $Q_s(t)$, can be estimated by integrating the FTP anomalies along the whole soil column at every yearly time step as follows:

$$Q_s(t) = A \sum_{j=1}^{n} \Delta z(j)\ C_v(j)\ \frac{FTP(t, j) + FTP(t, j+1)}{2} \tag{4.3}$$

where $\Delta z(j)$, $C_v(j)$, and $FTP(t, j)$ are thickness, volumetric heat capacity, and global mean FTP of layer j, respectively, and A is the Earth's land surface area excluding glacier areas in Antarctica and Greenland ($1.34\ 10^{14}$ m^2, Cuesta-Valero et al., 2023). FTPs were calculated using an evenly spaced layering of 1 m thickness. Land heat uptake from both P2k+ (Table 2.6) and CMIP6 (Table 2.8) was also calculated from the simulated model subsurface temperatures down to the BBCP, i.e., STPs, by making use of Equation 4.2, albeit temperature layers are unevenly spaced in these cases. LSM vertical layering thickness for both shallow and deep configurations of the MPI-ESM is given in Table 2.5. These values can also be consulted for the CMIP6 models used in this thesis following the different references in Table 2.8. Analogous to what it is done to compute thermal diffusivity (see Sect. 4.1.1), three values of volumetric heat capacity were derived using

a Monte Carlo approach (Davison and Hinkley, 1997; Cuesta-Valero et al., 2022) for every source in Tables 2.8 and 2.9 using randomly sampled values between 2.5 and 3.5 10^6 $Jm^{-3}K^{-1}$. The combination of three values for volumetric heat capacity and three for thermal diffusivity yield nine land heat uptake estimates, which are represented hereby in terms of mean and variability (two standard deviations).

4.2 Results

4.2.1 Influence of a realistically deep LSM

The comparison of the MPI-ESM P2k+s and P2k+d simulated SAT, GST, and soil temperature at layer 5 (ST5) allows for assessing the thermal impact of increasing the BBCP depth (Fig. 4.1). ST5 is selected because it is the deepest level for P2k+s, reaching 9.83 m, and can be compared with the corresponding layer in P2k+d. Figure 4.1a-d shows the time evolution of SAT, GST, and ST5 for the two simulations both in annual averages and with 31-year running means to emphasize the low-frequency response. The response to the common external forcing during the last two millennia (Jungclaus et al., 2017) generates similar interannual (e.g., volcanic events), multidecadal, and centennial variability for P2k+s and P2k+d for SAT and GST (Fig. 4.1a,b,d), indicating no systematic changes in preindustrial mean state (Fig. 4.1f) and variability (Fig. 4.1g,h) from using the deep or shallow versions of the model. The resulting SAT and GST warming of about 5.5 ^{o}C at the end of the 21st century agrees well with the range of warming in the ensemble of MPI-ESM runs (Fig. 4.1e) and with a climate sensitivity of 3.2 ^{o}C for the MPI-ESM (Mauritsen et al., 2019). Note that for each simulation SAT and GST virtually overlap, showing long-term SAT–GST coupling (Melo-Aguilar et al., 2018). However, the impacts of deepening the LSM are noticeable in ST5, consistent with González-Rouco et al. (2021), with P2k+d showing lower high-frequency volcanic cooling (e.g., 1257, 1457, and 1815, Fig. 4.1c), preindustrial variability (Fig. 4.1f-h) and warming (0.8 ^{o}C by 2100, Fig. 4.1e,i) than P2k+s. The reduced warming is significant ($p < 0.05$) if compared to the range of 21st-century warming values produced by the 30ENS of MPI-ESM simulations.

Therefore, increasing the depth of the LSM produces significant changes in the subsurface temperatures, yet it does not change surface temperatures. The GST of the P2k+s and P2k+d can be considered equal in terms of their range of variability and long-term trends, indicating that the surface temperatures simulated

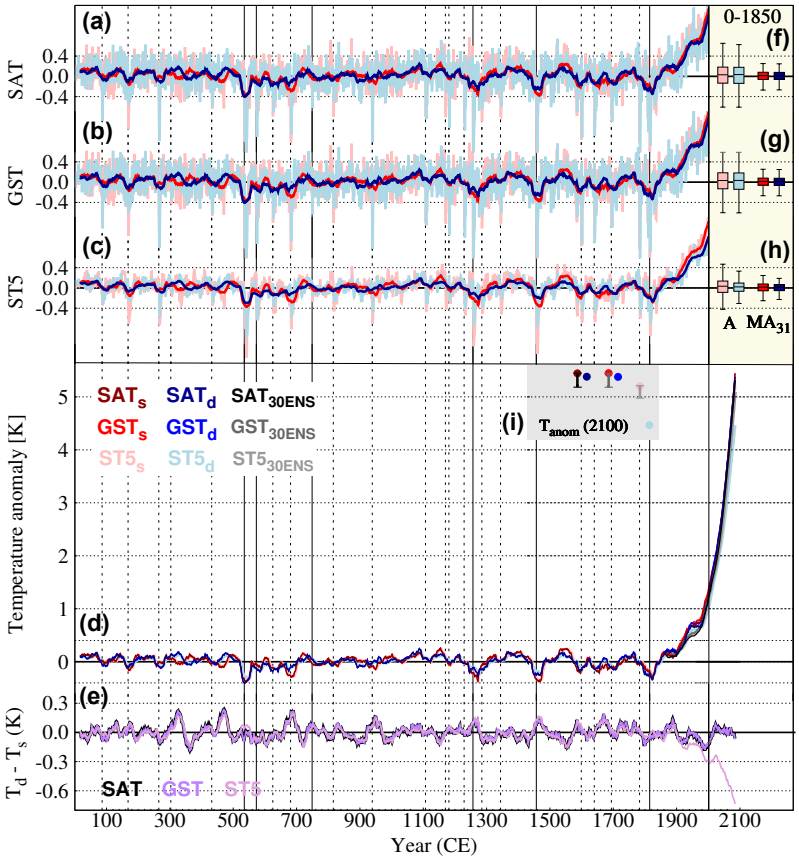

Figure 4.1: Past2k, historical, and SSP5-8.5 (P2k+) global means for a) SAT, b) GST, and c) ST5 anomalies over land areas (excluding Greenland and Antarctica) in 0–2000 CE relative to 1850–1900 for a simulation run with the MPI-ESM1.2-LR with a shallow (subscript s, red lines) and a deep (subscript d, blue lines) version of its LSM, JSBACH. Annual time series are shown in light, while 31-year moving averages are portrayed in dark colors. (d) 31-year moving averages in a-c (see legend for colors) are represented here together with the ensemble of 30 MPI-ESM1.2-LR CMIP6 standard shallow historical and SSP5-8.5 simulations (30ENS, grey lines) in 1850–2100 CE for comparison. (e) SAT (black), GST (purple), and ST5 (pink) differences between P2k+s and P2k+d, filtered with a 31-year moving average. For a,b,c,d, and e, vertical solid (dashed) lines indicate the 6 (19) strongest (weakest) volcanic events of 0–1850 CE. (f,g,h) Range of temperature variability of annual (A) and 31-yr moving average (MA31) time series in the preindustrial period (0–1850 CE) for SAT (f), GST (g), and ST5 (h). Whiskers represent percentiles 10 and 90, and boxes 25 and 75, respectively. (i) Temperature anomaly at 2100 with respect to 0–1850 CE (K) in P2k+ (see legend for colors). In this case, whiskers show the range of variability (percentiles 10, and 90) of the total warming (K) in 30ENS.

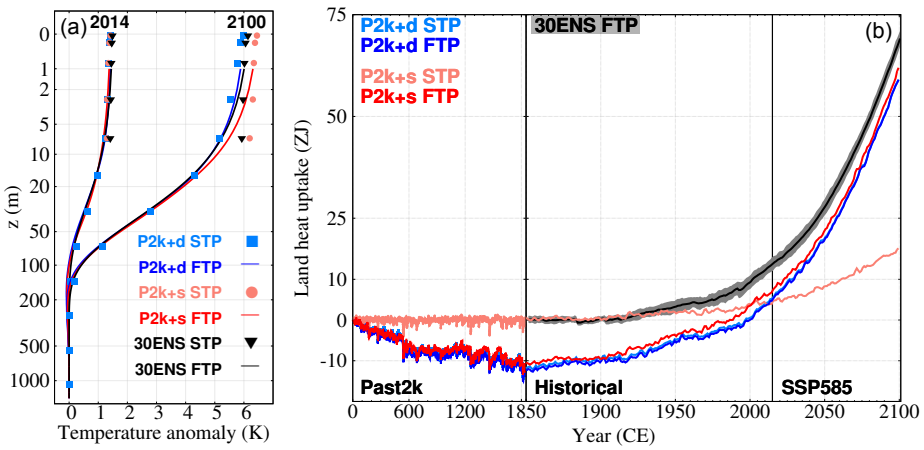

Figure 4.2: (a) FTPs (continuous lines) and MPI-ESM STPs (symbols, see legend) for P2k+d (blue) and P2k+s (red) and for the 30-member ensemble mean of MPI-ESM historical and SSP5-8.5 simulations (30ENS, black) in years 2014 and 2100. Y-axis is logarithmic. (b) Land heat uptake derived from the yearly time step-wise vertical integration of FTPs and STPs for P2k+d, P2k+s, and 30ENS. The time x-axis is unevenly spaced to enhance land heat gain since 1850. For the 30ENS, the confidence interval is also shown in grey ($p < 0.05$).

by a LSM are not affected by its BBCP depth. This result offers the potential to use GSTs from different sources, e.g., reanalysis or CMIP6 simulations, as a boundary condition for forcing an infinite half-space standalone forward model and deriving realistic land energy storage estimates. This is first verified in Fig. 4.2 using the P2k+ runs. Figure 4.2a shows both STPs from P2k+s, P2k+d, and the ensemble mean STP from 30ENS, and their respective FTPs by the end of the historical period (2014) and SSP5-8.5 (2100). Both STPs and FTPs can capture the different degrees of warming between 2014 and 2100 and agree to portray its penetration down to a depth of about 150 m (Fig. 4.2a). However, there is a remarkable difference when comparing the FTPs and STPs for P2k+s, P2k+d, and the 30ENS. Whilst P2k+d FTP is capable of reproducing its analogous STP, FTPs, and STPs for P2k+s diverge in depth. This is because the forward model is run with no zero-flux BBCP imposed, which can be considered analogous to the deep configuration of JSBACH (1417 m). Consequently, FTP warm anomalies are smaller in depth than the ones corresponding to the STP, which complies with a BBCP at 10 m. Imposing a shallow BBCP generates a warm bias with depth since the heat flux is halted from penetrating downwards due to the existence of a zero-flux condition (Smerdon and Stieglitz, 2006; Alexeev et al., 2007; Steinert et al., 2021a). Thus, FTPs derived from P2k+s and 30ENS reproduce

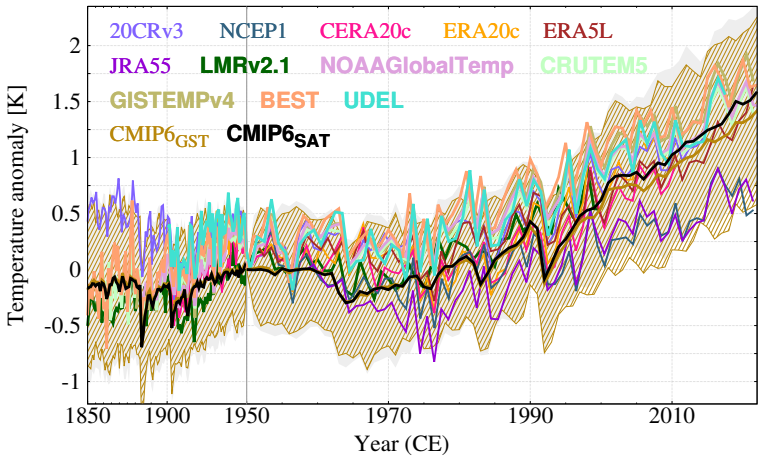

Figure 4.3: Global land mean temperature anomaly in 1850–2020 with respect to 1950 for reanalyses, observational, and a 38-member CMIP6 ensemble. SAT is plotted both for observational and CMIP6 sources and LMRv2.1 (tags in bold), whereas GST is given for the remaining reanalyses and CMIP6 simulations (see Tables 2.8 and 2.9). GST and SAT spread ranges for the CMIP6 ensemble are also portrayed ($p<0.05$).

P2k+d STP and FTP, realistically representing the half-infinite space thermal conduction that governs heat propagation in observational BTPs (Mareschal and Beltrami, 1992; Cuesta-Valero et al., 2021b).

Figure 4.2b shows the land heat uptake since 0 CE resulting from the stepwise integration of FTPs and STPs for the P2k+ simulations, and FTPs for 30ENS. Both STP and FTP-derived heat energy uptake estimates for P2k+d and the FTP-derived for P2k+s depict a preindustrial land heat loss, which gets more acute in the LIA (from 1400 to 1850, Miller et al., 2012), and a noticeable heat uptake since 1900. The STP-based heat uptake evolution for P2k+s misses to simulate the heat loss and largely underestimates the magnitude of the subsequent heat uptake shown by P2k+d, yielding a heat uptake of around 18 ZJ by the end of the 21st century, which is 4 times smaller than the values derived from deep FTPs and P2k+d STP (about 75 ZJ). The agreement of P2k+s and P2k+d on the land heat uptake when the forward modeling approach is used evidences the viability of using surface temperatures as boundary conditions to derive FTPs and estimate heat uptake when subsurface thermal schemes are too shallow.

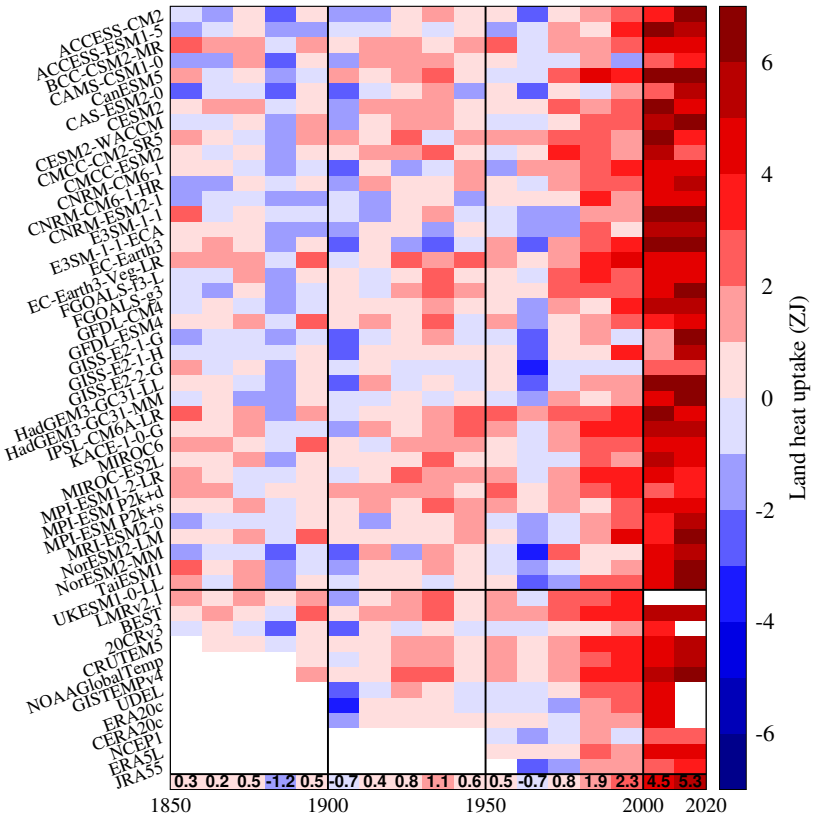

Figure 4.4: Decadal global land heat uptake in the industrial period (1850–2020) from the different data sources in Fig. 4.3. Red (blue) tones in the heatmap represent decadal energy gains (losses). The black horizontal line separates CMIP6 models (38 members), including MPI-ESM P2k+ simulations, from reanalysis and observational data sources (12 members). CMIP6 sources are sorted downwards alphabetically, while the rest are ordered by length of decreasing periods. The last row (values in bold) represents the multi-source decadal mean.

4.2.2 Multi-source land heat uptake estimates

The previous analysis opens the possibility of estimating land heat uptake from a variety of sources. Global mean land surface temperature anomalies with respect to 1950 for the seven reanalyses, five observational databases, and the CMIP6 model ensemble are shown in Fig. 4.3. By averaging 38 CMIP6 members, the ef-

fect of internal variability is minimized, thus emphasizing the response to forced variability. It can be seen that both SAT and GST CMIP6 multi-model means (thick lines) are fully coupled up to 2000, depicting sudden cooling events in the 1880 and 1990 decades, associated with the volcanic activity of Krakatoa or later El Chichón and Pinatubo (Self and Rampino, 1981; Mccormick et al., 1995). They also capture the cooling during the 1950s and 1960s and the subsequent warming. However, the warming trend is slightly higher for SAT than GST, which produces a small temperature offset of about 0.1 K by 2020. This offset is negligible compared to the range of temperature variability of the 38 members (SAT, shaded grey; GST, scratched gold), so SAT and GST can be considered as coupled, and therefore SAT can be used as alternative boundary information to feed the forward model when GST data are not available. Regarding the observational and reanalysis datasets, surface temperatures lie within the range of CMIP6 multi-model variability. Nevertheless, observational data render higher temperature anomaly values than all the reanalyses, showing higher temperature trends in 1950–2000 and 1960–2020 (Table 2.9). Moreover, NCEP1 and JRA55 depict the coldest GST evolutions of all observational-based sources, even lying beneath the multi-model spread of CMIP6 models at some years in the mid-70s.

The decadal evolution of the different surface temperature datasets impacts their land heat uptake, as it is shown in Fig. 4.4, where decadal heat gains and losses are assembled for the time span of each of the 50 datasets collected in this work. All the sources agree on depicting a progressive land warming, only interrupted by transient coolings in the 1880s, 1900s, and 1960s, that coincide with the volcanic eruptions of Krakatoa (Self and Rampino, 1981), Péleé (Gueugneau et al., 2020) and Agung (Hansen et al., 1978). Moreover, heat gain is enhanced in 1980–2020, rendering a land uptake of around 14 ZJ. Even though land heat uptake intensifies in these decades, its increase is not linear, with 1990–2000 and 2010–2020 showing a deceleration in the heat uptake trend (0.4 and 0.8 ZJ, respectively) with respect to the 1970–2020 values (increasing land heat uptake of 1.2 ZJ per decade on average). The uncertainty associated with variability in soil properties is negligible and accounts for less than 0.1 ZJ decadally. Differences between sources in the intensity or the time occurrence of decadal heat gains (losses) can result from differences in the representation of internal variability, as suggested by the higher consistency among estimates from observations compared to those from CMIP6 models. Products showing the greatest decadal temperature trends in Tables 2.8 and 2.9, such as ACCESS-ESM1-5 or GISTEMPv4, generate the largest storage of energy, with 16.4 and 17.2 ZJ during 1980–2020, respectively.

The estimates of land heat uptake derived from reanalyses, observational data, and CMIP6 models (Fig. 4.4) are compared to values previously reported in

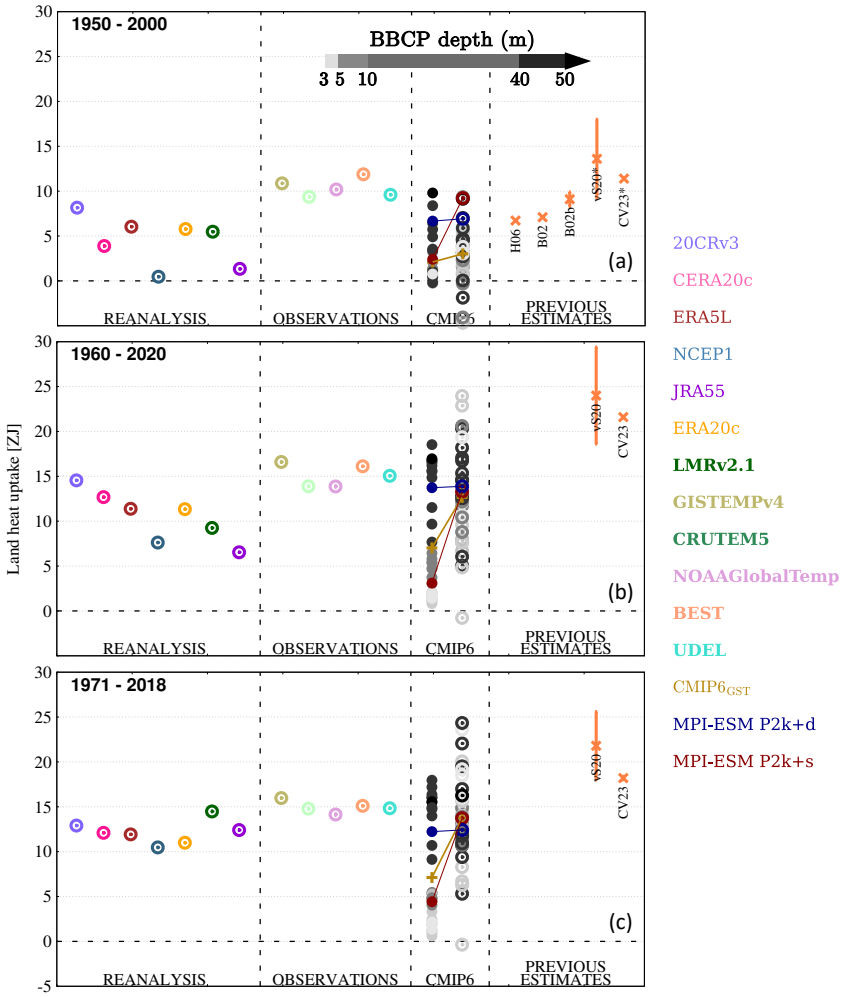

Figure 4.5: Land heat uptake estimates from different sources and periods. Land heat uptake during 1950–2000 (a), 1960–2020 (b), and 1971–2018 (c) derived from FTPs (hollow points) of reanalysis and observational databases (Table 2.9), CMIP6 FTPs (right hollow) and direct integration of CMIP6 STPs (left solid points, Table 2.8), and previous estimates: B02 (Beltrami, 2002), B02b (Beltrami et al., 2002), H06 (Huang, 2006), vS20 (von Schuckmann et al., 2020), and CV23 (Cuesta-Valero et al., 2023), orange crosses. The vS20 and CV23 estimates for 1950–2000 refer in fact to 1960–2000 and are marked with a star. The BBCP depth for every CMIP6 model used in this work is given by a grey shading (see legend above), while the multi-model mean both for the STP and FTP-based values is given by gold crosses. MPI-ESM P2k+d (P2k+s) estimates are plotted in dark blue (red).

the literature derived from logged BTPs (Beltrami et al., 2002; Beltrami, 2002; von Schuckmann et al., 2020; Cuesta-Valero et al., 2023) and CRUTEM2 SAT (Huang, 2006) for the periods 1950–2000, 1960–2020, and 1971–2018 (Fig. 4.5). The selection of these time intervals enables the comparison with previous works. In the case of CMIP6 models, both the heat estimates obtained through direct integration of the STPs and FTPs are depicted. The MPI-ESM P2k+ estimates (Fig. 4.2) are also included. All the estimates from this work and the previous literature show an increasing trend of land heat uptake towards the present. The 1950–2000 interval (Fig. 4.5a) shows less warming in the reanalyses than in the observational derived estimates, which is particularly noteworthy for LMRv2.1 and JRA55. These two reanalyses show no heat uptake in 1950–2000, which stems from a long-lasting negative temperature anomaly in 1950–1980 that is not shown by the rest of the sources (Fig. 4.3). Furthermore, CMIP6 depth-corrected estimates using FTPs are in range with the reanalysis and slightly below the observational estimates. Hence, all estimates based on FTPs agree overall with the previous estimates, with von Schuckmann et al. (2020) giving the highest land heat uptake values across all data sets. Figure 4.5b and c portray similar results for the periods 1960–2020 and 1971–2018, respectively. In both cases, the estimates derived from the different FTPs are consistent, with observational estimates at the upper end and some reanalyses showing the smallest land heat uptake values. For instance, land heat uptake estimates for the period 1971–2018 (Fig. 4.5c) range from 10.5 to 16.0 ZJ, yielding an ensemble mean of 13.9 ZJ for the CMIP6 FTPs, 12.2 ZJ for the reanalyses, and 15.0 ZJ for the observational-driven estimates. These differences are due to the smaller temperature trends shown by reanalyses and CMIP6 models when compared to observational data sets from the 1970s to the present, as shown by Fig. 4.3 (see Tables 2.8 and 2.9 for the exact trend values).

Furthermore, Fig. 4.5 shows the dependence of land heat uptake on BBCP depth for CMIP6 STP-derived estimates (note gray shading on the left side), evidencing a significant increase when the forward model is applied to correct estimates stemming from shallow ESMs (from 6.9 to 12.6 ZJ in 1960–2020, Fig. 4.5b, and from 7.0 to 13.9 ZJ in 1971–2018, Fig. 4.5c). Since 1950–2000 warming is very small for most of the CMIP6 models and very sensitive to the internal variability of each one (see Table 2.8), correcting the estimates in this case does not make a remarkable difference (Fig. 4.5a). Even after correcting the BBCP depth bias on land heat uptake, the range of CMIP6 multi-model variability is still very large, with a standard deviation of 5.4 (5.1) ZJ in 1960–2020 (1971–2018). This large variability is explained by some outlier estimates (e.g., CAMS-CSM1-0 and GISS-E2-2-G) which yield very small or even negative land heat uptakes, linked to the small climate sensitivity of these models in the periods

of study, as shown by Table 2.8. By contrast, the CMIP6 simulations showing the greatest temperature trends also show the largest corrected FTP values, some of them yielding greater estimates than the state-of-the-art estimates from von Schuckmann et al. (2020); Cuesta-Valero et al. (2023). In all periods shown in Fig. 4.5, the multi-model CMIP6 mean is consistent with estimates yielded by reanalyses and observational data sets. Despite the consistency among the estimates obtained from the different data sets in this work, all of them yield results in the range of past literature values for the 1950–2000 period (Beltrami et al., 2002; Beltrami, 2002; Huang, 2006), but are lower than those in recent literature for 1960–2020 and 1971–2018, which quantified land heat uptake to be between 18.6 and 25 ZJ in 1971–2018 (von Schuckmann et al., 2020; Forster et al., 2021), and subsequently narrowed and lowered this range to be 18.0-18.4 ZJ (Cuesta-Valero et al., 2023).

4.3 Discussion and conclusions

We compare land surface and soil temperatures as well as land heat uptake from two simulations of the period 0-2100 CE made with two versions of the MPI-ESM, one including a standard shallow and the other one a more realistic deep LSM. The deep LSM included in MPI-ESM generates about four times more heat uptake than the shallow version by the end of the historical period. This underestimation by the shallow LSM version only grows up to the end of the 21st century, reaching 18 (75) ZJ for the shallow (deep) LSM versions. Also, while it produces relatively colder near-surface soil temperatures after 1850 CE, GST low-frequency variability and trends remain unchanged. This finding suggests the potential utility of employing GSTs to drive a forward model and obtaining deep FTPs and subsequently unbiased estimates of land heat uptake. The concurrence of estimates from both STPs of P2k+d and FTPs of P2k+s and P2k+d supports the application of the forward modeling method to correct insufficient land heat uptake values stemming from shallow LSMs. The results portray a land heat uptake in the industrial period that has intensified in the last decades of the 20th and the first two decades of the 21st century. The FTP strategy is also applied to estimate land heat uptake from both observation-based products and CMIP6 simulations. Results are compared with previous estimates based on observational BTPs, thus providing additional information to assess consistency between model and observational-based estimates. Land heat uptake in 1971–2018 is between 10 and 16 ZJ for all sources, being around 14 ZJ for CMIP6 models. This figure doubles the 7 ZJ CMIP6 models capture when their heat uptake capability is

constrained by imposing a shallow zero-flux BBCP, which shows the relevance of forward model in correcting model-based estimates. Reanalysis-based estimates are slightly smaller than those obtained from applying the forward model driven by observational gridded datasets or corrected CMIP6 simulations, in consistency with the generally smaller reanalyses warming since 1950 relative to other data sets. SAT observation-based estimates render the highest values, in consistency with SAT trends being slightly larger than GST's. SAT-related values can be thus regarded as an upper-limit land heat uptake estimate.

Nevertheless, all observational-based and corrected CMIP6 estimates underestimate the most recent values of land heat uptake based on BTPs. This discrepancy may stem from different sources of uncertainty. One possibility is that since borehole-derived surface temperature and ground heat flux stories have a low time resolution (e.g., 25-year time step in Cuesta-Valero et al., 2021b), they may not consider the decadal cold anomalies occurring in 1960–1980 (Fig. 4.3). This discrepancy may play a major role since decadal surface temperature differences might alter inter-decadal land heat imbalance due to subsurface thermal inertia (Beltrami et al., 2015). Moreover, BTP logs are scarce in the last decades and non-existent after the 2000s, so borehole-based estimates for the last two decades stemming from von Schuckmann et al. (2020) and Cuesta-Valero et al. (2023) for 1960–2020 and 1971–2018 are yielded extrapolating the ground heat flux temperature reconstructed in the last decades of the 20th century to the 21st century (2000–2018, and 2000–2020, respectively). This could be overlooking the global warming hiatus (1998–2012, Karl et al., 2015) effect on a relative slowdown in land heat uptake. Furthermore, the different methodological approaches used to yield observational and simulation-based (STP, FTP) heat uptake estimates might play a role. While STP and FTP-based heat uptake values in a certain time period are rendered by integrating the differences in the temperature profiles between the initial and the final time steps of that period, previous observational land heat uptake values are yielded by estimating ground heat flux stories based on single-time BTPs at different locations to then reconstruct the global heat uptake evolution (Beltrami et al., 2002; Cuesta-Valero et al., 2023). That entails BTP-based estimates do not represent net land heat variations in a certain time span, but a continuous variation of land heat uptake by aggregating logs taken in different dates and locations. This subsequently implies that this methodology preserves land energy changes due to past climate signals (Beltrami et al., 2017), which may contribute to comparatively greater heat uptake estimates in recent decades. A recent study by Cuesta-Valero et al. (2025) combining boreholes and satellite data reports lower land heat uptake values than those based solely on BTPs. Their estimates are more consistent with the multi-source estimates presented in this thesis. With these differences reconciled, this work contributes to

bringing observational and model-based land heat uptake estimates to the same frame of comparison, by removing the bias associated with imposing too shallow BBCP depths. The comparison between CMIP6-based and observational data-driven land heat uptake estimates can also serve as an additional metric to assess the realism of ESMs in reproducing current global warming.

Chapter 5
Analyzing the impact of LSM depth on ground heat flux and surface energy balance*

Chapter 4 established the clear relationship between the BBCP depth and land heat uptake in fully-coupled ESM experiments. Prescribing an insufficiently deep BBCP disrupts the underground heat thermal transfer at long-term scales, biasing subsurface temperature variability and trends and constraining land heat uptake. These outcomes evidence the relevance of having deeper LSMs in correctly quantifying the land heat uptake, which is crucial to correctly representing the terrestrial energy partitioning (Section 1.6). Nevertheless, the physical mechanism responsible for increasing land heat uptake with BBCP deepening, despite unchanged GST, has not been explained so far.

This chapter demonstrates how changing the BBCP impacts on the GHF, i.e., the vertical derivative of the GST scaled by the soil thermal conductivity. This is attained by studying the global mean and distribution of the GHF given by an ensemble of standalone simulations with different number of subsurface layers and BBCP depth performed with the LSM of the MPI-ESM, JSBACH (Sect. 5.1.1, 5.2.1). GHF dependence on the BBCP depth is also assessed using a finite heat conduction forward model forced by global mean JSBACH GSTs for different warming levels over the pre-industrial period (Sect. 5.1.2, 5.2.2). Additionally, the capability of GHF biases associated with the BBCP depth to reshape surface turbulent heat fluxes, i.e., the LHF and SHF, as well as net surface radiation, is also studied for different hydroclimates (Sect. 5.1.3, 5.2.3). Overall, the analysis presented in this chapter shows, for the first time, consistent impacts of deepening the BBCP on climate variability at the ground surface.

* The main contents of the chapter are included in a manuscript in preparation:
García-Pereira, F., J. F. González-Rouco, et al., 2025b: Insufficient soil depth constrains ground heat flux in Land Surface Models. *Geophysical Research Letters* (In preparation).

5.1 Methods

5.1.1 GHF simulated with JSBACH

GHF, SAT, and GST from an ensemble of standalone LSM simulations with the JSBACH are used (see Table 2.6). The ensemble includes a total number of eight land-only historical (1850–2005) and RCP8.5 scenario (2006–2100) experiments with a varying number of subsurface vertical layers (from 5 to 12) increasingly wide with depth. Thus, a progressive expansion of the BBCP depth from the 9.83 m for the standard JSBACH 5-layer to 1416.84 m for the 12-layer simulation is achieved (see a detailed description of the discretization in Fig. 2.4a and Table 2.5). This depth is sufficient to ensure that the temperature at the LSM bottom layer is decoupled from GST changes at centennial and millennial timescales (González-Rouco et al., 2021). The ensemble was originally conceived to analyze the sensitivity of the ground surface and subsurface temperature variability and land heat uptake to changes in the BBCP depth under industrial warming conditions. The technical details on the standard hydrological and thermodynamic features of JSBACH, and the enhanced vertical discretization together with the experimental setup of the JSBACH ensemble used here are described by Reick et al. (2021) and González-Rouco et al. (2021), respectively, and summarized in Section 2.2. JSBACH evaluates the GHF as follows (Reick et al., 2021):

$$GHF = -\lambda \frac{\partial T}{\partial z}(z = 0), \tag{5.1}$$

where λ is the thermal conductivity, which is the result of the product of the volumetric heat capacity and the thermal diffusivity, i.e., $\lambda = C_v \kappa$. Both volumetric heat capacity and thermal diffusivity are set constant over time, prescribing five pairs of spatial values according to the soil types of the FAO (see Fig. 2.4b and Table 2.4). In this work, positive (negative) values of the GHF mean upward (downward) fluxes.

5.1.2 Forward model GHF estimates

Since GST variability is independent of the BBCP depth (see Section 4.2.1, García-Pereira et al., 2024b), simple one-dimensional heat conduction forward models forced by GSTs as top boundary conditions can yield reliable estimates of the land heat uptake. The dependence of the GHF on the BBCP depth is further evaluated herein using a simple limited heat conduction forward model (Con-

ForM, Garcia-Pereira and González-Rouco, 2024). This model numerically discretizes the vertical heat conduction partial derivative equation (Eq. 1.1, Carslaw and Jaeger, 1959). The numerical solution is obtained using a Finite Time Centered Space finite difference scheme, consisting of an explicit Euler scheme for time resolution and a second-order central difference for the spatial dimension (Roache, 1998). The resulting numerical solution of the heat conduction equation is expressed as:

$$T_i^{n+1} = T_i^n + \kappa \Delta t \frac{T_{i-1}^n - 2T_i^n + T_{i+1}^n}{\Delta z^2}, \tag{5.2}$$

with T_i^n representing the temperature value at soil level i during time step n. The model produces the subsurface vertical temperature structure at each time step, employing a thermal equilibrium boundary condition at the ground surface, i.e., $T[z = 0] = T_0$, and a zero-flux boundary condition at the bottom, i.e., $T'[z = z_{max}] = 0$. To ensure the stability of the numerical scheme, governed by the Courant-Friedrichs-Lewy condition $\Delta t \leq \Delta x^2 / 2\kappa$ (Courant et al., 1928), a constant time step of one hour and a subsurface layer thickness of 0.1 m is employed. The GHF is simply computed as the discrete temperature difference between the first two layers at the top, as follows:

$$GHF^{n+1} = -\lambda \frac{T_1^n - T_2^n}{\Delta z} \tag{5.3}$$

To obtain the relation between GHF and the BBCP depth, ConForM is run forced by the global mean GST of the JSBACH ensemble average for different values of the BBCP depth (from 5 to 1500 m). The subsurface thermal diffusivity and heat conductivity parameters are set constant and computed as the weighted global mean values of the FAO data used in JSBACH (Table 2.4).

5.1.3 Evaluation of the surface energy balance for different hydroclimates

The positive energy imbalance resulting from a warming climate at the top of the atmosphere is distributed between the different climate components (Section 1.6), eventually modifying the ground surface energy balance (SEB). In transient fully-coupled ESM simulations, changes in the physical representation or the parameterizations of the different subsystems can lead to a redistribution of the energy within the climate system. For instance, Steinert et al. (2024) demonstrated that a deeper representation of the LSM in MPI-ESM industrial climate

change experiments slightly increases the land contribution to the terrestrial energy surplus partitioning from 1 % to 3 % during 1850–2100. This increase is counterbalanced by a smaller ratio of ocean heat uptake, which is reduced from 98 % to 96 %. However, the changes in land and ocean heat uptake produced by deepening the BBCP are difficult to disentangle from internal variability, given their relatively small magnitude compared to the absolute ocean heat content and its interannual to multicentennial fluctuations. This dilemma does not operate in land-only simulations, since energy variations at the top of the atmosphere can only produce changes in the SEB, given that the land component is the only one participating. Moreover, SAT is imposed as a boundary condition to comply with the land-atmosphere coupling at the ground surface, so only very little variations of GST are to be expected. The SEB, as given by JSBACH, would satisfy the following:

$$R_N + LHF + SHF + GHF - hC_v \frac{\partial GST}{\partial t} = 0, \tag{5.4}$$

where R_N represents the net radiation, and h and C_v the thickness and volumetric heat capacity of the surface layer, respectively. Hence, given that the GST temporal changes with BBCP depth are negligible, variations in the GHF can only alter SHF, LHF, or the R_N. Since these variations may depend on the local temperature and soil moisture conditions at the ground surface, the relative changes in SHF, LHF, and R_N are studied for different surface hydroclimates defined in terms of the modified Bowen ratio (BR_{mod}, Han et al., 2017):

$$BR_{mod} = \langle \overline{SHF} \rangle \left| \frac{\overline{SHF}}{\overline{LHF}} \right|, \tag{5.5}$$

where $\overline{SHF}$ and $\overline{LHF}$ represent the mean SHF and LHF of the eight JSBACH simulations for the pre-industrial mean state in 1850–1900. Han et al. (2017) identified five regions as per their different BR_{mod} values: extremely cold (EC, $BR_{mod} < 0$), extremely wet (EW, $0 < BR_{mod} < 0.5$), semi-wet (SW, $0.5 < BR_{mod} < 2$), semi-dry (SD, $2 < BR_{mod} < 10$), and extremely dry (ED, $BR_{mod} > 10$). Since JSBACH does not regard soil moisture thawing and freezing processes (Reick et al., 2021), soils in permafrost areas are predominantly wet (Steinert et al., 2021b), so EC behave as EW areas. Therefore, only four types of surface hydroclimate based on BR_{mod} are distinguished in this work, merging EC and EW into a single EW category ($BR_{mod} < 0.5$).

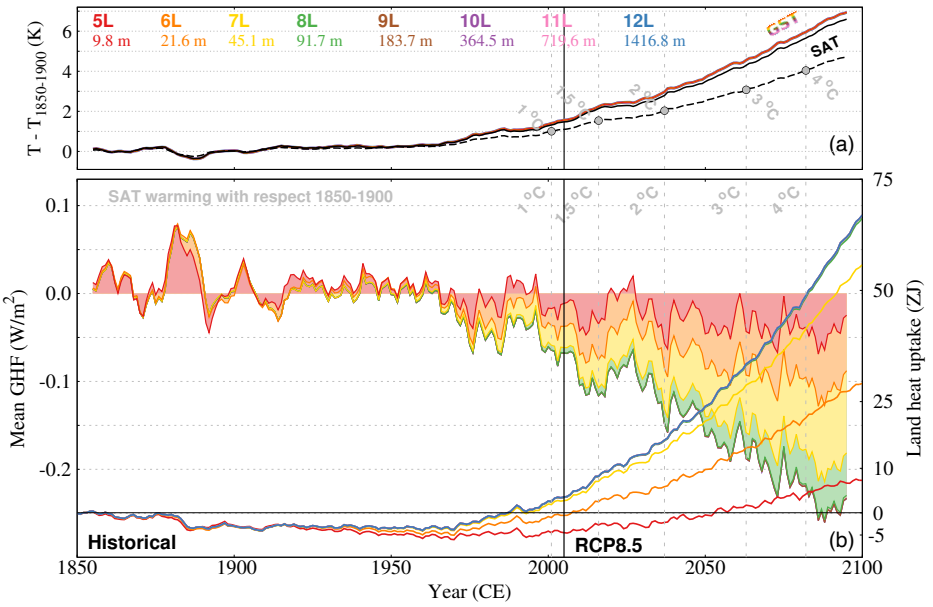

Figure 5.1: (a) 11-year moving average global mean (dashed black) and over-land mean SAT (solid black) and GST anomalies with respect to 1850–1900 (colored lines, see legend) for the ensemble of standalone JSBACH simulations used in this work. Grey dots indicate the sequence of warming levels defined in this work (see Section 5.1.4). (b) 11-year moving average global mean GHF value (filled contours, W/m^2) stemming from the ensemble of JSBACH historical (1850–2005) and RCP8.5 scenario (2006–2100) simulations with different number of layers and BBCP depth (see colored labels on top). The integrated value in time multiplied by the global continental area (excluding Greenland and Antarctica), which is equivalent to the land heat uptake (lines, ZJ), is also plotted. Dotted vertical bars portray the warming levels in (a).

5.1.4 GHF and SEB under increasing levels of warming

In order to more clearly depict the global mean and spatial intensity of the response of the GHF and SEB to different BBCP depths, warming levels are used in this work. Five warming levels were defined herein as the first year when the 11-year moving average global mean SAT anomaly with respect to 1850–1900 reached 1, 1.5, 2, 3, and 4 °C. This approach is commonly followed in the IPCC ARs, specially since the Special Report on 1.5 °C (Masson-Delmotte et al., 2018), for methodological and policy-relevant reasons. On the one hand, adopting a warming-level-based framework rather than a scenario-based one facilitates the comparison between ESMs with different climate sensitivities, and the compari-

son between scenarios (Evin et al., 2024). Moreover, many phenomena related to climate tipping points or ecological persistence thresholds depend on the magnitude of the warming and not in the timing (e.g., Schleussner et al., 2016). On the other hand, warming levels are directly aligned with international climate targets (i.e., Paris Agreement), making impact assessments and adaptation plans more accessible for policymakers (Zommers et al., 2020).

5.2 Results

5.2.1 Impact of the BBCP on the simulated GHF

Figure 5.1a illustrates the time evolution of the global mean SAT and over-land mean SAT and GST for the eight land-only JSBACH simulations (Section 5.1.1). Since SAT is an atmospheric variable, it serves as a boundary condition imposed to JSBACH. Hence, SAT is the same for the eight simulations. JSBACH must comply with the land-atmosphere coupling at the ground surface, so only minimal variations of GST are to be expected. That is portrayed by the different color lines in Fig. 5.1a, which overlap throughout the experiment (1850–2100). Indeed, the ensemble standard deviation of the eight global mean GSTs at yearly resolution (not shown) peaks at 2.27 x 10^{-3} K in 1975, which is two orders of magnitude lower than the average GST variability (0.26 K) in the individual experiments. Thus, GST can be considered as virtually equal for the eight simulations, independent of the BBCP depth. Figure 5.1a also reveals a very close agreement between over-land GSTs and SAT, which evidences the existence of a long-term SAT–GST coupling (see Sections 1.4 and 4.2.1). Both over-land SAT and GST means are greater than global mean SAT, which encompasses the weaker ocean warming. The JSBACH global mean SAT is used in this work to define warming levels of 1, 1.5, 2, 3, and 4 °C, which coincide with years 2001, 2016, 2037, 2063, and 2082, respectively (see grey points in Fig. 5.1a).

The global mean continental GHF and land heat uptake for the eight JSBACH standalone simulations are shown in Figure 5.1b. Glacial areas (Antarctica and Greenland) were excluded from the calculations, as in previous works addressing these quantities (Cuesta-Valero et al., 2016, 2021a; García-Pereira et al., 2024b). Land heat uptake here is calculated as the time cumulative sum of global mean GHF values. It can be seen that the accelerated increase in GST, which starts in the 1970s (Fig. 5.1a), results in an increasing negative (downward) GHF. However, the intensity of this magnitude is clearly dependent on the BBCP depth. For the JSBACH five-layer simulation (JSBACH_{5L}), with a BBCP imposed at

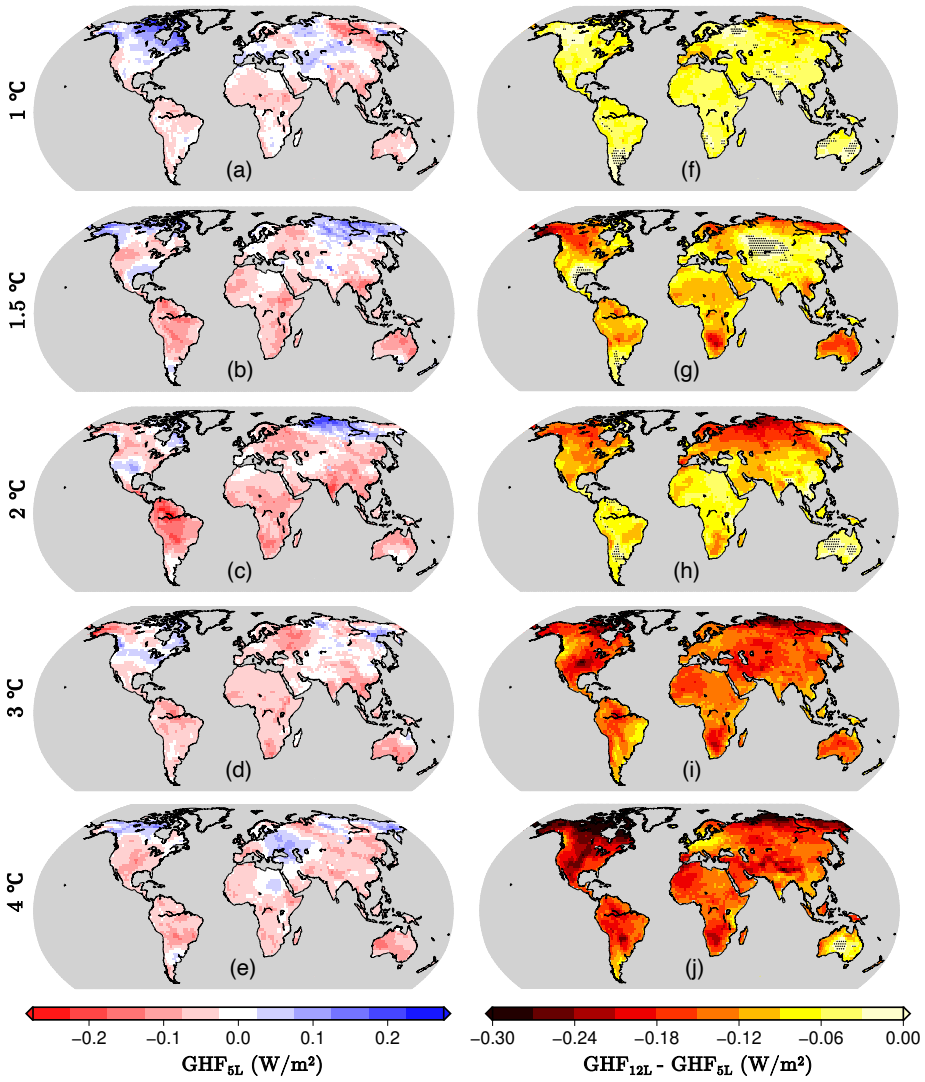

Figure 5.2: GHF values for JSBACH$_{5L}$ (a-e) and GHF JSBACH$_{12L}$ - JSBACH$_{5L}$ differences (f-j) at warming levels of 1 (a,f), 1.5 (b,g), 2 (c,h), 3 (d,i), and 4 ^{o}C (e,j) with respect to 1850–1900 (Section 5.1.4). Reddish (blueish) colors in (a-e) indicate incoming (outgoing) GHF, and darker colors in (f-j) more intense incoming GHF. Stippling in f-j indicate non-significant differences ($p < 0.05$).

9.8 m, the downward GHF saturates at a value of about -0.04 W/m^2, with GHF values of -0.01, -0.03, -0.06, -0.04, -0.04 at warming levels of 1, 1.5, 2, 3, and 4 °C with respect to 1850–1900 (Section 5.1.4), respectively. This saturation results in a positive but small land heat uptake of 13.3 ZJ since the minimum at 1970 until 2100. Just doubling the BBCP depth to 21.6 m by adding an extra layer (JSBACH$_{6L}$) partially prevents the GHF from saturating and increases its values to -0.03, -0.07, -0.08, -0.09, -0.10 W/m^2, scaling up land heat uptake by a factor of 2.5 to 34.1 ZJ in 1971–2100. Both the global mean GHF and land heat uptake increase progressively with BBCP deepening, saturating for JSBACH$_{9L}$ simulation, which features a BBCP depth of 183.7 m. For this simulation and the deeper ones (JSBACH$_{10L,11L,12L}$), GHF values reach -0.07, -0.11, -0.14, -0.18, -0.21 W/m^2 and land heat uptake 70.7 ZJ. This coincides with results by González-Rouco et al. (2021), which observed a saturation of the annual heat content change, i.e., the global mean land heat uptake by unit of area and year, for JSBACH$_{9L}$. This means that deepening the BBCP by an order of magnitude, from 10 to 100 m, implies scaling GHF and land heat uptake by a factor of five. Furthermore, it is worth noting the remarkable response to the sharp cooling associated to Krakatoa (1883, Self and Rampino, 1981) and Santa María (1902, Berry et al., 2021) volcanic events in the form of positive (i.e., upwards) GHF values. In these two cases GHF values are quite similar for the eight simulations, of approximately 0.07 and 0.04 W/m^2, respectively, which might be related to the high-frequency nature of this kind of events. Since temperature signals of a few years only penetrate around 20 to 30 m, according to the heat conduction law (see Section 1.4, Carslaw and Jaeger, 1959; Smerdon and Stieglitz, 2006), biases in their amplitude attenuation with depth due to the BBCP are much less noticeable. The industrial era land heat uptake estimates derived here by performing a cumulative sum of global mean GHF are consistent with estimates by García-Pereira et al. (2024b), which reported values of 14.9 and 62.6 ZJ in 1970–2100 for the P2k+ simulations with the 5- and the 12-layer JSBACH schemes, respectively (Figure 4.2, Section 4.2.1).

GHF global patterns for JSBACH$_{5L}$ and GHF differences between JSBACH$_{12L}$ and JSBACH$_{5L}$ at different warming levels (Section 5.1.4) are given in Fig. 5.2. As warming intensifies, negative (i.e., downward) GHF values dominate over positive values for JSBACH$_{5L}$. However, for a warming level of 4 °C (Fig. 5.2e), there are still some areas (e.g., northern North America, eastern Europe, and northern Siberia) showing positive GHF values. Overall, negative GHF values are small, rarely reaching -0.2 W/m^2 in absolute terms. Moreover, regional patterns are not spatially consistent at different warming levels. For instance, it can be seen that positive GHF areas for a warming level of 4 °C do not fully coincide with regions showing positive values under 2 °C (Fig. 5.2c) or 3 °C (Fig. 5.2d) warm-

ings. This suggests that the GHF signal in shallow LSM simulations is dominated by internal variability, as the very limited BBCP depth severely constrains the heat downward propagation, compromising the representation of long-term GHF trends.

The constrained GHF for $JSBACH_{5L}$ is more evident when evaluating the GHF $JSBACH_{12L}$ - $JSBACH_{5L}$ difference values. Figure 5.2f-j depict these differences at warming levels of 1, 1.5, 2, 3, and 4 °C. For a warming level of 1 °C, the deep LSM configuration shows an overall significant change in the GHF of approximately -0.06 W/m^2, with NH high latitudes showing greater differences, up to -0.15 W/m^2. $JSBACH_{12L}$ - $JSBACH_{5L}$ GHF difference values consistently grow with warming, with slight regional variations likely due to differences in internal variability between $JSBACH_{5L}$ and $JSBACH_{12L}$. At a 4 °C warming level (Fig. 5.2j), the GHF $JSBACH_{12L}$ - $JSBACH_{5L}$ differences are widespread and significant (except for Australia), with a global mean value of around -0.17 W/m^2. Moreover, it can be observed that these differences are much higher in the NH high latitude regions, ranging from -0.25 to -0.4 W/m^2. This is attributable to higher positive GST anomalies there due to Arctic amplification (Rantanen et al., 2022). In conclusion, there is a significant impact of BBCP depth on increasing downward GHF with global warming, which becomes more remarkable at higher warming levels.

5.2.2 Comparison of JSBACH simulated and forward modeled GHF estimates

Figure 5.3a portrays GHF as a function of BBCP depth. Punctual estimates stemming from the standalone JSBACH simulations at different warming levels in Fig. 5.1b are depicted by solid points, whilst continuous solid lines are derived by driving ConForM with the JSBACH ensemble mean GST as the top boundary condition for different BBCP depths. To properly account for the different values of thermal parameters of the five soil types defined by JSBACH (Section 2.2.1, Table 2.4), five estimates of GHF were calculated using the GST means and parameter values over the different soil type areas. These estimates were subsequently averaged to yield the final results shown in Fig. 5.3. The analysis of GHF with ConForM allows for having a continuous picture of its increase with BBCP depth at a low computational cost. The GHF dependence on BBCP could also be studied using JSBACH standalone simulations. However, JSBACH simulations are more computationally demanding (higher dimensionality and more

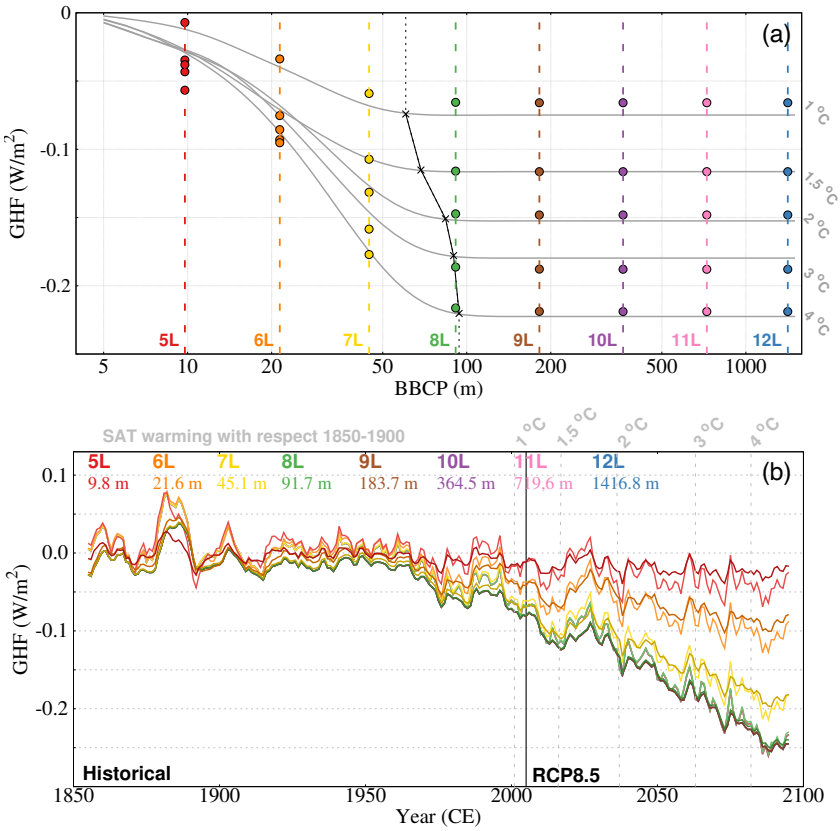

Figure 5.3: (a) Global mean GHF (W/m^2) as a function of BBCP (log axis, m) at different warming levels (Fig. 5.1a, see Section 5.1.4). The dots depict the GHF values stemming from the JSBACH simulations and the curves the GHF dependence on the BBCP depth computed by a limited one-dimensional heat conduction model using JSBACH GST data. The black line indicates the BBCP depth at which the GHF is 99 % the saturation value. (b) 11-year moving average GHF values for the different members of the JSBACH ensemble (clear) and computed using the ConForM forward model (dark lines, see legend for colors).

processes resolved) and the number of simulations required would be very large, making this strategy less effective.

There is a good agreement between the JSBACH global mean GHF values and the ConForM estimates for JSBACH$_{7L}$ to JSBACH$_{12L}$, i.e., for BBCP depth values greater than 40 m, both at different warming levels (Fig. 5.3a), and with time (Fig. 5.3b). However, ConForM slightly underestimates GHF values yielded

by JSBACH_{5L} and JSBACH_{6L} at high warming levels (from 2 °C upwards). This underestimation might stem from the fact that ConForM shows smaller long-term trends of JSBACH_{5L} and JSBACH_{6L} GHF values (dark red and orange lines in Fig. 5.3b, respectively). Even so, the overall increase in GHF with BBCP depth and posterior saturation is correctly captured by ConForM, with these saturation values being 0.07, 0.12, 0.15, 0.18, 0.22 W/m^2 at warming levels of 1, 1.5, 2, 3, and 4 °C, respectively. This dependence of GHF on the BBCP is also evidenced by the depth at which the GHF is 99 % of the saturation value (Fig. 5.3a). This threshold grows with warming, increasing from 60.4 m at a warming level of 1 °C to 93.8 m at 4 °C.

The close agreement between JSBACH GHF values and those estimated by ConForM (driven by JSBACH GSTs) confirms that the too small GHF in shallow LSMs is fundamentally due to insufficient BBCP depth, which limits subsurface heat propagation. Moreover, the increase of GHF with BBCP depth portrayed by both JSBACH and ConForM evidences, for the first time, that modifying the LSM thermal depth directly affects the SEB. This perspective adds a new dimension to existing studies that highlight the influence of insufficient BBCP depths in ESMs on subsurface temperature error (Alexeev et al., 2007; González-Rouco et al., 2021; Steinert et al., 2021a) and land heat uptake (Cuesta-Valero et al., 2016; García-Pereira et al., 2024b; Steinert et al., 2024).

5.2.3 Impacts of GHF biases on the SEB for different surface hydroclimates

In the closed system simulated by a LSM in standalone mode, a bias in the GHF due to the prescription of a shallow BBCP should produce a reconfiguration of the turbulent heat fluxes, i.e., the SHF and LHF, and the net radiation (Section 5.1.3). How the energy is redistributed will depend on the temperature and water availability of the surface. The BR_{mod} is a metric of the surface hydroclimate, and allows for classifying different areas of the globe as EW, SW, SD, or ED (see Section 5.1.3). Figure 5.4a shows the results of this classification for the JSBACH_{5L} mean state in 1850–1900. EW regions are mostly located in the eastern continental areas of the NH, Europe, and across the equatorial band, ED across the biggest terrestrial deserts at mid-latitudes of both hemispheres, and SW and SD at mid- and high-latitudes subtropical and temperate climate areas.

Figure 5.4b shows the mean SHF, LHF, R_N, and GHF values for JSBACH_{5L} in 1850–1900 grouped by the BR_{mod} shown in Fig. 5.4a. EW areas simultaneously depict the smallest SHF and the largest LHF values, with median regional SHF

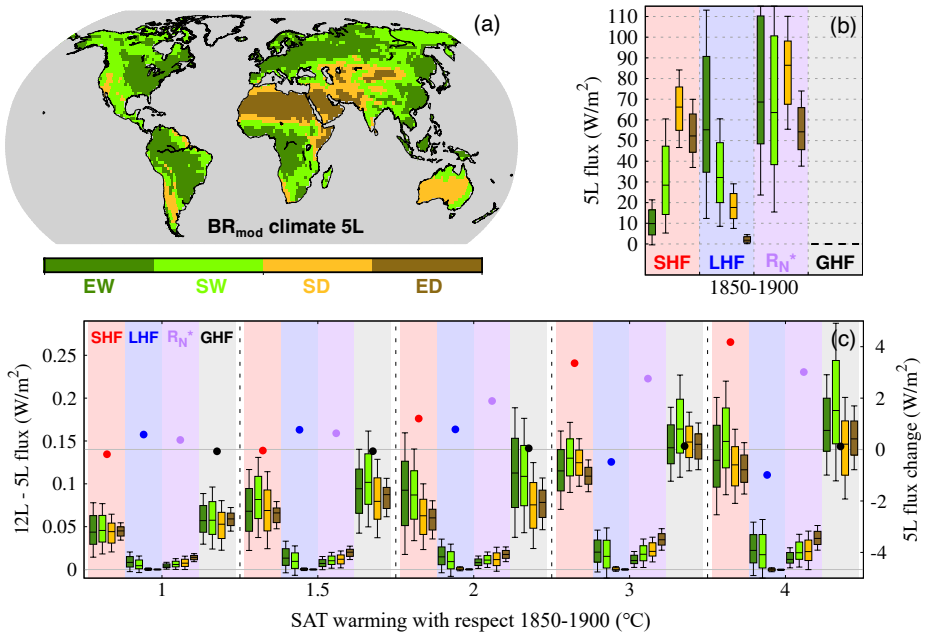

Figure 5.4: (a) Surface hydroclimate classification according to BR_{mod} values (see Section 5.1.3) for $JSBACH_{5L}$ in 1850–1900 (b) SHF (boxplots over light red shading), LHF (light blue), R_N (light purple), and GHF (light grey) values for the different hydroclimate types in (a). The inner ticks in the boxplots mark the median value, the bottom and top lines quartiles 1 and 3, and the bottom and top whiskers percentiles 10 and 90, respectively. Positive (negative) values indicate upward (downward) fluxes, except for R_N, which is inverted for better visualization (marked *). (c) $JSBACH_{12L}$ - $JSBACH_{5L}$ SHF, LHF, R_N, and GHF differences for the various surface hydroclimates in (a) and warming levels (Section 5.1.4, boxplots, left y-axis), and $JSBACH_{5L}$ SHF, LHF, R_N, and GHF changes at the same warming levels (dots, right y-axis). For a better visualization, both $JSBACH_{12L}$ - $JSBACH_{5L}$ and $JSBACH_{5L}$ GHF change signs are inverted (i.e., positive anomalies mean more downward flux).

and LHF of 10 and 55 W/m^2, respectively. However, the variability is much larger for the LHF than for the SHF, with interquartile ranges of 56 and 12 W/m^2. This is the result of the large GST differences across the EW domain (Fig. 5.4a), which encompasses a wide latitudinal range. As LHF is a direct function of temperature, extra-tropical (approx. 50 W/m^2) are much lower than the inter-tropical (approx. 100 W/m^2) LHF values. SW shows larger median and interquartile values of SHF, with 29 and 33 W/m^2, and much smaller LHFs, being 32 and 29 W/m^2, respectively. SHF is the greatest for SD areas, reaching higher values than for

the ED domain (66 vs. 52 W/m^2, respectively). LHF is much lower for these two domains than for EW and SW, being almost null for ED areas. For all the different surface hydroclimates, pre-industrial GHF for JSBACH$_{5L}$ is very close to 0, as already shown in Figs. 5.1b and 5.3. The sum of the outgoing SHF and LHF, and incoming GHF is balanced out by the incoming R_N, which ranges from 10 to 160 W/m^2 globally (not shown). These large variations are mostly explained by the reduction in the incoming solar radiation with latitude. However, albedo also plays a significant role. This is well depicted by relatively small values of the R_N in ED areas (Fig. 5.4b), which are mostly deserts located in the low latitudes of the NH. Likewise to the behavior shown by EW and SW areas for the LHF, the R_N shows a great range of variability, associated again to the wide latitudinal range covered by these surface hydroclimates.

The pre-industrial surface fluxes change with warming, as depicted by Fig. 5.4c, which represents the global mean SHF, LHF, R_N, and GHF variations for the JSBACH$_{5L}$ at different warming levels. The global mean SHF, LHF, R_N, and GHF change by 4.18, -0.99, 3.01, and 0.04 W/m^2 at a warming level of 4 °C, respectively. These values differ when deepening the BBCP to comply with Eq. 5.4 (see Section 5.1.3). This is illustrated by the partition of the positive JSBACH$_{12L}$ - JSBACH$_{5L}$ GHF difference into SHF, LHF, and R_N for the different BR$_{mod}$ regions (Fig. 5.4a). As it was already portrayed in Fig. 5.2f-j, the JSBACH$_{12L}$ - JSBACH$_{5L}$ GHF differences increase with warming, affecting all surface hydroclimate regions. However, these differences are greater for wet than for dry areas. This is because the NH high latitudes, which show higher JSBACH$_{12L}$ - JSBACH$_{5L}$ GHF differences (Fig 5.2f-j), have predominantly EW and SW hydroclimates. Overall, the incoming JSBACH$_{12L}$ - JSBACH$_{5L}$ GHF gain is mainly balanced out by an increase in the outgoing SHF. This is particularly remarkable for SD and ED regions, where LHF changes are extremely low. For instance, at warming levels of 2 and 4 °C, median GHF differences of 0.08 and 0.15 W/m^2 across the SD domain produce SHF changes of 0.07 and 0.12 W/m^2, but LHF changes of less than 10^{-3} W/m^2. In EW and SW regions, a small share of the GHF bias is compensated by changes in the outgoing LHF. For instance, a median GHF JSBACH$_{12L}$ - JSBACH$_{5L}$ gain of 0.16 W/m^2 for a warming level of 4 °C in the EW domain is partitioned in SHF and LHF changes of 0.13 and 0.02 W/m^2, respectively. The sum of LHF and SHF differences associated to BBCP depth compensate much of the GHF bias in wet areas, but not so in dry regions. This is explained by notable variations of the R_N in ED and SD regions with warming, reaching values that are greater than LHF changes in SW and EW areas for the highest levels of warming, e.g., R_N changes by 0.04 W/m^2 across the ED domain for a 4 °C warming. Once the contribution of the changes in R_N is accounted for, the SEB determined by Eq. 5.4 is fully closed. This arguably

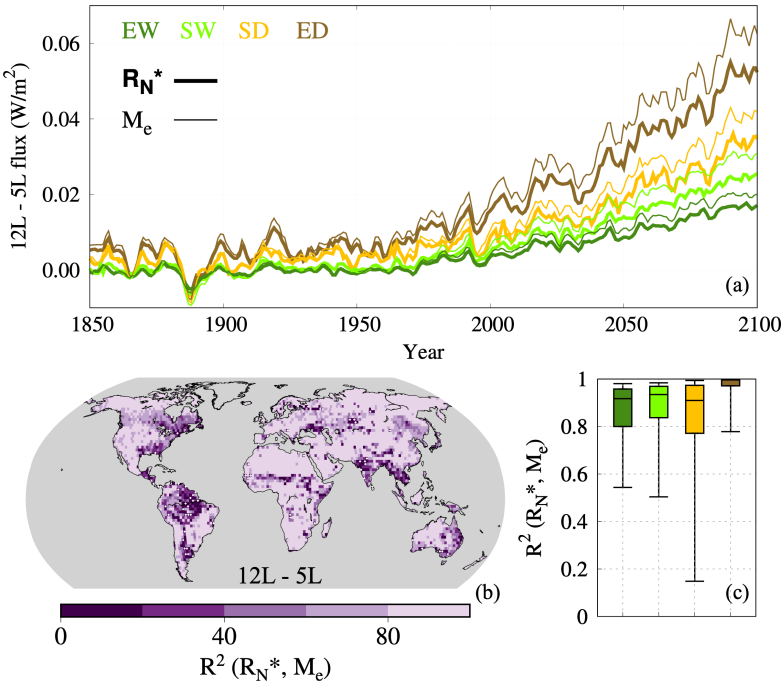

Figure 5.5: (a) Mean evolution of R_N (thick) and M_e (thin lines) $JSBACH_{12L}$ - $JSBACH_{5L}$ differences (in W/m^2) for the different surface hydroclimates in Fig. 5.4a. (b) Explained variance (R^2, in %) of R_N vs. M_e $JSBACH_{12L}$ - $JSBACH_{5L}$ differences in 1850–2100. Lighter purple tones indicate higher R^2 values. White stippling indicates non-significant R^2 values ($p>0.05$) (c) R^2 values shown in (b) grouped by surface hydroclimate types. The inner ticks in the boxplots mark the median value, the bottom and top lines quartiles 1 and 3, and the bottom and top whiskers percentiles 10 and 90, respectively.

demonstrates there exists a clear effect of the BBCP depth on reshaping the SEB, even if flux changes are small. Figure 5.4c also illustrates that the extent and distribution of the $JSBACH_{12L}$ - $JSBACH_{5L}$ GHF bias into LHF, SHF, and R_N changes depend on the surface hydroclimate, which is mainly determined by the surface wetness.

Figure 5.4c shows that GHF variations due to changes in the BBCP depth are fully compensated by a response of the SHF, LHF, and R_N terms of the SEB, which entails that GST does not vary with BBCP depth (i.e., $hC_v\ \partial GST/\partial t$ in Eq. 5.4 remains constant when changing the BBCP depth). This source of evidence complements previous results reporting no GST differences associated

with BBCP depth (e.g., González-Rouco et al., 2021; García-Pereira et al., 2024b) from a SEB perspective. Nevertheless, in the closed system represented by an offline LSM, fed by boundary conditions coming from an external atmosphere and biosphere, it is striking that net radiation can change while GST does not. Figure 5.5 illustrates the mechanism behind of R_N changes shown in Fig. 5.4c. As it is depicted by Fig. 5.5a, JSBACH$_1$2L - JSBACH$_5L$ R_N changes are significantly correlated with radiant exitance (M_e) variations:

$$M_e = \sigma \eta T^4, \tag{5.6}$$

with σ being the Stefan–Boltzmann constant and η the emissivity, and which scales with the GST to the power of four. M_e increase is especially prominent in SD and ED areas, which explains that R_N variations are stronger in these areas (Fig. 5.4c). In fact, the areas where M_e explains the highest R_N variance (Fig. 5.5b) coincide with the largest desert areas of the NH subtropics and mid-latitudes, which are fully encompassed by the ED hydroclimate type (Fig. 5.4a). Even though the ED areas show the largest R^2, there is a high and significant ($p < 0.05$) correlation for all hydroclimate types, with median values exceeding 0.9 in every case (Fig. 5.5c). Only small areas in the Amazon basin and the Deccan Plateau show low non-significant R^2 values (Fig. 5.5b). Since changes in M_e scale with the fourth power of GST, even small differences between GSTs simulated by JSBACH$_{12L}$ and JSBACH$_{5L}$ can lead to substantial changes in M_e. Although these temperature differences are minimal (no more than 0.02 K in some regions of the Gobi Desert, not shown), they are sufficient to cause noticeable variations in M_e, and thus in R_N. This highlights that, despite long-term GST differences due to BBCP deepening being statistically non-significant and indistinguishable from internal variability (see Sections 4.2.1 and 5.2.1), they can still lead to detectable changes in R_N, ultimately influencing the SEB.

5.3 Conclusions

The current generation of ESMs impose shallow zero-flux BBCP depths when resolving the downward thermal propagation of GST within their LSMs. This has the double effect of constraining land heat uptake and reducing temperature variability attenuation with depth, with impacts on thermally-driven processes, e.g., permafrost thawing, and on the terrestrial energy budget. Nevertheless, no differences in the GST produced by the BBCP depth were established in the literature. This work demonstrates that changing the BBCP depth modifies the GHF at the ground surface. To reach this conclusion, we use an ensemble of

land-only historical + RCP8.5 scenario (1850–2100) simulations performed with the LSM of the MPI-ESM, JSBACH, imposing different values of the BBCP depth (González-Rouco et al., 2021). The results show that $JSBACH_{5L}$ (9.8 m) saturates at very small values of the GHF (-0.04 W/m^2), being uncapable of correctly representing the increase in GHF due to the increasing warming under the RCP8.5 scenario. Just doubling the BBCP depth ($JSBACH_{6L}$, 21.6 m) is enough to avoid the GHF saturation and represent a progressive increase up to about -0.1 W/m^2. This number grows with BBCP depth up to $JSBACH_{9L}$ (183.7 m), which yields maximum GHF values of approx. -0.25 W/m^2. Hence, deepening the LSM by one order of magnitude scales the GHF by a factor of 5. This progressive increase in GHF with BBCP depth results in a higher land heat uptake, with values of 13.3, 34.1, and 70.7 ZJ in 1971-2100 for $JSBACH_{5L}$, $JSBACH_{6L}$, $JSBACH_{9,10,11,12L}$, respectively. This evidences that the insufficient land heat uptake estimated from ESMs is produced by a constrained GHF. The spatial patterns of GHF differences between the deepest ($JSBACH_{12L}$) and the shallowest ($JSBACH_{5L}$) simulations portray a progressive GHF bias at increasingly high warming levels with respect to 1850–1900.

To explore the progressive increase of GHF with BBCP depth, GHF estimates are derived using a simple one-dimensional heat conduction forward model (ConForM, Garcia-Pereira and González-Rouco, 2024) forced by the mean GST of the JSBACH simulations. Both estimates of the dependence of GHF on BBCP depth at different warming levels and the reconstruction of JSBACH GHF time series using ConForM overall coincide with the results from the JSBACH simulations, which indicates that the relationship between GHF and BBCP depth is robust. Moreover, it also strengthens the statement made by García-Pereira et al. (2024b) that one-dimensional heat conduction forward models can be used to correct biased subsurface thermal structures resolved by shallow ESMs.

Finally, the capability of GHF changes at reshaping the SEB, namely modifying SHF, LHF, and R_N, is explored for different surface hydroclimates. Results show that $JSBACH_{12L}$ - $JSBACH_{5L}$ GHF differences are mainly compensated by changes in the SHF. LHF contributes to balance GHF changes only in wet areas of the globe. By contrast, dry areas show an increase in the R_N that explains the mismatch between GHF and SHF $JSBACH_{12L}$ - $JSBACH_{5L}$ differences. This unexpected change in the R_N is mainly produced by changes in the M_e, which grows with GST to the power of four. Hence, very small GST variations of around 0.01 K between $JSBACH_{5L}$ and $JSBACH_{12L}$ in dry areas, yet non distinguishable from differences in the internal variability, modify the net radiation by 0.05 W/m^2. The biases in the SEB are robust and increase with warming, but they are overall small (< 0.2 W/m^2).

Chapter 6
Permafrost sensitivity to changes in soil hydro-thermodynamics*

Chapters 4 and 5 explored the thermodynamic and surface energy balance responses of LSMs within ESMs to changes in BBCP depth. A clear connection was established between BBCP depth and biases in land heat uptake, GHF, and surface turbulent fluxes under global warming. However, prescribing an insufficiently deep BBCP is not the only shortcoming of current LSMs. The interaction between hydrology and thermodynamics remains limitedly represented in most state-of-the-art models, particularly regarding vertical resolution and hydro-thermodynamic coupling. This weakness is especially critical for correctly representing permafrost degradation (Section 1.7), as rising temperatures and shifts in water availability driven by changes in atmospheric circulation significantly affect permafrost moisture and ice contents, and thermal structure.

This chapter explores the response of the MPI-ESM to changes in the hydrological and thermodynamic features in permafrost regions of its LSM, JSBACH. For that purpose, an ensemble of fully-coupled historical and future scenario simulations, the MPIESM-PePE, was performed, varying the subsurface vertical discretization and depth under different configurations that generate rather "dry" or "wet" soil water-table conditions across permafrost areas. The model version and ensemble of experiments is described in Section 2.2.2. The impact of these changes on permafrost temperature variability (Sections 6.1.1, 6.2.1), and ALT (Section 6.1.2 and 6.2.2), and PE (Section 6.1.3, 6.2.3, and 6.2.4) is assessed. The results of this chapter highlight the importance of refining hydrological and thermodynamic processes in ESMs to improve projections of permafrost responses under climate change scenarios.

* The main contents of the chapter are included in a manuscript under review:
García-Pereira, F., J. F. González-Rouco, N. Meabe-Yanguas, P. de Vrese, N. J. Steinert, J. Jungclaus, S. Lorenz, 2025: Permafrost sensitivity to changes in soil hydro-thermodynamics in historical and scenario simulations with a modified version of the MPI-ESM. *The Cryopshere* [preprint], DOI: 10.5194/egusphere-2025-2126.

6.1 Methods

6.1.1 Permafrost temperature variability

Surface and subsurface permafrost temperature variability is characterized by the mean annual air temperature at 2 m (MAAT), mean annual ground surface temperature (MAGST), which is here considered as the near-surface temperature at a depth of 0.1 m, and mean annual subsurface temperature at a depth of 5 m (MAST 5 m). The MAGST value is taken at 0.1 m depth for two reasons: to state a common depth for comparison between the 5L, 11L and 18L simulations, which have different mid-layer depths from layer 2 downwards (Table 2.7); and to fully account for the change in soil properties when there exists a snow cover. The latter is due to the fact that JSBACH considers that snow gradually replaces the top layers of the soil when calculating the heat capacity and thermal diffusivity (Reick et al., 2021), thus modifying near-surface heat transfer and temperature variability.

To address the temporal and spatial evolutions of MAAT, MAGST, and MAST 5 m, regional boxplots describing the distribution of these variables over the permafrost domain (Fig. 2.6a) are used for all the members of the MPIESM-PePE in different periods. Furthermore, to assess the insulation effects of the refined multiple-layer snow scheme and organic layer introduced by Ekici et al. (2014), the winter and summer temperature offsets are assessed, respectively. In this paper, the winter (summer) offset is computed as the ground surface temperature at 0.1 m depth (GST) vs. surface air temperature (SAT) differences (GST-SAT) in DJF (JJA), following a similar approach to Burke et al. (2020).

6.1.2 Active layer thickness (ALT)

ALT is defined as the annual maximum thaw depth, which in the NH high latitudes occurs in summer. This variable is computed by JSBACH as the annual maximum subsurface depth where the temperature exceeds the water freezing/melting point, i.e., 273.15 K. In case this depth does not specifically match a certain mid-layer depth value, JSBACH yields ALT using linear interpolation. To evaluate the temporal and regional variability of ALT, the same type of boxplot analysis as described for MAAT, MAGST, and MAST 5 m in Section 2.2.2 was used.

Furthermore, regional deepening of the ALT with industrial warming in the MPIESM-PePE is also assessed by computing the fraction of gridcells within the

initial permafrost domain (Fig. 2.6a) that have an ALT below a certain depth. This approach yields vertical profiles with values ranging from 0 (no gridcells) to 1 (all gridcells comply with the condition ALT $<$ depth). As a result of permafrost thaw and subsequent ALT deepening with warming, this profile is expected to displace leftwards, i.e., values become closer to 0; the opposite happens under permafrost formation with cooling conditions. Finally, near-surface and deep permafrost degradation is evaluated in terms of ALT deepening assessing the time evolution of maps with gridcells having an ALT above 3 m and ALT equal to the bottom mid-layer depth, respectively.

6.1.3 Permafrost extent (PE)

Permafrost is defined as the ground that remains perennially frozen for two or more consecutive years (Obu et al., 2019). However, there is a wide variety of metrics to evaluate whether the soil is frozen or not and subsequently determine PE based on different criteria that consider soil thermodynamics, hydrology, or soil coupling to the atmosphere (Steinert et al., 2023). Air-ground temperature coupling and some of the thermodynamic-based definitions capture near-surface PE variations, whilst others represent long-term deep PE changes. Hence, as the diverse definitions of PE target different aspects of permafrost physics, they can yield considerably different estimates. The PE differences between the different definitions are even larger than the inter-model variability of the CMIP6 ensemble (Steinert et al., 2023).

Since the WET and DRY configurations represent extreme states of the hydrological cycle in the permafrost domain, encompassing a substantial portion of the uncertainty range within the ensemble of state-of-the-art Earth System Models (de Vrese et al., 2023), it is of interest to assess whether they also capture the range of variability in PE responses. To address this question trying to minimize the uncertainty associated with the PE definition selection, the PE evolution for the 9 historical + SSP5-8.5 simulations of the MPIESM-PePE is estimated using two of these metrics: i) TTOP, which defines permafrost based on soil temperatures at the top of the permafrost layer being below 0 ^{o}C (Obu et al., 2019); and ii) ZAA, which considers permafrost existence when the temperature at the depth of zero annual amplitude is below freezing. TTOP has proven to be a comparatively better indicator of surface permafrost presence (Obu et al., 2019; Steinert et al., 2023), while ZAA is a more appropriate descriptor of deep permafrost occurrence than TTOP (Slater and Lawrence, 2013; Burke et al., 2020). The zero annual amplitude layer, defined as the subsurface layer where the annual

temperature varies less than 0.1 °C, is generally located below 15 m, depending on the thermal diffusivity and the annual GST amplitude of the site (Alexeev et al., 2007; Cermak et al., 2014; Burke et al., 2020; García-Pereira et al., 2024a). Therefore, as the 5L and 11L subsurface temperature bottom layers lie above this depth (at 6.98 and 7.86 m, respectively; Table 2.7), the ground temperatures at the deepest layer for 5L, and 11L, and at layer 11 for the 18L configuration are selected. To achieve a close-to-zero degree amplitude, the remaining annual cycle at these depths is filtered out by subtracting the annual cycle of monthly mean anomalies for 1850–1900. Subsequently, permafrost detection using ZAA is applied to the data.

The results for the MPIESM-PePE are compared with the ZAA and TTOP PE estimates stemming from Steinert et al. (2023) for an ensemble of 34 CMIP6 HIS and SSP5-8.5 experiments. Also, observations provided by the Permafrost Climate Research Data Package version 3 of the European Space Agency Climate Change Initiative database (ESApCCIv3) are used. ESApCCIv3 delivers mid- to high-latitude NH (north of 30°) gridded data of permafrost temperature and presence at yearly resolution for the period 1997–2018. The database is generated by using the CryoGrid permafrost model (Westermann et al., 2023) driven and constrained by satellite and reanalysis land surface temperature data. ESApCCIv3 is computed using ensemble modeling procedures to enhance accuracy and provide estimates of uncertainty (see Obu et al., 2021). In this study, permafrost temperatures at multiple depths from ESApCCIv3 within the mask in Fig. 2.6a are used to estimate the temperature at the top of the permafrost layer, from which the TTOP PE is derived. For the ZAA PE, the annual mean temperature at a depth of 10 m is assumed to represent the zero annual amplitude layer and is used to compute the corresponding PE.

6.2 Results and discussion

6.2.1 Temperature variability

The surface and subsurface temperature variability across the permafrost region (Fig. 2.6a) in the MPIESM-PePE is shown in Fig. 6.1. The median regional values for MAAT, MAGST, and MAST 5 m for the permafrost domain (Fig. 6.1a) remain stable during the PIC period for all simulations except 5-layer WET (hereafter WET5) and 11-layer WET (WET11), which start from warmer initial conditions that gradually converge toward the colder state of the 18-layer simulation (WET18) by the end of the PIC. Note that the 5L and 11L simulations

have a PIC duration of 50 years, whereas the 18L simulations are first equilibrated using a 100-year-long prePIC simulation and incorporating subsurface temperature corrections (Section 2.2.2). This strategy guarantees the departure from vertically uniform initial conditions for temperature at the beginning of the PIC and stable PIC temperatures for the deepest layers (not shown). For the near-surface temperatures, 18L simulations also show a stable PIC evolution and transition from the PIC to the HIS period. The thermal state established during the PIC period for all the simulations remains largely unchanged until the second half of the 20th century, when global warming begins to intensify. Consequently, the early-historical (1850–1900) period serves as a reliable representation of the pre-industrial thermal conditions, and the late historical (1995–2014), mid-21st century (2041–2060), and late 21st century (2081–2100) conveniently represent the progressive temperature increase and subsequent warming standstill (SSP1-1.9), stabilization (SSP2-4.5), or acceleration (SSP5-8.5) depending on the SSP scenario (Fig. 6.1a).

Early-historical temperature differences between WET and DRY simulations are of about 3 °C for the permafrost median regional MAAT (Fig. 6.1b), MAGST (Fig. 6.1d), and MAST 5 m (Fig. 6.1f) values. This agrees with previous results by de Vrese et al. (2023), who stated that WET permafrost soils lead to higher latent and sensible heat fluxes than DRY, enhancing evapotranspiration and subsequently increasing Arctic cloud cover. This, in turn, reduces the incoming solar radiation, resulting in colder temperatures for WET than DRY. Thus, the DRY configuration depicts the warmest state, with regional medians (10th, 90th percentile) for MAAT of -6.0 (-11.2, 0.0) °C; for MAGST of -3.5 (-9.4, 2.4) °C; and for MAST 5 m of -3.9 (-9.9, 2.3) °C. The WET simulations show colder MAATs than REF, with a permafrost median (10th, 90th percentile) MAAT of -9.3 (-14.9, -2.4) °C for WET vs. -8.0 (-13.7, -0.7) °C for REF. However, these differences are reversed within the soil, with WET MAGST and MAST 5 m being on average 1.4 and 0.3 °C warmer than REF, respectively. This is due to the enhanced snow insulation effect in winter in the WET and DRY simulations, as a result of the multi-layer snow scheme that superseded the more simplistic single-bucket scheme included in REF (see Section 2.2.2). Temperature differences between the 5L, 11L, and 18L vertical schemes are at most around 0.4 °C. Therefore, there is a noticeable effect of changing the hydrological state with the DRY/WET configurations but no evidence of the vertical discretization affecting surface regional temperature variability, as reported in previous studies with the MPI-ESM by González-Rouco et al. (2021), and García-Pereira et al. (2024b).

The warming increases during the late historical period to reach regional median MAATs 1.3–2.2 °C higher than in the early historical (Fig. 6.1b), depending on the MPIESM-PePE member. Overall, the temperature increase for MAAT,

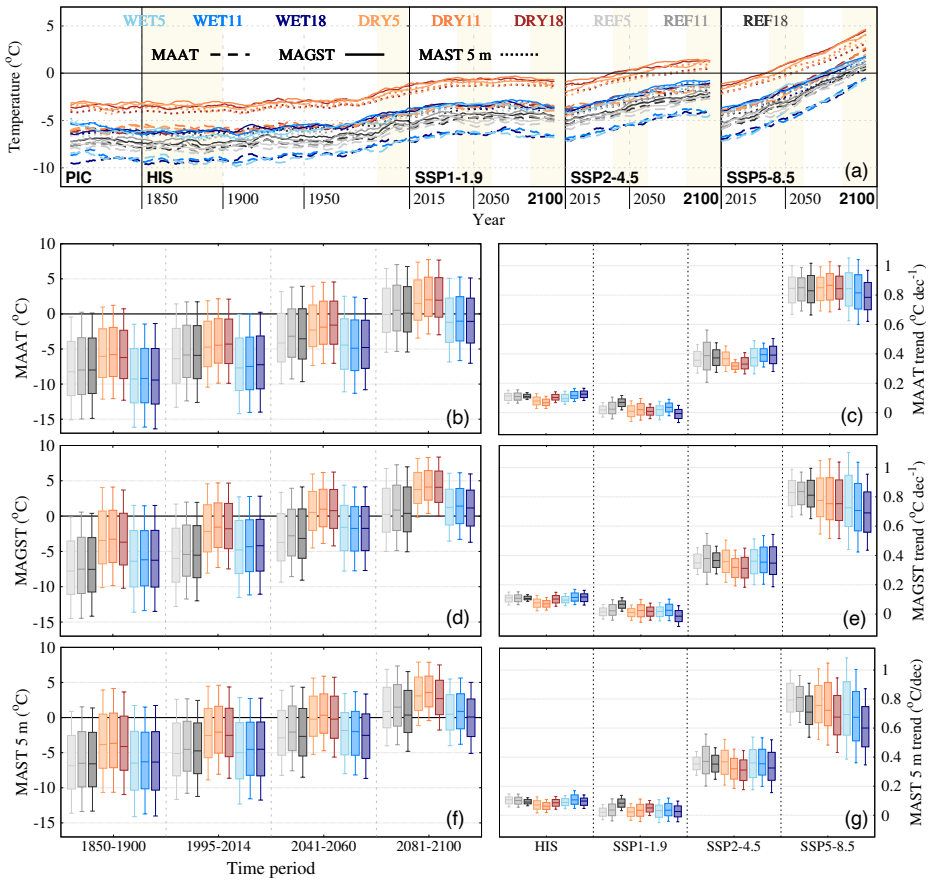

Figure 6.1: Temperature variability in the nine simulations of the MPIESM-PePE (see legend for colors) within the permafrost domain (Fig. 2.6a). (a) Time evolution (11-year moving average filtered outputs) of the median MAAT (dashed), MAGST (solid), and MAST 5 m (dotted line, °C) in the PIC, HIS, and different SSP scenarios (see Section 2.2.2). MAAT (b), MAGST (d), and MAST 5 m (f) regional boxplots of time averages for selected periods highlighted in (a) with light yellow bands: early historical (1850–1900), late historical (1995–2014), mid-21st century (2041–2060), and late 21st century (2081–2100) in the SSP5-8.5 scenario. The inner tick in the boxplot marks the median value within the permafrost mask area (Fig. 2.6a), the bottom and top lines the quartiles 1 and 3, and the bottom and top whiskers the 10th and 90th percentiles, respectively. MAAT (c), MAGST (e), and MAST 5 m (g) boxplots indicating the range of trends (°C dec^{-1}) within the permafrost domain, for the historical (HIS, 1850–2014) and SSP1-1.9, SSP2-4.5, and SSP5-8.5 scenarios (2015-2100) are also portrayed.

MAGST, and MAST 5 m is more intense for the WET simulations, with median regional values being significantly higher in 1995–2014 than in 1850–1900 (1.5–2.2 °C, $p < 0.05$). This increment is slightly smaller for DRY, but also significant (1.3–1.9 °C). The vertical discretization again has non-significant impact on regional warming differences. The combined effect of the 20th and early 21st temperature changes translates into decadal historical trends during 1850–2014 of about 0.1 °C dec^{-1} for MAAT, MAGST, and MAST 5 m (Fig. 6.1c,e,g), which are greater for WET and REF than for DRY in every case. The historical warming is followed for all the MPIESM-PePE simulations by an overall permafrost median warming trend of around 0.8 °C dec^{-1} in the 21st century for MAAT under SSP5-8.5, 0.4 °C dec^{-1} under SSP2-4.5, and non-significant MAAT trends for SSP1-1.9 (Fig. 6.1c). Moreover, regional variability increases with the intensity of the SSP scenario, with the interdecile range being around 0.1 °C dec^{-1} for all simulations in the SSP1-1.9 scenario, and ranging from 0.3 to 0.4 °C dec^{-1} for SSP5-8.5 simulations. Temperature trends are slightly smaller and regional variability is enhanced at the ground surface. The increase in MAGST median trends and regional variability varies with the configuration considered. For instance, while the MAGST trend values for the WET SSP5-8.5 simulations show a median (10th, 90th percentile) value of 0.70 °C dec^{-1} (0.42–1.13 °C dec^{-1}), the DRY simulations have a median of 0.76 °C dec^{-1} (0.54–1.04 °C dec^{-1}), and the REF median values increase to 0.83 °C dec^{-1} (0.66–0.99 °C dec^{-1}; Fig. 6.1e,f). The trends in the SSP5-8.5 experiments yield MAGST median values of permafrost by the end of the century that are the highest for the DRY configuration, with at least 90 % of the permafrost region (Fig. 2.6a) experiencing MAGST values that are above the melting point in 2081–2100 (Fig. 6.1d).

Regarding the effects of having different vertical discretizations, there is a particular noticeable effect of having an 18L scheme for MAGST WET trends, and for all the configurations in the case of the MAST 5 m under SSP5-8.5 warming. Deepening JSBACH produces an overall reduction in the SSP5-8.5 warming trend of 0.1 °C dec^{-1} at a depth of 5 m. This result aligns with previous results from González-Rouco et al. (2021) with the MPI-ESM in standalone experiments, where a deeper LSM results in a weaker near-surface warming.

A considerable reduction in permafrost regional temperature variability, especially noticeable for MAGST and MAST 5 m (Fig. 6.1d,f), starts at the beginning of the 21st century for the SSP5-8.5 scenario. Interdecile ranges are reduced by a factor of 1.08–1.21 for 2041–2060, and 1.14–1.49 for 2081–2100 with respect to 1995–2014, depending on the MPIESM-PePE configuration. This reduction is likely produced by a decrease in spatial near-surface temperature heterogeneity associated with the retreat of the snow cover area in winter. Figure 6.2a explores this by showing the variability of the winter offset (boxplots) and snow depth

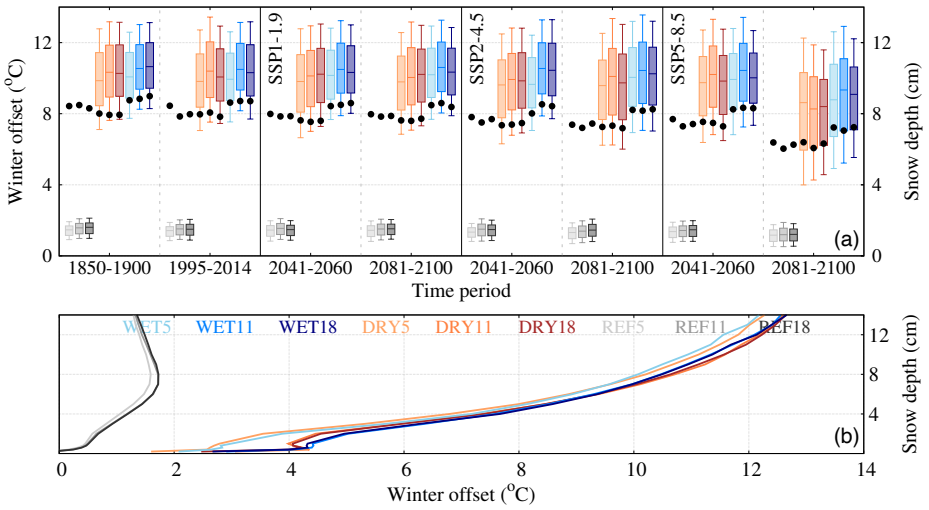

Figure 6.2: Winter offset, defined as GST-SAT in DJF (see Section 2.2.2), and snow depth. (a) Winter offset (°C) regional boxplots for the nine simulations of the MPIESM-PePE (see legend for colors) in the different periods shown in Fig. 6.1b,c,e. The inner tick in the boxplot marks the median value within the permafrost mask area (Fig. 2.6a), the bottom and top lines the quartiles 1 and 3, and the bottom and top whiskers the 10th and 90th percentiles, respectively. Snow depth median regional values (cm) for the same periods and simulations is shown with black dots. (b) Snow depth as a function of the winter offset within the permafrost domain for every simulation of the MPIESM-PePE.

(dots) in the permafrost domain for the same periods and scenarios as in Fig. 6.1. It can be seen that both snow cover and winter offset barely change in the historical, SSP1-1.9, and SSP2-4.5 periods, with very stable snow depth median values of 7.7 (REF), 7.2 (DRY), and 7.9 (WET) cm. A small decrease of around 1 cm is shown for SSP5-8.5 by the late 21st century. Even though snow depth values are quite similar between the three MPIESM-PePE configurations, winter offset shows remarkable differences between the REF, and the WET and DRY experiments. The regional median winter offset reaches 10–10.5 ^{o}C for WET and DRY, but is 8–9 ^{o}C lower in REF. This contrast extends to regional variability: the interdecile range (box width in Fig. 6.2a) ranges from 6–8 ^{o}C in WET and DRY, but is only of about 1 ^{o}C for REF. Both results reflect weaker insulation in the REF snow model. Moreover, WET winter offset values are systematically about 0.5 ^{o}C higher than DRY, which is consistent with WET being colder (Fig. 6.1) and having more snow cover. For the three configurations, thinning snow

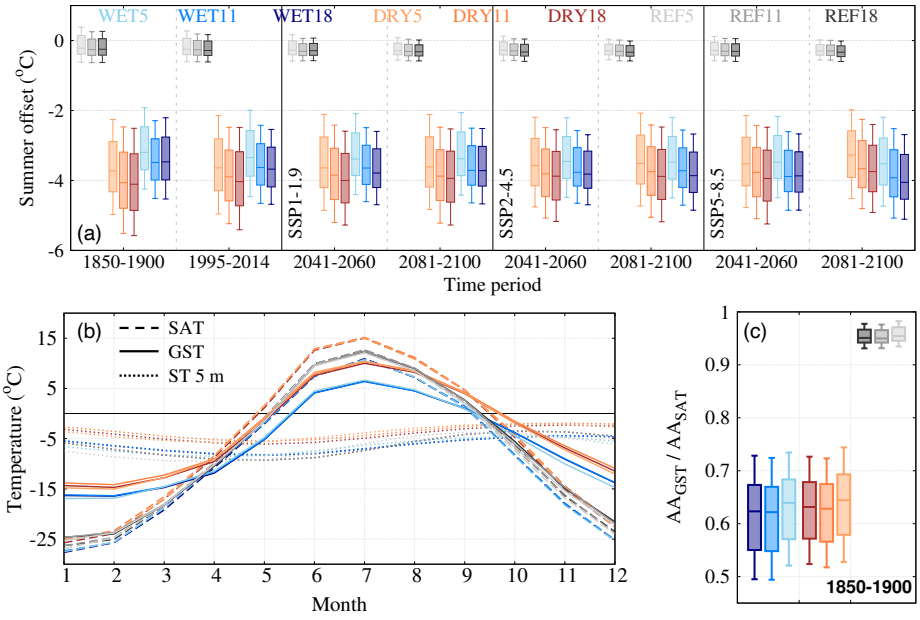

Figure 6.3: Summer offset and annual temperature cycle amplitude. (a) Summer offset (°C) regional boxplots (see Section 2.2.2) for the nine simulations of the MPIESM-PePE (see legend for colors) in the different periods shown in Figs. 6.1b,d,f and 6.2. The inner tick in the boxplot marks the median value within the permafrost mask area (Fig. 2.6a), the bottom and top lines the quartiles 1 and 3, and the bottom and top whiskers the 10th and 90th percentiles, respectively. (b) Amplitude (°C) of the regional median GST (solid), SAT (dashed), and ST 5 m (dotted line) annual cycles during 1850–1900 for the different MPIESM-PePE simulations in (a). (c) Ratio of GST vs. SAT annual cycle amplitude (AA) during 1850–1900 given by regional boxplots as in (a).

depth leads to less winter offset, being of 9.1 ^{o}C for WET and 8.4 ^{o}C for DRY by the end of the SSP5-8.5 period.

To better assess the dependence of the winter offset on snow depth for every simulation, a composite is computed for the DJF season by aggregating values of snow depth vs. winter offset for every grid cell and year during 1850–2100, including information of the historical period and the three SSP scenarios (Fig. 6.2b). This approach allows for reducing the heterogeneity in snow depth values associated with its temporal and spatial variability and reveals a strong relationship between the winter offset and snow depth for the WET and DRY simulations. The winter offset in REF remains significantly lower than in the WET and DRY

simulations, with a maximum of only 1.8 ^{o}C at 7–8 cm of snow depth and an increase of just 0.25 ^{o}C cm^{-1}. For snow depth values greater than 8 cm, the offset steadily declines at a rate of 0.07 ^{o}C cm^{-1}. In contrast, the WET and DRY simulations show a much stronger relationship between winter offset and snow depth, starting at 5 ^{o}C for a 2 cm snow cover and rising by 1 ^{o}C cm^{-1} up to 10 cm of snow, followed by a slower rate of 0.5 ^{o}C cm^{-1} for deeper snow cover values. These differences are primarily due to the implementation of a multi-layer snow scheme in WET and DRY (Section 2.2.2), which enables more realistic thermal insulation. As the snow depth increases, new layers are added every 5 cm up to a maximum of five, beyond which the top layer continues to accumulate snow (Ekici et al., 2014). Each layer's temperature is explicitly computed, and energy transfer between layers occurs via conduction. Since thermal conductivity of snow is very low but not so the volumetric heat capacity, the resulting thermal diffusivity is low (see Table 2.4), hindering heat transfer and effectively insulating the soil beneath the snow cover. REF lacks this vertical layering. Instead, snow depth only modifies the surface albedo and thermal properties of the uppermost soil layers (Reick et al., 2021). As a result, REF winter offset values remain small and less responsive to snow depth, as opposed to WET and DRY. These contrasting behaviors and the importance of layered snow schemes for capturing snow insulation effects have also been highlighted in standalone JSBACH simulations (Ekici et al., 2014; Steinert et al., 2021b).

In addition to the relationship between snow depth and winter temperature offset in the WET and DRY simulations, Fig. 6.2b shows that a temperature offset also exists even in the absence of snow for these configurations. This offset, which is not present in REF, results from the insulation effect of the organic layer in the MPIESM-PePE simulations (see Section 2.2.2, de Vrese et al., 2023). The organic layer helps smooth GST variability by dampening the response to SAT changes (Fig. 6.3). Specifically, it enhances the snow insulation effect in winter while mitigating GST increases in summer (Fig. 6.3a). As a result, the combined insulation effects of both the snow and the organic layer, along with latent heat exchanges from permafrost thawing and refreezing in summer and winter, lead to a reduced amplitude of the annual GST cycle in WET and DRY compared to REF (Fig. 6.3b). Thus, the regional median (10th, 90th percentiles) GST–SAT amplitude ratio in 1850–1900 is of 62 (50–72) % for WET11 and WET18, 65 (52–74) % for WET5, DRY11, and DRY18, 66 (53-75) %, but 95 (93–97) % for REF (Fig. 6.3c). The differences in the GST annual amplitude can influence ALT (Chadburn et al., 2015) and PE (Burke et al., 2020) variability.

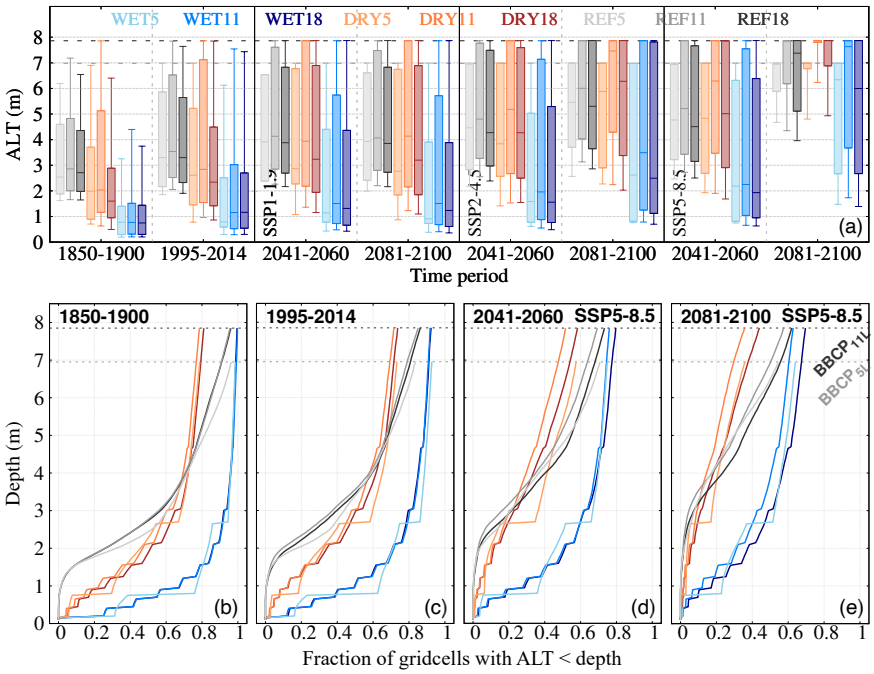

Figure 6.4: (a) ALT (m) for the ensemble of MPIESM-PePE simulations in the different periods shown in Fig. 6.1b,d,f and 6.2a. Fraction of gridcells within the MPIESM-PePE permafrost mask with a summer ALT greater than the indicated depth in the y-axis for 1850–1900 (b), 1995–2014 (c), 2041–2060 (d), and 2081–2100 (e). For every plot, dark (light) gray dashed line indicates the mid-layer depth of the bottom layer for the 11L (5L) configuration. 18L value is out of the bounds of the panels and, therefore, not included.

6.2.2 ALT

The spatial and temporal changes for ALT in the MPIESM-PePE simulations are represented in Fig. 6.4. Both the ALT regional median, quartiles, and 10th and 90th percentiles are the smallest for WET during the historical and scenario periods. This is due to the regional temperatures being on average 3 °C and 1.5 °C colder than for the DRY and REF simulations (Fig. 6.1), respectively. However, despite REF having colder MAAT, MAGST, and MAST 5 m than DRY (Fig. 6.1b,d,f, respectively), REF median ALT is approximately 1 m deeper than DRY in the historical period. Figure 6.4b,c further shows ALT for REF is greater than for DRY for ca. 70 % of the gridcells in 1850–1900, and 60 % in 1995–2014. The higher values of ALT in the REF simulations can be explained by the

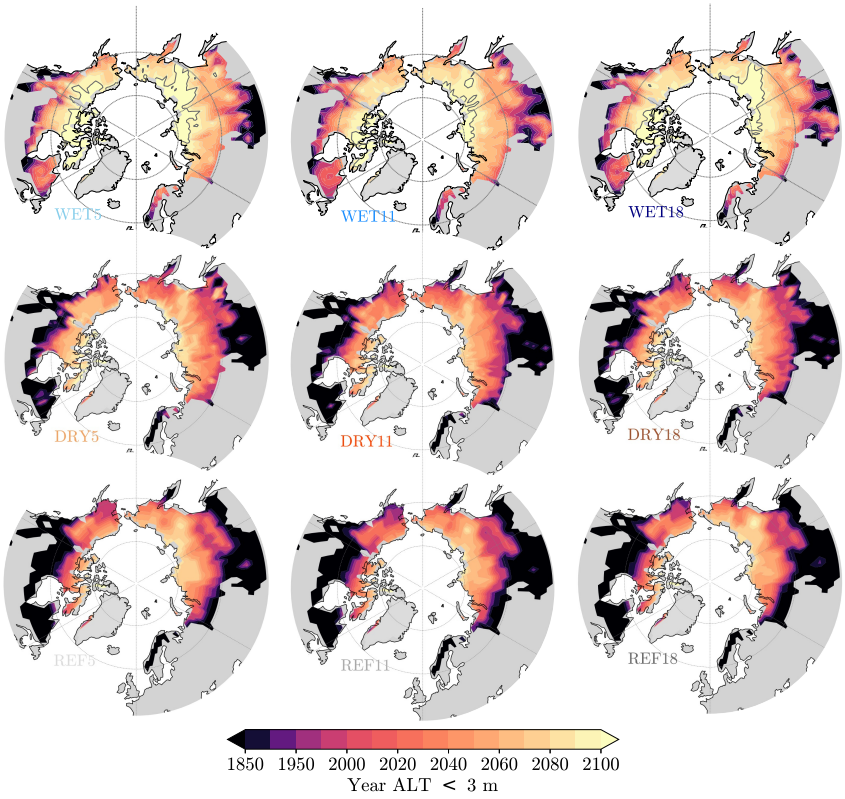

Figure 6.5: Near-surface permafrost presence with time for the combination of the three hydrological configurations (WET, DRY, REF) and vertical discretizations (5L, 11L, 18L). Spatial distribution of the last simulation year at which ALT is smaller than 3 m for every simulation of the MPIESM-PePE. The time evolution for historical and SSP5-8.5 experiments is shown in every case. Contour lines delimit areas where ALT does not reach 3 m within the temporal extent of the simulation. The colored distribution stands over the permafrost mask region displayed in Fig. 2.6a.

combination of two factors. Although REF MAGST is lower than DRY in 1850–1900 (Fig. 6.1b), summer GST is considerably higher (Fig. 6.3b). This is due to the lack of organic layer insulation and the absence of water phase changes with temperature in this configuration. When soil temperatures rise above 0 °C further warming is partially prevented, since an amount of heat is absorbed by the ice melt as latent heat. This phenomenon is known as the zero-curtain effect (Outcalt

et al., 1990; Mottaghy and Rath, 2006). Since the REF simulations do not include phase changes, summer warming is capable of penetrating deeper into the soil. The DRY configuration, in contrast, counterbalances the stronger temperature increase in summer with the zero-curtain effect, yielding lower ALT values than REF. Still, around 30 % of the gridcells for DRY have a thicker ALT than for REF in 1850–1900, increasing to 40 % in 1995–2014 (note the value of the x-axis when DRY and REF curves intersect). This indicates the zero-curtain effect does not outweigh the greater heat propagation from higher MAGST at depths below 4 (1850–1900, Fig. 6.4b) to 4.5 m (1995–2014, Fig. 6.4c), depth at which the annual cycle is very attenuated (Fig. 6.3b). Moreover, permafrost soils are very shallow across large areas of Siberia in JSBACH (Steinert et al., 2021b), so the absence of deep soil ice in these areas, and therefore of deep zero-curtain effect, promotes further ALT deepening as a response to the relative higher summer temperatures (Fig. 6.3b) in DRY than REF. The WET simulations, which yield colder regional temperatures (Fig. 6.1b,c,e) and more soil moisture (de Vrese et al., 2023), shows the highest fractions of gridcells holding permafrost for any value of ALT.

As permafrost warming intensifies in the 21st century under all scenarios, especially for the SSP5-8.5, ALT depth increases for all the simulations. That is evident from an extreme deepening of the permafrost regional ALT in 2081–2100 under the SSP5-8.5 scenario compared to 1995–2014, with median regional differences of 4.1 for REF, 5.8 for WET, and 4.4 m for DRY (Fig. 6.4a). These strong ALT variations are also illustrated by long-term changes in the vertical distribution of permafrost (Fig. 6.4d,e), including near-surface (i.e., shallower than 3 m, Fig. 6.5), and deep permafrost (Fig. 6.6). Even though most of the gridcells have a deeper ALT for REF than for DRY up to the late-historical period, the DRY simulations exhibit a greater deepening of ALT during the 21st century. That entails that only 36 % of the gridcells for DRY5, 36 % for DRY11, and 44 % for DRY18 still hold permafrost at the summer maximum thawing by 2081–2100 (Fig. 6.4e); these values are 18–20 % lower than those of REF.

The rapid ALT deepening for DRY is portrayed by maps in Fig. 6.5. While pre-2000 deeper near-surface permafrost thaw in summer (purple to red) extends over a greater area for the REF simulations, DRY is dominated by a more intense near-surface and deep permafrost thaw during the 21st century (orange). Indeed, Fig. 6.6 shows that a much greater area for REF than DRY still holds deep permafrost in 2100, with areas of 5.18 (REF5), 4.46 (REF11), 7.88 (REF18) versus 1.01 (DRY5), 1.45 (DRY11), and 2.93 (DRY18) 10^6 km^2. The WET configuration yields shallower ALT and greater gridcell fraction values than REF and DRY for the whole duration of the simulation. The median WET ALT difference with respect to DRY increases during the 21st century (Fig. 6.4a), which agrees with

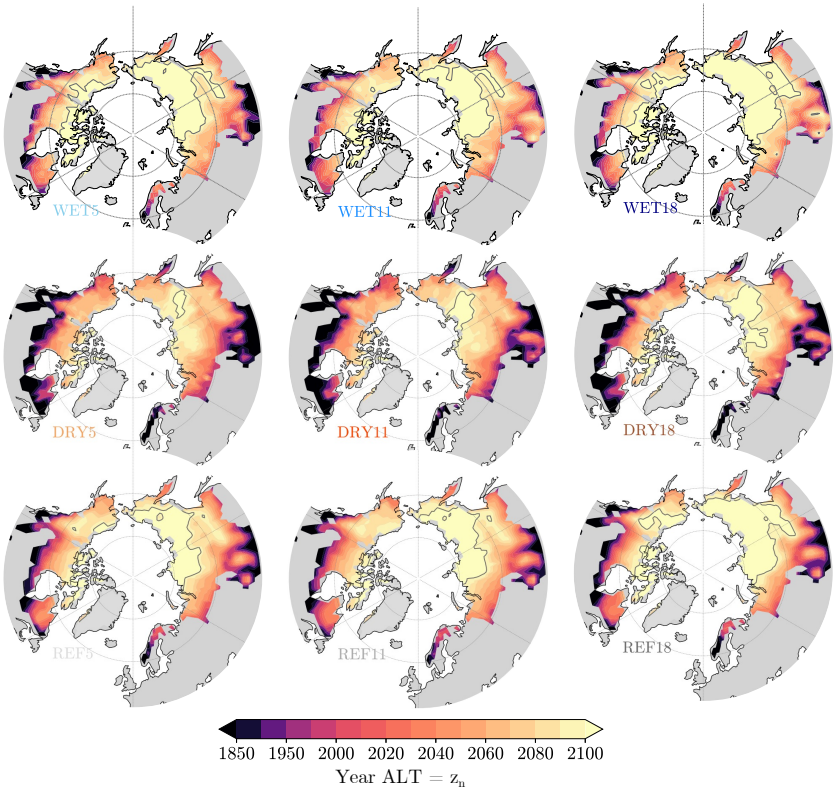

Figure 6.6: Deep permafrost presence with time for the combination of the three hydrological configurations (WET, DRY, REF) and vertical discretizations (5L, 11L, 18L). Spatial distribution of the last simulation year (HIS + SSP5-8.5) at which ALT is equal to the mid-layer depth of the bottom layer (ALT = z_n) for every simulation of the MPIESM-PePE. For the 18L simulations, 11L JSBACH z_n was taken in order to allow for comparison. Contour lines delimit areas where ALT do not reach z_n within the temporal extent of the simulation. The colored distribution stands over the permafrost mask region displayed in Fig. 2.6a.

higher MAGST (Fig. 6.1e) and MAST 5 m (Fig. 6.1g) trends, of 0.1–0.2 °C dec^{-1}, for DRY than WET for the SSP5-8.5 scenario. The relatively colder temperatures results in WET5, WET11, and WET18 still hold permafrost in summer for 64, 63, and 70 % of the gridcells in 2081–2100, which represents a deep permafrost area of 7.69, 6.11, and 9.09 10^6 km^2 by 2100, respectively. However, the SSP5-8.5 represents the most extreme warming scenario, and therefore the biggest response

in ALT. The SSP1-1.9 permafrost ALT response is clearly waeker, with median regional values from 0.2 (WET) to 1.2 (DRY) m deeper in 2081–2100 than by 1995–2014 (Fig. 6.4a). In turn, the SSP2-4.5 depicts a stronger ALT deepening occurrence than SSP1-1.9 in the 21st century, with an increase in ALT ranging from 2.0 (WET) to 4.2 (DRY) m. In both SSP1-1.9 and SSP2-4.5 scenarios, the differences between the different MPIESM-PePE configurations are equivalent to those already mentioned for SSP5-8.5, but comparatively smaller.

Apart from the differences in ALT due to the MPIESM-PePE configuration, there are also notable differences produced by the BBCP depth. All MPIESM-PePE configurations show increasing ALT differences during the 21st century among the 5L, 11L, and 18L schemes. This is depicted by a greater increment in the regional ALT values for the shallow (5L, 11L) than the 18L simulations in 2041–2060, and 2081–2100 for the SSP5-8.5 scenario (Fig. 6.4a). The effect of the BBCP depth is also evidenced by a growing offset in the gridcell fraction profiles during 2041–2060 (Fig. 6.4d), and 2081–2100 (Fig. 6.4e) between the shallow and 18L discretizations. Deepening the LSM also produces differences in deep permafrost that range from 1.4 to 3.4 10^6 km^2 in 2100, depending on the MPIESM-PePE configuration (Fig. 6.6). The shallow vs. deep vertical scheme differences are greater when comparing 11L with 18L than between 5L and 18L, which indicates that using a coarse vertical resolution reduces the ALT bias produced by using a too shallow BBCP depth (Chadburn et al., 2015). Even so, it is increasing the BBCP depth when resolving vertical heat conduction the factor that prevails in damping long-term warming (González-Rouco et al., 2021; Steinert et al., 2021a; García-Pereira et al., 2024b), producing a relative cooling of 18L vs. 5L and 11L simulations.

Although BBCP depth impacts the representation of deep permafrost, its near-surface effect is negligible. Fig 6.6b-e show no consistent differences in permafrost fraction of gridcells for historical ALT, and very small differences for gridcells having an ALT above 5 (2) m in 2041–2060 (2081–2100) under the SSP5-8.5 scenario. These small differences are also very hard to distinguish in terms of the evolution of near-surface permafrost existence, as shown in Fig. 6.5.

Regarding the spatial retreat pattern of permafrost in the MPIESM-PePE, both Figs. 6.5 and 6.6 show high agreement for the nine MPIESM-PePE simulations. All of them portray little to no presence of near-surface permafrost in Southern Siberia, Southern Canada, the Labrador Peninsula, and Scandinavia. The warming in the 20th and the first-half of the 21st century under SSP5-8.5 scenario affects much more near-surface than deep permafrost, yielding its retreat in Southern Alaska, Western, and Southeastern Siberia. By 2081–2100 for the SSP5-8.5 scenario, near-surface permafrost only remains in Northern Siberia for the WET simulations. In contrast, deep PE varies considerably with the

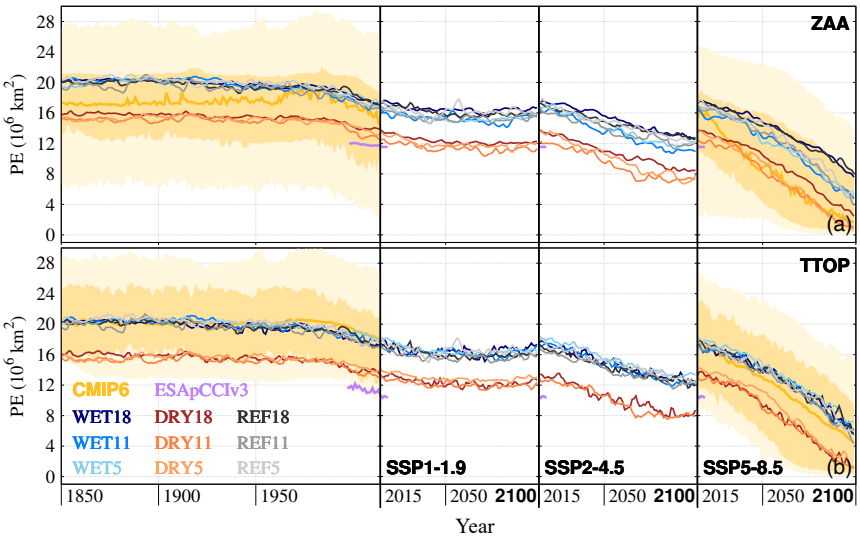

Figure 6.7: PE evolution according to ZAA and TTOP (see Section 6.1.3). (a) PE (10^6 km^2) using the ZAA definition for the different MPIESM-PePE simulations (solid lines, see legend for colors), the CMIP6 ensemble (gold solid line for the median, and dark (light) golden shading for the interquartile (interdecile) range), and the observational product ESApCCIv3 (purple solid line). (b) Same as (a), but for TTOP PE metric. CMIP6 PE data are only available for the historical period and SSP5-8.5 scenario (Steinert et al., 2023).

MPIESM-PePE configuration and vertical discretization, being maximum for WET18, where permafrost in 2100 is still present in Northern Canada and a vast area across Central, Eastern, and Northern Siberia, and minimum for DRY5 and DRY11, where only a small patch of deep permafrost remains in the Central Siberian highlands.

6.2.3 PE estimates: model-data comparison

The time evolution of PE for the nine simulations of the MPIESM-PePE in the three SSP scenarios are compared with the PE values derived from the ESApCCIv3 and CMIP6 PE estimates provided by Steinert et al. (2023) in Fig. 6.7. Both the MPIESM-PePE and the CMIP6 ensemble show a mostly constant permafrost area since 1850–1900 (see values in Table 6.1) until the last decades of the 20th century. WET and REF depict very similar early-historical PE values

Table 6.1: Initial state of PE ($PE_{1850-1900}$, in 10^6 km^2), and trends in the SSP1-1.9, SSP2-4.5, and SSP5-8.5 scenarios (in 10^6 km^2 dec^{-1}) for the nine simulations of the MPIESM-PePE and the 10th, 25th, 50th, 75th, and 90th percentiles of the CMIP6 ensemble stemming from Steinert et al. (2023). Values for both ZAA and TTOP definitions. Non-significant ($p > 0.05$) SSP trends are marked in bold.

	$PE_{1850-1900}$ (10^6 km^2)		Trend $PE_{SSP1-1.9}$ (10^6 km^{2}dec^{-1})		Trend $PE_{SSP2-4.5}$ (10^6 km^{2}dec^{-1})		Trend $PE_{SSP5-8.5}$ (10^6 km^{2}dec^{-1})	
	ZAA	TTOP	ZAA	TTOP	ZAA	TTOP	ZAA	TTOP
WET5	19.92	20.33	-0.11	-0.16	-0.71	-0.68	-1.49	-1.34
WET11	20.29	20.43	-0.10	-0.08	-0.75	-0.72	-1.42	-1.39
WET18	20.32	20.37	-0.09	**-0.01**	-0.64	-0.63	-1.15	-1.35
DRY5	15.22	15.49	-0.15	-0.10	-0.84	-0.90	-1.62	-1.65
DRY11	15.12	15.30	-0.13	-0.10	-0.73	-0.71	-1.52	-1.57
DRY18	15.87	16.05	-0.15	-0.11	-0.67	-0.70	-1.38	-1.58
REF5	20.52	20.78	**-0.04**	-0.06	-0.61	-0.61	-1.43	-1.40
REF11	19.73	20.01	-0.08	-0.08	-0.59	-0.57	-1.45	-1.44
REF18	20.03	20.26	-0.16	-0.15	-0.55	-0.62	-1.09	-1.36
$CMIP6_{P10}$	6.68	13.47					-0.39	-1.21
$CMIP6_{P25}$	12.91	16.07					-1.33	-1.60
$CMIP6_{P50}$	17.20	20.22					-1.79	-1.57
$CMIP6_{P75}$	21.01	24.75					-1.24	-1.49
$CMIP6_{P90}$	27.66	28.80					-1.25	-1.36

for both ZAA (Fig. 6.7a) and TTOP (Fig. 6.7b), in the range of 19.9–20.4 10^6 km^2 and 19.7–20.8 10^6 km^2, respectively (Table 6.1). However, REF5 and REF11 ZAA, and REF11 TTOP estimates show more variability, with the periods of the largest PE values coinciding with the strongest volcanic cooling events in the historical period (e.g., an abrupt PE rise in the 1880s as a response to the Krakatoa eruption). In contrast, the DRY simulations depict an area around 5 10^6 km^2 smaller than the REF and WET ones for both ZAA and TTOP (Table 6.1) and less temporal variability.

In general, CMIP6 PE median values lie in between WET and DRY when the ZAA permafrost definition is used, and agree with WET and REF for the TTOP definition. As ZAA and TTOP definitions physically target deep and near-surface permafrost degradation, respectively, this result indicates that the CMIP6 yields larger near-surface than deep permafrost estimates, which are approximately 20 and 17 10^6 km^2, respectively. However, the spread in CMIP6 PE is similar for ZAA and TTOP in terms of the interquartile range, of around 8 10^6 km^2, but greater for the deep permafrost (ZAA) when considering the interdecile range, of around 20–22 10^6 km^2. Thus, the differences in the PE early-historical equilibrium

state associated with imposing the WET or DRY conditions in high latitudes account for a quarter of the CMIP6 inter-model spread, which suggests that the representation of soil hydrology plays an important role in determining the extent of large-scale permafrost. In fact, state-of-the-art ESMs have been claimed to have difficulties in reproducing nowadays PE, due to their limitations in representing land surface processes (Chadburn et al., 2015; Burke et al., 2020; Steinert et al., 2023), the non-inclusion of specific processes accelerating permafrost degradation at local scales, such as soil subsidence (Andresen et al., 2020), talik formation or thermokarst (Farquharson et al., 2019; Nitzbon et al., 2024), or the inability to account for the permafrost-carbon warming feedback (Burke et al., 2013). These observation-simulation discrepancies in PE are suggested in Fig. 6.7, which exhibits that PE values from ESApCCIv3 in 1997–2019 are not only lower than the CMIP6 median, but also lower than all the MPIESM-PePE experiments, both for ZAA and TTOP. The differences are especially large for ZAA, which might be more sensitive to the aforementioned degradation processes enhancing deep permafrost losses that are not implemented in current LSMs, including JSBACH.

The steady state of PE in the 19th and most of the 20th century is followed by a decline that starts in the last quarter of the 20th century. The severity of the PE retreat mainly depends on the intensity of the SSP forcing (Fig. 6.7, Table 6.1). Hence, the low forcing SSP1-1.9 scenario shows a stabilization of PE after 2030 for the nine simulations of the MPIESM-PePE, with similar values for ZAA and TTOP DRY of around 12 10^6 km^2 and of 16 10^6 km^2 for WET and REF in their three vertical discretizations. SSP2-4.5 depicts a moderate loss until 2070 and a subsequent stabilization, with near-surface permafrost area values (TTOP, Fig. 6.7b) of 8 10^6 km^2 for DRY and 12 10^6 km^2 for WET and REF. For this scenario, there are moderate differences among 5L, 11L, and 18L simulations for ZAA, with PE values that differ by 1–2 10^6 km^2 by the end of the 21st century. Thus, DRY18 and WET18 PE are 8.6 and 13.1 10^6 km^2 in 2081–2100, but 7.3 and 11.1 10^6 km^2 for DRY11 and WET11, respectively. These differences in the deep permafrost are due to the increase in the BBCP depth better accommodating for the subsurface propagation of the 21st century warming (González-Rouco et al., 2021; Steinert et al., 2021a; García-Pereira et al., 2024b). Moreover, the PE loss shows no stabilization either for MPIESM-PePE or for the CMIP6 simulations under the SSP5-8.5 scenario. The deep permafrost (Fig. 6.7a) is intensively degraded for the 5L and 11L simulations, with PE around 2.1, 6.4, and 6.9 10^6 km^2 in 2081–2100, for DRY, WET, and REF, respectively. This degradation is less pronounced for the 18L experiments, with PE values of 4.0, 9.5, and 9.8 10^6 km^2, respectively. These PE differences by the late 21st century are consistent with differences in trends, which are between 0.14 and 0.36 10^6 km^2 dec^{-1} smaller for the 18L than for the 5L and 11L simulations (Table

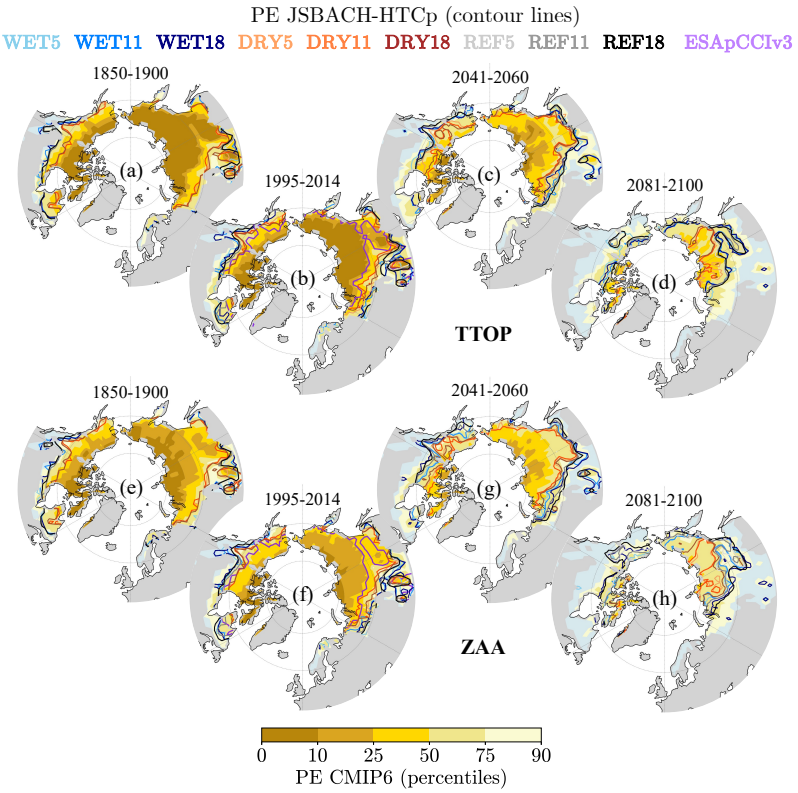

Figure 6.8: PE for different periods in the MPIESM-PePE and CMIP6 ensembles in the historical and SSP5-8.5 scenario, and observed historical extension. PE CMIP6 10th, 25th, 50th, 75th, and 90th percentiles spatial distribution (shading) for TTOP (a–d) and ZAA (e–h) for 1850–1900, 1995–2014, 2041–2060, and 2081–2100. The extent and distribution of PE for the different MPIESM-PePE experiments in the same periods are depicted with contour lines of different colors (see legend), whilst the observational ESApCCIv3 historical permafrost distribution in 1997–2019 is shown with a thicker purple contour line.

6.1). In contrast, near-surface permafrost degradation, although also intense, does not show notable differences between the 5L, 11L, and 18L schemes, with DRY TTOP by 2081–2100 being very similar for the three discretizations (2.4–2.9 10^6 km^2), WET and REF being in the range of 6.9–8.7 10^6 km^2, and the CMIP6 median PE being slightly lower than WET and REF (6.1 10^6 km^2). Both the 10th and 25th percentiles of the CMIP6 ensemble ZAA and TTOP PE are below

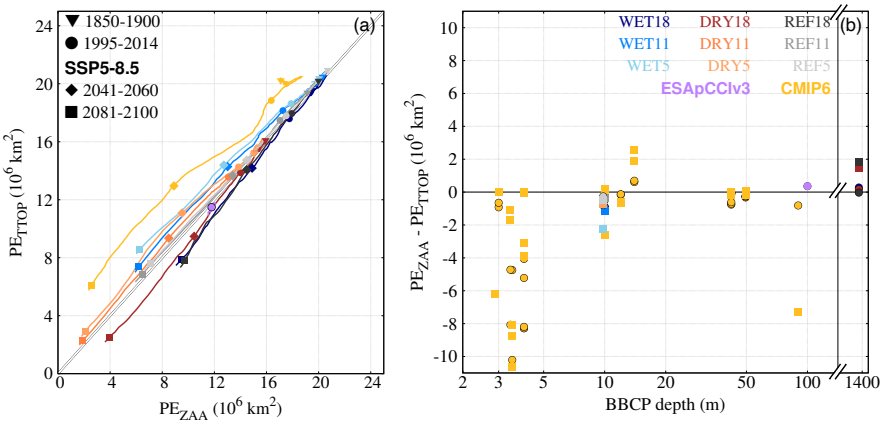

Figure 6.9: Relationship between PE and BBCP depth. (a) PE (10^6 km^2) for ZAA (x-axis) vs. TTOP (y-axis) for the CMIP6 median and the different members of MPIESM-PePE. Solid lines depict the year-by-year evolution of ZAA vs. TTOP values. The symbols (see legend) illustrate the mean ZAA vs. TTOP values for different periods. ZAA and TTOP PE estimates are filtered with a 15-year moving average. (b) ZAA - TTOP PE differences (10^6 km^2) in 1995–2014 (circles), and 2081–2100 (squares) for the 32 members of CMIP6 ensemble stemming from Steinert et al. (2023), the 9 MPIESM-PePE simulations, and the ESApCCIv3 observational PE data (only in 1997–2019). Data sources are sorted by their BBCP depth (m, logarithmic x-axis). Note the break in x-axis between 100 and 1400 m.

than 1 10^6 km^2 for the last three decades of the 21st century, which entails that near-surface permafrost is almost fully thawed for at least a quarter of CMIP6 models by the end of the century for the highest radiative forcing scenario.

Figure 6.8 shows the regional distribution of PE depicted in Fig. 6.7 for the historical and SSP5-8.5 scenario periods. At least 90 (75) % of CMIP6 models, all MPIESM-PePE members, and the observations display near-surface (deep) permafrost in Fig. 6.8c (Fig. 6.8h) across central, western, and eastern Siberia, southern Siberia highlands, northern Alaska and Canada, and Nunavut mainland and island territories by the end of the historical period (1995–2014). There is a notable decline in PE since 1995–2014 for both definitions under the SSP5-8.5 scenario (Fig. 6.8d,e,i,j). Permafrost degradation is more intense in southern Siberia, Fennoscandia, and the Labrador Peninsula, with only a quarter of the CMIP6 members and REF18, WET11, and WET18 still showing some permafrost patches in southern Siberia by 2041–2060 (Fig. 6.8d,i). By the end of the century (2081–2100, Fig. 6.8e,j), the existence of permafrost is predominantly reduced to central and northern Siberia, the highlands in southern Siberia, northern

Alaska, and the island territories of Nunavut. In these regions, at least half of CMIP6 models, and WET, REF, and DRY18 maintain some deep permafrost. In contrast, in DRY5 and DRY11 simulations near-surface and deep permafrost existence is reduced to Northern Siberia. In the WET18 and REF18 simulations, deep permafrost covers a much larger area in central Siberia and northern Canada than near-surface permafrost. Likewise, the DRY18 deep permafrost extends across vast areas in western Siberia, while near-surface permafrost is confined to eastern Siberia. Overall, the retreat pattern of PE for ZAA for 5L and 11L simulations is similar to TTOP, which indicates that shallow LSMs yield similar near-surface and deep permafrost degradation, whilst deep LSMs delay deep permafrost thawing as a response to intense surface warming (see also Fig. 6.7b).

6.2.4 PE and BBCP depth

To better disentangle the potential role of the BBCP depth from soil hydrology in producing differences in near-surface and deep permafrost estimates, the ZAA and TTOP definitions are compared in Fig. 6.9. As already exhibited in Fig. 6.7, the WET and REF simulations depart from a higher PE value in 1850–1900 than the DRY for both PE definitions. CMIP6 TTOP PE values are very similar to WET and REF, and ZAA PE closer to DRY. In general, the CMIP6 median always shows larger TTOP than ZAA PE values (golden line in Fig. 6.9a being above the grey diagonal). In contrast, all the MPIESM-PePE 18L simulations show negative values of ZAA - TTOP. Even though the DRY18 simulation starts from a smaller PE than WET18 and REF18, and further diverges by 2100, the evolution for the all three is quite robust in yielding a larger ZAA PE. However, this is not the case for the 5L and 11L simulations, which show a very close agreement in the evolution of TTOP and ZAA permafrost for REF simulations, and slightly greater TTOP than ZAA PE values by the end of the 21st century for WET and DRY. This entails that the MPIESM-PePE simulations with a shallow LSM (see Table 2.6 or Figs. 2.4a and 2.6b) experience a more intense deep permafrost thawing, as previously noted in Figs. 6.7b and 6.8j. This factor also accounts for the asymmetry observed in the median and spread of TTOP and ZAA PE estimates from CMIP6 simulations (Figs. 6.7 and 6.9), as previously noted by Steinert et al. (2023).

In fact, Burke et al. (2020) stated that having too shallow LSMs could result in an overestimation of deep permafrost thawing (i.e., an underestimation of PE with warming) using the ZAA metric. Since the zero-annual temperature ampli-

tude layer is usually found below 15 m (e.g., García-Pereira et al., 2024a), LSMs imposing zero-flux bottom boundary conditions above this depth would not experience a full attenuation of the annual cycle at any level. For the present analysis, we therefore apply a filter to remove the remaining annual temperature cycle in the lowest soil layer in the 5L and 11L simulations. However, this is not the only caveat about shallow LSMs. An insufficient BBCP depth produces an overestimation of the temperature variability with depth, as shown in González-Rouco et al. (2021) with the same modeling framework. This results in the amplification of the subsurface temperature trends associated with global warming. A BBCP depth of at least 170 m has to be imposed to ensure the full thermal decoupling between the ground surface and the bottom layer response in simulations spanning the historical and SSP periods until 2100 (Steinert et al., 2021a). This is not the case for any LSM incorporated in CMIP6 ESMs, as represented by Fig. 6.9b, which depicts the differences in deep vs. near-surface PE. There is an apparent bias in ZAA - TTOP for CMIP6 models having a very shallow land component, i.e., with a BBCP depth at 3–5 m (-3.1 $\pm$ 3.7 10^6 for 1995–2014, and -6.7 $\pm$ 3.6 10^6 km^2 for 2081–2100). This bias still exists but becomes non-significant ($p < 0.05$) for a subgroup of models having BBCP depths of around 10–15 m, which includes MPIESM-PePE 5L and 11L simulations (-0.4 $\pm$ 3.9 10^6 for 1995–2014, and -0.3 $\pm$ 1.4 10^6 km^2 for 2081–2100). ESMs having relatively deep LSM components (> 40 m) exhibit negligible ZAA - TTOP differences and dispersion (-0.2 $\pm$ 0.4 10^6 for 1995–2014, and 0.3 $\pm$ 0.7 10^6 km^2 for 2081–2100), excluding IPSL-CM6A-LR (BBCP depth of 90 m) in 2081–2100, which is an evident outlier (-7.3 10^6 km^2). This also includes WET18, DRY18, and REF18 simulations, which have deep vs. near-surface PE differences of 0.3, 0.2, and 0.0 for 1995–2014, and 1.5, 1.5, and 1.8 10^6 km^2 for 2081–2100, respectively. This reduction of ZAA - TTOP bias with BBCP depth agrees with Steinert et al. (2023), which reported more consistency in PE estimates by the end of the historical period between different permafrost definitions for the CMIP6 members having a deep LSM. The little impact observed in ZAA - TTOP PE when including a deep LSM in a set of simulations with varying conditions of Arctic soil wetness confirms the relevance of BBCP depth to yield unbiased PE estimates under global warming conditions.

6.3 Summary and conclusions

Permafrost degradation is a critical element for the sensitivity of the Earth system to climate change because of its significant impact on the terrestrial carbon cycle, society, and ecosystems. Despite observational data being important for

monitoring the ongoing state of permafrost soils, their coverage is often spatially sparse and uneven in time at a global scale. ESMs can overcome these spatial and temporal limitations, as well as provide comprehensive insights into permafrost dynamics. However, state-of-the-art ESMs exhibit considerable inter-model variability in their projections of PE, ALT, and permafrost hydrological state (Andresen et al., 2020; Burke et al., 2020; Steinert et al., 2023). Overall, ESMs disagree not only on the magnitude of future PE loss and ALT increase, but also on whether Arctic soils will become wetter or drier under global warming. These uncertainties arise from their different representation of soil thermodynamics and hydrology (Andresen et al., 2020; de Vrese et al., 2023; Matthes et al., 2025). This study assesses the impacts of changing both soil thermodynamics and hydrology on the Arctic permafrost dynamics for the first time in a fully-coupled ESM. This is achieved by modifying the LSM, including progressively refined and deeper vertical discretizations of the LSM (5L, 11L, and 18L) and generating comparatively wetter (WET) or dryer (DRY) conditions to quantitatively capture the permafrost conditions induced by changes in the LSM hydrological state (de Vrese et al., 2023).

Our results highlight the relevance of the representation of soil hydro-thermodynamic processes in determining permafrost temperature, ALT, and PE. Differences in the permafrost water table can produce very different thermal states, with MAAT differences of more than 3 °C between WET and DRY configurations, with REF exhibiting intermediate thermal conditions. However, differences in the GST seasonal variability are mainly produced by an improved representation of the snow cover and organic layer insulation effects, included in WET and DRY but not represented in REF. Higher summer temperatures, together with the omission of latent heat absorption due to permafrost thawing, leads to REF ALT being on average 1 to 2 m deeper in 1850–1900 than in DRY and WET, respectively. These differences decrease with warming, with the DRY simulation experiencing the greatest ALT values by the late 21st century under the SSP2-4.5 and SSP5-8.5 scenarios. Apart from the already mentioned factors, BBCP depth plays also a substantial role in determining future ALT. Deepening the LSM, i.e., switching from the 5L or 11L to the 18L discretization, prevents the full degradation of the permafrost profile for a 6–8 % of the gridcells within the permafrost mask, which is equivalent to an area of 1.5–2 10^6 km^2.

The implications of soil hydrology and BBCP depth are also noticeable for the evolution of the PE. Both TTOP, which physically represents near-surface PE, and ZAA, which tracks deep PE evolution, yield an initial PE of around 15 10^6 km^2 for DRY and 20 10^6 km^2 for REF and WET, respectively. These differences in soil hydrology explain up to a 76 % of the interquartile CMIP6 deep PE and a 54 % of the near-surface PE. Regarding the BBCP depth, the 5L and 11L with

respect to the 18L discretization show consistent PE differences, of 1.9–3.1 10^6 km^2, in the three hydrological configurations. This emphasizes the relevance of BBCP depth in reducing deep permafrost degradation. In fact, CMIP6 models having BBCPs deeper than 40 m show the smallest ZAA - TTOP PE differences, indicating that ESM simulations with deep LSM vertical schemes are more reliable to project future degradation of deep permafrost and its sensitivity to surface warming.

Chapter 7
Conclusions and outlook

This thesis investigates the long-term response of the land surface and subsurface to changes in the representation of thermodynamic and hydrological processes governing soil and bedrock dynamics under the ongoing global warming. Current LSMs provide a simplified treatment of these processes, resulting in biases and discrepancies with observed conditions. In reality, the subsurface behaves as a half-infinite medium for heat transfer, where temperature perturbations at the ground surface propagate downward over time mainly by heat conduction. Hydrological changes primarily occur within the soil layer and are closely coupled with soil thermodynamics. Soil hydro-thermodynamic coupling determines soil moisture phase changes, modifies thermal properties, and influences on the SEB and land-atmosphere interactions.

A key limitation in representing subsurface thermodynamics by LSMs is the imposition of an overly shallow zero-flux bottom boundary condition when resolving the underground heat conduction, which artificially halts heat transfer at depth. This shortcoming leads to an overestimation of long-term subsurface temperature trends, while also constraining land heat uptake with warming. The representation of soil hydrology within LSMs often omits critical processes that regulate the water cycle intensity and hydro-thermodynamic coupling. These include the neglect of soil moisture phase changes during freezing/thawing and supercooled liquid water, the absence of organic layers, the prescription of static soil thermal parameters, or the implementation of single bucket or too simplistic schemes for the computation of snow.

The main objective of this thesis is expanding the understanding of the hydrological and thermodynamic processes that control the subsurface heat propagation and storage, as well as assessing the sensi-

tivity of surface and subsurface climate variability to changes in these processes under global warming. The specific objectives posed by this thesis were (Section 1.8): (i) characterizing the underground thermal regime from subsurface temperature observations (Section 1.8.1); (ii) estimating land heat uptake in the industrial period from different data sources (Section 1.8.2); (iii) assessing why insufficient BBCP depths limit land heat uptake and its potential explanation at the ground surface (Section 1.8.3); (iv) evaluating permafrost sensitivity to climate change under different configurations of the subsurface thermo-hydrodynamics (Section 1.8.4).

While the main findings related to the research questions outlined in Section 1.8 are summarized within the conclusions of each chapter, this final chapter offers a synthesis of the overall main conclusions as well as some cross-chapter issues (Section 7.1). Research gaps and future lines of work are also summarized in an outlook (Section 7.2).

7.1 Main conclusions

The subsurface thermal structure is well described by the underground propagation of the surface temperature signal by heat conduction (Section 3.2.2).

A set of subsurface temperature time series at different depths from six monitoring stations in Sierra de Guadarrama enabled to assess the underground thermal propagation of GST signals. The evaluation focused on thermal diffusivity, a physical parameter that defines the rate and intensity of conductive heat transfer. A CA framework was applied, which tracks the exponential amplitude attenuation and linear phase shift of the GST annual wave with depth.

Results yielded apparent thermal diffusivity values of 1–1.3 10^{-6} $m^2 s^{-1}$ for deep profiles down to 20 m. These values are consistent with those for gneiss and granite, the dominant bedrock components in the Sierra de Guadarrama. Thermal diffusivity was found to change with depth, being smaller and more heterogeneous near the surface, with values of around 0.4–0.8 10^{-6} $m^2 s^{-1}$ across the six sites. The increase of thermal diffusivity with depth is consistent with a progressively higher compactness of the eroded material and debris constituting the soil with depth. An abrupt increase in thermal diffusivity was also observed between 4–8 m depth at four of the sites, corresponding to the transition from soil to bedrock. This transition was also identified in a stratigraphic analysis of unconsolidated material and rock samples, i.e., cores, extracted during the borehole drilling process.

Overall, the results confirm that conduction is the dominant mechanism of heat transfer in both soil and bedrock, with observed variations in thermal diffusivity primarily governed by changes in the parent material. The ability of CA to capture these depth-dependent variations suggests its potential for inferring subsurface composition in the absence of stratigraphic samples. It can also help identify the soil–bedrock transition, and thereby determine soil depth.

Soil temperature and moisture changes are connected near the surface (Section 3.2.3).

This thesis introduced a novel approach to compute the apparent thermal diffusivity of the subsurface, based on studying the attenuation of the full GST spectrum with depth, the SpM. The SpM enables the evaluation of short-term changes, i.e., of higher frequency than the annual cycle, in the soil thermal diffusivity near the surface.

SpM-derived diffusivity values show an increase with depth within the first meter of the soil. More interestingly, the time evolution of thermal diffusivities at 0.1 and 0.2 m at the HRR site exhibit coordinated seasonal variations with soil moisture. Following summer drought, thermal diffusivity decreases, while the onset and consolidation of wetter soil conditions in autumn and winter lead to a marked increase and eventual saturation in thermal diffusivity.

This time correlation between soil moisture content and thermal diffusivity is a promising finding, suggesting the potential for using soil temperature data to reconstruct soil moisture dynamics. Such reconstructions could complement the limited availability of *in situ* soil moisture observations and support studies of drought, extreme precipitation events, and land water availability, with valuable applications in agriculture and water resource management.

Imposing shallow BBCP depths constrains the land heat uptake in state-of-the-art ESMs (Sections 4.2.1 and 5.2.1).

Long-term impacts of the BBCP depth in surface and subsurface temperature variability and land heat uptake were evaluated comparing two fully-coupled ESM simulations of the past two millenia, historical, and future scenario periods (P2k+, until 2100) with the MPI-ESM: a standard shallow, with a BBCP at 10 m, and one presented in this thesis with a modified version of the MPI-ESM including a deep representation of the BBCP, at 1416 m depth. This depth is enough to virtually detach the bottom layer from surface temperature variations.

The deep simulation stores four times more heat than the shallow simulation by the end of the historical period (see Fig. 7.1). This underestimation by the shallow simulation reaches 60 ZJ by the end of the 21st century in the highest

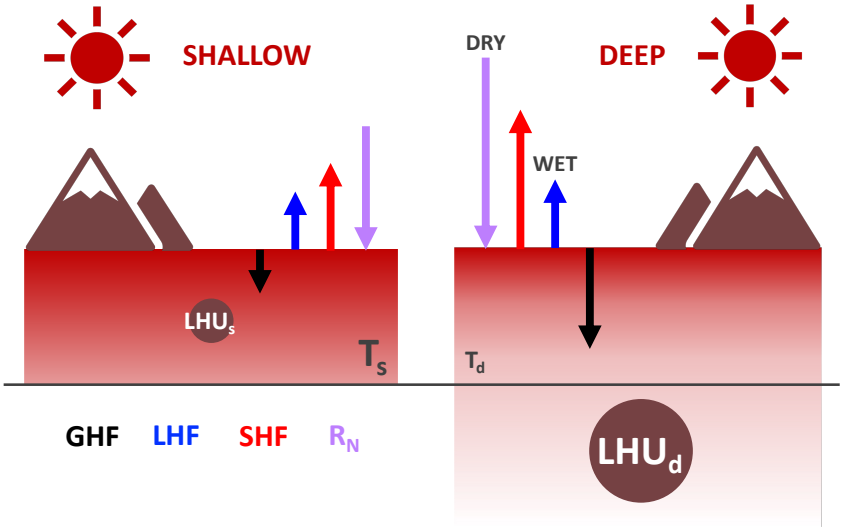

Figure 7.1: Schematic of the main conclusions stemming from Chapters 4 and 5. Under the same ground surface warming conditions (dark red), LSMs with a shallow BBCP limit the incoming GHF (black). This results in a reduced land heat uptake (brown bubble) and an overestimation of the bottom layer temperature (note the size of T_d and T_s labels). In contrast, deepening the BBCP induces greater GHF and land heat uptake values, and an increase in the SHF (red), LHF (blue), and R_N (purple arrow) globally, in wet, and dry areas, respectively.

radiative scenario (SSP5-8.5), which is equivalent to 3 times the observed land heat uptake in the industrial era.

The results evidence the need for deep LSM thermal components to properly reproduce the land heat uptake in standalone and fully-coupled ESM experiments, and therefore correctly portraying the terrestrial energy budget.

Surface temperature variability is unresponsive to changes in BBCP depth (Sections 4.2.1 and 5.2.1).

The comparison of the P2k+ deep and shallow simulations showed no differences neither in SAT nor in GST long-term variability or trends. This means that long-term changes in surface temperatures are independent from changes in the BBCP depth in fully-coupled ESM simulations, which agrees with previous results coming from standalone LSM experiments.

Therefore, GST information from different data sources (ESMs, reanalyses, gridded observations) can be used as a top boundary condition to drive sim-

ple half-infinite heat conduction forward models and derive unbiased land heat uptake estimates. This approach could also be used to correct subsurface temperature variability and trends computed by ESMs, with applications in borehole climatology and deep permafrost diagnosis.

One-dimensional heat conduction forward models driven by ground surface temperature data yield consistent estimates of land heat uptake with those obtained from BTPs (Section 4.2.2).

A collection of land heat uptake estimates was derived using a simple half-infinite heat conduction forward model (ConForM), forced by global mean continental GST data from 37 CMIP6 ESMs and 5 reanalyses, as well as SAT data from 5 gridded observational datasets. The analysis covers three different periods: 1950–2000, 1960–2020, and 1971–2018.

For the 1971–2018 period, land heat uptake ranges from 10 to 16 ZJ across all sources. CMIP6 models yield a land heat uptake of approximately 14 ZJ, which doubles the values simulated when limited by a shallow BBCP depth. Although the different data sources lead to consistent land heat uptake values, they all lie below the last borehole-based estimates, of around 18 ZJ in 1971–2018. This discrepancy is due to an overestimation of land heat uptake by boreholes that has been recently reconciled.

The results underscore the applicability of forward models in improving ESM-based estimates. Moreover, the comparison between model- and data-driven land heat uptake estimates can serve as an additional metric to assess the realism of ESMs in reproducing the subsurface response to current global warming.

The limited land heat uptake in shallow ESM simulations stems from a constrained GHF (Sections 5.2.1 and 5.2.2).

An ensemble of eight standalone simulations of the industrial-era and future scenario warming with the LSM of the MPI-ESM, JSBACH, was used to assess the relation between land heat uptake and long-term incoming GHF for different subsurface depths (Fig. 7.1).

Results indicate that GHF increases twofold when the BBCP depth is extended from 10 to 22 m, saturating at a factor of five for a BBCP depth of 184 m. Therefore, to ensure that GHF values in industrial and future climate change standalone LSM or fully-coupled ESM experiments are not underestimated, BBCPs must be prescribed at least at 184 m.

This outcome demonstrates for the first time that BBCP depth can influence the climate at the ground surface, thus extending previous findings that primarily focused on subsurface temperature biases and land heat uptake. This underlines again the need for deeper BBCPs to realistically represent ground surface and

subsurface thermodynamics in climate simulations.

Correcting the GHF biases associated with the BBCP depth reshape the long-term surface energy balance (Section 5.2.3).

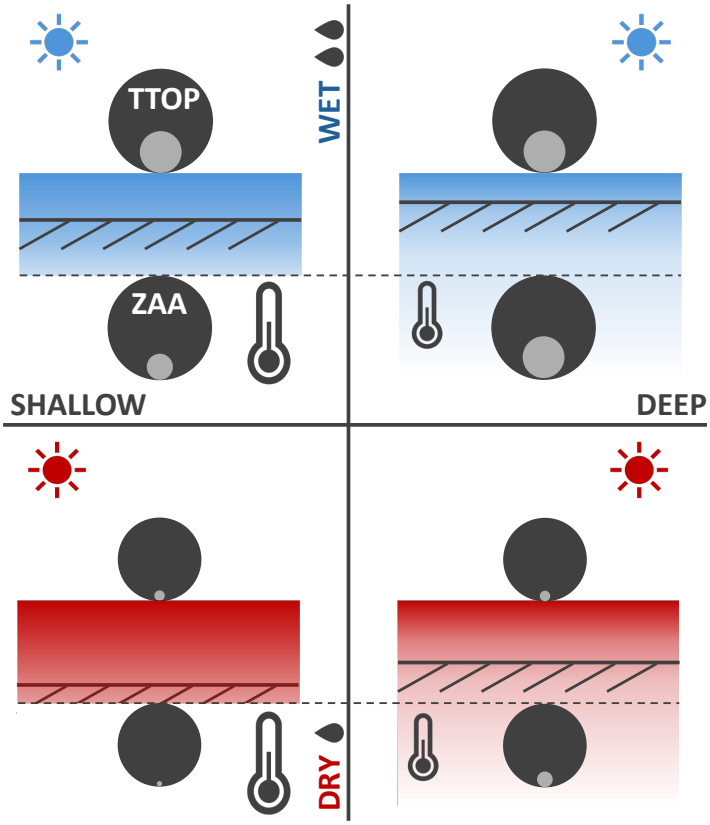

Figure 7.2: Schematic of the main conclusions achieved in Chapter 6. A WET (two drops) permafrost leads to relatively colder (blue) surface conditions than DRY (single drop, red), which results in a shallower ALT (scratched line) and greater initial PE, both for TTOP and ZAA (dark gray circle). Deepening the BBCP attenuates the bottom layer temperature increase (thermometer size), reducing future deep (ZAA) permafrost degradation (light gray circle).

The increase in the incoming GHF is mainly compensated by a global increase in the outgoing SHF, and a comparatively smaller increase of the LHF and net radiation in wet and dry areas, respectively (Fig. 7.1).

This finding complements the previous conclusion, highlighting for the first time the impacts of an insufficiently deep BBCP at the surface climate. Moreover, the fact that the BBCP modifies the SEB evidences again the close connection between subsurface hydrology and thermodynamics, with implications for the understanding of land-atmosphere interaction.

The interaction between the subsurface hydrology and thermodynamics is especially sensitive in permafrost regions (Section 6.2).

This thesis explored the response of permafrost temperature variability, ALT, and PE to changes in its soil hydrology and thermodynamics. An ensemble of fully-coupled ESM historical and climate change scenario simulations with the MPI-ESM, the MPIESM-PePE, was performed under three configurations of JSBACH: the standard model version, REF, and two variants that generate rather DRY or WET conditions across permafrost areas. Moreover, two vertical discretizations were implemented, with 11 and 18 layers, and BBCP depths at 10 and 1391 m, respectively. These discretizations complement the standard 5-layer discretization of JSBACH and were used to explore the effects of the BBCP depth and vertical resolution.

Both the pre-industrial state and future evolution of permafrost are strongly influenced by hydrology. WET simulations depict an overall 3 ^{o}C colder permafrost region than DRY, which results in a 1–2 m thinner ALT, and an initial PE larger by 5 10^6 km^2 (Fig. 7.2). All simulations depict a rapid increase in permafrost temperatures, ALT thickening, and PE reduction in the 21st century, with changes being most pronounced under the SSP5-8.5 scenario. In this scenario, however, BBCP depth reduces the intensity of near-surface soil warming by 0.1 ^{o}C dec^{-1}, diminishing the loss of permafrost area by up to 1.9–3.1 10^6 km^2 by the end of the century (Fig. 7.2).

Overall, this final part of the thesis underscores the importance of refining hydrological and thermodynamic processes and their interactions in ESMs to improve projections of permafrost dynamics under climate change. A more exhaustive representation of permafrost hydro-thermodynamics in ESMs is relevant for assessing risks associated with global carbon feedbacks and infrastructure vulnerability in Arctic regions.

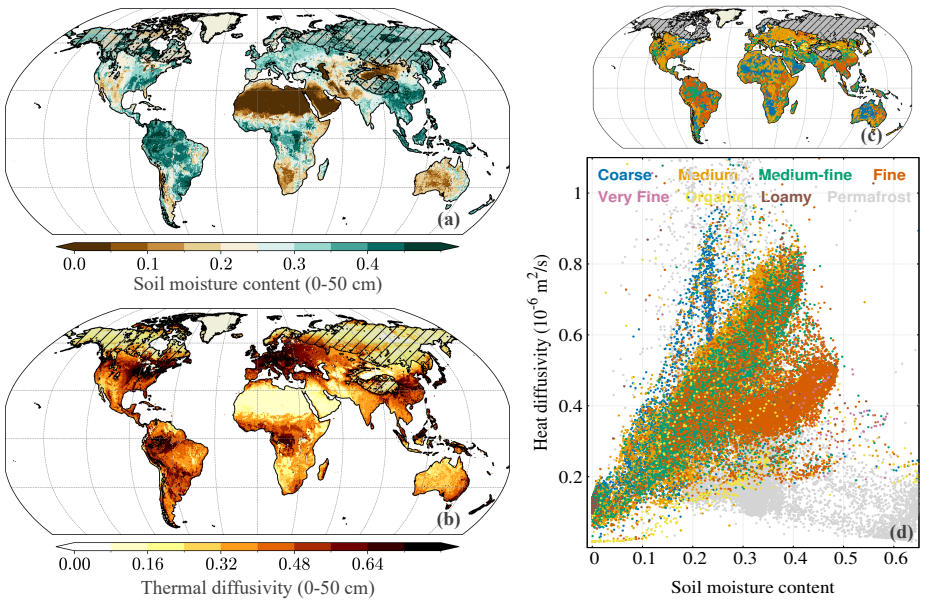

Figure 7.3: Soil thermal diffusivity and moisture content in ERA5-Land. (a) Mean soil moisture content and (b) thermal diffusivity down to 50 cm depth over the period 1948–2024. Thermal diffusivity in (b) was derived using the CA amplitude attenuation method applied to each grid cell (see Section 3.1). (c) Soil types defined by ERA5-Land based on soil texture (legend in panel d).(d) Scatterplot of thermal diffusivity versus soil moisture, clustered by ERA5-Land soil type. The mean permafrost region for 1948–2024 is shown with hatching in maps (a–c) and represented in gray in panel (d).

7.2 Outlook

The main conclusions of this thesis (Section 7.1) demonstrate that soil hydrology and thermodynamics are closely interconnected. This mutual dependence is particularly relevant in the context of ongoing climate change, where shifts in the soil hydrological state can either dampen or amplify its warming. Given the scarcity of observational soil moisture data, having alternative indirect sources of information can be highly valuable. This thesis has shown that soil temperature can serve as a proxy for soil moisture through its relationship with thermal diffusivity. However, since this connection was demonstrated here using short-term *in situ* data from a single station (HRR), it would be worthwhile to extend this analysis both spatially and temporally. Future work will aim at better char-

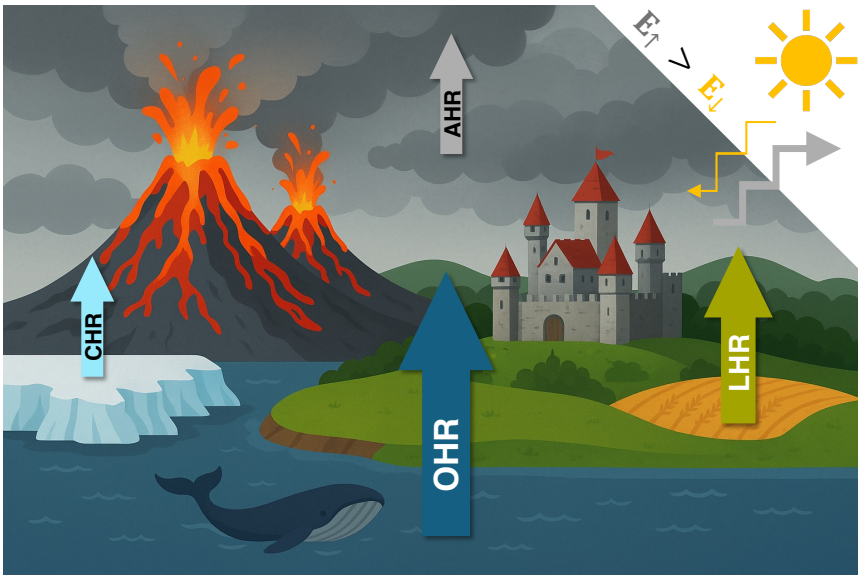

Figure 7.4: Terrestrial energy budget under massive cooling volcano events in the CE. The large emission of stratospheric aerosols leads to a comparatively lower incoming than outgoing radiation, which results in a negative energy imbalance. The imbalance is partitioned between the different climate components in the form of ocean (O), land (L), cryosphere (C), and atmosphere (A) heat releases (HRs). The relative contribution of OHR, LHR, CRH, and AHR is still an open question. Modified from von Schuckmann et al. (2023) using OpenAI (2025).

acterizing the relationship between thermal diffusivity and soil moisture across different soil types, using soil reanalysis datasets, such as ERA5-Land. Preliminary results using ERA5-Land soil temperature and moisture content monthly data at different levels show that thermal diffusivity increases with soil moisture content (Fig. 7.3). The increase rate is higher for coarse soils (Fig. 7.3d), which is consistent with a stronger increase of thermal conductivity for this soil texture associated with a higher volume fraction of the high-conductivity parent material. However, the increase rate in thermal diffusivity with soil moisture is not constant, but decays for higher soil moisture values (Dai et al., 2019). This can hinder the inference of accurate soil moisture absolute values, artificially dampening soil moisture seasonal and spatial variability. The plausibility of this idea and the associated caveats will be explored in the near future.

Another line of research that remains open following this thesis is the impact of correctly representing land heat on the terrestrial energy budget. This thesis

has extensively considered land heat uptake as a consequence of the positive energy imbalance driven by the ongoing anthropogenic greenhouse effect. However, as discussed in Sections 1.5 and 4.2.1, there have been periods during the CE characterized by a series of intense volcanic eruptions, e.g., the LIA. Unlike the increase in GHGs, these eruptions induced intense and rapid negative energy imbalances, resulting in a long-term net heat release from the various components of the climate system (Fig. 7.4). For instance, the eruption of the Samalas in 1257 induced a negative energy imbalance of -32.8 W m^{-2} (Sigl et al., 2015), which is equivalent to a global energy loss of 517 ZJ. This value amounts for around one and a half times the ocean heat uptake in the last six decades (von Schuckmann et al., 2023), seven times the land heat uptake by P2k+d in 1850–2100, or 35 times for P2k+s. However, how the volcanic-driven negative imbalance is partitioned between the different climate components remains an open scientific question. Since future scenario ESM simulations do not regard possible future volcanic events, this question could be addressed using simulations of the CE (Fig. 7.4). Furthermore, comparing the MPI-ESM P2k+ simulations presented in this thesis could help determine to what extent this partitioning is influenced by having shallow LSM configurations. Future work computing the terrestrial energy budget in the context of strong volcanism could contribute to the understanding of the subsurface as a net heat source and a climate regulator in past and future climate scenarios.

Finally, this thesis underlined the relevance of incorporating a more realistic and detailed representation of soil hydro-thermodynamic processes in ESMs to improve the simulation of permafrost dynamics. A modified version of JSBACH including new hydro-thermodynamic features in permafrost regions was run in coupled-mode to assess the sensitivity of permafrost to different configurations of the Arctic hydrology and vertical discretizations of the LSM under current and future scenario warming. Results show that permafrost temperatures are particularly sensitive to the mean Arctic hydrological state, with overall differences of around 3 °C between WET and DRY configurations, and even larger discrepancies locally. However, changes in the permafrost temperature do not only affect permafrost dynamics, but have an atmospheric impact due to the operation of different land-atmosphere feedbacks related to latent heat release and evaporation, cloudiness, and snow-albedo changes (de Vrese et al., 2023). For instance, de Vrese et al. (2024) showed how permafrost degradation can lead to changes in the seasonal cloud cover, enhancing low cloudiness in winter and reducing cloud cover in summer, which further amplifies Arctic warming. Future work will target how changes in the hydrological state of permafrost can drive differences in the Arctic temperature response, subsequently leading to changes in Arctic amplification (Meabe-Yanguas et al., 2025). Whether this Arctic land-atmosphere

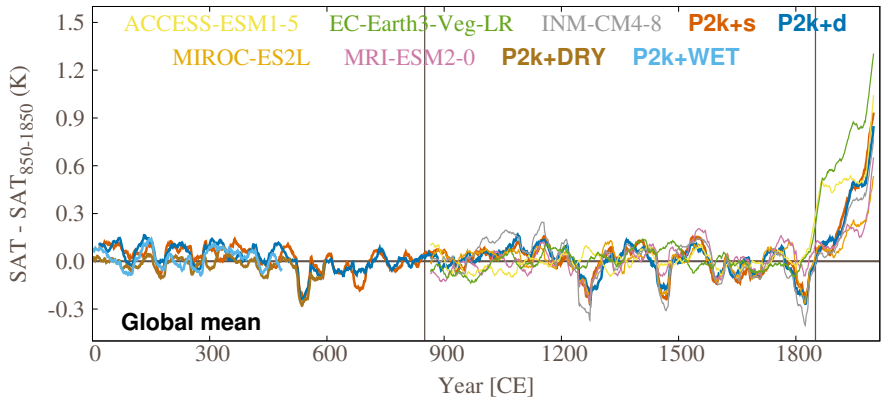

Figure 7.5: Global mean SAT anomalies in the CE with respect 850–1950 for the available last millennium PMIP4 simulations Jungclaus et al. (2017), the P2k+ simulations presented in this thesis (see Table 2.4 and Sections 2.2.1 and 4.2.1), and a couple of ongoing P2k+ WET and DRY simulations.

interaction has implications for the global climate patterns, via changes in the circulation at mid-latitudes or teleconnections with the tropics, will be also explored.

Another open question stemming from the last part of the thesis is whether the hydrological state of permafrost can also have influenced the evolution of temperature, ALT, and PE throughout the CE. To investigate this, extended WET18 and DRY18 simulations covering the whole CE are currently in production (P2k+WET and P2k+DRY, Fig. 7.5). These runs will complement the existing MPI-ESM P2k+ experiments, contributing to expand the scarce number of experiments of the last millennium within PMIP4. Assessing long-term permafrost responses to variations in soil hydro-thermodynamics during a period of relatively weak external forcing can help disentangle low-frequency signals unaffected by strong anthropogenic trends. Additionally, differences in the WET vs. DRY responses to abrupt volcanic cooling events may provide further insights into permafrost sensitivity to rapid climate perturbations in the short- and long-term.

Publications related to this thesis

The findings of this thesis are included in the following publications.

- **García-Pereira, F.**, J. F. González-Rouco, T. Schmid, C. Melo-Aguilar, C. Vegas-Cañas, N. J. Steinert, P. J. Roldán-Gómez, F. J. Cuesta-Valero, A. García-García, H. Beltrami, and P. de Vrese, 2024: Thermodynamic and hydrological drivers of the soil and bedrock thermal regimes in central Spain. *SOIL*, 10, 1–21, DOI: 10.5194/soil-10-1-2024.

- **García-Pereira, F.**, J. F. González-Rouco, C. Melo-Aguilar, N. J. Steinert, E. García-Bustamante, P. de Vrese, J. Jungclaus, S. Lorenz, S. Hagemann, F. J. Cuesta-Valero, A. García-García, and H. Beltrami, 2024: First comprehensive assessment of industrial-era land heat uptake from multiple sources. *Earth System Dynamics*, 15, 547–564, DOI: 10.5194/esd-15-547-2024.

- **García-Pereira, F.**, J. F. González-Rouco, N. Meabe-Yanguas, P. de Vrese, N. J. Steinert, J. Jungclaus, and S. Lorenz, 2025: Permafrost sensitivity to changes in soil hydro-thermodynamics in historical and scenario simulations with a modified version of the MPI-ESM. *The Cryopshere* [preprint], DOI: 10.5194/egusphere-2025-2126.

- **García-Pereira, F.**, et al., 2025: Insufficient soil depth constrains ground heat flux in Land Surface Models. *Geophysical Research Letters* (In preparation).

Additionally, the author has also participated in other published research articles as a coauthor, whose results are overall relevant for this thesis:

- Vegas-Cañas, C., J. F. González-Rouco, J. Navarro-Montesinos, E. García-Bustamante, E. E. Lucio-Eceiza, **F. García-Pereira**, E. Rodríguez-Camino, A. Chazarra-Bernabé, and I. Álvarez-Arévalo, 2020: An Assessment of Observed and Simulated Temperature Variability in Sierra de Guadarrama. *Atmosphere*, 11(9), 985, DOI: 10.3390/atmos11090985.

- González-Rouco, J. F., N. J. Steinert, E. García-Bustamante, S. Hagemann, P. de Vrese, J. H. Jungclaus, S. J. Lorenz, C. Melo-Aguilar, **F. García-Pereira**, and J. Navarro, 2021: Increasing the depth of a Land Surface Model. Part I: Impacts on the soil thermal regime and energy storage. *Journal of Hydrometeorology*, 22(12), 3211–3230, DOI: 10.1175/JHM-D-21-0024.1.

- Steinert, N. J., J. F. González-Rouco, C. Melo Aguilar, **F. García-Pereira**, E. García-Bustamante, P. de Vrese, V. Alexeev, J. H. Jungclaus, S. J. Lorenz, and S. Hagemann, 2021: Agreement of analytical and simulation-based estimates of the required land depth in climate models. *Geophysical Research Letters*, 48, e2021GL094273, DOI: 10.1029/2021GL094273.

- Melo-Aguilar, C., F. González-Rouco, N. J. Steinert, H. Beltrami, F. J. Cuesta-Valero, A. García-García, **F. García-Pereira**, E. García-Bustamante, P. J. Roldán-Gómez, T. Schmid, and J. Navarro, 2022: Near-surface soil thermal regime and land–air temperature coupling: A case study over Spain. *International Journal of Climatology*, 42(15), 1–19, DOI: 10.1002/joc.7662.

- Roldán-Gómez, P. J., J. F. González-Rouco, J. E. Smerdon, and **F. García-Pereira**, 2023: Model and proxy evidence for coordinated changes in the hydroclimate of distant regions over the Last Millennium. *Climate of the Past*, 19, 2361–2387, DOI: 10.5194/cp-19-2361-2023.

- Steinert, N. J., M. Debolskiy, E. Burke, **F. García-Pereira**, and H. Lee, 2024: Evaluating permafrost definitions for global permafrost area estimates in CMIP6 climate models. *Environmental Research Letters*, 19, 014033, DOI: 10.1088/1748-9326/ad10d7.

- Steinert, N. J., F. J. Cuesta-Valero, **F. García-Pereira**, P. de Vrese, C. A. Melo Aguilar, E. García-Bustamante, J. Jungclaus, and J. F. González-Rouco, 2024: Underestimated land heat uptake alters the global energy distribution in CMIP6 climate models. *Geophysical Research Letters*, 51, e2023GL107613,

DOI: 10.1029/2023GL107613.

- Cuesta-Valero, F. J., A. García-García, H. Beltrami, **F. García-Pereira**, J. F. González-Rouco, and J. Peng, 2025: Robust increase in observed heat storage by the global subsurface. *Science Advances* (Accepted).

- Meabe-Yanguas, N., J. F. González-Rouco, **F. García-Pereira**, P. de Vrese, A. Martínez-Vila, N. J. Steinert, J. Jungclaus, and S. Lorenz, 2025: Long term influence of changing soil hydrology in an Earth System Model on Arctic Amplification, *The Cryopshere* (In preparation).

The author has also participated in some non-reviewed publications:

- González-Rouco, J. F., E. García-Bustamante, **F. García Pereira**, E. Lucio Eceiza, C. Melo Aguilar J. Navarro Montesinos, C. Rojas Labanda, P. Roldán, N. Steinert, and C. Vegas Cañas, 2021: Cambio climático: una perspectiva global. In: "Cambio climático en el Mediterráneo: procesos, riesgos y políticas". Romero J., J. Olcina (Eds.). Ch. 2, 49–73, *Tirant Humanidades*, Valencia, ISBN: 978-84-18534-19-5.

- González-Rouco, J. F., **F. García-Pereira**, C. Vegas Cañas, N. Meabe Yanguas, 2024: Proyectando el futuro: Modelos climáticos. In: "Cambio climático en España", R. Serrano-Notivoli, J. Olcina, J. Martín-Vide (Eds.). Ch. 5, 149–192, *Tirant Humanidades*, Valencia, ISBN: 978-84-1183-727-9.

- Ministry for the Ecological Transition and the Demographic Challenge (MITECO), 2024: CLIVAR-Spain Report 2024: Impacts, vulnerability and adaptation to climate change in Spain. **F. García-Pereira** as contributing author to Ch. 1, 18–83. Madrid, ISBN: 978-84-18778-49-0.

- **García-Pereira, F.**, J. F. González-Rouco, N. Meabe Yanguas, and J. Jungclaus, 2025: Una profundidad insuficiente del subsuelo limita el flujo de calor del suelo en los modelos de superficie terrestre. In: "Modelos y escenarios climáticos". M. Y. Luna, F. González-Rouco (Eds.), 31–42, Serie A, *Publicaciones de la Asociación Española de Climatología. XIII Congreso de la AEC*, Madrid, ISBN: 978-84-125772-3-5.

References

2k Consortium, P., 2013: Continental-scale temperature variability during the past two millennia. *Nature Geosciences*, **6**, 339–346, DOI: 10.1038/ngeo1797.

Abbott, B. W. and J. B. Jones, 2015: Permafrost collapse alters soil carbon stocks, respiration, CH4, and N2O in upland tundra. *Global Change Biology*, **21**, 4570–4587, DOI: 10.1111/gcb.13069.

Abdelhamed, M. S., M. E. Elshamy, S. Razavi, and H. S. Wheater, 2023: Challenges in Hydrologic-Land Surface Modeling of Permafrost Signatures—A Canadian Perspective. *Journal of Advances in Modeling Earth Systems*, **15**, e2022MS003013, DOI: 10.1029/2022MS003013.

Abraham, J. P., M. Baringer, N. L. Bindoff, T. Boyer, L. J. Cheng, J. A. Church, J. L. Conroy, C. M. Domingues, J. T. Fasullo, J. Gilson, G. Goni, S. A. Good, J. M. Gorman, V. Gouretski, M. Ishii, G. C. Johnson, S. Kizu, J. M. Lyman, A. M. Macdonald, W. J. Minkowycz, S. E. Moffitt, M. D. Palmer, A. R. Piola, F. Reseghetti, K. Schuckmann, K. E. Trenberth, I. Velicogna, and J. K. Willis, 2013: A review of global ocean temperature observations: Implications for ocean heat content estimates and climate change. *Reviews of Geophysics*, **51**, 450–483, DOI: 10.1002/rog.20022.

Alexeev, V. A., D. J. Nicolsky, V. E. Romanovsky, and D. M. Lawrence, 2007: An evaluation of deep soil configurations in the CLM3 for improved representation of permafrost. *Geophysical Research Letters*, **34**, L09502, DOI: 10.1029/2007GL029536.

Andresen, C. G., D. M. Lawrence, C. J. Wilson, A. D. McGuire, C. Koven, K. Schaefer, E. Jafarov, S. Peng, X. Chen, I. Gouttevin, E. Burke, S. Chadburn, D. Ji, G. Chen, D. Hayes, and W. Zhang, 2020: Soil moisture and hydrology projections of the permafrost region - a model intercomparison. *The Cryosphere*, **14**, 445–459, DOI: 10.5194/tc-14-445-2020.

Antón, S. C., 2012: Early Homo: Who, When, and Where. *Current Anthropology*, **53**, S278–S298, DOI: 10.1086/667695.

Arkhangelskaya, T. and K. Lukyashchenko, 2018: Estimating soil thermal diffusivity at different water contents from easily available data on soil texture, bulk density, and organic carbon content. *Biosystems Engineering*, **168**, 83–95, DOI: 10.1016/j.biosystemseng.2017.06.011.

Ban-Weiss, G. A., G. Bala, L. Cao, J. Pongratz, and K. Caldeira, 2011: Climate forcing and response to idealized changes in surface latent and sensible heat. *Environmental Research Letters*, **6**, 034032, DOI: 10.1088/1748-9326/6/3/034032.

Bartlett, M. G., D. S. Chapman, and R. N. Harris, 2005: Snow effect on North American ground temperatures, 1950–2002. *Journal of Geophysical Research: Earth Surface*, **110**, F03008, DOI: 10.1029/2005JF000293.

— 2006: A Decade of Ground–Air Temperature Tracking at Emigrant Pass Observatory, Utah. *Journal of Climate*, **19**, 3722–3731, DOI: 10.1175/JCLI3808.1.

Bell, J. E., M. A. Palecki, C. B. Baker, W. G. Collins, J. H. Lawrimore, R. D. Leeper, M. E. Hall, J. Kochendorfer, T. P. Meyers, T. Wilson, and H. J. Diamond, 2013: U.S. Climate Reference Network Soil Moisture and Temperature Observations. *Journal of Hydrometeorology*, **14**, 977–988, DOI: 10.1175/JHM-D-12-0146.1.

Beltrami, H., 2002: Climate from borehole data: Energy fluxes and temperatures since 1500. *Geophysical Research Letters*, **29**, 26–1–26–4, DOI: 10.1029/2002GL015702.

Beltrami, H., G. S. Matharoo, and J. E. Smerdon, 2015: Impact of borehole depths on reconstructed estimates of ground surface temperature histories and energy storage. *Journal of Geophysical Research: Earth Surface*, **120**, 763–778, DOI: 10.1002/2014JF003382.

Beltrami, H., G. S. Matharoo, J. E. Smerdon, L. Illanes, and L. Tarasov, 2017: Impacts of the Last Glacial Cycle on ground surface temperature reconstructions over the last millennium. *Geophysical Research Letters*, **44**, 355–364, DOI: 10.1002/2016GL071317.

Beltrami, H., J. E. Smerdon, H. N. Pollack, and S. Huang, 2002: Continental heat gain in the global climate system. *Geophysical Research Letters*, **29**, 8–1–8–3, DOI: 10.1029/2001GL014310.

Berger, A., 1978: Long-term variations of daily insolation and Quaternary climatic changes. *Journal of Atmospheric Sciences*, **35**, 2362–2367, DOI: 10.1175/1520-0469(1978)035¡2362:LTVODI¿2.0.CO;2.

Berry, H. C., K. V. Cashman, and C. A. Williams, 2021: The 1902 Plinian eruption of Santa María volcano, Guatemala: A new assessment of magnitude and

impact using historical sources. *Journal of Volcanology and Geothermal Research*, **414**, 107167, DOI: 10.1016/j.jvolgeores.2020.107167.

Bi, D., M. Dix, S. Marsland, S. O'Farrell, A. Sullivan, R. Bodman, R. Law, I. Harman, S. Jhan, H. Rashid, P. Dobrohotoff, M. Chloe, Y. Hailin, H. Tony, A. Savita, F. Dias, R. Fiedler, and A. Heerdegen, 2020: Configuration and spin-up of ACCESS-CM2, the new generation Australian Community Climate and Earth System Simulator Coupled Model. *Journal of Southern Hemisphere Earth System Science*, **70**, DOI: 10.1071/ES19040.

Birch, A. F., 1948: The effects of Pleistocene climatic variations upon geothermal gradients. *American Journal of Science*, **246**, 729–760, DOI: 10.2475/AJS.246.12.729.

Biskaborn, B., S. Smith, J. Noetzli, H. Matthes, G. Vieira, D. Streletskiy, P. Schoeneich, V. Romanovsky, A. Lewkowicz, A. Abramov, M. Allard, J. Boike, W. Cable, H. Christiansen, R. Delaloye, B. Diekmann, D. Drozdov, B. Etzelmüller, G. Grosse, and H. Lantuit, 2019: Permafrost is warming at a global scale. *Nature Communications*, **10**, 264, DOI: 10.1038/s41467-018-08240-4.

Biskaborn, B. K., J.-P. Lanckman, H. Lantuit, K. Elger, D. A. Streletskiy, W. L. Cable, and V. E. Romanovsky, 2015: The new database of the Global Terrestrial Network for Permafrost (GTN-P). *Earth System Science Data*, **7**, 245–259, DOI: 10.5194/essd-7-245-2015.

Blunden, J. and T. Boyer, 2021: State of the Climate in 2020. *Bulletin of the American Meteorological Society*, **102**, S1–S475, DOI: 10.1175/2021BAMSStateoftheClimate.1.

Blyth, E. M., V. K. Arora, D. B. Clark, S. J. Dadson, M. G. De Kauwe, D. M. Lawrence, J. R. Melton, J. Pongratz, R. H. Turton, K. Yoshimura, and H. Yuan, 2021: Advances in land surface modelling. *Current Climate Change Reports*, **7**, 45–71, DOI: 10.1007/s40641-021-00171-5.

Boltzmann, L., 1884: Ableitung des Stefan'schen Gesetzes, betreffend die Abhängigkeit der Wärmestrahlung von der Temperatur aus der electromagnetischen Lichttheorie. *Annalen der Physik*, **258**, 291–294, DOI: 10.1002/andp.18842580616.

Bonan, G. B., 2008: Forests and Climate Change: Forcings, Feedbacks, and the Climate Benefits of Forests. *Science*, **320**, 1444–1449, DOI: 10.1126/science.1155121.

Bonan, G. B. and S. C. Doney, 2018: Climate, ecosystems, and planetary futures: The challenge to predict life in Earth system models. *Science*, **359**, eaam8328, DOI: 10.1126/science.aam8328.

Bond-Lamberty, B. and A. Thomson, 2010: Temperature-Associated Increases in the Global Soil Respiration Record. *Nature*, **464**, 579–582, DOI: 10.1038/na-

ture08930.

Boucher, O., J. Servonnat, A. L. Albright, O. Aumont, Y. Balkanski, V. Bastrikov, S. Bekki, R. Bonnet, S. Bony, L. Bopp, P. Braconnot, P. Brockmann, P. Cadule, A. Caubel, F. Cheruy, F. Codron, A. Cozic, D. Cugnet, F. D'Andrea, P. Davini, C. de Lavergne, S. Denvil, J. Deshayes, M. Devilliers, A. Ducharne, J.-L. Dufresne, E. Dupont, C. Éthé, L. Fairhead, L. Falletti, S. Flavoni, M.-A. Foujols, S. Gardoll, G. Gastineau, J. Ghattas, J.-Y. Grandpeix, B. Guenet, E. Guez, Lionel, E. Guilyardi, M. Guimberteau, D. Hauglustaine, F. Hourdin, A. Idelkadi, S. Joussaume, M. Kageyama, M. Khodri, G. Krinner, N. Lebas, G. Levavasseur, C. Lévy, L. Li, F. Lott, T. Lurton, S. Luyssaert, G. Madec, J.-B. Madeleine, F. Maignan, M. Marchand, O. Marti, L. Mellul, Y. Meurdesoif, J. Mignot, I. Musat, C. Ottlé, P. Peylin, Y. Planton, J. Polcher, C. Rio, N. Rochetin, C. Rousset, P. Sepulchre, A. Sima, D. Swingedouw, R. Thiéblemont, A. K. Traore, M. Vancoppenolle, J. Vial, J. Vialard, N. Viovy, and N. Vuichard, 2020: Presentation and Evaluation of the IPSL-CM6A-LR Climate Model. *Journal of Advances in Modeling Earth Systems*, **12**, e2019MS002010, DOI: 10.1029/2019MS002010.

Brady, N. C. and R. R. Weil, 2017: *The nature and properties of soils. 15th edition*. Pearson Prentice Hall, Upper Saddle River, NJ, United States.

Brandsma, T. and G. P. Können, 2006: Application of nearest-neighbor resampling for homogenizing temperature records on a daily to sub-daily level. *International Journal of Climatology*, **26**, 75–89, DOI: 10.1002/joc.1236.

Brewer, P. G. and E. T. Peltzer, 2019: The Molecular Basis for the Heat Capacity and Thermal Expansion of Natural Waters. *Geophysical Research Letters*, **46**, 13227–13233, DOI: 10.1029/2019GL085117.

Brigham, E. O. and R. E. Morrow, 1967: The fast Fourier transform. *IEEE Spectrum*, **4**, 63–70, DOI: 10.1109/MSPEC.1967.5217220.

Brown, J., O. Ferrians, J. A. Heginbottom, and E. Melnikov., 2002: Circum-Arctic Map of Permafrost and Ground-Ice Conditions, Version 2.

Brown, J., K. Hinkel, and F. Nelson, 2000: The Circumpolar Active Layer Monitoring (CALM) program. *Polar Geography*, **24**, 166–258, DOI: 10.1080/10889370009377698.

Budyko, M. I., 1969: The effect of solar radiation variations on the climate of the Earth. *Tellus*, **21**, 611–619, DOI: https://doi.org/10.1111/j.2153-3490.1969.tb00466.x.

Burke, E. J., S. E. Chadburn, and A. Ekici, 2017: A vertical representation of soil carbon in the JULES land surface scheme (vn4.3_permafrost) with a focus on permafrost regions. *Geoscientific Model Development*, **10**, 959–975, DOI: 10.5194/gmd-10-959-2017.

Burke, E. J., C. D. Jones, and C. D. Koven, 2013: Estimating the Permafrost-Carbon Climate Response in the CMIP5 Climate Models Using a Simplified Approach. *Journal of Climate*, **26**, 4897–4909, DOI: 10.1175/JCLI-D-12-00550.1.

Burke, E. J., Y. Zhang, and G. Krinner, 2020: Evaluating permafrost physics in the Coupled Model Intercomparison Project 6 (CMIP6) models and their sensitivity to climate change. *The Cryosphere*, **14**, 3155–3174, DOI: 10.5194/tc-14-3155-2020.

Burke, M., S. Hsiang, and E. Miguel, 2015: Global non-linear effect of temperature on economic production. *Nature*, **527**, 235–239, DOI: 10.1038/nature15725.

Butchart, S. H. M., M. Walpole, B. Collen, A. van Strien, J. P. W. Scharlemann, R. E. A. Almond, J. E. M. Baillie, B. Bomhard, C. Brown, J. Bruno, K. E. Carpenter, G. M. Carr, J. Chanson, A. M. Chenery, J. Csirke, N. C. Davidson, F. Dentener, M. Foster, A. Galli, J. N. Galloway, P. Genovesi, R. D. Gregory, M. Hockings, V. Kapos, J.-F. Lamarque, F. Leverington, J. Loh, M. A. McGeoch, L. McRae, A. Minasyan, M. H. Morcillo, T. E. E. Oldfield, D. Pauly, S. Quader, C. Revenga, J. R. Sauer, B. Skolnik, D. Spear, D. Stanwell-Smith, S. N. Stuart, A. Symes, M. Tierney, T. D. Tyrrell, J.-C. Vié, and R. Watson, 2010: Global Biodiversity: Indicators of Recent Declines. *Science*, **328**, 1164–1168, DOI: 10.1126/science.1187512.

Canadell, J., P. Monteiro, M. Costa, L. Cotrim da Cunha, P. Cox, A. Eliseev, S. Henson, M. Ishii, S. Jaccard, C. Koven, A. Lohila, P. Patra, S. Piao, J. Rogelj, S. Syampungani, S. Zaehle, and K. Zickfeld, 2021: Global Carbon and other Biogeochemical Cycles and Feedbacks. *Climate Change 2021: The Physical Science Basis. Contribution of Working Group I to the Sixth Assessment Report of the Intergovernmental Panel on Climate Change*, V. Masson-Delmotte, P. Zhai, A. Pirani, S. L. Connors, C. Péan, S. Berger, N. Caud, Y. Chen, L. Goldfarb, M. I. Gomis, M. Huang, K. Leitzell, E. Lonnoy, J. B. R. Matthews, T. K. Maycock, T. Waterfield, O. Yelekçi, R. Yu, and B. Zhou, eds., Cambridge University Press, Cambridge, UK and New York, NY, USA, Chapter 5, 673–815.

Carslaw, H. S. and J. C. Jaeger, 1959: *Conduction of heat in solids*, volume 2nd ed. Oxford University Press, New York.

Ceballos, G. and P. R. Ehrlich, 2023: Mutilation of the tree of life via mass extinction of animal genera. *Proceedings of the National Academy of Sciences*, **120**, e2306987120, DOI: 10.1073/pnas.2306987120.

Cermak, V., 1971: Underground temperature and inferred climatic temperature of the past millenium. *Palaeogeography, Palaeoclimatology, Palaeoecology*, **10**, 1–19, DOI: 10.1016/0031-0182(71)90043-5.

Cermak, V. and L. Bodri, 2016: Attribution of precipitation changes on ground–air temperature offset: Granger causality analysis. *International Journal of Earth Sciences*, **107**, 145–152, DOI: 10.1007/s00531-016-1351-y.

Cermak, V., L. Bodri, M. Kresl, P. Dedecek, and J. Safanda, 2017: Eleven years of ground–air temperature tracking over different land cover types. *International Journal of Climatology*, **37**, 1084–1099, DOI: 10.1002/joc.4764.

Cermak, V., L. Bodri, J. Šafanda, M. Kresl, and P. Dedecek, 2014: Ground-air temperature tracking and multi-year cycles in the subsurface temperature time series at geothermal climate-change observatory. *Studia Geophysica et Geodaetica*, **58**, 403–424, DOI: 10.1007/s11200-013-0356-2.

Chadburn, S. E., E. J. Burke, R. L. H. Essery, J. Boike, M. Langer, M. Heikenfeld, P. M. Cox, and P. Friedlingstein, 2015: Impact of model developments on present and future simulations of permafrost in a global land-surface model. *The Cryosphere*, **9**, 1505–1521, DOI: 10.5194/tc-9-1505-2015.

Chen, D., M. Rojas, B. Samset, K. Cobb, A. Diongue Niang, P. Edwards, S. Emori, S. Faria, E. Hawkins, P. Hope, P. Huybrechts, M. Meinshausen, S. Mustafa, G.-K. Plattner, and A.-M. Tréguier, 2021: Framing, context, and Methods. *Climate Change 2021: The Physical Science Basis. Contribution of Working Group I to the Sixth Assessment Report of the Intergovernmental Panel on Climate Change*, V. Masson-Delmotte, P. Zhai, A. Pirani, S. L. Connors, C. Péan, S. Berger, N. Caud, Y. Chen, L. Goldfarb, M. I. Gomis, M. Huang, K. Leitzell, E. Lonnoy, J. B. R. Matthews, T. K. Maycock, T. Waterfield, O. Yelekçi, R. Yu, and B. Zhou, eds., Cambridge University Press, Cambridge, UK and New York, NY, USA, Chapter 1, 147–286.

Chen, H.-M., J. Li, J.-Z. Su, L.-J. Hua, X.-Y. Rong, Y.-F. Xin, and Z.-Q. Zhang, 2019: Introduction of CAMS-CSM model and its participation in CMIP6. *Advances in Climate Change Research*, **15**, 540–544, DOI: 10.12006/j.issn.1673-1719.2019.186.

Chen, Y., F. Liu, L. Kang, D. Zhang, D. Kou, C. Mao, S. Qin, Q. Zhang, and Y. Yang, 2021: Large-scale evidence for microbial response and associated carbon release after permafrost thaw. *Global Change Biology*, **27**, 3218–3229, DOI: 10.1111/gcb.15487.

Cherchi, A., P. G. Fogli, T. Lovato, D. Peano, D. Iovino, S. Gualdi, S. Masina, E. Scoccimarro, S. Materia, A. Bellucci, and A. Navarra, 2019: Global Mean Climate and Main Patterns of Variability in the CMCC-CM2 Coupled Model. *Journal of Advances in Modeling Earth Systems*, **11**, 185–209, DOI: 10.1029/2018MS001369.

Claussen, M., L. Mysak, A. Weaver, M. Crucifix, T. Fichefet, M.-F. Loutre, S. Weber, J. Alcamo, V. Alexeev, A. Berger, R. Calov, A. Ganopolski, H. Goosse, G. Lohmann, F. Lunkeit, I. Mokhov, V. Petoukhov, P. Stone, and Z. Wang,

2002: Earth system models of intermediate complexity: closing the gap in the spectrum of climate system models. *Climate Dynamics*, **18**, 579–586, DOI: 10.1007/s00382-001-0200-1.

Cook, B., G. Bonan, S. Levis, and H. Epstein, 2008: The thermoinsulation effect of snow cover within a climate model. *Climate Dynamics*, **31**, 107–124, DOI: 10.1007/S00382-007-0341-Y.

Courant, R., K. Friedrichs, and H. Lewy, 1928: Über die partiellen Differenzengleichungen der mathematischen Physik. *Math. Ann.*, **100**, 32–74.

Craig, A., S. Valcke, and L. Coquart, 2017: Development and performance of a new version of the OASIS coupler, OASIS3-MCT_3.0. *Geoscientific Model Development*, **10**, 3297–3308, DOI: 10.5194/gmd-10-3297-2017.

Crowley, T. J., 2000: Causes of Climate Change Over the Past 1000 Years. *Science*, **289**, 270–277, DOI: 10.1126/science.289.5477.270.

Cuesta-Valero, F. J., H. Beltrami, A. García-García, G. Krinner, M. Langer, A. H. MacDougall, J. Nitzbon, J. Peng, K. von Schuckmann, S. I. Seneviratne, W. Thiery, I. Vanderkelen, and T. Wu, 2023: Continental heat storage: contributions from the ground, inland waters, and permafrost thawing. *Earth System Dynamics*, **14**, 609–627, DOI: 10.5194/esd-14-609-2023.

Cuesta-Valero, F. J., H. Beltrami, S. Gruber, A. García-García, and J. F. González-Rouco, 2022: A new bootstrap technique to quantify uncertainty in estimates of ground surface temperature and ground heat flux histories from geothermal data. *Geoscientific Model Development*, **15**, 7913–7932, DOI: 10.5194/gmd-15-7913-2022.

Cuesta-Valero, F. J., A. García-García, H. Beltrami, and J. Finnis, 2021a: First assessment of the earth heat inventory within CMIP5 historical simulations. *Earth System Dynamics*, **12**, 581–600, DOI: 10.5194/esd-12-581-2021.

Cuesta-Valero, F. J., A. García-García, H. Beltrami, F. García-Pereira, J. F. González-Rouco, and J. Peng, 2025: Robust increase in observed heat storage by the global subsurface. *Science Advances*, in review.

Cuesta-Valero, F. J., A. García-García, H. Beltrami, J. F. González-Rouco, and E. García-Bustamante, 2021b: Long-term global ground heat flux and continental heat storage from geothermal data. *Climate of the Past*, **17**, 451–468, DOI: 10.5194/cp-17-451-2021.

Cuesta-Valero, F. J., A. García-García, H. Beltrami, and J. E. Smerdon, 2016: First assessment of continental energy storage in CMIP5 simulations. *Geophysical Research Letters*, **43**, 5326–5335, DOI: 10.1002/2016GL068496.

Dai, Y., N. Wei, H. Yuan, S. Zhang, W. Shangguan, S. Liu, X. Lu, and Y. Xin, 2019: Evaluation of Soil Thermal Conductivity Schemes for Use in Land Surface Modeling. *Journal of Advances in Modeling Earth Systems*, **11**, 3454–3473, DOI: 10.1029/2019MS001723.

Danabasoglu, G., J.-F. Lamarque, J. Bacmeister, D. A. Bailey, A. K. DuVivier, J. Edwards, L. K. Emmons, J. Fasullo, R. Garcia, A. Gettelman, C. Hannay, M. M. Holland, W. G. Large, P. H. Lauritzen, D. M. Lawrence, J. T. M. Lenaerts, K. Lindsay, W. H. Lipscomb, M. J. Mills, R. Neale, K. W. Oleson, B. Otto-Bliesner, A. S. Phillips, W. Sacks, S. Tilmes, L. van Kampenhout, M. Vertenstein, A. Bertini, J. Dennis, C. Deser, C. Fischer, B. Fox-Kemper, J. E. Kay, D. Kinnison, P. J. Kushner, V. E. Larson, M. C. Long, S. Mickelson, J. K. Moore, E. Nienhouse, L. Polvani, P. J. Rasch, and W. G. Strand, 2020: The Community Earth System Model Version 2 (CESM2). *Journal of Advances in Modeling Earth Systems*, **12**, e2019MS001916, DOI: 10.1029/2019MS001916.

Davison, A. C. and D. V. Hinkley, 1997: *Bootstrap Methods and their Application*. Cambridge Series in Statistical and Probabilistic Mathematics, Cambridge University Press.

de Vrese, P., L. Beckebanze, L. d. A. Galera, D. Holl, T. Kleinen, L. Kutzbach, Z. Rehder, and V. Brovkin, 2023: Sensitivity of Arctic CH_4 emissions to landscape wetness diminished by atmospheric feedbacks. *Nature Climate Change*, **13**, 832–839, DOI: 10.1038/s41558-023-01715-3.

de Vrese, P. and V. Brovkin, 2021: Timescales of the permafrost carbon cycle and legacy effects of temperature overshoot scenarios. *Nature Communications*, **12**, 2688, DOI: 10.1038/s41467-021-23010-5.

de Vrese, P., G. Georgievski, J. F. Gonzalez Rouco, D. Notz, T. Stacke, N. J. Steinert, S. Wilkenskjeld, and V. Brovkin, 2023: Representation of soil hydrology in permafrost regions may explain large part of inter-model spread in simulated Arctic and subarctic climate. *The Cryosphere*, **17**, 2095–2118, DOI: 10.5194/tc-17-2095-2023.

de Vrese, P., T. Stacke, V. Gayler, and V. Brovkin, 2024: Permafrost cloud feedback may amplify climate change. *Geophysical Research Letters*, **51**, e2024GL109034, DOI: 10.1029/2024GL109034.

de Vries, D. A., 1963: Thermal properties of soil. *Physics of Plant Environment*, W. R. van Dijk, ed., North Holland Publishing, Amsterdam, 210–235.

Demetrescu, C., D. Nitoiu, C. Boroneant, A. Marica, and B. Lucaschi, 2007: Thermal signal propagation in soils in Romania: conductive and non-conductive processes. *Climate of the Past*, **3**, 637–645, DOI: 10.5194/cp-3-637-2007.

Diao, N., Q. Li, and Z. Fang, 2004: Heat transfer in ground heat exchangers with groundwater advection. *International Journal of Thermal Sciences*, **43**, 1203–1211, DOI: 10.1016/J.IJTHERMALSCI.2004.04.009.

Dorau, K., C. Bamminger, D. Koch, and T. Mansfeldt, 2022: Evidences of soil warming from long-term trends (1951–2018) in North Rhine-Westphalia, Germany. *Climatic Change*, **170**, 1–13, DOI: 10.1007/s10584-021-03293-.

Döscher, R., M. Acosta, A. Alessandri, P. Anthoni, A. Arneth, T. Arsouze, T. Bergmann, R. Bernadello, S. Bousetta, L.-P. Caron, G. Carver, M. Castrillo, F. Catalano, I. Cvijanovic, P. Davini, E. Dekker, F. J. Doblas-Reyes, D. Docquier, P. Echevarria, U. Fladrich, R. Fuentes-Franco, M. Gröger, J. v. Hardenberg, J. Hieronymus, M. P. Karami, J.-P. Keskinen, T. Koenigk, R. Makkonen, F. Massonnet, M. Ménégoz, P. A. Miller, E. Moreno-Chamarro, L. Nieradzik, T. van Noije, P. Nolan, D. O'Donnell, P. Ollinaho, G. van den Oord, P. Ortega, O. T. Prims, A. Ramos, T. Reerink, C. Rousset, Y. Ruprich-Robert, P. Le Sager, T. Schmith, R. Schrödner, F. Serva, V. Sicardi, M. Sloth Madsen, B. Smith, T. Tian, E. Tourigny, P. Uotila, M. Vancoppenolle, S. Wang, D. Wårlind, U. Willén, K. Wyser, S. Yang, X. Yepes-Arbós, and Q. Zhang, 2021: The EC-Earth3 Earth System Model for the Climate Model Intercomparison Project 6. *Geoscientific Model Development Discussions*, **2021**, 1–90, DOI: 10.5194/gmd-2020-446.

Duan, H., G. Zhang, S. Wang, and Y. Fan, 2019: Robust climate change research: a review on multi-model analysis. *Environmental Research Letters*, **14**, 033001, DOI: 10.1088/1748-9326/aaf8f9.

Dunne, J. P., L. W. Horowitz, A. J. Adcroft, P. Ginoux, I. M. Held, J. G. John, J. P. Krasting, S. Malyshev, V. Naik, F. Paulot, E. Shevliakova, C. A. Stock, N. Zadeh, V. Balaji, C. Blanton, K. A. Dunne, C. Dupuis, J. Durachta, R. Dussin, P. P. G. Gauthier, S. M. Griffies, H. Guo, R. W. Hallberg, M. Harrison, J. He, W. Hurlin, C. McHugh, R. Menzel, P. C. D. Milly, S. Nikonov, D. J. Paynter, J. Ploshay, A. Radhakrishnan, K. Rand, B. G. Reichl, T. Robinson, D. M. Schwarzkopf, L. T. Sentman, S. Underwood, H. Vahlenkamp, M. Winton, A. T. Wittenberg, B. Wyman, Y. Zeng, and M. Zhao, 2020: The GFDL Earth System Model Version 4.1 (GFDL-ESM 4.1): Overall Coupled Model Description and Simulation Characteristics. *Journal of Advances in Modeling Earth Systems*, **12**, e2019MS002015, DOI: 10.1029/2019MS002015.

Dunne, K. A. and C. J. Willmott, 1996: Global distribution of plant-extractable water capacity of soil. *International Journal of Climatology*, **16**, 841–859, DOI: 10.1002/(SICI)1097-0088(199608)16:8¡841::AID-JOC60¿3.0.CO;2-8.

Ebita, A., S. Kobayashi, Y. Ota, M. Moriya, R. Kumabe, K. Onogi, Y. Harada, S. Yasui, K. Miyaoka, K. Takahashi, H. Kamahori, C. Kobayashi, H. Endo, M. Soma, Y. Oikawa, and T. Ishimizu, 2011: The Japanese 55-year Reanalysis JRA-55: An Interim Report. *SOLA*, **7**, 149–152, DOI: 10.2151/sola.2011-038.

Ekici, A., C. Beer, S. Hagemann, J. Boike, M. Langer, and C. Hauck, 2014: Simulating high-latitude permafrost regions by the JSBACH terrestrial ecosystem model. *Geoscientific Model Development*, **7**, 631–647, DOI: 10.5194/gmd-7-631-2014.

Evin, G., A. Ribes, and L. Corre, 2024: Assessing CMIP6 uncertainties at global warming levels. *Climate Dynamics*, **62**, 8057–8072, DOI: 10.1007/s00382-024-07323-x.

Eyring, V., S. Bony, G. A. Meehl, C. A. Senior, B. Stevens, R. J. Stouffer, and K. E. Taylor, 2016: Overview of the Coupled Model Intercomparison Project Phase 6 (CMIP6) experimental design and organization. *Geoscientific Model Development*, **9**, 1937–1958, DOI: 10.5194/gmd-9-1937-2016.

Farquharson, L. M., V. E. Romanovsky, W. L. Cable, D. A. Walker, S. V. Kokelj, and D. Nicolsky, 2019: Climate Change Drives Widespread and Rapid Thermokarst Development in Very Cold Permafrost in the Canadian High Arctic. *Geophysical Research Letters*, **46**, 6681–6689, DOI: 10.1029/2019GL082187.

Ferguson, G., 2015: Screening for Heat Transport by Groundwater in Closed Geothermal Systems. *Groundwater*, **53**, 503–506, DOI: 10.1111/gwat.12162.

Fernández-Castillo, P., C. Román-Cascón, and C. Yagüe, 2025: Impact of snow cover on the surface energy balance and its contribution to the extreme cold wave in Spain after snowstorm Filomena. *Atmospheric Research*, **320**, 108015, DOI: 10.1016/j.atmosres.2025.108015.

Fernández-Donado, L., J. F. González-Rouco, C. C. Raible, C. M. Ammann, D. Barriopedro, E. García-Bustamante, J. H. Jungclaus, S. J. Lorenz, J. Luterbacher, S. J. Phipps, J. Servonnat, D. Swingedouw, S. F. B. Tett, S. Wagner, P. Yiou, and E. Zorita, 2013: Large-scale temperature response to external forcing in simulations and reconstructions of the last millennium. *Climate of the Past*, **9**, 393–421, DOI: 10.5194/cp-9-393-2013.

Fisher, R. A. and C. D. Koven, 2020: Perspectives on the Future of Land Surface Models and the Challenges of Representing Complex Terrestrial Systems. *Journal of Advances in Modeling Earth Systems*, **12**, e2018MS001453, DOI: 10.1029/2018MS001453.

Fisher, R. A., W. R. Wieder, B. M. Sanderson, C. D. Koven, K. W. Oleson, C. Xu, J. B. Fisher, M. Shi, A. P. Walker, and D. M. Lawrence, 2019: Parametric Controls on Vegetation Responses to Biogeochemical Forcing in the CLM5. *Journal of Advances in Modeling Earth Systems*, **11**, 2879–2895, DOI: 10.1029/2019MS001609.

Flato, G. M., 2011: Earth system models: an overview. *WIREs Climate Change*, **2**, 783–800, DOI: 10.1002/wcc.148.

Forster, P., T. Storelvmo, K. Armour, W. Collins, J.-L. Dufresne, D. Frame, D. Lunt, T. Mauritsen, M. Palmer, M. Watanabe, M. Wild, and H. Zhang, 2021: The Earth's Energy Budget, Climate Feedbacks, and Climate Sensitivity. *Climate Change 2021: The Physical Science Basis. Contribution of Working Group I to the Sixth Assessment Report of the Intergovernmental Panel*

on Climate Change, V. Masson-Delmotte, P. Zhai, A. Pirani, S. L. Connors, C. Péan, S. Berger, N. Caud, Y. Chen, L. Goldfarb, M. I. Gomis, M. Huang, K. Leitzell, E. Lonnoy, J. B. R. Matthews, T. K. Maycock, T. Waterfield, O. Yelekçi, R. Yu, and B. Zhou, eds., Cambridge University Press, Cambridge, UK and New York, NY, USA, Chapter 7, 923–1054.

Forzieri, G., V. Dakos, N. G. McDowell, A. Ramdane, and A. Cescatti, 2022: Emerging signals of declining forest resilience under climate change. *Nature*, **608**, 534–539, DOI: 10.1038/s41586-022-04959-9.

Friedlingstein, P., M. W. Jones, M. O'Sullivan, R. M. Andrew, D. C. E. Bakker, J. Hauck, C. Le Quéré, G. P. Peters, W. Peters, J. Pongratz, S. Sitch, J. G. Canadell, P. Ciais, R. B. Jackson, S. R. Alin, P. Anthoni, N. R. Bates, M. Becker, N. Bellouin, L. Bopp, T. T. T. Chau, F. Chevallier, L. P. Chini, M. Cronin, K. I. Currie, B. Decharme, L. M. Djeutchouang, X. Dou, W. Evans, R. A. Feely, L. Feng, T. Gasser, D. Gilfillan, T. Gkritzalis, G. Grassi, L. Gregor, N. Gruber, O. Gürses, I. Harris, R. A. Houghton, G. C. Hurtt, Y. Iida, T. Ilyina, I. T. Luijkx, A. Jain, S. D. Jones, E. Kato, D. Kennedy, K. Klein Goldewijk, J. Knauer, J. I. Korsbakken, A. Körtzinger, P. Landschützer, S. K. Lauvset, N. Lefèvre, S. Lienert, J. Liu, G. Marland, P. C. McGuire, J. R. Melton, D. R. Munro, J. E. M. S. Nabel, S.-I. Nakaoka, Y. Niwa, T. Ono, D. Pierrot, B. Poulter, G. Rehder, L. Resplandy, E. Robertson, C. Rödenbeck, T. M. Rosan, J. Schwinger, C. Schwingshackl, R. Séférian, A. J. Sutton, C. Sweeney, T. Tanhua, P. P. Tans, H. Tian, B. Tilbrook, F. Tubiello, G. R. van der Werf, N. Vuichard, C. Wada, R. Wanninkhof, A. J. Watson, D. Willis, A. J. Wiltshire, W. Yuan, C. Yue, X. Yue, S. Zaehle, and J. Zeng, 2022: Global Carbon Budget 2021. *Earth System Science Data*, **14**, 1917–2005, DOI: 10.5194/essd-14-1917-2022.

Frölicher, T. L., M. Winton, and J. L. Sarmiento, 2014: Continued global warming after CO_2 emissions stoppage. *Nature Climate Change*, **4**, 40–44, DOI: 10.1038/nclimate2060.

Frölicher, T. L. and D. J. Paynter, 2015: Extending the relationship between global warming and cumulative carbon emissions to multi-millennial timescales. *Environmental Research Letters*, **10**, 075002, DOI: 10.1088/1748-9326/10/7/075002.

Ganopolski, A., 2024: Toward generalized Milankovitch theory (GMT). *Climate of the Past*, **20**, 151–185, DOI: 10.5194/cp-20-151-2024.

Gao, Z., D. H. Lenschow, R. Horton, M. Zhou, L. Wang, and J. Wen, 2008: Comparison of two soil temperature algorithms for a bare ground site on the Loess Plateau in China. *Journal of Geophysical Research: Atmospheres*, **113**, D18105, DOI: 10.1029/2008JD010285.

García-Pereira, F., J. F. González-Rouco, N. Meabe-Yanguas, and J. Jungclaus, 2025b: Insufficient soil depth constrains ground heat flux in Land Surface Models. *Geophysical Research Letters*, In preparation.

García-Pereira, F., J. F. González-Rouco, N. Meabe-Yanguas, N. J. Steinert, P. de Vrese, J. Jungclaus, and S. Lorenz, 2025a: Permafrost sensitivity to changes in soil hydro-thermodynamics in historical and scenario simulations with a modified version of the MPI-ESM. *The Cryopshere*, [preprint], DOI: 10.5194/egusphere-2025-2126.

García-Pereira, F., J. F. González-Rouco, C. Melo-Aguilar, N. J. Steinert, E. García-Bustamante, P. de Vrese, J. Jungclaus, S. Lorenz, S. Hagemann, F. J. Cuesta-Valero, A. García-García, and H. Beltrami, 2024b: First comprehensive assessment of industrial-era land heat uptake from multiple sources. *Earth System Dynamics*, **15**, 547–564, DOI: 10.5194/esd-15-547-2024.

García-Pereira, F., J. F. González-Rouco, T. Schmid, C. Melo-Aguilar, C. Vegas-Cañas, N. J. Steinert, P. J. Roldán-Gómez, F. J. Cuesta-Valero, A. García-García, H. Beltrami, and P. de Vrese, 2024a: Thermodynamic and hydrological drivers of the soil and bedrock thermal regimes in central Spain. *SOIL*, **10**, 1–21, DOI: 10.5194/soil-10-1-2024.

Garcia-Pereira, F. and J. F. González-Rouco, 2024: Conform: a one-dimensional heat conduction forward model. 10.5281/zenodo.10371439.

García-García, A., F. J. Cuesta-Valero, H. Beltrami, and J. E. Smerdon, 2016: Simulation of air and ground temperatures in PMIP3/CMIP5 last millennium simulations: implications for climate reconstructions from borehole temperature profiles. *Environmental Research Letters*, **11**, 044022, DOI: 10.1088/1748-9326/11/4/044022.

— 2019: Characterization of Air and Ground Temperature Relationships within the CMIP5 Historical and Future Climate Simulations. *Journal of Geophysical Research: Atmospheres*, **124**, 3903–3929, DOI: 10.1029/2018JD030117.

García-García, A., F. J. Cuesta-Valero, D. Miralles, M. Mahecha, J. Quaas, M. Reichstein, J. Zscheischler, and J. Peng, 2023: Soil heat extremes can outpace air temperature extremes. *Nature Climate Change*, 1–5, DOI: 10.1038/s41558-023-01812-3.

Gaybullaev, B., S. Chen, and Y. Kuo, 2012: Large-scale desiccation of the Aral Sea due to over-exploitation after 1960. *Journal of Mountain Science*, **9**, 538–546, DOI: 10.1007/s11629-012-2273-1.

Gettelman, A., M. J. Mills, D. E. Kinnison, R. R. Garcia, A. K. Smith, D. R. Marsh, S. Tilmes, F. Vitt, C. G. Bardeen, J. McInerny, H.-L. Liu, S. C. Solomon, L. M. Polvani, L. K. Emmons, J.-F. Lamarque, J. H. Richter, A. S. Glanville, J. T. Bacmeister, A. S. Phillips, R. B. Neale, I. R. Simpson, A. K. DuVivier, A. Hodzic, and W. J. Randel, 2019: The Whole Atmosphere Commu-

nity Climate Model Version 6 (WACCM6). *Journal of Geophysical Research: Atmospheres*, **124**, 12380–12403, DOI: 10.1029/2019JD030943.

Gettelman, A. and S. C. Sherwood, 2016: Processes Responsible for Cloud Feedback. *Current Climate Change Reports*, **2**, 179–189, DOI: 10.1007/s40641-016-0052-8.

Gioia, R., J. Dachs, L. Nizzetto, N. Berrojalbiz, C. Galbán, S. Del Vento, L. Méjanelle, and K. C. Jones, 2011: *Sources, Transport and Fate of Organic Pollutants in the Oceanic Environment*, Springer, Berlin, Heidelberg, Chapter 8. 111–139.

Giorgetta, M., R. Brokopf, T. Crueger, M. Esch, S. Fiedler, J. Helmert, C. Hohenegger, L. Kornblueh, M. Köhler, E. Manzini, T. Mauritsen, C. Nam, T. Raddatz, S. Rast, D. Reinert, M. Sakradzija, H. Schmidt, R. Schneck, R. Schnur, L. Silvers, H. Wan, G. Zängl, and B. Stevens, 2018: ICON-A, the Atmosphere Component of the ICON Earth System Model: I. Model Description. *Journal of Advances in Modeling Earth Systems*, **10**, 1613–1637, DOI: 10.1029/2017MS001242.

Golaz, J.-C., P. M. Caldwell, L. P. Van Roekel, M. R. Petersen, Q. Tang, J. D. Wolfe, G. Abeshu, V. Anantharaj, X. S. Asay-Davis, D. C. Bader, S. A. Baldwin, G. Bisht, P. A. Bogenschutz, M. Branstetter, M. A. Brunke, S. R. Brus, S. M. Burrows, P. J. Cameron-Smith, A. S. Donahue, M. Deakin, R. C. Easter, K. J. Evans, Y. Feng, M. Flanner, J. G. Foucar, J. G. Fyke, B. M. Griffin, C. Hannay, B. E. Harrop, M. J. Hoffman, E. C. Hunke, R. L. Jacob, D. W. Jacobsen, N. Jeffery, P. W. Jones, N. D. Keen, S. A. Klein, V. E. Larson, L. R. Leung, H.-Y. Li, W. Lin, W. H. Lipscomb, P.-L. Ma, S. Mahajan, M. E. Maltrud, A. Mametjanov, J. L. McClean, R. B. McCoy, R. B. Neale, S. F. Price, Y. Qian, P. J. Rasch, J. E. J. Reeves Eyre, W. J. Riley, T. D. Ringler, A. F. Roberts, E. L. Roesler, A. G. Salinger, Z. Shaheen, X. Shi, B. Singh, J. Tang, M. A. Taylor, P. E. Thornton, A. K. Turner, M. Veneziani, H. Wan, H. Wang, S. Wang, D. N. Williams, P. J. Wolfram, P. H. Worley, S. Xie, Y. Yang, J.-H. Yoon, M. D. Zelinka, C. S. Zender, X. Zeng, C. Zhang, K. Zhang, Y. Zhang, X. Zheng, T. Zhou, and Q. Zhu, 2019: The DOE E3SM Coupled Model Version 1: Overview and Evaluation at Standard Resolution. *Journal of Advances in Modeling Earth Systems*, **11**, 2089–2129, DOI: 10.1029/2018MS001603.

González-Rouco, J. F., F. García-Pereira, C. Vegas Cañas, and N. Meabe Yanguas, 2024: Proyectando el futuro: Modelos climáticos. *Cambio climático en España*, R. Serrano-Notivoli, J. Olcina, and J. Martín-Vide, eds., Tirant Humanidades, Valencia, Chapter 5, 149–192.

González-Rouco, J. F., H. Beltrami, E. Zorita, and M. B. Stevens, 2009: Borehole climatology: a discussion based on contributions from climate modeling. *Climate of the Past*, **5**, 97–127, DOI: 10.5194/cp-5-97-2009.

González-Rouco, J. F., H. Beltrami, E. Zorita, and H. von Storch, 2006: Simulation and inversion of borehole temperature profiles in surrogate climates: Spatial distribution and surface coupling. *Geophysical Research Letters*, **33**, L01703, DOI: 10.1029/2005GL024693.

González-Rouco, J. F., N. J. Steinert, E. García-Bustamante, S. Hagemann, P. de Vrese, J. H. Jungclaus, S. J. Lorenz, C. Melo-Aguilar, F. García-Pereira, and J. Navarro, 2021: Increasing the depth of a Land Surface Model. Part I: Impacts on the soil thermal regime and energy storage. *Journal of Hydrometeorology*, **22**, 3211–3230, DOI: 10.1175/JHM-D-21-0024.1.

González-Rouco, J. F., H. von Storch, and E. Zorita, 2003: Deep soil temperature as proxy for surface air-temperature in a coupled model simulation of the last thousand years. *Geophysical Research Letters*, **30**, 2116, DOI: 10.1029/2003GL018264.

Goode, P. R., J. Qiu, V. Yurchyshyn, J. Hickey, M.-C. Chu, E. Kolbe, C. T. Brown, and S. E. Koonin, 2001: Earthshine observations of the Earth's reflectance. *Geophysical Research Letters*, **28**, 1671–1674, DOI: 10.1029/2000GL012580.

Green, J., A. Konings, H. Alemohammad, J. Berry, D. Entekhabi, J. Kolassa, J.-E. Lee, and P. Gentine, 2017: Regionally strong feedbacks between the atmosphere and terrestrial biosphere. *Nature Geoscience*, **10**, 410–414, DOI: 10.1038/ngeo2957.

Groenke, B., M. Langer, F. Miesner, S. Westermann, G. Gallego, and J. Boike, 2024: Robust Reconstruction of Historical Climate Change From Permafrost Boreholes. *Journal of Geophysical Research: Earth Surface*, **129**, e2024JF007734, DOI: 10.1029/2024JF007734.

Gueugneau, V., K. Kelfoun, S. Charbonnier, A. Germa, and G. Carazzo, 2020: Dynamics and Impacts of the May 8th, 1902 Pyroclastic Current at Mount Pelée (Martinique): New Insights From Numerical Modeling. *Frontiers in Earth Science*, **8**, DOI: 10.3389/feart.2020.00279.

Guimberteau, M., D. Zhu, F. Maignan, Y. Huang, C. Yue, S. Dantec-Nédélec, C. Ottlé, A. Jornet-Puig, A. Bastos, P. Laurent, D. Goll, S. Bowring, J. Chang, B. Guenet, M. Tifafi, S. Peng, G. Krinner, A. Ducharne, F. Wang, T. Wang, X. Wang, Y. Wang, Z. Yin, R. Lauerwald, E. Joetzjer, C. Qiu, H. Kim, and P. Ciais, 2018: ORCHIDEE-MICT (v8.4.1), a land surface model for the high latitudes: model description and validation. *Geoscientific Model Development*, **11**, 121–163, DOI: 10.5194/gmd-11-121-2018.

Gulev, S., P. Thorne, J. Ahn, F. Dentener, C. Domingues, S. Gerland, D. Gong, D. Kaufman, H. Nnamchi, J. Quaas, J. Rivera, S. Sathyendranath, S. Smith, B. Trewin, K. von Schuckmann, and R. Vose, 2021: Changing State of the Climate System. *Climate Change 2021: The Physical Science Basis. Contribution*

of Working Group I to the Sixth Assessment Report of the Intergovernmental Panel on Climate Change, V. Masson-Delmotte, P. Zhai, A. Pirani, S. L. Connors, C. Péan, S. Berger, N. Caud, Y. Chen, L. Goldfarb, M. I. Gomis, M. Huang, K. Leitzell, E. Lonnoy, J. B. R. Matthews, T. K. Maycock, T. Waterfield, O. Yelekçi, R. Yu, and B. Zhou, eds., Cambridge University Press, Cambridge, UK and New York, NY, USA, Chapter 2, 287–422.

Haarsma, R. J., M. J. Roberts, P. L. Vidale, C. A. Senior, A. Bellucci, Q. Bao, P. Chang, S. Corti, N. S. Fučkar, V. Guemas, J. von Hardenberg, W. Hazeleger, C. Kodama, T. Koenigk, L. R. Leung, J. Lu, J.-J. Luo, J. Mao, M. S. Mizielinski, R. Mizuta, P. Nobre, M. Satoh, E. Scoccimarro, T. Semmler, J. Small, and J.-S. von Storch, 2016: High Resolution Model Intercomparison Project (HighResMIP v1.0) for CMIP6. *Geoscientific Model Development*, **9**, 4185–4208, DOI: 10.5194/gmd-9-4185-2016.

Hajima, T., M. Watanabe, A. Yamamoto, H. Tatebe, M. A. Noguchi, M. Abe, R. Ohgaito, A. Ito, D. Yamazaki, H. Okajima, A. Ito, K. Takata, K. Ogochi, S. Watanabe, and M. Kawamiya, 2020: Development of the MIROC-ES2L Earth system model and the evaluation of biogeochemical processes and feedbacks. *Geoscientific Model Development*, **13**, 2197–2244, DOI: 10.5194/gmd-13-2197-2020.

Halliday, A. N. and R. M. Canup, 2023: The accretion of planet Earth. *Nature Reviews Earth & Environment*, **4**, 19–35, DOI: 10.1038/s43017-022-00370-0.

Han, B., S. Lyu, R. Li, X. Wang, L. Zhao, Z. Cailing, D. Wang, and X. Meng, 2017: Global Land Surface Climate Analysis Based on the Calculation of a Modified Bowen Ratio. *Advances in Atmospheric Sciences*, **34**, 663–678, DOI: 10.1007/s00376-016-6175-y.

Hansen, J., L. Nazarenko, R. Ruedy, M. Sato, J. Willis, A. D. Genio, D. Koch, A. Lacis, K. Lo, S. Menon, T. Novakov, J. Perlwitz, G. Russell, G. A. Schmidt, and N. Tausnev, 2005: Earth's Energy Imbalance: Confirmation and Implications. *Science*, **308**, 1431–1435, DOI: 10.1126/science.1110252.

Hansen, J., M. Sato, and R. Ruedy, 1995: Long-term changes of the diurnal temperature cycle: implications about mechanisms of global climate change. *Atmospheric Research*, **37**, 175–209, DOI: 10.1016/0169-8095(94)00077-Q.

Hansen, J. E., W.-C. Wang, and A. A. Lacis, 1978: Mount Agung Eruption Provides Test of a Global Climatic Perturbation. *Science*, **199**, 1065–1068, DOI: 10.1126/science.199.4333.1065.

Hayhoe, K., J. Edmonds, R. Kopp, A. LeGrande, B. Sanderson, M. Wehner, and D. Wuebbles, 2017: Climate models, scenarios, and projections. *Climate Science Special Report: Fourth National Climate Assessment, Volume I*, Wuebbles, D.J. and Fahey, D.W. and Hibbard, K.A. and Dokken, D.J. and Stewart,

B.C. and Maycock, T.K., ed., U.S. Global Change Research Program, Washington, DC, USA, 133–160.

Hays, J. D., J. Imbrie, and N. J. Shackleton, 1976: Variations in the Earth's Orbit: Pacemaker of the Ice Ages. *Science*, **194**, 1121–1132, DOI: 10.1126/science.194.4270.1121.

HE, B., Y. YU, Q. BAO, P. LIN, H. LIU, J. LI, L. WANG, Y. LIU, G. WU, K. CHEN, Y. GUO, S. ZHAO, X. ZHANG, M. SONG, and J. XIE, 2020: CAS FGOALS-f3-L model dataset descriptions for CMIP6 DECK experiments. *Atmospheric and Oceanic Science Letters*, **13**, 582–588, DOI: 10.1080/16742834.2020.1778419.

Hegerl, G. and F. Zwiers, 2011: Use of models in detection and attribution of climate change. *WIREs Climate Change*, **2**, 570–591, DOI: 10.1002/wcc.121.

Held, I. M., H. Guo, A. Adcroft, J. P. Dunne, L. W. Horowitz, J. Krasting, E. Shevliakova, M. Winton, M. Zhao, M. Bushuk, A. T. Wittenberg, B. Wyman, B. Xiang, R. Zhang, W. Anderson, V. Balaji, L. Donner, K. Dunne, J. Durachta, P. P. G. Gauthier, P. Ginoux, J.-C. Golaz, S. M. Griffies, R. Hallberg, L. Harris, M. Harrison, W. Hurlin, J. John, P. Lin, S.-J. Lin, S. Malyshev, R. Menzel, P. C. D. Milly, Y. Ming, V. Naik, D. Paynter, F. Paulot, V. Rammaswamy, B. Reichl, T. Robinson, A. Rosati, C. Seman, L. G. Silvers, S. Underwood, and N. Zadeh, 2019: Structure and Performance of GFDL's CM4.0 Climate Model. *Journal of Advances in Modeling Earth Systems*, **11**, 3691–3727, DOI: 10.1029/2019MS001829.

Hermoso de Mendoza, I., H. Beltrami, A. H. MacDougall, and J.-C. Mareschal, 2020: Lower boundary conditions in land surface models - effects on the permafrost and the carbon pools: a case study with CLM4.5. *Geoscientific Model Development*, **13**, 1663–1683, DOI: 10.5194/gmd-13-1663-2020.

Heuvelink, G. B. M., 2018: Uncertainty and Uncertainty Propagation in Soil Mapping and Modelling. *Pedometrics*, McBratney, Alex. B. and Minasny, Budiman and Stockmann, Uta, ed., Springer International Publishing, Cham, Chapter 14, 439–461.

Hjort, J., O. Karjalainen, J. Aalto, S. Westermann, V. Romanovsky, F. Nelson, B. Etzelmüller, and M. Luoto, 2018: Degrading permafrost puts Arctic infrastructure at risk by mid-century. *Nature Communications*, **9**, 5147, DOI: 10.1038/s41467-018-07557-4.

Hoek van Dijke, A. J., K. Mallick, M. Schlerf, M. Machwitz, M. Herold, and A. J. Teuling, 2020: Examining the link between vegetation leaf area and land-atmosphere exchange of water, energy, and carbon fluxes using FLUXNET data. *Biogeosciences*, **17**, 4443–4457, DOI: 10.5194/bg-17-4443-2020.

Hopcroft, P. O., K. Gallagher, and C. C. Pain, 2007: Inference of past climate from borehole temperature data using Bayesian Reversible Jump Markov

chain Monte Carlo. *Geophysical Journal International*, **171**, 1430–1439, DOI: 10.1111/j.1365-246X.2007.03596.x.

Hopcroft, P. O., K. Gallagher, C. C. Pain, and F. Fang, 2009: Three-dimensional simulation and inversion of borehole temperatures for reconstructing past climate in complex settings. *Journal of Geophysical Research: Earth Surface*, **114**, F02019, DOI: 10.1029/2008JF001165.

Hsiang, S., R. Kopp, A. Jina, J. Rising, M. Delgado, S. Mohan, D. J. Rasmussen, R. Muir-Wood, P. Wilson, M. Oppenheimer, K. Larsen, and T. Houser, 2017: Estimating economic damage from climate change in the United States. *Science*, **356**, 1362–1369, DOI: 10.1126/science.aal4369.

Hu, T., X. Zhang, S. Khanal, R. Wilson, G. Leng, E. M. Toman, X. Wang, Y. Li, and K. Zhao, 2024: Climate change impacts on crop yields: A review of empirical findings, statistical crop models, and machine learning methods. *Environmental Modelling & Software*, **179**, 106119, DOI: 10.1016/j.envsoft.2024.106119.

Hu, X., J. S. Næss, C. M. Iordan, B. Huang, W. Zhao, and F. Cherubini, 2021: Recent global land cover dynamics and implications for soil erosion and carbon losses from deforestation. *Anthropocene*, **34**, 100291, DOI: 10.1016/j.ancene.2021.100291.

Huang, S., 2006: 1851–2004 annual heat budget of the continental landmasses. *Geophysical Research Letters*, **33**, L04707, DOI: 10.1029/2005GL025300.

Huang, S., H. Pollack, and P. Shen, 2000: Temperature trends over the five past centuries reconstructed from borehole temperature. *Nature*, **403**, 756–758, DOI: 10.1038/35001556.

Hugelius, G., J. G. Bockheim, P. Camill, B. Elberling, G. Grosse, J. W. Harden, K. Johnson, T. Jorgenson, C. D. Koven, P. Kuhry, G. Michaelson, U. Mishra, J. Palmtag, C.-L. Ping, J. O'Donnell, L. Schirrmeister, E. A. G. Schuur, Y. Sheng, L. C. Smith, J. Strauss, and Z. Yu, 2013: A new data set for estimating organic carbon storage to 3 m depth in soils of the northern circumpolar permafrost region. *Earth System Science Data*, **5**, 393–402, DOI: 10.5194/essd-5-393-2013.

Hugelius, G., J. Strauss, S. Zubrzycki, J. W. Harden, E. A. G. Schuur, C.-L. Ping, L. Schirrmeister, G. Grosse, G. J. Michaelson, C. D. Koven, J. A. O'Donnell, B. Elberling, U. Mishra, P. Camill, Z. Yu, J. Palmtag, and P. Kuhry, 2014: Estimated stocks of circumpolar permafrost carbon with quantified uncertainty ranges and identified data gaps. *Biogeosciences*, **11**, 6573–6593, DOI: 10.5194/bg-11-6573-2014.

Hurley, S. and R. Wiltshire, 1993: Computing thermal diffusivity from soil temperature measurements. *Computers & Geosciences*, **19**, 475–477, DOI: 10.1016/0098-3004(93)90096-N.

Hurtt, G. C., L. Chini, R. Sahajpal, S. Frolking, B. L. Bodirsky, K. Calvin, J. C. Doelman, J. Fisk, S. Fujimori, K. Klein Goldewijk, T. Hasegawa, P. Havlik, A. Heinimann, F. Humpenöder, J. Jungclaus, J. O. Kaplan, J. Kennedy, T. Krisztin, D. Lawrence, P. Lawrence, L. Ma, O. Mertz, J. Pongratz, A. Popp, B. Poulter, K. Riahi, E. Shevliakova, E. Stehfest, P. Thornton, F. N. Tubiello, D. P. van Vuuren, and X. Zhang, 2020: Harmonization of global land use change and management for the period 850–2100 (LUH2) for CMIP6. *Geoscientific Model Development*, **13**, 5425–5464, DOI: 10.5194/gmd-13-5425-2020.

Ilyina, T., K. D. Six, J. Segschneider, E. Maier-Reimer, H. Li, and I. Núñez-Riboni, 2013: Global ocean biogeochemistry model HAMOCC: Model architecture and performance as component of the MPI-Earth system model in different CMIP5 experimental realizations. *Journal of Advances in Modeling Earth Systems*, **5**, 287–315, DOI: 10.1029/2012MS000178.

Jaume-Santero, F., C. Pickler, H. Beltrami, and J.-C. Mareschal, 2016: North American regional climate reconstruction from ground surface temperature histories. *Climate of the Past*, **12**, 2181–2194, DOI: 10.5194/cp-12-2181-2016.

Jones, P., K. Briffa, T. Osborn, J. Lough, T. van Ommen, B. Vinther, J. Luterbacher, E. Wahl, F. Zwiers, M. Mann, G. Schmidt, C. Ammann, B. Buckley, K. Cobb, J. Esper, H. Goosse, N. Graham, E. Jansen, T. Kiefer, C. Kull, M. Küttel, E. Mosley-Thompson, J. Overpeck, N. Riedwyl, M. Schulz, A. Tudhope, R. Villalba, H. Wanner, E. Wolff, and E. Xoplaki, 2009: High-resolution palaeoclimatology of the last millennium: a review of current status and future prospects. *The Holocene*, **19**, 3–49, DOI: 10.1177/0959683608098952.

Jung, M., M. Reichstein, P. Ciais, S. Seneviratne, J. Sheffield, M. Goulden, G. Bonan, A. Cescatti, J. Chen, R. de Jeu, H. A. Dolman, W. Eugster, D. Gerten, D. Gianelle, N. Gobron, J. Heinke, J. Kimball, B. Law, and L. Montagnani, 2010: Recent decline in the global land evapotranspiration trend due to limited moisture supply. *Nature*, **467**, 951–954, DOI: 10.1038/nature09396.

Jungclaus, J. H., E. Bard, M. Baroni, P. Braconnot, J. Cao, L. P. Chini, T. Egorova, M. Evans, J. F. González-Rouco, H. Goosse, G. C. Hurtt, F. Joos, J. O. Kaplan, M. Khodri, K. Klein Goldewijk, N. Krivova, A. N. LeGrande, S. J. Lorenz, J. Luterbacher, W. Man, A. C. Maycock, M. Meinshausen, A. Moberg, R. Muscheler, C. Nehrbass-Ahles, B. I. Otto-Bliesner, S. J. Phipps, J. Pongratz, E. Rozanov, G. A. Schmidt, H. Schmidt, W. Schmutz, A. Schurer, A. I. Shapiro, M. Sigl, J. E. Smerdon, S. K. Solanki, C. Timmreck, M. Toohey, I. G. Usoskin, S. Wagner, C.-J. Wu, K. L. Yeo, D. Zanchettin, Q. Zhang, and E. Zorita, 2017: The PMIP4 contribution to CMIP6 - Part 3: The last millennium, scientific objective, and experimental design for the PMIP4 *past1000* simulations. *Geoscientific Model Development*, **10**, 4005–4033, DOI: 10.5194/gmd-10-4005-

2017.

Jungclaus, J. H., N. Fischer, H. Haak, K. Lohmann, J. Marotzke, D. Matei, U. Mikolajewicz, D. Notz, and J. S. von Storch, 2013: Characteristics of the ocean simulations in the Max Planck Institute Ocean Model (MPIOM) the ocean component of the MPI-Earth system model. *Journal of Advances in Modeling Earth Systems*, **5**, 422–446, DOI: 10.1002/jame.20023.

Jungclaus, J. H., S. J. Lorenz, C. Timmreck, C. H. Reick, V. Brovkin, K. Six, J. Segschneider, M. A. Giorgetta, T. J. Crowley, J. Pongratz, N. A. Krivova, L. E. Vieira, S. K. Solanki, D. Klocke, M. Botzet, M. Esch, V. Gayler, H. Haak, T. J. Raddatz, E. Roeckner, R. Schnur, H. Widmann, M. Claussen, B. Stevens, and J. Marotzke, 2010: Climate and carbon-cycle variability over the last millennium. *Climate of the Past*, **6**, 723–737, DOI: 10.5194/cp-6-723-2010.

Justice, C., J. Townshend, E. Vermote, E. Masuoka, R. Wolfe, N. Saleous, D. Roy, and J. Morisette, 2002: An overview of MODIS Land data processing and product status. *Remote Sensing of Environment*, **83**, 3–15, DOI: 10.1016/S0034-4257(02)00084-6.

Kageyama, M., P. Braconnot, S. P. Harrison, A. M. Haywood, J. H. Jungclaus, B. L. Otto-Bliesner, J.-Y. Peterschmitt, A. Abe-Ouchi, S. Albani, P. J. Bartlein, C. Brierley, M. Crucifix, A. Dolan, L. Fernandez-Donado, H. Fischer, P. O. Hopcroft, R. F. Ivanovic, F. Lambert, D. J. Lunt, N. M. Mahowald, W. R. Peltier, S. J. Phipps, D. M. Roche, G. A. Schmidt, L. Tarasov, P. J. Valdes, Q. Zhang, and T. Zhou, 2018: The PMIP4 contribution to CMIP6 - Part 1: Overview and over-arching analysis plan. *Geoscientific Model Development*, **11**, 1033–1057, DOI: 10.5194/gmd-11-1033-2018.

Kalnay, E., M. Kanamitsu, R. Kistler, W. Collins, D. Deaven, L. Gandin, M. Iredell, S. Saha, G. White, J. Woollen, Y. Zhu, M. Chelliah, W. Ebisuzaki, W. Higgins, J. Janowiak, K. C. Mo, C. Ropelewski, J. Wang, A. Leetmaa, R. Reynolds, R. Jenne, and D. Joseph, 1996: The NCEP/NCAR 40-Year Reanalysis Project. *Bulletin of the American Meteorological Society*, **77**, 437–472, DOI: 10.1175/1520-0477(1996)077¡0437:TNYRP¿2.0.CO;2.

Karl, T. R., A. Arguez, B. Huang, J. H. Lawrimore, J. R. McMahon, M. J. Menne, T. C. Peterson, R. S. Vose, and H.-M. Zhang, 2015: Possible artifacts of data biases in the recent global surface warming hiatus. *Science*, **348**, 1469–1472, DOI: 10.1126/science.aaa5632.

Kasahara, A. and W. Washington, 1967: NCAR global General Circulation Model of the atmosphere. *Monthly Weather Review*, **95**, 389–402, DOI: 10.1175/1520-0493(1967)095¡0389:NGGCMO¿2.3.CO;2.

Kaspar, T. C. and W. L. Bland, 1992: Soil Temperature and Root Growth. *Soil Science*, **154**, 290–299, DOI: 10.1097/00010694-199210000-00005.

Kelley, M., G. A. Schmidt, L. S. Nazarenko, S. E. Bauer, R. Ruedy, G. L. Russell, A. S. Ackerman, I. Aleinov, M. Bauer, R. Bleck, V. Canuto, G. Cesana, Y. Cheng, T. L. Clune, B. I. Cook, C. A. Cruz, A. D. Del Genio, G. S. Elsaesser, G. Faluvegi, N. Y. Kiang, D. Kim, A. A. Lacis, A. Leboissetier, A. N. LeGrande, K. K. Lo, J. Marshall, E. E. Matthews, S. McDermid, K. Mezuman, R. L. Miller, L. T. Murray, V. Oinas, C. Orbe, C. P. García-Pando, J. P. Perlwitz, M. J. Puma, D. Rind, A. Romanou, D. T. Shindell, S. Sun, N. Tausnev, K. Tsigaridis, G. Tselioudis, E. Weng, J. Wu, and M.-S. Yao, 2020: GISS-E2.1: Configurations and Climatology. *Journal of Advances in Modeling Earth Systems*, **12**, e2019MS002025, DOI: 10.1029/2019MS002025.

Knight, J. H., B. Minasny, A. B. McBratney, T. B. Koen, and B. W. Murphy, 2018: Soil temperature increase in eastern Australia for the past 50 years. *Geoderma*, **313**, 241–249, DOI: 10.1016/j.geoderma.2017.11.015.

Knoblauch, C., C. Beer, S. Liebner, M. Grigoriev, and E. Pfeiffer, 2017: Methane production as key to the greenhouse gas budget of thawing permafrost. *Nature Climate Change*, **8**, 309–312, DOI: 10.1038/s41558-018-0095-z.

Kondratyev, K. Y., C. A. Varotsos, V. F. Krapivin, and V. P. Savinykh, 2004: *Biogeochemical cycles of pollutants in the environment*, Springer, Berlin, Heidelberg, Chapter 6. 381–480.

Koven, C. D., W. J. Riley, and A. Stern, 2013: Analysis of Permafrost Thermal Dynamics and Response to Climate Change in the CMIP5 Earth System Models. *Journal of Climate*, **26**, 1877–1900, DOI: 10.1175/JCLI-D-12-00228.1.

Krakauer, N. Y., M. J. Puma, and B. I. Cook, 2013: Impacts of soil–aquifer heat and water fluxes on simulated global climate. *Hydrology and Earth System Sciences*, **17**, 1963–1974, DOI: 10.5194/hess-17-1963-2013.

Krinner, G., C. Derksen, R. Essery, M. Flanner, S. Hagemann, M. Clark, A. Hall, H. Rott, C. Brutel-Vuilmet, H. Kim, C. B. Ménard, L. Mudryk, C. Thackeray, L. Wang, G. Arduini, G. Balsamo, P. Bartlett, J. Boike, A. Boone, F. Chéruy, J. Colin, M. Cuntz, Y. Dai, B. Decharme, J. Derry, A. Ducharne, E. Dutra, X. Fang, C. Fierz, J. Ghattas, Y. Gusev, V. Haverd, A. Kontu, M. Lafaysse, R. Law, D. Lawrence, W. Li, T. Marke, D. Marks, M. Ménégoz, O. Nasonova, T. Nitta, M. Niwano, J. Pomeroy, M. S. Raleigh, G. Schaedler, V. Semenov, T. G. Smirnova, T. Stacke, U. Strasser, S. Svenson, D. Turkov, T. Wang, N. Wever, H. Yuan, W. Zhou, and D. Zhu, 2018: ESM-SnowMIP: assessing snow models and quantifying snow-related climate feedbacks. *Geoscientific Model Development*, **11**, 5027–5049, DOI: 10.5194/gmd-11-5027-2018.

Laird, N. F. and D. Kristovich, 2002: Variations of Sensible and Latent Heat Fluxes from a Great Lakes Buoy and Associated Synoptic Weather Patterns. *Journal of Hydrometeorology*, **3**, 3–12, DOI: 10.1175/1525-7541(2002)003¡0003:VOSALH¿2.0.CO;2.

Laloyaux, P., E. de Boisseson, M. Balmaseda, J.-R. Bidlot, S. Broennimann, R. Buizza, P. Dalhgren, D. Dee, L. Haimberger, H. Hersbach, Y. Kosaka, M. Martin, P. Poli, N. Rayner, E. Rustemeier, and D. Schepers, 2018: CERA-20C: A Coupled Reanalysis of the Twentieth Century. *Journal of Advances in Modeling Earth Systems*, **10**, 1172–1195, DOI: 10.1029/2018MS001273.

Lamb, W. F., M. Grubb, F. Diluiso, and J. C. Minx, 2022: Countries with sustained greenhouse gas emissions reductions: an analysis of trends and progress by sector. *Climate Policy*, **22**, 1–17, DOI: 10.1080/14693062.2021.1990831.

Lane, A. C., 1923: Geotherms of Lake Superior Copper Country. *GSA Bulletin*, **34**, 703–720, DOI: 10.1130/GSAB-34-703.

Lawrence, D. M., R. A. Fisher, C. D. Koven, K. W. Oleson, S. C. Swenson, G. Bonan, N. Collier, B. Ghimire, L. van Kampenhout, D. Kennedy, E. Kluzek, P. J. Lawrence, F. Li, H. Li, D. Lombardozzi, W. J. Riley, W. J. Sacks, M. Shi, M. Vertenstein, W. R. Wieder, C. Xu, A. A. Ali, A. M. Badger, G. Bisht, M. van den Broeke, M. A. Brunke, S. P. Burns, J. Buzan, M. Clark, A. Craig, K. Dahlin, B. Drewniak, J. B. Fisher, M. Flanner, A. M. Fox, P. Gentine, F. Hoffman, G. Keppel-Aleks, R. Knox, S. Kumar, J. Lenaerts, L. R. Leung, W. H. Lipscomb, Y. Lu, A. Pandey, J. D. Pelletier, J. Perket, J. T. Randerson, D. M. Ricciuto, B. M. Sanderson, A. Slater, Z. M. Subin, J. Tang, R. Q. Thomas, M. Val Martin, and X. Zeng, 2019: The Community Land Model Version 5: Description of New Features, Benchmarking, and Impact of Forcing Uncertainty. *Journal of Advances in Modeling Earth Systems*, **11**, 4245–4287, DOI: 10.1029/2018MS001583.

Lawrence, D. M. and A. G. Slater, 2008: Incorporating organic soil into a global climate model. *Climate Dynamics*, **30**, 145–160, DOI: 10.1007/s00382-007-0278-1.

Lawrence, D. M., A. G. Slater, V. E. Romanovsky, and D. J. Nicolsky, 2008: Sensitivity of a model projection of near-surface permafrost degradation to soil column depth and representation of soil organic matter. *Journal of Geophysical Research: Earth Surface*, **113**, F02011, DOI: 10.1029/2007JF000883.

Le Hir, G., Y. Donnadieu, Y. Goddéris, B. Meyer-Berthaud, G. Ramstein, and R. C. Blakey, 2011: The climate change caused by the land plant invasion in the Devonian. *Earth and Planetary Science Letters*, **310**, 203–212, DOI: 10.1016/j.epsl.2011.08.042.

Lee, J., J. Kim, M.-A. Sun, B.-H. Kim, H. Moon, H. M. Sung, J. Kim, and Y.-H. Byun, 2019: Evaluation of the Korea Meteorological Administration Advanced Community Earth-System model (K-ACE). *Asia-Pacific Journal of Atmospheric Sciences*, **56**, 381–395, DOI: 10.1007/s13143-019-00144-7.

Lenssen, N. J. L., G. A. Schmidt, J. E. Hansen, M. J. Menne, A. Persin, R. Ruedy, and D. Zyss, 2019: Improvements in the GISTEMP Uncertainty

Model. *Journal of Geophysical Research: Atmospheres*, **124**, 6307–6326, DOI: 10.1029/2018JD029522.

Levitus, S., J. I. Antonov, T. P. Boyer, O. K. Baranova, H. E. Garcia, R. A. Locarnini, A. V. Mishonov, J. R. Reagan, D. Seidov, E. S. Yarosh, and M. M. Zweng, 2012: World ocean heat content and thermosteric sea level change (0–2000 m), 1955–2010. *Geophysical Research Letters*, **39**, L10603, DOI: 10.1029/2012GL051106.

Li, L., Y. Yu, Y. Tang, P. Lin, J. Xie, M. Song, L. Dong, T. Zhou, L. Liu, L. Wang, Y. Pu, X. Chen, L. Chen, Z. Xie, H. Liu, L. Zhang, X. Huang, T. Feng, W. Zheng, K. Xia, H. Liu, J. Liu, Y. Wang, L. Wang, B. Jia, F. Xie, B. Wang, S. Zhao, Z. Yu, B. Zhao, and J. Wei, 2020: The Flexible Global Ocean-Atmosphere-Land System Model Grid-Point Version 3 (FGOALS-g3): Description and Evaluation. *Journal of Advances in Modeling Earth Systems*, **12**, e2019MS002012, DOI: 10.1029/2019MS002012.

Loeb, N. G., B. A. Wielicki, D. R. Doelling, G. L. Smith, D. F. Keyes, S. Kato, N. Manalo-Smith, and T. Wong, 2009: Toward Optimal Closure of the Earth's Top-of-Atmosphere Radiation Budget. *Journal of Climate*, **22**, 748–766, DOI: 10.1175/2008JCLI2637.1.

Lovato, T., D. Peano, M. Butenschön, S. Materia, D. Iovino, E. Scoccimarro, P. G. Fogli, A. Cherchi, A. Bellucci, S. Gualdi, S. Masina, and A. Navarra, 2022: CMIP6 Simulations With the CMCC Earth System Model (CMCC-ESM2). *Journal of Advances in Modeling Earth Systems*, **14**, e2021MS002814, DOI: 10.1029/2021MS002814.

Lucazeau, F., 2019: Analysis and Mapping of an Updated Terrestrial Heat Flow Data Set. *Geochemistry, Geophysics, Geosystems*, **20**, 4001–4024, DOI: 10.1029/2019GC008389.

MacDougall, A. H., J. F. González-Rouco, M. B. Stevens, and H. Beltrami, 2008: Quantification of subsurface heat storage in a GCM simulation. *Geophysical Research Letters*, **35**, L13702, DOI: 10.1029/2008GL034639.

Maher, N., S. Milinski, L. Suarez-Gutierrez, M. Botzet, M. Dobrynin, L. Kornblueh, J. Kröger, Y. Takano, R. Ghosh, C. Hedemann, C. Li, H. Li, E. Manzini, D. Notz, D. Putrasahan, L. Boysen, M. Claussen, T. Ilyina, D. Olonscheck, T. Raddatz, B. Stevens, and J. Marotzke, 2019: The Max Planck Institute Grand Ensemble: Enabling the Exploration of Climate System Variability. *Journal of Advances in Modeling Earth Systems*, **11**, 2050–2069, DOI: 10.1029/2019MS001639.

Manabe, S., 1969: Climate and the ocean circulation: I. The atmospheric circulation and the hydrology of the Earth's surface. *Monthly Weather Review*, **97**, 739–774, DOI: 10.1175/1520-0493(1969)097¡0739:CATOC¿2.3.CO;2.

Manabe, S., R. J. Stouffer, M. J. Spelman, and K. Bryan, 1991: Transient Responses of a Coupled Ocean–Atmosphere Model to Gradual Changes of Atmospheric CO2. Part I. Annual Mean Response. *Journal of Climate*, **4**, 785–818, DOI: 10.1175/1520-0442(1991)004¡0785:TROACO¿2.0.CO;2.

Mann, M. and G. Schmidt, 2003: Ground vs. surface air temperature trends: Implications for borehole surface temperature reconstructions. *Geophysical Research Letters*, **30**, 1607, DOI: 10.1029/2003GL017170.

Mansfield, L. A., A. Gupta, A. C. Burnett, B. Green, C. Wilka, and A. Sheshadri, 2023: Updates on Model Hierarchies for Understanding and Simulating the Climate System: A Focus on Data-Informed Methods and Climate Change Impacts. *Journal of Advances in Modeling Earth Systems*, **15**, e2023MS003715, DOI: 10.1029/2023MS003715.

Mareschal, J. and H. Beltrami, 1992: Evidence for recent warming from perturbed geothermal gradients: examples from eastern Canada. *Climate Dynamics*, **6**, 135–143, DOI: 10.1007/BF00193525.

Masson-Delmotte, V., M. Schulz, A. Abe-Ouchi, J. Beer, A. Ganopolski, J. González-Rouco, E. Jansen, K. Lambeck, J. Luterbacher, T. Naish, T. Osborn, B. Otto-Bliesner, T. Quinn, R. Ramesh, M. Rojas, X. Shao, and A. Timmermann, 2013: Information from Paleoclimate Archives. *Climate Change 2013: The Physical Science Basis. Contribution of Working Group I to the Fifth Assessment Report of the Intergovernmental Panel on Climate Change*, T. Stocker, D. Qin, G.-K. Plattner, M. Tignor, S. Allen, J. Boschung, A. Nauels, Y. Xia, V. Bex, and P. Midgley, eds., Cambridge University Press, Cambridge, United Kingdom and New York, NY, USA, Chapter 5, 383–464.

Masson-Delmotte, V., P. Zhai, A. Pirani, S. L. Connors, C. Péan, S. Berger, N. Caud, Y. Chen, L. Goldfarb, M. I. Gomis, M. Huang, K. Leitzell, E. Lonnoy, J. B. R. Matthews, T. K. Maycock, T. Waterfield, O. Yelekçi, R. Yu, and B. Zhou, eds., 2021: *Climate Change 2021: The Physical Science Basis. Contribution of Working Group I to the Sixth Assessment Report of the Intergovernmental Panel on Climate Change*. Cambridge University Press, Cambridge, UK and New York, NY, USA, 2391 pp.

Masson-Delmotte, V., P. Zhai, H.-O. Pörtner, D. Roberts, J. Skea, P. R. Shukla, A. Pirani, W. Moufouma-Okia, C. Péan, R. Pidcock, S. Connors, J. B. R. Matthews, Y. Chen, X. Zhou, M. I. Gomis, E. Lonnoy, T. Maycock, M. Tignor, T. Waterfield, A. Pirani, W. Moufouma-Okia, C. Péan, R. Pidcock, S. Connors, J. B. R. Matthews, Y. Chen, X. Zhou, M. I. Gomis, E. Lonnoy, T. Maycock, M. Tignor, and T. Waterfield, eds., 2018: *Global Warming of 1.5°C: An IPCC Special Report on the impacts of global warming of 1.5°C above pre-industrial levels and related global greenhouse gas emission pathways, in the context of strengthening the global response to the threat of climate change, sustainable*

development, and efforts to eradicate poverty. World Meteorological Organization, Geneva, Switzerland.

Matthes, H., A. Damseaux, S. Westermann, C. Beer, A. Boone, E. Burke, B. Decharme, H. Genet, E. Jafarov, M. Langer, F.-J. Parmentier, P. Porada, A. Gagne-Landmann, D. Huntzinger, B. M. Rogers, C. Schädel, T. Stacke, J. Wells, and W. R. Wieder, 2025: Advances in Permafrost Representation: Biophysical Processes in Earth System Models and the Role of Offline Models. *Permafrost and Periglacial Processes*, **36**, 302–318, DOI: 10.1002/ppp.2269.

Mauder, M., T. Foken, and J. Cuxart, 2020: Surface-Energy-Balance Closure over Land: A Review. *Boundary-Layer Meteorology*, **177**, 395–426, DOI: 10.1007/s10546-020-00529-6.

Mauritsen, T., J. Bader, T. Becker, J. Behrens, M. Bittner, R. Brokopf, V. Brovkin, M. Claussen, T. Crueger, M. Esch, I. Fast, S. Fiedler, D. Fläschner, V. Gayler, M. Giorgetta, D. S. Goll, H. Haak, S. Hagemann, C. Hedemann, C. Hohenegger, T. Ilyina, T. Jahns, D. Jimenéz-de-la Cuesta, J. Jungclaus, T. Kleinen, S. Kloster, D. Kracher, S. Kinne, D. Kleberg, G. Lasslop, L. Kornblueh, J. Marotzke, D. Matei, K. Meraner, U. Mikolajewicz, K. Modali, B. Möbis, W. A. Müller, J. E. M. S. Nabel, C. C. W. Nam, D. Notz, S.-S. Nyawira, H. Paulsen, K. Peters, R. Pincus, H. Pohlmann, J. Pongratz, M. Popp, T. J. Raddatz, S. Rast, R. Redler, C. H. Reick, T. Rohrschneider, V. Schemann, H. Schmidt, R. Schnur, U. Schulzweida, K. D. Six, L. Stein, I. Stemmler, B. Stevens, J.-S. von Storch, F. Tian, A. Voigt, P. Vrese, K.-H. Wieners, S. Wilkenskjeld, A. Winkler, and E. Roeckner, 2019: Developments in the MPI-M Earth System Model version 1.2 (MPI-ESM1.2) and Its Response to Increasing CO2. *Journal of Advances in Modeling Earth Systems*, **11**, 998–1038, DOI: 10.1029/2018MS001400.

Mccormick, M., L. Thomason, and C. Trepte, 1995: Atmospheric effects of the Mt Pinatubo eruption. *Nature*, **373**, 399–404, DOI: 10.1038/373399a0.

Meabe-Yanguas, N., J. F. González-Rouco, F. García-Pereira, P. de Vrese, A. Martínez-Vila, N. J. Steinert, J. Jungclaus, and S. Lorenz, 2025: Long term influence of changing soil hydrology in an Earth System Model on Arctic Amplification. *The Cryopshere*, In preparation.

Meinshausen, M., E. Vogel, A. Nauels, K. Lorbacher, N. Meinshausen, D. M. Etheridge, P. J. Fraser, S. A. Montzka, P. J. Rayner, C. M. Trudinger, P. B. Krummel, U. Beyerle, J. G. Canadell, J. S. Daniel, I. G. Enting, R. M. Law, C. R. Lunder, S. O'Doherty, R. G. Prinn, S. Reimann, M. Rubino, G. J. M. Velders, M. K. Vollmer, R. H. J. Wang, and R. Weiss, 2017: Historical greenhouse gas concentrations for climate modelling (CMIP6). *Geoscientific Model Development*, **10**, 2057–2116, DOI: 10.5194/gmd-10-2057-2017.

Melo-Aguilar, C., J. F. González-Rouco, E. García-Bustamante, N. Steinert, J. H. Jungclaus, J. Navarro, and P. J. Roldán-Gómez, 2020: Methodological and physical biases in global to subcontinental borehole temperature reconstructions: an assessment from a pseudo-proxy perspective. *Climate of the Past*, **16**, 453–474, DOI: 10.5194/cp-16-453-2020.

Melo-Aguilar, C., F. González-Rouco, N. J. Steinert, H. Beltrami, F. J. Cuesta-Valero, A. García-García, F. García-Pereira, E. García-Bustamante, P. J. Roldán-Gómez, T. Schmid, and J. Navarro, 2022: Near-surface soil thermal regime and land–air temperature coupling: a case study over Spain. *International Journal of Climatology*, **42**, 1–19, DOI: 10.1002/joc.7662.

Melo-Aguilar, C., J. F. González-Rouco, E. García-Bustamante, J. Navarro-Montesinos, and N. Steinert, 2018: Influence of radiative forcing factors on ground-air temperature coupling during the last millennium: implications for borehole climatology. *Climate of the Past*, **14**, 1583–1606, DOI: 10.5194/cp-14-1583-2018.

Menard, C. B., R. Essery, G. Krinner, G. Arduini, P. Bartlett, A. Boone, C. Brutel-Vuilmet, E. Burke, M. Cuntz, Y. Dai, B. Decharme, E. Dutra, X. Fang, C. Fierz, Y. Gusev, S. Hagemann, V. Haverd, H. Kim, M. Lafaysse, T. Marke, O. Nasonova, T. Nitta, M. Niwano, J. Pomeroy, G. Schädler, V. A. Semenov, T. Smirnova, U. Strasser, S. Swenson, D. Turkov, N. Wever, and H. Yuan, 2021: Scientific and Human Errors in a Snow Model Intercomparison. *Bulletin of the American Meteorological Society*, **102**, E61–E79, DOI: 10.1175/BAMS-D-19-0329.1.

Milankovitch, M., 1941: *Kanon der Erdbestrahlung und Seine Anwendung auf das Eiszeitenproblem*, volume 33(132) of *Special Publications*. Royal Serbian Academy, Belgrade, 633 pp.

Miller, G. H., A. Geirsdóttir, Y. Zhong, D. J. Larsen, B. L. Otto-Bliesner, M. M. Holland, D. A. Bailey, K. A. Refsnider, S. J. Lehman, J. R. Southon, C. Anderson, H. Björnsson, and T. Thordarson, 2012: Abrupt onset of the Little Ice Age triggered by volcanism and sustained by sea-ice/ocean feedbacks. *Geophysical Research Letters*, **39**, L02708, DOI: 10.1029/2011GL050168.

Miralles, D. G., P. Gentine, S. I. Seneviratne, and A. J. Teuling, 2019: Land–atmospheric feedbacks during droughts and heatwaves: state of the science and current challenges. *Annals of the New York Academy of Sciences*, **1436**, 19–35, DOI: 10.1111/nyas.13912.

Mottaghy, D. and V. Rath, 2006: Latent heat effects in subsurface heat transport modelling and their impact on palaeotemperature reconstructions. *Geophysical Journal International*, **164**, 236–245, DOI: 10.1111/j.1365-246X.2005.02843.x.

Mu, M., M. G. De Kauwe, A. M. Ukkola, A. J. Pitman, W. Guo, S. Hobeichi, and P. R. Briggs, 2021: Exploring how groundwater buffers the influence of

heatwaves on vegetation function during multi-year droughts. *Earth System Dynamics*, **12**, 919–938, DOI: 10.5194/esd-12-919-2021.

Muñoz Sabater, J., E. Dutra, A. Agustí-Panareda, C. Albergel, G. Arduini, G. Balsamo, S. Boussetta, M. Choulga, S. Harrigan, H. Hersbach, B. Martens, D. G. Miralles, M. Piles, N. J. Rodríguez-Fernández, E. Zsoter, C. Buontempo, and J.-N. Thépaut, 2021: ERA5-Land: a state-of-the-art global reanalysis dataset for land applications. *Earth System Science Data*, **13**, 4349–4383, DOI: 10.5194/essd-13-4349-2021.

Mudryk, L., M. Santolaria-Otín, G. Krinner, M. Ménégoz, C. Derksen, C. Brutel-Vuilmet, M. Brady, and R. Essery, 2020: Historical Northern Hemisphere snow cover trends and projected changes in the CMIP6 multi-model ensemble. *The Cryosphere*, **14**, 2495–2514, DOI: 10.5194/tc-14-2495-2020.

Myhre, G., D. Shindell, F.-M. Bréon, W. Collins, J. Fuglestvedt, J. Huang, D. Koch, J.-F. Lamarque, D. Lee, B. Mendoza, T. Nakajima, A. Robock, G. Stephens, T. Takemura, and H. Zhang, 2013: Anthropogenic and Natural Radiative Forcing. *Climate Change 2013: The Physical Science Basis. Contribution of Working Group I to the Fifth Assessment Report of the Intergovernmental Panel on Climate Change*, T. Stocker, D. Qin, G.-K. Plattner, M. Tignor, S. Allen, J. Boschung, A. Nauels, Y. Xia, V. Bex, and P. Midgley, eds., Cambridge University Press, Cambridge, United Kingdom and New York, NY, USA, Chapter 8, 659–740.

Nitzbon, J., G. Krinner, T. Schneider von Deimling, M. Werner, and M. Langer, 2023: First Quantification of the Permafrost Heat Sink in the Earth's Climate System. *Geophysical Research Letters*, **50**, e2022GL102053, DOI: 10.1029/2022GL102053.

Nitzbon, J., T. Schneider von Deimling, M. Aliyeva, S. Chadburn, G. Grosse, S. Laboor, H. Lee, G. Lohmann, N. Steinert, S. Stuenzi, M. Werner, S. Westermann, and M. Langer, 2024: No respite from permafrost-thaw impacts in the absence of a global tipping point. *Nature Climate Change*, **14**, 573–585, DOI: 10.1038/s41558-024-02011-4.

Niu, G.-Y. and Z.-L. Yang, 2004: Effects of vegetation canopy processes on snow surface energy and mass balances. *Journal of Geophysical Research: Atmospheres*, **109**, D23111, DOI: 10.1029/2004JD004884.

O, S., A. Bastos, M. Reichstein, W. Li, J. Denissen, H. Graefen, and R. Orth, 2022: The Role of Climate and Vegetation in Regulating Drought–Heat Extremes. *Journal of Climate*, **35**, 5677–5685, DOI: 10.1175/JCLI-D-21-0675.1.

Obu, J., S. Westermann, C. Barboux, A. Bartsch, R. Delaloye, G. Grosse, B. Heim, G. Hugelius, A. Irrgang, A. Kääb, C. Kroisleitner, H. Matthes, I. Nitze, C. Pellet, F. Seifert, T. Strozzi, U. Wegmüller, M. Wieczorek, and A. Wiesmann, 2021: ESA Permafrost Climate Change Initiative

(Permafrost_cci): Permafrost Ground Temperature for the Northern Hemisphere, v3.0. *NERC EDS Centre for Environmental Data Analysis*, , , DOI: 10.5285/b25d4a6174de4ac78000d034f500a268.

Obu, J., S. Westermann, A. Bartsch, N. Berdnikov, H. Christiansen, D. Avirmed, R. Delaloye, B. Elberling, B. Etzelmüller, A. Kholodov, A. Khomutov, A. Kääb, M. Leibman, A. Lewkowicz, S. Panda, V. Romanovsky, R. Way, A. Westergaard-Nielsen, T. Wu, and D. Zou, 2019: Northern Hemisphere permafrost map based on TTOP modelling for 2000–2016 at 1 km2 scale. *Earth-Science Reviews*, **193**, 299–316, DOI: 10.1016/j.earscirev.2019.04.023.

Ochsner, T., R. Horton, and T. Ren, 2001: A New Perspective on Soil Thermal Properties. *Soil Science Society of America Journal*, **65**, 1641–1647, DOI: 10.2136/SSSAJ2001.1641.

Oleson, K. W., M. Lawrence, B. Bonan, B. A. Drewniak, M. Huang, C. DeKoven, S. Levis, F. Li, J. P. Riley, M. C. Subin, S. C. Swenson, E. Thornton, A. Bozbiyik, R. A. Fisher, L. Heald, E. Kluzek, J.-F. Lamarque, J. Lawrence, R. L. Leung, W. H. Lipscomb, P. Muszala, M. Ricciuto, J. Sacks, Y. Sun, J. Tang, and Z.-L. Yang, 2013: Technical description of version 4.5 of the Community Land Model (CLM). *NCAR Technical Notes*.

Olofsson, B., 1994: Flow Of Groundwater From Soil To Crystalline Rock. *Hydrogeology Journal*, **2**, 71–83, DOI: 10.1007/S100400050052.

O'Neill, B. C., C. Tebaldi, D. P. van Vuuren, V. Eyring, P. Friedlingstein, G. Hurtt, R. Knutti, E. Kriegler, J.-F. Lamarque, J. Lowe, G. A. Meehl, R. Moss, K. Riahi, and B. M. Sanderson, 2016: The Scenario Model Intercomparison Project (ScenarioMIP) for CMIP6. *Geoscientific Model Development*, **9**, 3461–3482, DOI: 10.5194/gmd-9-3461-2016.

OpenAI, 2025: Ai-generated image of volcanic landscape with medieval elements. https://chat.openai.com, image generated using DALL·E via ChatGPT.

Oreskes, N., K. Shrader-Frechette, and K. Belitz, 1994: Verification, Validation, and Confirmation of Numerical Models in the Earth Sciences. *Science*, **263**, 641–646, DOI: 10.1126/science.263.5147.641.

Osborn, T. J., P. D. Jones, D. H. Lister, C. P. Morice, I. R. Simpson, J. P. Winn, E. Hogan, and I. C. Harris, 2021: Land Surface Air Temperature Variations Across the Globe Updated to 2019: The CRUTEM5 Data Set. *Journal of Geophysical Research: Atmospheres*, **126**, e2019JD032352, DOI: 10.1029/2019JD032352.

Outcalt, S. I., F. E. Nelson, and K. M. Hinkel, 1990: The zero-curtain effect: Heat and mass transfer across an isothermal region in freezing soil. *Water Resources Research*, **26**, 1509–1516, DOI: 10.1029/WR026i007p01509.

Paillard, D., 2015: Quaternary glaciations: from observations to theories. *Quaternary Science Reviews*, **107**, 11–24, DOI: 10.1016/j.quascirev.2014.10.002.

Palmer, T. and B. Stevens, 2019: The scientific challenge of understanding and estimating climate change. *Proceedings of the National Academy of Sciences*, **116**, 24390–24395, DOI: 10.1073/pnas.1906691116.

Park, J. T., 2015: Climate Change and Capitalism. *Consilience: journal of sustainable development*, **14**, 189–206, DOI: 10.7916/D8DN45HM.

Parmesan, C., M. Morecroft, Y. Trisurat, R. Adrian, G. Anshari, A. Arneth, Q. Gao, P. Gonzalez, R. Harris, J. Price, N. Stevens, and G. Talukdarr, 2022: Terrestrial and Freshwater Ecosystems and Their Services. *Climate Change 2022: Impacts, Adaptation and Vulnerability. Contribution of Working Group II to the Sixth Assessment Report of the Intergovernmental Panel on Climate Change*, H. O. Pörtner, D. C. Roberts, M. Tignor, E. S. Poloczanska, K. Mintenbeck, A. Alegría, M. Craig, S. Langsdorf, S. Löschke, V. Möller, A. Okem, and B. Rama, eds., Cambridge University Press, Cambridge, UK and New York, NY, USA, Chapter 2, 197–378.

Pegoraro, E. F., M. E. Mauritz, K. Ogle, C. H. Ebert, and E. A. G. Schuur, 2021: Lower soil moisture and deep soil temperatures in thermokarst features increase old soil carbon loss after 10 years of experimental permafrost warming. *Global Change Biology*, **27**, 1293–1308, DOI: 10.1111/gcb.15481.

Peixóto, J. P. and A. H. Oort, 1984: Physics of climate. *Rev. Mod. Phys.*, **56**, 365–429, DOI: 10.1103/RevModPhys.56.365.

Pereira, H. M., L. M. Navarro, and I. S. Martins, 2012: Global Biodiversity Change: The Bad, the Good, and the Unknown. *Annual Review of Environment and Resources*, **37**, 25–50, DOI: 10.1146/annurev-environ-042911-093511.

Petersen, G. N., 2022: Trends in soil temperature in the Icelandic highlands from 1977 to 2019. *International Journal of Climatology*, **42**, 2299–2310, DOI: 10.1002/joc.7366.

Pielke, R., 2001: Influence of the spatial distribution of vegetation and soils on the prediction of cumulus Convective rainfall. *Reviews of Geophysics*, **39**, 151–177, DOI: 10.1029/1999RG000072.

Pitman, A. J., 2003: The evolution of, and revolution in, land surface schemes designed for climate models. *International Journal of Climatology*, **23**, 479–510, DOI: 10.1002/joc.893.

Pitman, A. J., N. de Noblet-Ducoudré, F. T. Cruz, E. L. Davin, G. B. Bonan, V. Brovkin, M. Claussen, C. Delire, L. Ganzeveld, V. Gayler, B. J. J. M. van den Hurk, P. J. Lawrence, M. K. van der Molen, C. Müller, C. H. Reick, S. I. Seneviratne, B. J. Strengers, and A. Voldoire, 2009: Uncertainties in climate responses to past land cover change: First results from the LUCID intercomparison study. *Geophysical Research Letters*, **36**, L14814, DOI: 10.1029/2009GL039076.

Poli, P., H. Hersbach, D. P. Dee, P. Berrisford, A. J. Simmons, F. Vitart, P. Laloyaux, D. G. H. Tan, C. Peubey, J.-N. Thépaut, Y. Trémolet, E. V. Hólm, M. Bonavita, L. Isaksen, and M. Fisher, 2016: ERA-20C: An atmospheric reanalysis of the twentieth century. *Journal of Climate*, **29**, 4083–4097, DOI: 10.1175/JCLI-D-15-0556.1.

Pollack, H. N. and S. Huang, 2000: Climate Reconstruction from Subsurface Temperatures. *Annual Review of Earth and Planetary Sciences*, **28**, 339–365, DOI: 10.1146/annurev.earth.28.1.339.

Pollack, H. N., J. E. Smerdon, and P. E. van Keken, 2005: Variable seasonal coupling between air and ground temperatures: A simple representation in terms of subsurface thermal diffusivity. *Geophysical Research Letters*, **32**, L15405, DOI: 10.1029/2005GL023869.

Pongratz, J., C. H. Reick, T. Raddatz, and M. Claussen, 2010: Biogeophysical versus biogeochemical climate response to historical anthropogenic land cover change. *Geophysical Research Letters*, **37**, L08702, DOI: 10.1029/2010GL043010.

Pries, C. E. H., C. Castanha, R. C. Porras, and M. S. Torn, 2017: The whole-soil carbon flux in response to warming. *Science*, **355**, 1420–1423, DOI: 10.1126/science.aal1319.

Putnam, S. N. and D. S. Chapman, 1996: A geothermal climate change observatory: First year results from Emigrant Pass in northwest Utah. *Journal of Geophysical Research: Solid Earth*, **101**, 21877–21890, DOI: 10.1029/96JB01903.

Qian, B., E. G. Gregorich, S. Gameda, D. W. Hopkins, and X. L. Wang, 2011: Observed soil temperature trends associated with climate change in Canada. *Journal of Geophysical Research: Atmospheres*, **116**, D02106, DOI: 10.1029/2010JD015012.

Rahmstorf, S. and D. Coumou, 2011: Increase of extreme events in a warming world. *Proceedings of the National Academy of Sciences*, **108**, 17905–17909, DOI: 10.1073/pnas.1101766108.

Randall, D. A., C. M. Bitz, G. Danabasoglu, A. S. Denning, P. R. Gent, A. Gettelman, S. M. Griffies, P. Lynch, H. Morrison, R. Pincus, and J. Thuburn, 2018: 100 Years of Earth System Model Development. *Meteorological Monographs*, **59**, 12.1–12.66, DOI: 10.1175/AMSMONOGRAPHS-D-18-0018.1.

Randall, D. A., R. A. Wood, S. Bony, R. Colman, T. Fichefet, J. Fyfe, V. Kattsov, A. Pitman, J. Shukla, J. Srinivasan, R. J. Stouffer, A. Sumi, and K. E. Taylor, 2007: Climate Models and Their Evaluation. *Climate Change 2007: The Physical Science Basis. Contribution of Working Group I to the Fourth Assessment Report of the Intergovernmental Panel on Climate Change*, S. Solomon, D. Qin, M. Manning, Z. Chen, M. Marquis, K. B. Averyt, M. Tignor, and

H. L. Miller, eds., Cambridge University Press, Cambridge, United Kingdom and New York, NY, USA, Chapter 8, 589–662.

Rantanen, M., A. Karpechko, A. Lipponen, K. Nordling, O. Hyvarinen, K. Ruosteenoja, T. Vihma, and A. Laaksonen, 2022: The Arctic has warmed nearly four times faster than the globe since 1979. *Communications Earth & Environment*, **3**, 168, DOI: 10.1038/s43247-022-00498-3.

Reick, C. H., V. Gayler, D. Goll, S. Hagemann, M. Heidkamp, J. E. M. S. Nabel, T. Raddatz, E. Roeckner, R. Schnur, and S. Wilkenskjeld, 2021: JSBACH 3 - The land component of the MPI Earth System Model: documentation of version 3.2. Berichte zur Erdsystemforschung. Technical Report 240, MPI für Meteorologie, Hamburg.

Rind, D., C. Orbe, J. Jonas, L. Nazarenko, T. Zhou, M. Kelley, A. Lacis, D. Shindell, G. Faluvegi, A. Romanou, G. Russell, N. Tausnev, M. Bauer, and G. Schmidt, 2020: GISS Model E2.2: A Climate Model Optimized for the Middle Atmosphere—Model Structure, Climatology, Variability, and Climate Sensitivity. *Journal of Geophysical Research: Atmospheres*, **125**, e2019JD032204, DOI: 10.1029/2019JD032204.

Roache, P. J., 1998: *Computational Fluid Dynamics*. Hermosa, 2 edition.

Robock, A., 2000: Volcanic eruptions and climate. *Reviews of Geophysics*, **38**, 191–219, DOI: 10.1029/1998RG000054.

Rohde, R. A. and Z. Hausfather, 2020: The Berkeley Earth Land/Ocean Temperature Record. *Earth System Science Data*, **12**, 3469–3479, DOI: 10.5194/essd-12-3469-2020.

Rotta Loria, A., 2023: The silent impact of underground climate change on civil infrastructure. *Communications Engineering*, **2**, 44, DOI: 10.1038/s44172-023-00092-1.

Sadeghi, M., A. Ebtehaj, M. Guala, and J. Wang, 2021: Physical connection of sensible and ground heat flux. *Journal of Hydrology*, **602**, 126687, DOI: 10.1016/j.jhydrol.2021.126687.

Sapriza-Azuri, G., P. Gamazo, S. Razavi, and H. S. Wheater, 2018: On the appropriate definition of soil profile configuration and initial conditions for land surface-hydrology models in cold regions. *Hydrology and Earth System Sciences*, **22**, 3295–3309, DOI: 10.5194/hess-22-3295-2018.

Schaefer, K., Y. Elshorbany, E. Jafarov, P. Schuster, R. Striegl, K. Wickland, and E. Sunderland, 2020: Potential impacts of mercury released from thawing permafrost. *Nature Communications*, **11**, 4650, DOI: 10.1038/s41467-020-18398-5.

Schlesinger, W. H. and S. B. Emily, 2013: *Biogeochemistry: an analysis of global change, 3rd edn*. Academic Press, Amsterdam, Netherlands.

Schleussner, C.-F., T. K. Lissner, E. M. Fischer, J. Wohland, M. Perrette, A. Golly, J. Rogelj, K. Childers, J. Schewe, K. Frieler, M. Mengel, W. Hare,

and M. Schaeffer, 2016: Differential climate impacts for policy-relevant limits to global warming: the case of 1.5 °C and 2 °C. *Earth System Dynamics*, **7**, 327–351, DOI: 10.5194/esd-7-327-2016.

Schopf, J. W., 1993: Microfossils of the Early Archean Apex Chert: New Evidence of the Antiquity of Life. *Science*, **260**, 640–646, DOI: 10.1126/science.260.5108.640.

Schulz, J.-P., L. Dümenil, and J. Polcher, 2001: On the Land Surface–Atmosphere Coupling and Its Impact in a Single-Column Atmospheric Model. *Journal of Applied Meteorology*, **40**, 642–663, DOI: 10.1175/1520-0450(2001)040¡0642:OTLSAC¿2.0.CO;2.

Schuur, E. A., B. W. Abbott, R. Commane, J. Ernakovich, E. Euskirchen, G. Hugelius, G. Grosse, M. Jones, C. Koven, V. Leshyk, D. Lawrence, M. M. Loranty, M. Mauritz, D. Olefeldt, S. Natali, H. Rodenhizer, V. Salmon, C. Schädel, J. Strauss, C. Treat, and M. Turetsky, 2022: Permafrost and Climate Change: Carbon Cycle Feedbacks From the Warming Arctic. *Annual Review of Environment and Resources*, **47**, 343–371, DOI: 10.1146/annurev-environ-012220-011847.

Seland, Ø., M. Bentsen, D. Olivié, T. Toniazzo, A. Gjermundsen, L. S. Graff, J. B. Debernard, A. K. Gupta, Y.-C. He, A. Kirkevåg, J. Schwinger, J. Tjiputra, K. S. Aas, I. Bethke, Y. Fan, J. Griesfeller, A. Grini, C. Guo, M. Ilicak, I. H. H. Karset, O. Landgren, J. Liakka, K. O. Moseid, A. Nummelin, C. Spensberger, H. Tang, Z. Zhang, C. Heinze, T. Iversen, and M. Schulz, 2020: Overview of the Norwegian Earth System Model (NorESM2) and key climate response of CMIP6 DECK, historical, and scenario simulations. *Geoscientific Model Development*, **13**, 6165–6200, DOI: 10.5194/gmd-13-6165-2020.

Self, S. and M. R. Rampino, 1981: The 1883 eruption of Krakatau. *Nature*, **294**, 699–704, DOI: 10.1038/294699a0.

Sellar, A. A., C. G. Jones, J. P. Mulcahy, Y. Tang, A. Yool, A. Wiltshire, F. M. O'Connor, M. Stringer, R. Hill, J. Palmieri, S. Woodward, L. de Mora, T. Kuhlbrodt, S. T. Rumbold, D. I. Kelley, R. Ellis, C. E. Johnson, J. Walton, N. L. Abraham, M. B. Andrews, T. Andrews, A. T. Archibald, S. Berthou, E. Burke, E. Blockley, K. Carslaw, M. Dalvi, J. Edwards, G. A. Folberth, N. Gedney, P. T. Griffiths, A. B. Harper, M. A. Hendry, A. J. Hewitt, B. Johnson, A. Jones, C. D. Jones, J. Keeble, S. Liddicoat, O. Morgenstern, R. J. Parker, V. Predoi, E. Robertson, A. Siahaan, R. S. Smith, R. Swaminathan, M. T. Woodhouse, G. Zeng, and M. Zerroukat, 2019: UKESM1: Description and Evaluation of the U.K. Earth System Model. *Journal of Advances in Modeling Earth Systems*, **11**, 4513–4558, DOI: 10.1029/2019MS001739.

Sellers, W. D., 1969: A Global Climatic Model Based on the Energy Balance of the Earth-Atmosphere System. *Journal of Applied Meteorology and Climatology*,

8, 392–400, DOI: 10.1175/1520-0450(1969)008¡0392:AGCMBO¿2.0.CO;2.

Seneviratne, S., X. Zhang, M. Adnan, W. Badi, C. Dereczynski, A. Di Luca, S. Ghosh, I. Iskandar, J. Kossin, S. Lewis, F. Otto, I. Pinto, M. Satoh, S. Vicente-Serrano, M. Wehner, and B. Zhou, 2021: Weather and Climate Extreme Events in a Changing Climate. *Climate Change 2021: The Physical Science Basis. Contribution of Working Group I to the Sixth Assessment Report of the Intergovernmental Panel on Climate Change*, V. Masson-Delmotte, P. Zhai, A. Pirani, S. L. Connors, C. Péan, S. Berger, N. Caud, Y. Chen, L. Goldfarb, M. I. Gomis, M. Huang, K. Leitzell, E. Lonnoy, J. B. R. Matthews, T. K. Maycock, T. Waterfield, O. Yelekçi, R. Yu, and B. Zhou, eds., Cambridge University Press, Cambridge, UK and New York, NY, USA, Chapter 11, 1513–1765.

Serreze, M. C., 2010: Understanding Recent Climate Change. *Conservation Biology*, **24**, 10–17, DOI: 10.1111/j.1523-1739.2009.01408.x.

Shangguan, W., T. Hengl, J. Mendes de Jesus, H. Yuan, and Y. Dai, 2017: Mapping the global depth to bedrock for land surface modeling. *Journal of Advances in Modeling Earth Systems*, **9**, 65–88, DOI: 10.1002/2016MS000686.

Sherstyukov, A. B. and B. G. Sherstyukov, 2015: Spatial features and new trends in thermal conditions of soil and depth of its seasonal thawing in the permafrost zone. *Russian Meteorology and Hydrology*, **40**, 73–78, DOI: 10.3103/S1068373915020016.

Sigl, M., M. Winstrup, J. Mcconnell, K. Welten, G. Plunkett, F. Ludlow, U. Büntgen, M. Caffee, N. Chellman, D. Dahl-Jensen, H. Fischer, S. Kipfstuhl, C. Kostick, O. Maselli, F. Mekhaldi, R. Mulvaney, R. Muscheler, D. Pasteris, J. Pilcher, and T. Woodruff, 2015: Timing and climate forcing of volcanic eruptions for the past 2,500 years. *Nature*, **523**, 543—-549, DOI: 10.1038/nature14565.

Slater, A. G. and D. M. Lawrence, 2013: Diagnosing Present and Future Permafrost from Climate Models. *Journal of Climate*, **26**, 5608–5623, DOI: 10.1175/JCLI-D-12-00341.1.

Slivinski, L. C., G. P. Compo, J. S. Whitaker, P. D. Sardeshmukh, B. S. Giese, C. McColl, R. Allan, X. Yin, R. Vose, H. Titchner, J. Kennedy, L. J. Spencer, L. Ashcroft, S. Brönnimann, M. Brunet, D. Camuffo, R. Cornes, T. A. Cram, R. Crouthamel, F. Domínguez-Castro, J. E. Freeman, J. Gergis, E. Hawkins, P. D. Jones, S. Jourdain, A. Kaplan, H. Kubota, F. L. Blancq, T.-C. Lee, A. Lorrey, J. Luterbacher, M. Maugeri, C. J. Mock, G. K. Moore, R. Przybylak, C. Pudmenzky, C. Reason, V. C. Slonosky, C. A. Smith, B. Tinz, B. Trewin, M. A. Valente, X. L. Wang, C. Wilkinson, K. Wood, and P. Wyszyński, 2019: Towards a more reliable historical reanalysis: Improvements for version 3 of the Twentieth Century Reanalysis system. *Quarterly Journal of the Royal Meteorological Society*, **145**, 2876–2908, DOI: 10.1002/qj.3598.

Smerdon, J. E. and H. N. Pollack, 2016: Reconstructing Earth's surface temperature over the past 2000 years: the science behind the headlines. *WIREs Climate Change*, **7**, 746–771, DOI: 10.1002/wcc.418.

Smerdon, J. E., H. N. Pollack, V. Cermak, J. W. Enz, M. Kresl, J. Safanda, and J. F. Wehmiller, 2004: Air-ground temperature coupling and subsurface propagation of annual temperature signals. *Journal of Geophysical Research: Atmospheres*, **109**, D21107, DOI: 10.1029/2004JD005056.

Smerdon, J. E., H. N. Pollack, J. W. Enz, and M. J. Lewis, 2003: Conduction-dominated heat transport of the annual temperature signal in soil. *Journal of Geophysical Research: Solid Earth*, **108**, 2431, DOI: 10.1029/2002JB002351.

Smerdon, J. E. and M. Stieglitz, 2006: Simulating heat transport of harmonic temperature signals in the Earth's shallow subsurface: Lower-boundary sensitivities. *Geophysical Research Letters*, **33**, L14402, DOI: 10.1029/2006GL026816.

Sokratov, S. A. and R. G. Barry, 2002: Intraseasonal variation in the thermoinsulation effect of snow cover on soil temperatures and energy balance. *Journal of Geophysical Research: Atmospheres*, **107**, D10, DOI: 10.1029/2001JD000489.

Solow, A. R., 1987: Testing for Climate Change: An Application of the Two-Phase Regression Model. *Journal of Applied Meteorology and Climatology*, **26**, 1401–1405, DOI: 10.1175/1520-0450(1987)026¡1401:TFCCAA¿2.0.CO;2.

— 1995: Testing for Change in the Frequency of El Niño Events. *Journal of Climate*, **8**, 2563–2566, DOI: 10.1175/1520-0442(1995)008¡2563:TFCITF¿2.0.CO;2.

Soong, J. L., C. Castanha, C. E. H. Pries, N. Ofiti, R. C. Porras, W. J. Riley, M. W. Schmidt, and M. S. Torn, 2021: Five years of whole-soil warming led to loss of subsoil carbon stocks and increased CO2 efflux. *Science Advances*, **7**, eabd1343, DOI: 10.1126/sciadv.abd1343.

Sorour, M., M. Saleh, and R. Mahmoud, 1990: Thermal conductivity and diffusivity of soil. *International Communications in Heat and Mass Transfer*, **17**, 189–199, DOI: 10.1016/0735-1933(90)90053-M.

Steinert, N. J., F. J. Cuesta-Valero, F. García-Pereira, P. de Vrese, C. A. Melo Aguilar, E. García-Bustamante, J. Jungclaus, and J. F. González-Rouco, 2024: Underestimated Land Heat Uptake Alters the Global Energy Distribution in CMIP6 Climate Models. *Geophysical Research Letters*, **51**, e2023GL107613, DOI: 10.1029/2023GL107613.

Steinert, N. J., M. V. Debolskiy, E. J. Burke, F. García-Pereira, and H. Lee, 2023: Evaluating permafrost definitions for global permafrost area estimates in CMIP6 climate models. *Environmental Research Letters*, **19**, 014033, DOI: 10.1088/1748-9326/ad10d7.

Steinert, N. J., J. F. González-Rouco, P. de Vrese, E. García-Bustamante, S. Hagemann, C. Melo-Aguilar, J. H. Jungclaus, and S. J. Lorenz, 2021b:

Increasing the depth of a Land Surface Model. Part II: Sensitivity to improved coupling between soil hydrology and thermodynamics and associated permafrost response. *Journal of Hydrometeorology*, **22**, 3231–3254, DOI: 10.1175/JHM-D-21-0023.1.

Steinert, N. J., J. F. González-Rouco, C. A. Melo Aguilar, F. García Pereira, E. García-Bustamante, P. de Vrese, V. Alexeev, J. H. Jungclaus, S. J. Lorenz, and S. Hagemann, 2021a: Agreement of Analytical and Simulation-Based Estimates of the Required Land Depth in Climate Models. *Geophysical Research Letters*, **48**, e2021GL094273, DOI: 10.1029/2021GL094273.

Stenchikov, G., T. L. Delworth, V. Ramaswamy, R. J. Stouffer, A. Wittenberg, and F. Zeng, 2009: Volcanic signals in oceans. *Journal of Geophysical Research: Atmospheres*, **114**, D16, DOI: 10.1029/2008JD011673.

Stephens, G. L., 2005: Cloud Feedbacks in the Climate System: A Critical Review. *Journal of Climate*, **18**, 237–273, DOI: 10.1175/JCLI-3243.1.

Stevens, B., M. Giorgetta, M. Esch, T. Mauritsen, T. Crueger, S. Rast, M. Salzmann, H. Schmidt, J. Bader, K. Block, R. Brokopf, I. Fast, S. Kinne, L. Kornblueh, U. Lohmann, R. Pincus, T. Reichler, and E. Roeckner, 2013: Atmospheric component of the MPI-M Earth System Model: ECHAM6. *Journal of Advances in Modeling Earth Systems*, **5**, 146–172, DOI: 10.1002/jame.20015.

Stevens, B., J. E. Smerdon, J. F. González-Rouco, M. Stieglitz, and H. Beltrami, 2007: Effects of bottom boundary placement on subsurface heat storage: Implications for climate model simulations. *Geophysical Research Letters*, **34**, L02702, DOI: 10.1029/2006GL028546.

Stjern, C. W., B. H. Samset, O. Boucher, T. Iversen, J.-F. Lamarque, G. Myhre, D. Shindell, and T. Takemura, 2020: How aerosols and greenhouse gases influence the diurnal temperature range. *Atmospheric Chemistry and Physics*, **20**, 13467–13480, DOI: 10.5194/acp-20-13467-2020.

Stoica, P. and R. Moses, 1997: *Introduction to spectral analysis*. Prentice Hall, Upper Saddle River, N.J.

Stoler, J., A. L. Pearson, A. Y. Rosinger, A. E. Lee, R. Bombardi, A. Brewis, S. B. Keough, D. López-Carr, C.-H. Shrader, C. E. Stauber, E. G. J. Stevenson, A. Sullivan, and R. A. Tutu, 2022: The role of water in environmental migration. *WIREs Water*, **9**, e1584, DOI: 10.1002/wat2.1584.

Sturm, M., J. Holmgren, M. König, and K. Morris, 1997: The thermal conductivity of seasonal snow. *Journal of Glaciology*, **43**, 26–41, DOI: 10.3189/S0022143000002781.

Svoray, T., 2022: *Soil Erosion: The General Problem*, Springer International Publishing, Cham, Chapter 1. 1–38.

Swart, N. C., J. N. S. Cole, V. V. Kharin, M. Lazare, J. F. Scinocca, N. P. Gillett, J. Anstey, V. Arora, J. R. Christian, S. Hanna, Y. Jiao, W. G. Lee, F. Majaess,

O. A. Saenko, C. Seiler, C. Seinen, A. Shao, M. Sigmond, L. Solheim, K. von Salzen, D. Yang, and B. Winter, 2019: The Canadian Earth System Model version 5 (CanESM5.0.3). *Geoscientific Model Development*, **12**, 4823–4873, DOI: 10.5194/gmd-12-4823-2019.

Séférian, R., P. Nabat, M. Michou, D. Saint-Martin, A. Voldoire, J. Colin, B. Decharme, C. Delire, S. Berthet, M. Chevallier, S. Sénési, L. Franchisteguy, J. Vial, M. Mallet, E. Joetzjer, O. Geoffroy, J.-F. Guérémy, M.-P. Moine, R. Msadek, A. Ribes, M. Rocher, R. Roehrig, D. Salas-y Mélia, E. Sanchez, L. Terray, S. Valcke, R. Waldman, O. Aumont, L. Bopp, J. Deshayes, C. Éthé, and G. Madec, 2019: Evaluation of CNRM Earth System Model, CNRM-ESM2-1: Role of Earth System Processes in Present-Day and Future Climate. *Journal of Advances in Modeling Earth Systems*, **11**, 4182–4227, DOI: 10.1029/2019MS001791.

Tardif, R., G. J. Hakim, W. A. Perkins, K. A. Horlick, M. P. Erb, J. Emile-Geay, D. M. Anderson, E. J. Steig, and D. Noone, 2019: Last Millennium Reanalysis with an expanded proxy database and seasonal proxy modeling. *Climate of the Past*, **15**, 1251–1273, DOI: 10.5194/cp-15-1251-2019.

Tatebe, H., T. Ogura, T. Nitta, Y. Komuro, K. Ogochi, T. Takemura, K. Sudo, M. Sekiguchi, M. Abe, F. Saito, M. Chikira, S. Watanabe, M. Mori, N. Hirota, Y. Kawatani, T. Mochizuki, K. Yoshimura, K. Takata, R. O'ishi, D. Yamazaki, T. Suzuki, M. Kurogi, T. Kataoka, M. Watanabe, and M. Kimoto, 2019: Description and basic evaluation of simulated mean state, internal variability, and climate sensitivity in MIROC6. *Geoscientific Model Development*, **12**, 2727–2765, DOI: 10.5194/gmd-12-2727-2019.

Taylor, K. E., R. J. Stouffer, and G. A. Meehl, 2012: An Overview of CMIP5 and the Experiment Design. *Bulletin of the American Meteorological Society*, **93**, 485–498, DOI: 10.1175/BAMS-D-11-00094.1.

Tong, B., Z. Gao, R. Horton, Y. Li, and L. Wang, 2016: An Empirical Model for Estimating Soil Thermal Conductivity from Soil Water Content and Porosity. *Journal of Hydrometeorology*, **17**, 601–613, DOI: 10.1175/JHM-D-15-0119.1.

Tong, B., Z. Gao, R. Horton, and L. Wang, 2017: Soil Apparent Thermal Diffusivity Estimated by Conduction and by Conduction–Convection Heat Transfer Models. *Journal of Hydrometeorology*, **18**, 109–118, DOI: 10.1175/JHM-D-16-0086.1.

Toohey, M. and M. Sigl, 2017: Volcanic stratospheric sulfur injections and aerosol optical depth from 500 BCE to 1900 CE. *Earth System Science Data*, **9**, 809–831, DOI: 10.5194/essd-9-809-2017.

Tukey, J. W., 1977: *Exploratory Data Analysis*. Addison-Wesley Publishing Company Reading, Massachusetts.

Turetsky, M., B. Abbott, M. Jones, K. Walter Anthony, D. Olefeldt, E. Schuur, C. Koven, A. McGuire, G. Grosse, P. Kuhry, G. Hugelius, D. Lawrence, C. Gibson, and A. Sannel, 2019: Permafrost collapse is accelerating carbon release. *Nature*, **569**, 32–34, DOI: 10.1038/d41586-019-01313-4.

van Dijk, E., J. Jungclaus, S. Lorenz, C. Timmreck, and K. Krüger, 2022: Was there a volcanic-induced long-lasting cooling over the Northern Hemisphere in the mid-6th-7th century? *Climate of the Past*, **18**, 1601–1623, DOI: 10.5194/cp-18-1601-2022.

Vegas-Cañas, C., J. F. González-Rouco, J. Navarro-Montesinos, E. García-Bustamante, E. E. Lucio-Eceiza, F. García-Pereira, E. Rodríguez-Camino, A. Chazarra-Bernabé, and I. Álvarez Arévalo, 2020: An Assessment of Observed and Simulated Temperature Variability in Sierra de Guadarrama. *Atmosphere*, **11(9)**, DOI: 10.3390/atmos11090985.

Vicente-Serrano, S., C. Azorin-Molina, A. Sanchez-Lorenzo, E. Morán-Tejeda, J. Lorenzo-Lacruz, J. Revuelto, J. López-Moreno, and F. Espejo, 2013: Temporal evolution of surface humidity in Spain: Recent trends and possible physical mechanisms. *Climate Dynamics*, **42**, 2655–2674, DOI: 10.1007/s00382-013-1885-7.

Vieira, L. E. A., S. K. Solanki, N. A. Krivova, and I. Usoskin, 2011: Evolution of the solar irradiance during the Holocene. *Astronomy & Astrophysics*, **531**, A6, DOI: 10.1051/0004-6361/201015843.

Vitousek, P. M., H. A. Mooney, J. Lubchenco, and J. M. Melillo, 1997: Human Domination of Earth's Ecosystems. *Science*, **277**, 494–499, DOI: 10.1126/science.277.5325.494.

Voldoire, A., D. Saint-Martin, S. Sénési, B. Decharme, A. Alias, M. Chevallier, J. Colin, J.-F. Guérémy, M. Michou, M.-P. Moine, P. Nabat, R. Roehrig, D. Salas y Mélia, R. Séférian, S. Valcke, I. Beau, S. Belamari, S. Berthet, C. Cassou, J. Cattiaux, J. Deshayes, H. Douville, C. Ethé, L. Franchistéguy, O. Geoffroy, C. Lévy, G. Madec, Y. Meurdesoif, R. Msadek, A. Ribes, E. Sanchez-Gomez, L. Terray, and R. Waldman, 2019: Evaluation of CMIP6 DECK Experiments With CNRM-CM6-1. *Journal of Advances in Modeling Earth Systems*, **11**, 2177–2213, DOI: 10.1029/2019MS001683.

von Schuckmann, K., L. Cheng, M. D. Palmer, J. Hansen, C. Tassone, V. Aich, S. Adusumilli, H. Beltrami, T. Boyer, F. J. Cuesta-Valero, D. Desbruyères, C. Domingues, A. García-García, P. Gentine, J. Gilson, M. Gorfer, L. Haimberger, M. Ishii, G. C. Johnson, R. Killick, B. A. King, G. Kirchengast, N. Kolodziejczyk, J. Lyman, B. Marzeion, M. Mayer, M. Monier, D. P. Monselesan, S. Purkey, D. Roemmich, A. Schweiger, S. I. Seneviratne, A. Shepherd, D. A. Slater, A. K. Steiner, F. Straneo, M.-L. Timmermans, and S. E. Wijf-

fels, 2020: Heat stored in the Earth system: where does the energy go? *Earth System Science Data*, **12**, 2013–2041, DOI: 10.5194/essd-12-2013-2020.

von Schuckmann, K., A. Minière, F. Gues, F. J. Cuesta-Valero, G. Kirchengast, S. Adusumilli, F. Straneo, M. Ablain, R. P. Allan, P. M. Barker, H. Beltrami, A. Blazquez, T. Boyer, L. Cheng, J. Church, D. Desbruyeres, H. Dolman, C. M. Domingues, A. García-García, D. Giglio, J. E. Gilson, M. Gorfer, L. Haimberger, M. Z. Hakuba, S. Hendricks, S. Hosoda, G. C. Johnson, R. Killick, B. King, N. Kolodziejczyk, A. Korosov, G. Krinner, M. Kuusela, F. W. Landerer, M. Langer, T. Lavergne, I. Lawrence, Y. Li, J. Lyman, F. Marti, B. Marzeion, M. Mayer, A. H. MacDougall, T. McDougall, D. P. Monselesan, J. Nitzbon, I. Otosaka, J. Peng, S. Purkey, D. Roemmich, K. Sato, K. Sato, A. Savita, A. Schweiger, A. Shepherd, S. I. Seneviratne, L. Simons, D. A. Slater, T. Slater, A. K. Steiner, T. Suga, T. Szekely, W. Thiery, M.-L. Timmermans, I. Vanderkelen, S. E. Wjiffels, T. Wu, and M. Zemp, 2023: Heat stored in the Earth system 1960-2020: where does the energy go? *Earth System Science Data*, **15**, 1675–1709, DOI: 10.5194/essd-15-1675-2023.

von Storch, H., 2010: Climate models and modeling: an editorial essay. *WIREs Climate Change*, **1**, 305–310, DOI: 10.1002/wcc.12.

Vonk, J. E., S. E. Tank, W. B. Bowden, I. Laurion, W. F. Vincent, P. Alekseychik, M. Amyot, M. F. Billet, J. Canário, R. M. Cory, B. N. Deshpande, M. Helbig, M. Jammet, J. Karlsson, J. Larouche, G. MacMillan, M. Rautio, K. M. Walter Anthony, and K. P. Wickland, 2015: Reviews and syntheses: Effects of permafrost thaw on Arctic aquatic ecosystems. *Biogeosciences*, **12**, 7129–7167, DOI: 10.5194/bg-12-7129-2015.

Voss, R. and U. Mikolajewicz, 2001: The climate of 6000 years BP in near-equilibrium simulations with a coupled AOGCM. *Geophysical Research Letters*, **28**, 2213–2216, DOI: 10.1029/2000GL012498.

Walvoord, M. A. and B. L. Kurylyk, 2016: Hydrologic Impacts of Thawing Permafrost—A Review. *Vadose Zone Journal*, **15**, vzj2016.01.0010, DOI: 10.2136/vzj2016.01.0010.

Wang, F., F. Cheruy, and J.-L. Dufresne, 2016: The improvement of soil thermodynamics and its effects on land surface meteorology in the IPSL climate model. *Geoscientific Model Development*, **9**, 363–381, DOI: 10.5194/gmd-9-363-2016.

Wang, K. and R. E. Dickinson, 2012: A review of global terrestrial evapotranspiration: Observation, modeling, climatology, and climatic variability. *Reviews of Geophysics*, **50**, RG2005, DOI: 10.1029/2011RG000373.

Wang, Y.-C., H.-H. Hsu, C.-A. Chen, W.-L. Tseng, P.-C. Hsu, C.-W. Lin, Y.-L. Chen, L.-C. Jiang, Y.-C. Lee, H.-C. Liang, W.-M. Chang, W.-L. Lee, and C.-J. Shiu, 2021: Performance of the Taiwan Earth System Model in Simulating Climate Variability Compared With Observations and CMIP6 Model Simula-

tions. *Journal of Advances in Modeling Earth Systems*, **13**, e2020MS002353, DOI: 10.1029/2020MS002353.

Weber, S. L., 2010: The utility of Earth system Models of Intermediate Complexity (EMICs). *WIREs Climate Change*, **1**, 243–252, DOI: 10.1002/wcc.24.

Westermann, S., T. Ingeman-Nielsen, J. Scheer, K. Aalstad, J. Aga, N. Chaudhary, B. Etzelmüller, S. Filhol, A. Kääb, C. Renette, L. S. Schmidt, T. V. Schuler, R. B. Zweigel, L. Martin, S. Morard, M. Ben-Asher, M. Angelopoulos, J. Boike, B. Groenke, F. Miesner, J. Nitzbon, P. Overduin, S. M. Stuenzi, and M. Langer, 2023: The CryoGrid community model (version 1.0) - a multi-physics toolbox for climate-driven simulations in the terrestrial cryosphere. *Geoscientific Model Development*, **16**, 2607–2647, DOI: 10.5194/gmd-16-2607-2023.

Williams, K. D., D. Copsey, E. W. Blockley, A. Bodas-Salcedo, D. Calvert, R. Comer, P. Davis, T. Graham, H. T. Hewitt, R. Hill, P. Hyder, S. Ineson, T. C. Johns, A. B. Keen, R. W. Lee, A. Megann, S. F. Milton, J. G. L. Rae, M. J. Roberts, A. A. Scaife, R. Schiemann, D. Storkey, L. Thorpe, I. G. Watterson, D. N. Walters, A. West, R. A. Wood, T. Woollings, and P. K. Xavier, 2018: The Met Office Global Coupled Model 3.0 and 3.1 (GC3.0 and GC3.1) Configurations. *Journal of Advances in Modeling Earth Systems*, **10**, 357–380, DOI: 10.1002/2017MS001115.

Willmott, C. J. and K. Matsuura, 2018: Terrestrial Air Temperature and Precipitation: Monthly and Annual Time Series (1900–2017). https://psl.noaa.gov/data/gridded/data.UDel_AirT_Precip.html.

Winkler, K., R. Fuchs, M. Rounsevell, and M. Herold, 2021: Global land use changes are four times greater than previously estimated. *Nature Communications*, **12**, 2501, DOI: 10.1038/s41467-021-22702-2.

Wu, T., Y. Lu, Y. Fang, X. Xin, L. Li, W. Li, W. Jie, J. Zhang, Y. Liu, L. Zhang, F. Zhang, Y. Zhang, F. Wu, J. Li, M. Chu, Z. Wang, X. Shi, X. Liu, M. Wei, A. Huang, Y. Zhang, and X. Liu, 2019: The Beijing Climate Center Climate System Model (BCC-CSM): the main progress from CMIP5 to CMIP6. *Geoscientific Model Development*, **12**, 1573–1600, DOI: 10.5194/gmd-12-1573-2019.

Yokohata, T., K. Saito, K. Takata, T. Nitta, Y. Satoh, T. Hajima, T. Sueyoshi, and G. Iwahana, 2020: Model improvement and future projection of permafrost processes in a global land surface model. *Progress in Earth and Planetary Science*, **7**, 69, DOI: 10.1186/s40645-020-00380-w.

Yuan, K., Q. Zhu, S. Zheng, L. Zhao, M. Chen, W. Riley, X. Cai, H. Ma, F. Li, H. Wu, and L. Chen, 2021: Deforestation reshapes land-surface energy-flux partitioning. *Environmental Research Letters*, **16**, 024014, DOI: 10.1088/1748-9326/abd8f9.

Yukimoto, S., H. Kawai, T. Koshiro, N. Oshima, K. Yoshida, S. Urakawa, H. Tsujino, M. Deushi, T. Tanaka, M. Hosaka, S. Yabu, H. Yoshimura, E. Shindo, R. Mizuta, A. Obata, Y. Adachi, and M. Ishii, 2019: The Meteorological Research Institute Earth System Model Version 2.0, MRI-ESM2.0: Description and Basic Evaluation of the Physical Component. *Journal of the Meteorological Society of Japan. Ser. II*, **97**, 931–965, DOI: 10.2151/jmsj.2019-051.

Zeebe, R. E., A. Ridgwell, and J. C. Zachos, 2016: Anthropogenic carbon release rate unprecedented during the past 66 million years. *Nature Geoscience*, **9**, 325–329, DOI: 10.1038/ngeo2681.

Zhang, H., E. Wang, D. Zhou, Z. Luo, and Z. Zhang, 2016: Rising soil temperature in China and its potential ecological impact. *Scientific Reports*, **6**, 35530, DOI: 10.1038/srep35530.

Zhang, H., M. Zhang, J. Jin, K. Fei, D. Ji, C. Wu, J. Zhu, J. He, Z. Chai, J. Xie, X. Dong, D. Zhang, X. Bi, H. Cao, H. Chen, K. Chen, X. Chen, X. Gao, H. Hao, J. Jiang, X. Kong, S. Li, Y. Li, P. Lin, Z. Lin, H. Liu, X. Liu, Y. Shi, M. Song, H. Wang, T. Wang, X. Wang, Z. Wang, Y. Wei, B. Wu, Z. Xie, Y. Xu, Y. Yu, L. Yuan, Q. Zeng, X. Zeng, S. Zhao, G. Zhou, and J. Zhu, 2020: Description and Climate Simulation Performance of CAS-ESM Version 2. *Journal of Advances in Modeling Earth Systems*, **12**, e2020MS002210, DOI: 10.1029/2020MS002210.

Zhang, H.-M., B. Huang, J. H. Lawrimore, M. J. Menne, and T. M. Smith, 2019: NOAA Global Surface Temperature Dataset (NOAAGlobalTemp), Version 5.0. *NOAA National Centers for Environmental Information*, DOI: 10.25921/9qth-2p70.

Zhang, T., 2005: Influence of the seasonal snow cover on the ground thermal regime: An overview. *Reviews of Geophysics*, **43**, RG4002, DOI: 10.1029/2004RG000157.

Zhang, Y., A. B. Sherstiukov, B. Qian, S. V. Kokelj, and T. C. Lantz, 2018: Impacts of snow on soil temperature observed across the circumpolar north. *Environmental Research Letters*, **13**, 044012, DOI: 10.1088/1748-9326/aab1e7.

Zhu, X., S.-Y. Lee, X. Wen, Z. Wei, Z. Ji, Z. Zheng, and W. Dong, 2021: Historical evolution and future trend of Northern Hemisphere snow cover in CMIP5 and CMIP6 models. *Environmental Research Letters*, **16**, 065013, DOI: 10.1088/1748-9326/ac0662.

Ziehn, T., M. Chamberlain, R. Law, A. Lenton, R. Bodman, M. Dix, L. Stevens, Y. Wang, and J. Srbinovsky, 2020: The Australian Earth System Model: ACCESS-ESM1.5. *Journal of Southern Hemisphere Earth Systems Science*, **70**, 193–214, DOI: 10.1071/ES19035.

Zommers, Z., P. Marbaix, A. Fischlin, Z. Z. Ibrahim, S. Grant, A. K. Magnan, H.-O. Pörtner, M. Howden, K. Calvin, K. Warner, W. Thiery, Z. Sebesvari, E. L.

Davin, J. P. Evans, C. Rosenzweig, B. C. O'Neill, A. Patwardhan, R. Warren, M. K. van Aalst, and M. Hulbert, 2020: Burning embers: towards more transparent and robust climate-change risk assessments. *Nature Reviews Earth & Environment*, **1**, 516–529, DOI: 10.1038/s43017-020-0088-0.